A Novel Approach to Investigating Chlorophyll-a Fluorescence Quantum Yield Variability in the Southern Ocean

Emma Lewis Bone

Thesis presented for the degree of
Doctor of Philosophy

Department of Oceanography
University of Cape Town
October 2019

Declaration

The present work has been written by me, with full support of my supervisors: A/ Prof. Marcello Vichi of the Department of Oceanography, University of Cape Town, and Drs. Sandy J. Thomalla, Stewart Bernard, Marié E. Smith, and Thomas J. Ryan-Keogh, of the Natural Resources and the Environment research sector of the Council for Scientific and Industrial Research. In addition, important contributions to the approach used in this study are clearly acknowledged through referencing within the text. I confirm that I have been granted permission by the University of Cape Town's Doctoral Degrees Board to include the following publication in my thesis, and where co-authorships are involved, my co-authors have agreed that I may include the publication:

- Griffith, D.J., Bone, E.L., Thomalla, S.J., and Bernard, S. (2018). Calibration of an in-water multi-excitation fluorometer for the measurement of phytoplankton chlorophyll-a fluorescence quantum yield. Optics Express, 26(15):18863-18877.

I, Emma Lewis Bone, hereby declare that the work on which this thesis is based is my original work (except where indicated otherwise) and that neither the whole work nor any part of it has been, is being, or is to be submitted for another degree at the University of Cape Town, or any other university. I authorise the University of Cape Town to reproduce the thesis, in whole or in part, for the purpose of research.

Signed by candidate

Emma Lewis Bone October 2019

Abstract

The apparent fluorescence quantum yield of chlorophyll-*a* (Φ_F), i.e. the ratio of photons emitted as chlorophyll-*a* fluorescence to those absorbed by phytoplankton, serves as a first order measure of photosynthetic efficiency and a photophysiological indicator of the resident phytoplankton community. Drivers of Φ_F variability, including taxonomy, nutrient availability, and light history, differ in magnitude of influence across various biogeographic provinces and seasons. A Multi-Exciter Fluorometer (MFL, JFE Advantech Co., Ltd.) was selected for use in *in situ* Φ_F derivation and underwent an extensive radiometric calibration for this purpose. Wavelength-specific Φ_F was determined for 66 *in situ* field stations, sampled in the Atlantic Southern Ocean during the austral winter of 2012 and summer of 2013/ 2014. Phytoplankton pigments, macronutrient concentrations, and light levels were simultaneously measured to investigate their influence on Φ_F. While no relationship was observed between macronutrient levels and Φ_F, an inverse relationship between light and Φ_F was apparent. This was likely due to the influence of species-specific fluorescence quenching mechanisms employed by local populations. Φ_F derived from ocean colour products (Φ_{sat}) from the Moderate Resolution Imaging Spectroradiometer (MODIS) were compared to *in situ* Φ_F to assess the performance of three existing Φ_{sat} algorithms. Results indicate that accounting for chlorophyll-*a* fluorescence reabsorption, the inherent optical properties of the surrounding water column, and the sensor angle of observation, is crucial to reducing Φ_{sat} uncertainty. A hybrid combination of two of the algorithms performed best, and was used to derive Φ_{sat} for stations co-located to *in situ* iron measurements in the Atlantic Southern Ocean. A significant negative relationship was observed, indicative of the effects of iron availability on quantum yield and its potential as a proxy for iron limitation. However, separating the individual contributions of light, taxonomy, and iron limitation to Φ_{sat} variability remains a challenge. A time series analysis of Φ_{sat} was also undertaken, which revealed a prominent Φ_{sat} seasonal cycle. Ultimately, increased *in situ* sampling would expedite the development of improved Φ_{sat} algorithms; the routine retrieval of Φ_{sat} would offer insight into phytoplankton dynamics in undersampled regions such as the climate relevant Southern Ocean.

Acknowledgements

For academic support, time, and guidance I would like to thank my supervisors A/Prof. Marcello Vichi and Drs. Sandy J. Thomalla, Stewart Bernard, Marié E. Smith, and Thomas. J. Ryan-Keogh. For funding, I gratefully acknowledge: The National Research Foundation (NRF), the Applied Centre for Climate and Earth System Science (ACCESS), the Marine-Research (Ma-Re) Institute at the University of Cape Town, and the Nansen-Tutu Centre for Marine Environmental Research; with thanks to Sharon Bosma for efficiently mediating the transfer of funds. For time and effort, I am grateful to Derek J. Griffith (CSIR) for his extensive help in re-purposing the Multi-Exciter Fluorometer, and Bertus Theron (CSIR) for his technical assistance in the lab. Without the unwavering support of Derek over the 5 year calibration process, this thesis would not have been possible. For additional technical support, thank you to Josephine Ras (LOV) for HPLC training, to Trevor Probyn (DAFF) for the use of various oceanographic equipment, and to Derek Needham and his team at Sea Technology Services, for always ensuring the optimal running of equipment. Many thanks to the crew operating onboard the *S.A. Agulhas* and *S.A. Agulhas II* between 2012-2015. To the many fellow post-graduate students, surfing associates, and friends for seeing me through from start to finish, I thank you (alphabetically, of course): Amber J., Amy S-K., Bongani X., Cathryn S., Chelsea N., Chloë H., Cyril N., Gemma R., Johno, H., Lara R., Lauren D., Linda D., Lisl R., Luke G., Marié S., Meg F., Michael H., Penny S., Robin DK., Robin K., Ryan B., Sandile M., Sarah N., Simon B., Tammy R., Tarryn C., and Wade B.; with a special thank you to my nearest and dearest: Ali, Bronny, Kirsty, and Tommy. A big thank you to my partner Kyle, whose love, understanding, support, and flawless cooking skills have got me through this thesis; thank you for everything, you are my rock. Final thanks go to my family, including the Sutherlands, the Davissons, and all the Bones and Weavers around the world. To my mom Julie, thank you for always encouraging my academic endeavours and providing invaluable emotional support. To my dad Martin, thanks for all the dad humour and looking after me well past my expiry date! To my brother James, thank you for being the best brother I could ask for.

List of Notation

a	-	Absorption (m^{-1})
a_d	-	Detrital absorption (m^{-1})
a_{ij}	-	Absorption coefficient of fluorophore i over LED j spectrum (cm^{-1})
a_j^*	-	Phytoplankton-specific absorption coefficient, LED j (cm^{-1})
a_p	-	Total particulate absorption (m^{-1})
a_{ph}	-	Phytoplankton-specific absorption (m^{-1})
a_{ph}^*	-	Chl-a-specific absorption (m^2 mg chl-a^{-1})
$\overline{a}_\phi^*$	-	Mean chl-a-specific absorption (m^2 mg chl-a^{-1})
a_s	-	Absorption by dissolved material (m^{-1})
a_w	-	Absorption by water (0.461 m^{-1} Pope and Fry (1997))
ACC	-	Antarctic Circumpolar Current
Allo.	-	Alloxanthin
AOP	-	Apparent optical properties
AVISO	-	Archiving, Validation, and Interpretation of Satellite Oceanographic data
AZ	-	Antarctic zone
BRx	-	Buoy Run (SANAE53)
C	-	Carbon
c	-	Speed of light ($3e^8$ m s^{-1})
C_f	-	MODIS proportionality factor (43.38 nm)
CDOM	-	Coloured dissolved organic material
CEF	-	Cyclic electron flow
CHEMTAX	-	CHEMical TAXonomy
chl-a	-	Chlorophyll-a (mg m^{-3})
chlor_a	-	MODIS OC3M [chl-a] estimate (mg m^{-3})
CLS	-	Collecte Localisation Satellites
CO_2	-	Carbon dioxide
CZCS	-	Coastal Zone Color Scanner (NASA)
Dd	-	Diadinoxanthin
DFe	-	Dissolved iron (nM)
dH_2O	-	Distilled water

DP	-	Diagnostic pigments
Dt	-	Diatoxanthin
ENSO	-	El Niño-Southern Oscillation
EOF	-	Empirical orthogonal function
Fe	-	Iron
FOV	-	Field-of-view
FQY	-	Fluorescence quantum yield
FTU	-	Formazine Turbidity Units
Fuco.	-	Fucoxanthin
$g_j(z)$	-	Distance calibration functions for MFL, LED j
G_j	-	MFL calibration factors for LED j
GHNx	-	GoodHope North leg (SANAE53)
GHSx	-	GoodHope South leg (SANAE53)
GMT	-	Greenwich Mean Time
h	-	Planck's constant ($6.63e^{-34}$)
H_2O	-	Water
Hex.	-	19'Hexanoyloxyfucoxanthin
HNLC	-	High nutrient low chlorophyll
HPLC	-	High performance liquid chromatography
IOP	-	Inherent optical properties
iPAR	-	MODIS instantaneous PAR (mol m^{-2} s^{-1})
Kd_490	-	($K_d(490)$) Diffuse attenuation coefficient for downwelling irradiance at 490 nm (m^{-1})
k_{ij}	-	MFL calibration constant for fluorophore i, LED j
k_j	-	MFL calibration constant, LED j
LED	-	Light emitting diode
LET	-	Linear electron transport
LHC	-	Light-harvesting complex
MADT	-	Maps of absolute dynamic topography
MARD	-	Mean absolute relative difference
MFL	-	Multi-Exciter Fluorometer (JFE Advantech, Co., Ltd.)
MIZ	-	Marginal ice zone
mLD	-	Mixed layer depth
MODIS	-	Moderate Resolution Imaging Spectroradiometer
N	-	Nitrogen
NASA	-	National Aeronautics and Space Administration
NetCDF	-	Network common data form
nflh	-	(FLH) MODIS normalised fluorescence line height (W m^{-2} μm^{-1} sr^{-1})
NO_3^-	-	Nitrate (μM)

O_2	-	Oxygen
P	-	Phosphorous
PO_4^{3-}	-	Phosphate
p_c	-	MFL-relative partial quantum yield factor for chl-a
p_i	-	MFL-relative partial quantum yield factor for fluorophore i
PAR	-	Photosynthetically available radiation (400-700 nm)
PC	-	Phycocyanin
PE	-	Phycoerythrin
Per.	-	Peridinin
PF	-	Polar front
PFZ	-	Polar frontal zone
POC	-	Particulate organic carbon
POOZ	-	Permanently open ocean zone
ppb	-	Parts-per-billion
PS	-	Photosystem
Q_a^*	-	Chl-a fluorescence reabsorption factor (unitless)
qE	-	qN: Energy dependent quenching
qI	-	qN: Photoinhibition
qN	-	Non-photochemical quenching of chl-a fluorescence
qP	-	Photochemical quenching of chl-a fluorescence
qT	-	qN: State transitions
R_{ij}	-	MFL output response to fluorophore i, LED j
R_j	-	MFL output response in LED j
r_s	-	Spearman's *rho*
RMSD	-	Root mean square difference
RMSE	-	Root mean square error
R_{rs}	-	Remote sensing reflectance
RWT	-	Rhodamine-WT
S	-	Detrital absorption slope value (nm^{-1})
S_{beh}	-	Correction factor (Behrenfeld et al. (2009) Φ_{sat} algorithm, 100 mW cm^{-2} μm^{-1} sr^{-1})
$S_i(\lambda)$	-	Relative fluorescent emission spectrum for solution i
SACCf	-	Southern Antarctic Circumpolar Current front
SAF	-	Sub-Antarctic front
SAM	-	Southern Annular Mode
SANAE	-	South African National Antarctic Expedition 53
SAZ	-	Sub-Antarctic zone
SBdy	-	Southern boundary of the ACC
SCF	-	Spectral correction factor

SD	-	Standard deviation
SDS	-	Scientific Data System
SeaWiFS	-	Sea-Viewing Wide Field-of-View Sensor (NASA)
SICF	-	Sun-induced chlorophyll fluorescence
$Si(OH)_4$	-	Silicate (μM)
SIZ	-	Seasonal ice zone
SST	-	Sea-surface temperature (°C)
STF	-	Sub-tropical front
STZ	-	Sub-tropical zone
t	-	Physical thickness (cm)
$T(\lambda)$	-	Spectral transmittance
T_{fj}	-	Effective filter transmittance for LED j
T_{ij}	-	Effective fluorophore transmittance for LED j
TOA	-	Top of the atmosphere
XC	-	Xanthophyll cycle
z	-	Distance
Zea.	-	Zeaxanthin
Δ	-	Change
$\Gamma(\lambda)$	-	MFL sensor relative quantum spectral response
λ	-	Wavelength (nm)
Φ_F	-	Fluorescence quantum yield of chl-a
$\Phi_F(435)$	-	*In situ* Φ_F derived from MFL LED 435 nm
$\Phi_F(570)$	-	*In situ* Φ_F derived from MFL LED 570 nm
Φ_{Bab}	-	Φ_{sat} derived through the Babin et al. (1996b) algorithm
Φ_{Beh}	-	Φ_{sat} derived through the Behrenfeld et al. (2009) algorithm
Φ_{Huo}	-	Φ_{sat} derived through the Huot et al. (2005) algorithm
Φ_{HB}	-	Φ_{sat} derived through the hybrid Huot et al. (2005)/ Babin et al. (1996b) algorithm
Φ_i	-	Total fluorescence quantum yield for fluorophore i
Φ_j	-	Total fluorescence quantum yield for LED j
Φ_{sat}	-	Satellite-derived fluorescence quantum yield of chl-a
Φ_F(sc)	-	Spectrally-corrected *in situ* $\Phi_F(435)$
ΣPARx	-	Cumulative PAR over 20 min/ 6 h/ 12 h/ 24 h (mol m^{-2} s^{-1})
θ'	-	Sensor viewing angle of observation (radians)

Contents

List of Figures

List of Tables

Chapter 1

Introduction

1.1 The Southern Ocean and the Global Carbon Cycle

1.1.1 The Southern Ocean

The Southern Ocean constitutes ∼20% of the world oceans and plays a significant role in global climate regulation (Boyd, 2002; Frölicher et al., 2015; Sarmiento et al., 1998). These waters connect the Atlantic, Indian, and Pacific Oceans and are defined by meridional gradients in surface characteristics that separate the Southern Ocean from the warmer and saltier waters of the subtropical circulation (Orsi et al., 1995). The Southern Ocean exists south of ∼30°S, with the northern boundary ∼5° of latitude north of the mean position of the northern Subtropical Front, as defined by Belkin and Gordon (1996).

The Southern Ocean comprises several zones separated by circumpolar fronts, subdividing water masses with different physicochemical features including density, salinity, temperature, and nutrients (Figure 1.1) (Pollard et al., 2002; Sokolov and Rintoul, 2002). These fronts vary temporally and with longitude (Orsi et al., 1995). From north to south the major fronts are the Subtropical Front (STF), the Subantarctic Front (SAF), the Polar Front (PF), the Southern Antarctic Circumpolar Current Front (SACCf), and the Southern Boundary of the ACC (SBdy). The Subantarctic Zone (SAZ) lies between the STF and the SAF, the Polar Frontal Zone (PFZ) between the SAF and the PF, and the Antarctic Zone (AZ) between the PF and the SBdy.

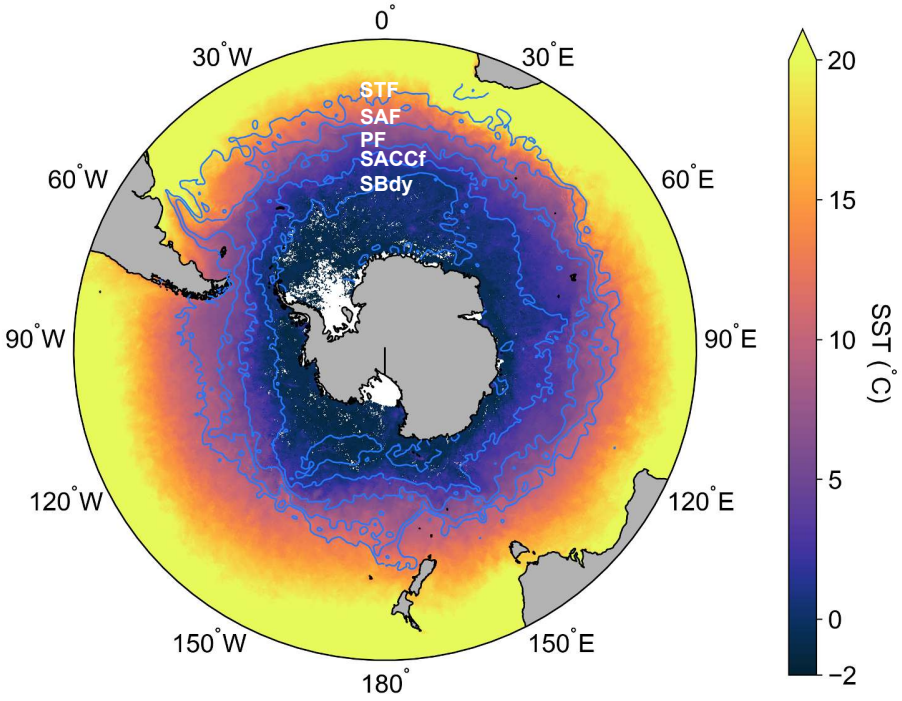

Figure 1.1: Composite map of Moderate Resolution Imaging Spectroradiometer (MODIS)-Aqua-derived sea-surface temperature (SST, monthly, 9 km) for December 2013 and January 2014. The Southern Ocean fronts for this point in time were determined by maps of absolute dynamic topography (MADT) from the CLS/AVISO product (Rio et al., 2011; Swart et al., 2010). The fronts are listed from north to south as follows: the Subtropical Front (STF), the Subantarctic Front SAF), the Polar Front (PF), Southern Antarctic Circumpolar Current Front (SACCf), and the Southern Boundary of the ACC (SBdy).

1.1.2 Climate change and carbon cycling

Human activity is responsible for the rapid restructuring of the earth's atmosphere, contributing to warming from excess carbon dioxide (CO_2), along with other greenhouse gases including water vapour, chlorofluorocarbons, and methane. These trace gases increase the infrared opacity of the atmosphere and regulate the earth's climate (Feely et al., 2001). The rate of change of atmospheric CO_2 is indicative of the equilibrium that exists between natural and anthropogenic carbon emissions and various terrestrial and ocean processes that remove or emit CO_2 (Sabine et al., 2004). The release of CO_2 from fossil consumption and other human activities contributes about 7 Pg C (1 Pg = 1 X 10^{15} g) to the atmosphere annually, with 3 Pg C accumulating in the atmosphere and the residual 4 Pg C being sequestered by the terrestrial biosphere and the oceans (Feely et al., 2001); the Southern Ocean alone accounts for 43±3% of the global anthropogenic CO_2 up-take from the atmosphere from 1870 to 1995 (Frölicher et al., 2015), signifying its importance in buffering the impact of climate change. The ocean acts as a significant reservoir that

efficiently exchanges carbon with the atmosphere, with CO_2 reacting with seawater to form carbonic acid and carbonate ions. This process, known as ocean acidification, leads to a decrease in ocean pH, which has important consequences for calcifying organisms such as coccolithophores (Orr et al., 2005).

There are two fundamental mechanisms responsible for the uptake and storage of atmospheric CO_2 in the ocean, namely the physical solubility and biological carbon pumps (Figure 1.2). The solubility pump involves the exchange of CO_2 at the surface ocean and export of its chemical species through thermohaline circulation. The biological pump is a collective property of an intricate phytoplankton-based food web, contingent on the drawdown of CO_2 by phytoplankton photosynthesis and vertical transport of biologically sequestered carbon to depth.

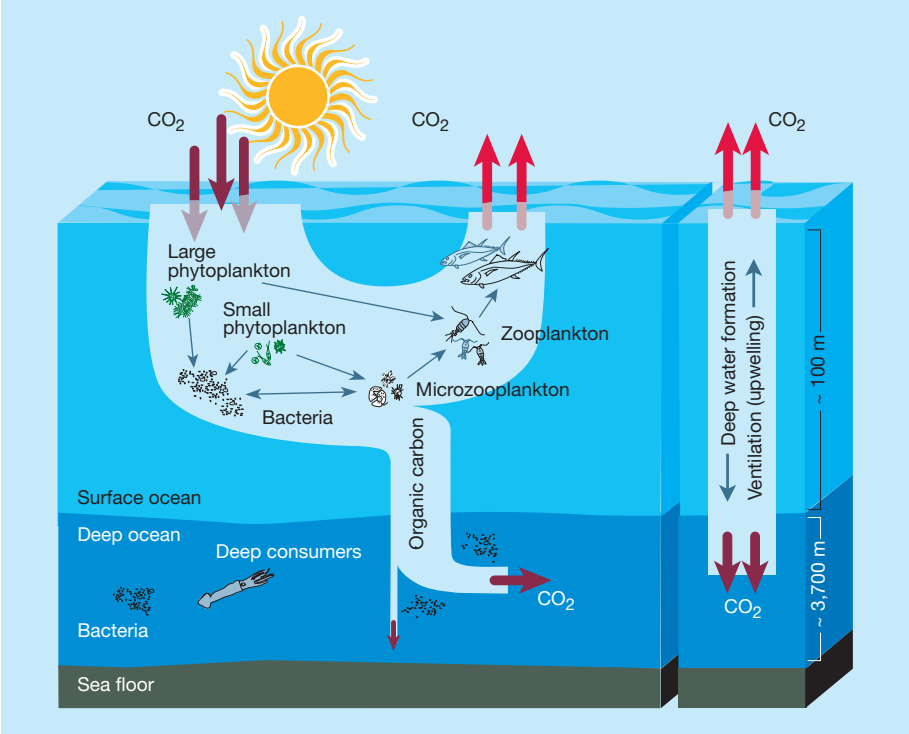

Figure 1.2: Graphic depicting the biological carbon pump (left) and the physical solubility carbon pump (right), reproduced from Chisholm (2000).

1.1.3 The role of the Southern Ocean in carbon uptake

The Southern Ocean has been described as the earth's most important anthropogenic CO_2 sink (Frölicher et al., 2015; Mikaloff Fletcher et al., 2006), with model predictions indicating that it will dominate the ocean's CO_2 exchange over the next few decades (DeVries et al., 2017; Orr et al., 2005; Sarmiento et al., 1998). The global oceans have taken up between 25 and 30% of the anthropogenic CO_2 released into the atmosphere, with $\sim$

40% of this uptake occurring in the Southern Ocean (Frölicher et al., 2015; Sabine et al., 2004; Takahashi et al., 2009). The biological pump is believed to account for 10% of this export (Cox et al., 2000; Siegel et al., 2014), with the physical solubility pump proving to be of substantial importance (Caldeira and Duffy, 2000; Gruber et al., 2009). The solubility pump is largely influenced by the Southern Ocean overturning circulation. In brief, Circumpolar Deep Water (CDW) is upwelled, aided by the strong westerly winds that circulate around Antarctica, and carried northwards across the SAZ by Ekman transport. This water comprises a lower partial pressure of CO_2 than the surrounding atmosphere, allowing for the uptake of CO_2 into the ocean. North of the SAF, surface water is subducted to depth as Antarctic Intermediate Water (AAIW) and Subantarctic Mode Water (SAMW) (Rintoul et al., 2001). This process is responsible for exporting $\sim$1 Gt C yr^{-1} to the oceans interior and connects the upper and lower components of the global overturning circulation (Metzl et al., 1999; Sloyan and Rintoul, 2001a,b). Regarding the biological carbon pump, phytoplankton production and associated seasonal blooms play an important role in biogeochemical cycling, mediating the transport of organic material from the surface sunlit waters to the ocean's interior. The export flux when this biomass sinks to depth contributes to the net annual uptake of atmospheric CO_2 (Takahashi et al., 2009). Remineralisation of particulate organic carbon (POC) to CO_2 by bacteria and zooplankton means that only a small fraction of this flux reaches the interior, with the depth distribution of remineralisation controlling atmospheric CO_2 levels (Kwon et al., 2009). Phytoplankton production has originally been proposed to be the highest in the region between 30-50°S (Banse, 1996; Moore and Abbott, 2000), however, as climate change advances, regions contributing to the greatest carbon export are expected to shift (Hauck et al., 2015). Le Quéré et al. (2007) demonstrated a reduction in Southern Ocean carbon uptake between the early 1980s and early 2000s, with Landschützer et al. (2015) showing a strengthening in the rate of carbon uptake south of 35°S from 2002 to 2012; this discrepancy may in part be explained by changes in upper-ocean overturning circulation (DeVries et al., 2017) or through variation in the interannual seasonal cycle of CO_2 in the region (Gregor et al., 2018). Opinion on the fate of future Southern Ocean carbon uptake remains mixed, with studies reporting either a diminished (Le Quéré et al., 2007; Lovenduski et al., 2007, 2008; Roy et al., 2003) or increased (DeVries et al., 2017; Hauck et al., 2015; Landschützer et al., 2015; Munro et al., 2015) carbon carrying capacity.

1.2 Nutrient Signatures in the Southern Ocean

1.2.1 The High-Nutrient Low-Chlorophyll condition

Nutrient limitation in the ocean is based upon two central theories, namely that nutrient availability can limit rate processes such as photosynthesis and growth (Blackman, 1905), as well as the overall yield of a phytoplankton population (von Liebig, 1841). Redfield (1934) examined the specific stoichiometry of the fundamental macronutrients within phytoplankton, from which the fundamental Redfield ratio evolved (C_{106}:N_{16}:P_1). The element present in the lowest quantity relative to the growth requirements of phytoplankton will become the limiting factor (Redfield, 1958), in accordance with Liebig's law of the minimum (von Liebig, 1841).

Oceanic High-Nutrient Low-Chlorophyll (HNLC) regions are characterised primarily by the persistence of major macronutrients and concomitant low biomass. The Southern Ocean is the largest HNLC region in the world (Minas and Minas, 1992), and is defined by an abundance of unused macronutrients (Levitus et al., 1993) and unexpectedly low average phytoplankton biomass that is widely variable in its spatial and temporal distribution (Arrigo et al., 2008; Moore and Abbott, 2000; Sullivan et al., 1993). The low phytoplankton standing stocks have been attributed to multiple factors (Boyd, 2002; Boyd et al., 1999), including the limitation of phytoplankton growth by low iron (Fe) levels (de Baar et al., 1995; Martin et al., 1990a), light limitation (Mitchell et al., 1991), and silicate ($Si(OH)_4$) availability (Dugdale et al., 1995; Hutchins et al., 2001; Zentara and Kamykowski, 1981). In addition, top-down control by zooplankton predation has also been implicated (Behrenfeld, 2010; Le Quéré et al., 2015; Smetacek et al., 2004).

1.2.2 Iron availability

Numerous early studies proposed that limitation of the micronutrient Fe may be responsible for limiting macronutrient uptake in HNLC regions (Brand, 1991; Brand et al., 1983; Gran, 1933; Harvey, 1937; Menzel and Ryther, 1961; Ryther and Kramer, 1961). It wasn't until the advent of trace metal clean techniques that Fe was confirmed to be the physiological rate- and biomass-limiting nutrient in HNLC oceans, significantly influencing regional phytoplankton dynamics (de Baar et al., 1990, 1995; Martin et al., 1990a,b, 1991). In conjunction with these detailed *in situ* studies, early remote sensing observations further hinted at Fe availability as a key regulator of phytoplankton abundance and distribution. Both Comiso et al. (1993) and Sullivan et al. (1993) examined Coastal Zone Color Scanner (CZCS) ocean colour data for the Southern Ocean and noticed a large

accumulation of phytoplankton biomass (blooms) occurring in localised regions linked to sea ice retreat, shallow waters, strong upwelling areas, hydrographic frontal zones, and coastal/ shelf regions, both relating the locale to replete Fe levels. Furthermore, the role of Fe-limited biological productivity has been evidenced in various Fe-addition experiments (Boyd et al., 2001, 2000; Coale et al., 2004; Gervais et al., 2016; Ryan-Keogh et al., 2018), and observed in naturally Fe-fertilised regions, such as those in the lee of Sub-Antarctic islands, e.g. South Georgia (Korb et al., 2004), the Crozet Plateau (Pollard and Read, 2001; Poulton et al., 2007; Salter et al., 2007), and the Kerguelen Plateau (Blain et al., 2007). The Southern Ocean has a diverse range of Fe supply mechanisms, ranging from aerosol dust and eddy shedding to sea-ice and iceberg meltwaters (Boyd and Ellwood, 2010; Lancelot et al., 2009; Shaw et al., 2011). Boyd et al. (2012) recently mapped Fe utilisation in the Southern Ocean to better understand the supply-and-demand dynamics that govern the region; all sectors of the Southern Ocean displayed small inter-annual variability in Fe utilisation, with the Atlantic sector displaying the most, largely due to variation in the high latitudes.

1.3 Phytoplankton

1.3.1 Background

Coined in 1897, the term phytoplankton transpires from Greek origin, comprising the words *phyton* (plant) and *planktos* (wanderer or drifter) (Falkowski and Raven, 2007). Phytoplankton are a diverse group of aquatic photoautotrophs, that essentially use sunlight and the chromophoric pigment chlorophyll to convert CO_2 to carbohydrates through a process known as photosynthesis. While phytoplankton account for less than 1% of the world's photosynthetic biomass, they are accountable for ∼50% of annual global net primary production (Field et al., 1998). There are ∼25 000 morphologically distinct types of phytoplankton, arranged into eight distinct phyla that span nine orders of magnitude in cell size (Falkowski et al., 2004; Finkel et al., 2010; Sieburth et al., 1978). The phyla Cyanophyta is composed of the earliest oxygenic photosynthetic organisms, the Cyanobacteria, while the others comprise more recently evolved eukaryotes. The largest and most prominent phytoplankton are represented by the phyla Bacillariophyta (diatoms), Dinophyta (dinoflagellates), and Haptophyta (golden-brown flagellates). Smaller phytoplankton are typically represented by picoeukaryotes and the prokaryotic classes of Cyanophyceae (cyanobacteria) and Prochlorophyceae (prochlorophytes). These different phytoplankton groups are typically well suited to the light and nutrient conditions of their

surrounding environments (Falkowski et al., 2004).

Phytoplankton cell size and elemental stoichiometry impose fundamental constraints on growth rates, food web structure, and the biogeochemical cycling of carbon (Finkel et al., 2010; Moore et al., 2013). Exogenous nitrates are consumed by large phytoplankton (microphytoplankton), which contribute to new production (Goldman, 1993), while regenerated forms of nitrogen, such as ammonia and urea, are the likely source for small phytoplankton (nano- and picoplankton). On the basis of the size of the primary producers, two types of food web pathways can be resolved (Legendre and Rassoulzadegan, 1995), namely the herbivorous food web, based on large phytoplankton, herbivorous zooplankton and fish, and the microbial food web, consisting of small phytoplankton, heterotrophic bacteria and protozoa. When large phytoplankton and the herbivorous food chain dominates there is an efficient export of particulate organic matter to depth, whereas the microbial chain, comprising recycling and many more steps in the food chain, leads to the weak export of organic materials (Michaels and Silver, 1988), negatively influencing the biological carbon pump.

1.3.2 Determining species composition of natural assemblages

Numerous techniques exist to discern phytoplankton species within a mixed population; these include both remote sensing approaches (e.g. Brewin et al. (2011); Moisan et al. (2013)) and *in situ* methods, such as microscopy (e.g. Patil et al. (2013)), flow cytometry (e.g. Hutchins et al. (2001)), genetic assessments (e.g. Moon-van der Staay et al. (2000)), bio-optical investigations (e.g. Organelli et al. (2017)), and pigment analysis through High-Performance Liquid Chromatography (HPLC) (e.g. Zapata et al. (2004)). All methods have their pros and cons; while microscopy allows for identification of certain taxa down to the genus and species level, it is a time consuming process with questionable sample preservation techniques (Gieskes and Kraay, 1983; Modigh and Castaldo, 2005; Stoecker et al., 1994). The development of species-specific genetic markers has proven useful (Moon-van der Staay et al., 2000), however these highly specific probes will only identify their target species, excluding additional community members. Flow cytometry has numerous applications, yet is best used in conjunction with complementary techniques when examining assemblage composition (Veldhuis and Kraay, 2000). The ideal approach to determining species composition would be using a combination of available techniques (Gall et al., 2001). Isolating specific phytoplankton pigments through HPLC and using signature diagnostic pigments as taxonomic markers is perhaps the most time-effective and reliable method for determining the relative contribution of a species to a mixed

assemblage. The amount of different pigments identified through HPLC is extensive, allowing for the implementation of computational algorithms to effectively derive species present (Mackey et al., 1996). However, the reliability of such data is dependant upon the quality of HPLC sample retrieval and processing.

In the late 1980s and early 1990s, there were numerous attempts to estimate the abundances of various phytoplankton classes quantitatively from marker pigment concentrations (Claustre, 1994; Everitt et al., 1990; Gieskes and Kraay, 1986; Gieskes et al., 1988; Letelier et al., 1993). Mackey et al. (1996) developed a computation program to calculate phytoplankton class abundances from HPLC-derived chlorophyll and carotenoid pigments. The program uses factor analysis and a steepest decent algorithm to establish the optimal fit to the data based on a preliminary estimate of the pigment ratios for the classes to be determined. The program is called CHEMTAX (CHEMical TAXonomy) and has successfully been used in multiple Southern Ocean studies with satisfactory results (Gibberd et al., 2013; Kozlowski et al., 2011; Mendes et al., 2012; Rozema et al., 2017; Ryan-Keogh et al., 2018, 2017b; Wright et al., 2010; Wulff and Wängberg, 2004). CHEMTAX results have correlated strongly with those from microscopy and in some instances revealed the presence of groups not detected by other more traditional enumeration techniques, for example cryptophytes (Wright et al., 1996) and *Phaeocystis* (Kozlowski et al., 2011). Primary concerns centre around the use of non-unique pigment markers (Zapata et al., 2004) and potential fluctuations of pigment ratios both at a species and a cellular level to various physiological stressors (DiTullio et al., 2007; Goericke and Montoya, 1998). In addition, there have been reports of CHEMTAX underestimating cyanobacteria populations (Havskum et al., 2004), however, prior knowledge of potential populations within the sample region will reduce such under-representations (Irigoien et al., 2004). CHEMTAX is considered appropriate for regions of low pigment concentrations and demonstrates a good overall performance within the Atlantic Southern Ocean (Gibberd et al., 2013; Mendes et al., 2012; Ryan-Keogh et al., 2018, 2017b).

Another approach to population deconstruction was devised by Vidussi et al. (2001), who used diagnostic pigments as size class markers of phytoplankton groups. Vidussi et al. (2001) had a large data set (804 stations) and sought to condense the information contained within the full suite of available pigments, with the objective of identifying taxonomic composition through the use of a minimal set of marker pigments. Seven suitable pigments were selected, allowing for the extraction of relevant, comparable information, whilst emphasising the importance of phytoplankton size structure over community composition (Table 1.1).

Table 1.1: Diagnostic pigments used as biomarkers and their respective taxonomic significance, reproduced from Vidussi et al. (2001). The taxonomic significance of pigments to the following taxa include cyanobacteria (cyano.), prochlorophytes (prochloro.), green flagellates (green flag.), chromophytes (chromo.), nanoflagellates (nanoflag.), crytophtes, diatoms, and dinoflagellates. The Chl-a_{Zeu}: P_{Zeu} ratio refers to the chl-a content relative to the seven DPs, vertically integrated across the euphotic depth, as per Uitz et al. (2006).

Pigments	Abbr.	Taxonomic significance	Size (μm)	Chl-a_{Zeu}: P_{Zeu}
Zeaxanthin	Zea	cyano. & prochloro.	< 2	0.86±0.09
Chl-b + Dv-Chl-b	TChl-b	green flag. & prochloro.	< 2	1.01±0.10
19'hexanoyloxyfucoxanthin	19'HF	chromo. & nanoflag.	2- 20	1.27±0.02
19'butanoyloxyfucoxanthin	19'BF	chromo. & nanoflag.	2- 20	0.35±0.25
Alloxanthin	Allo	cryptophytes	2- 20	0.6±0.16
Fucoxanthin	Fuco	diatoms	> 20	1.41±0.02
Peridinin	Peri	dinoflagellates	> 20	1.41±0.10

The size classes are based on the classification of Sieburth et al. (1978), i.e. picophytoplankton are between 0 and 2 μm, nanophytoplankton are between 2 and 20 μm, and microphytoplankton are between 20 and 200 μm. One limitation of the DP approach is that the pigment grouping may not strictly reflect the true size of phytoplankton populations; this is due to the fact that some chlorophylls and carotenoids are shared by algal classes, to the potential presence of certain phytoplankton group spanning more than one size class and that pigment composition and ratios are affected by certain environmental conditions (DiTullio et al., 2007, 2003). Despite these limitations, the pigment-derived indices are useful tools to extract ecologically relevant information from pigment records across a variety of oceanic environments (Babin et al., 2003). Gieskes et al. (1988) carried out a multiple regression analysis of chl-a concentration ([chl-a]) and the concentration of key pigments, with the partial slopes of their analysis providing the best estimates of chl-a to DP ratios. Uitz et al. (2006) combined the multiple regression approach and the three size class groupings proposed by Vidussi et al. (2001). The group performed multiple regression analysis on 2419 samples, between the chl-a content and the seven marker pigments content, over a vertically integrated euphotic depth. This regression was found to be highly significant ($p < 0.001$), with the coefficients representing the best estimates of the seven ratios listed in Table 1.1 (see Chapter 2, Section 2.2.3 for equations).

1.3.3 Phytoplankton distribution across Southern Ocean provinces

Both numerical models (Hauck et al., 2015; Sarmiento et al., 2004; Schlitzer, 2002) and remote sensing observations (Arrigo et al., 2008; Behrenfeld and Falkowski, 1997; Moore and Abbott, 2000) have highlighted the complex spatial and temporal distribution of

phytoplankton in the Southern Ocean. Factors controlling phytoplankton biomass, distribution, and community structure in the Southern Ocean include the light environment (Alderkamp et al., 2013; Arrigo et al., 2010; Helbling et al., 1996; Kropuenske et al., 2009; van de Poll et al., 2009, 2005), macronutrient availability (Closset et al., 2014; Dugdale et al., 1995; Redfield, 1958; Timmermans et al., 2004), Fe availability (Boyd and Abraham, 2001; Martin et al., 1991; Russo et al., 2015; Sosik and Olson, 2002; Strzepek et al., 2011), zooplankton grazing (Banse, 1994; Le Quéré et al., 2015; Smetacek et al., 2004), the seasonal cycle (Llort et al., 2015; Ryan-Keogh et al., 2018; Thomalla et al., 2011), as well as certain hydrographic feature e.g. wind and temperature (Patil et al., 2013), vertical mixing (Fauchereau et al., 2011; Llort et al., 2015; Sverdrup, 1953), storms (Carranza and Gille, 2015; Nicholson et al., 2016), and eddies (du Plessis et al., 2017; Swart et al., 2015). It is likely that not just one factor is responsible for phytoplankton distribution in the Southern Ocean, but rather a dynamic mix with different combinations operating over space and time (Boyd et al., 2001, 1999; Cassar et al., 2011; Hickman et al., 2010; Hutchins et al., 2001; Russo et al., 2015; Strzepek et al., 2012). In the austral winter, across the Southern Ocean, light is considered to be the limiting factor of phytoplankton growth, with increased light limitation due to geometrically thicker cloud systems (Haynes et al., 2011) and deep mixed layers caused by high rates of convective overturning (de Boyer Montégut et al., 2004). The austral summer is more complex, with zonal variability driving phytoplankton production, biomass, and species composition.

A simplified schematic showing a summary of the broad distribution of Southern Ocean phytoplankton across different zones is shown in Fig. 1.3.

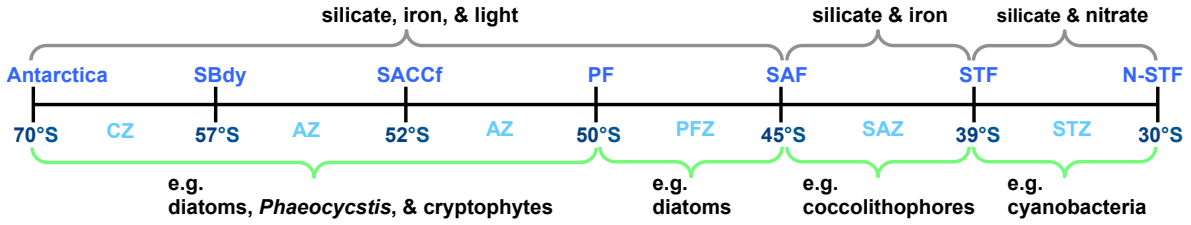

Figure 1.3: The zonal separation of Southern Ocean phytoplankton. The factors listed along the top of the zones are considered limiting in their respective regions. Examples of species known to populate the different zones are listed along the bottom. All latitudes are approximate values. N-STF: Northern-Subtropical Front; STF: Subtropical Front; SAF: Subantarctic Front; PF: Polar Front; SACCf: Southern Antarctic Circumpolar Current Front; SBdy: Southern Boundary of the ACC; SAZ: Subantarctic Zone; PFZ: Polar Frontal Zone; AZ: Antarctic Zone; CZ: Continental Zone.

1.3.3.1 The Subtropical Zone

The STZ, located north of the STF, is typically considered an oligotrophic region, i.e. low levels of macronutrients (Chever et al., 2010). Cyanobacteria sub-types *Prochlorococcus* and *Synechoccocus* have been observed in the STZ, SAZ, and extending, in low abundance, to the Antarctic continent (Wilkins et al., 2013). Cyanobacterial abundances in the Southern Ocean decrease over four orders of magnitude between latitudes 45°S and 60°S (Marchant et al., 1987). *Prochlorococcus* are present from the surface to depth (∼150 m) in the open ocean between 40°N and 40°S, with the population being latitudinally limited to warmer waters (Johnson et al., 2006). While *Prochlorococcus* has been observed in small amounts in the STZ as far south as 42°S (Gibberd et al., 2013), they have seldom been detected south of the STF in the Indian (Fouilland et al., 1999) and Atlantic sectors (Doolittle et al., 2008) of the Southern Ocean, and are believed to be absent from polar waters (Partensky et al., 1999b). *Synechoccocus* exhibit a shallower vertical distribution than *Prochloroccocus*, but they are more wide spread, covering a larger geographic and thermal area, including high-nutrient waters and occasionally reaching polar latitudes (Letelier and Karl, 1989; Marchant et al., 1987; Partensky et al., 1999a). The photosynthetic pigments of most cyanobacteria includes chl-*a*, carotenoids, and phycobiliproteins, including phycocyanin (PC), allophycocyanin (APC), and phycoerythrin (PE). *Synechoccocus* are easily recognisable through fluorescence techniques due to the intense orange fluorescence emitted by PE under blue light (Letelier and Karl, 1989; Olson et al., 1988). The smaller *Prochloroccocus* uniquely comprise divinyl derivatives of chl-*a* and *b*, and contain low or absent amounts of PE, PC, and APC (Hess et al., 1996).

1.3.3.2 The Subantarctic Zone

In the SAZ, irradiance levels, through alteration of phytoplankton Fe requirements, is a key determinant of phytoplankton growth rate, when $Si(OH)_4$ is non-limiting (Boyd et al., 2001). While concentrations of nitrate (NO_3^-) are considered replete in the Southern Ocean (∼25 μM, (Dafner and Mordasova, 1994; Tréguer and Jacques, 1992)), dissolved $Si(OH)_4$ concentrations are typically low (1-15 μM) north of the PFZ (Coale et al., 2004; Franck et al., 2000; Tréguer and Jacques, 1992). As such, spring and summer phytoplankton populations in the SAZ are regulated by an interplay of $Si(OH)_4$, Fe, and light levels (Boyd et al., 2001, 1999; Hoffmann et al., 2008; Hutchins et al., 2001). As the mean irradiance increases over the growing season, both $Si(OH)_4$ and Fe concentrations are depleted and levels become insufficient to meet biological demand, resulting in growth limitation by Fe, Si, or Fe/ $Si(OH)_4$ (Boyd et al., 1999; Martin et al., 2013; Ryan-Keogh et al., 2018).

Silicate limitation is known to result in species succession from large, heavily silicified diatoms to other species and/ or smaller taxa such as coccolithophores, dinoflagellates, nanoflagellates, cyanobacteria, and small or lightly silicified diatoms (Balch et al., 2016; de Salas et al., 2011; Odate and Fukuchi, 1995; Salter et al., 2007). Species succession from diatoms to haptophytes has also been observed under Fe-limiting conditions in the SAZ (Ryan-Keogh et al., 2018). In the summer, the mLD plays a vital role in regulating light and nutrient supply to resident phytoplankton (Joubert et al., 2014; Swart et al., 2015), with mesoscale features (du Plessis et al., 2017) and storms (Carranza and Gille, 2015; Nicholson et al., 2016) facilitating mixing regimes.

A representative species of SAZ resident phytoplankton include the coccolithophores. These phytoplankton are characterised by calcium carbonate ($CaCO_3$)-containing, external armoured plates, known as coccoliths. While belonging to a single functional group of phytoplankton, i.e. calcifying phytoplankton, they populate numerous hydrographic and light conditions (Balch et al., 2011), and have been identified in the higher-latitude regions of both hemispheres (Brown and Yoder, 1994; Buma et al., 1992). The coccolithophore *Emiliania huxleyi* is responsible for blooms occurring within a few weeks of summer solstice in the respective hemispheres (Balch, 2004). Blooms, identified from various remote sensing platforms (Moore et al., 2012), are known to occur over consecutive summers in the SAZ (Balch et al., 2005), with bloom locations consistent across the Atlantic (Balch et al., 2016; Balch and Utgoff, 2009; Gibberd et al., 2013), Pacific (Gravalosa et al., 2008), Indian (Mohan et al., 2008) and Australian (Cubillos et al., 2007) sectors of the Southern Ocean. The southern boundary of coccolithophore extent, across the Southern Ocean, is roughly considered to be the PFZ (Bathmann et al., 1997; Cubillos et al., 2007; Gravalosa et al., 2008; Mohan et al., 2008).

1.3.3.3 The Polar Frontal Zone

The PFZ forms an important transitional boundary where coccolithophores typically dominate to the north and diatoms to the south (Honjo, 2004; Tremblay et al., 2002; Trull et al., 2001a,b). Phytoplankton dynamics in the PFZ are predominantly influenced by light, $Si(OH)_4$, and Fe levels (Boyd et al., 2001; Cassar et al., 2011; Franck et al., 2000). Franck et al. (2000) demonstrated the addition of Fe had little effect on $Si(OH)_4$ uptake rates in low-$Si(OH)_4$ conditions north of the PFZ, while it significantly increased $Si(OH)_4$ uptakes rates in the high-$Si(OH)_4$ environment south of the PFZ. The high $Si(OH)_4$ concentrations that typically prevail south of the PF create a favourable environment for diatoms (Coale et al., 2004), which require $Si(OH)_4$ to synthesise their siliceous frustules, and are thus responsible for $Si(OH)_4$ uptake. In the Atlantic sector, blooms of large di-

atoms develop in the PFZ, during late spring (Bathmann et al., 1997) and summer (Tremblay et al., 2002), leading to a depletion in $Si(OH)_4$ (Le Moigne et al., 2013; Quéguiner and Brzezinski, 2002) and subsequent reduction in biogenic silica export (DeMaster, 1981; Le Moigne et al., 2013). Diatoms dominate primary production in the ACC, particularly south of the PF where their productivity results in a third of the global marine silica production (Buesseler et al., 2001; Pondaven et al., 2000). Along with $Si(OH)_4$ concentrations regulating the local diatom populations, light and Fe availability are critical in mediating carbon export from the region (Cassar et al., 2011), with diatoms displaying high inter-species variability in response to varying Fe, $Si(OH)_4$ and light regimes (Hoffmann et al., 2008; Strzepek et al., 2012; Sunda and Huntsman, 1995; Timmermans et al., 2001). In the summer, mLDs are deepest in the PFZ (> 70 m) and shallowest south of the SACCf (30 m) (Trull et al., 2001b), with wind stress mixing in the PFZ leading to persistently deep mLDs and fluctuating light and Fe levels (Chever et al., 2010; Klunder et al., 2011).

1.3.3.4 The Antarctic Zone

The Antarctic Zone (AZ) stretches approximately from south of the PF to the SBdy (Pollard et al., 2002). There may be overlap with the Permanently Open Ocean Zone (POOZ), including subsections such as the Seasonal Ice Zone (SIZ) and MIZ. The POOZ forms a natural barrier between the temperate conditions to the north (5-10°C) and the cold Antarctic waters to the south (< 2°C) (Pollard et al., 2002; Sokolov and Rintoul, 2009). Phytoplankton populations in the AZ are mixed and often show a seasonal succession of species (Arrigo, 1999). Tremblay et al. (2002) showed that during mid-December, in the Atlantic sector of the Southern Ocean, that the total chl-*a* concentration in the POOZ and SIZ was low, with the contribution of pico-, nano-, and microplankton averaging at 18%, 44%, and 38% of the total, respectively. By mid-January chl-*a* levels increased in the southern SIZ, which coincided with a mixed diatom- *Phaeocystis* bloom. Microplankton comprised 63% of total chl-*a*, followed by nanoplankton (26%), and picoplankton (11%).

The MIZ is the ice-covered portion of (sea) ice that seasonally advances and retreats, and is affected by metocean processes, i.e. waves. It has been estimated that MIZ blooms account for 15% of net primary production in the Southern Ocean, with a proposed two-thirds occurring under partial ice coverage (Taylor et al., 2013), indicating that remote-sensing estimates might underestimate their contribution. The stability of a shallow pycnocline, associated with melting sea ice, is key in the development of phytoplankton blooms in the MIZ, relating specifically to PAR availability associated with shallow mLDs (Taylor et al., 2013). Iron supply to the ocean surface is typically dominated glob-

ally by atmospheric deposition (Mahowald et al., 2005), however, in the Southern Ocean this component is small, so that interactions between the ACC and bottom topography, upwelling, vertical diffusion, and melting of ice and icebergs provide comparatively important sources of bioavailable Fe (Fung et al., 2000; Holm-Hansen et al., 2005; Law et al., 2003; Sedwick and Ditullio, 1997; Shaw et al., 2011). Some of the interannual variability in the region relate ice coverage to anomalous forcings associated with El Niño-Southern Oscillation (ENSO) and the Southern Annular Mode (SAM), which are major modes of coupled climatic variability that impact this part of the Southern Ocean (DeVries et al., 2017; Liu et al., 2004; Stammerjohn et al., 2008). The termination of blooms in this region coincide with a reduction in partial sea ice coverage and a deepening of the mLD in response to wind-driven mixing (Fitch and Moore, 2007).

Examples of resident phytoplankton include *Phaeocystis* (Prymnesiophyceae) (Alderkamp et al., 2013; Arrigo, 1999; Arrigo et al., 2010) and cryptophytes (Cryptophyceae) (Bathmann et al., 1997; Becquevort et al., 1992; Buma et al., 1992). *Phaeocystis* exhibit a heteromorphic life cycle, alternating between free-living, flagellated zoospores and a gelatinous aggregation of non-motile, colonial cells (Rousseau et al., 1994). These phytoplankton act as an important intermediary in carbon (DiTullio et al., 2000) and sulphur (Koga et al., 2014) flux between the ocean and atmosphere. *Phaeocystis* produce dimethylsulfoniopropionate (DMSP) before enzymatically breaking it down into dimethylsulfide (DMS) and acrylate (Stefels and Van Boekel, 1993). Aside from its role in cloud formation (Wang et al., 2018), DMS is known to impact the chemical quality of the atmosphere and global climate regulation (Gondwe et al., 2003). *Phaeocystis* and diatoms often compete for ice-edge bloom dominance in the Southern Ocean, with irradiance levels and vertical stability often driving the population composition (Alderkamp et al., 2013; Arrigo, 1999; Kropuenske et al., 2010; Moisan and Mitchell, 2001; van de Poll et al., 2011). In the Ross Sea, for example, Arrigo et al. (2010) observed that diatoms dominated stratified waters and *Phaeocystis antarctica* dominated regions of deep mixing. Furthermore, the seasonal depletion of Fe in this region is thought to play a role in the succession from *Phaeocystis* to diatoms, the latter species being more adept to dealing with low Fe (Boyd, 2002; Ryan-Keogh et al., 2017a; Strzepek et al., 2012). In the MIZ, during the summer months, diatom blooms are often succeeded by cryptophyte dominance (Buma et al., 1992; Garibotti et al., 2005; Jacques and Panouse, 1991; Rozema et al., 2017). The grazing pressure on the diatoms and the little appetance of the herbivorous zooplankton for cryptophytes plays strongly in their favour (Alder et al., 1989). Cryptophytes populate waters as far north as the SAZ, but are typically found south of the PF and in the MIZ (Buma et al., 1992; Jacques and Panouse, 1991; Mendes et al., 2013; Wright et al., 1996;

Wulff and Wängberg, 2004). They are believed to populate offshore regions, following the summer sea-ice retreat towards the Antarctic continent (Garibotti et al., 2005). Cryptophytes are typically identified through the presence of their signature photoprotective pigment, alloxanthin (Jeffrey and Vesk, 1997). In terms of light harvesting they comprise both chl-a/c and the phycobilipigment PE (abs_{max} = 545-567 nm) and/ or PC (abs_{max} = 585-620 nm) (Doust et al., 2004, 2006).

1.4 Photosynthesis and Related Photochemistry

1.4.1 Intracellular pigment arrangement

Photosynthetic pigments, responsible for efficiently capturing light energy between 400 and 700 nm, consist of three chemically distinguished classes of molecules including the chlorophylls, the carotenoids, and the biliproteins. All photosynthetic plants contain chlorophylls and carotenoids, with red algae, Cyanophyta, and Chryptophyta additionally containing biliproteins. The light reactions of photosynthesis take place in two characteristic pigment-protein/ electron carrier systems, known as photosystem (PS) I and II. Each PS is equipped with a network of light harvesting pigment-proteins that function purely to extend the range of light collection for photosynthesis, funnelling received radiation to the reaction centre core. These pigments are referred to as antennae pigments, which, when associated with PSI and II collectively form light harvesting complexes (LHCs). These LHCs are arranged within the thylakoid membranes, either free-standing in the cytoplasm (Cyanophyta) or bound within chloroplasts (Fig. 1.4).

1.4.2 Photoacclimation and photoadaptation

Phytoplankton are constantly adjusting their photosynthetic apparatus to the surrounding light environment, optimising the capture of photons while mitigating potential photodamage. Photoacclimation describes the phenotypic response of phytoplankton to changes in irradiance and can be measured in the photosynthetic physiology or biochemistry of a given species in response to growth at a range of light intensities (Falkowski and LaRoche, 1991). Photoacclimation involves compensatory changes in certain components of the photosynthetic apparatus, for example, under increased irradiation there is typically a decrease in photosynthetic pigment across all taxa (MacIntyre et al., 2002). Photoadaptation describes the genotypic response of phytoplankton to irradiance that has developed during evolution (Falkowski and LaRoche, 1991). Photoadaptation may be examined by observing differences in the photosynthetic physiology or biochemistry of different

taxa grown under identical light environments. Two basic strategies for photoacclimation are typically observed, namely a change in the absorption cross-section area of PSII (σ_{PSII}) and a change in the number of PSII reaction centres (Falkowski and Kolber, 1993; Falkowski and Owens, 1980; Moore et al., 2006; Suggett et al., 2009). Changes in the number of PSII reaction centres changes the Fe requirements of the phytoplankton (Section 1.4.4.2), while changes in σ_{PSII} leads to an adjustment in the amount of chlorophyll-to-carbon (Chl:C_{phyto}) present in their cells, with no change to Fe requirement. Hence, in Fe-limiting conditions there is a preference for phytoplankton to photoacclimate to low light conditions by adjusting σ_{PSII}. Under low irradiance phytoplankton increase the amount of chl-*a* to enhance energy capture, while under high irradiance they decrease their chl-*a* content to balance energy availability with downstream carbon fixation rates (Halsey and Jones, 2015). While this quantifiable shift in Chl:C_{phyto} may be used to study the light environment, the species composition must be taken in to consideration, as, for example, diatoms that are well adapted to fluctuating light environments display limited flexibility in their Chl:C_{phyto}, rather investing energy into the upregulation of their photoprotection mechanisms (Talmy et al., 2013).

1.4.3 Chloroplast ultrastructure

Taxonomic variability in fluorescence-based parameters reflects differences in antennae size, arrangement, and functioning in particular regions of the photosynthetically active spectrum (Suggett et al., 2009); the site of these light-driven dynamics are housed within chloroplasts. In eukaryotic plants, photosynthesis occurs within these cellular organelles, which are the best known member of the plastids family (Lodish, 2004). Chloroplasts are double-membraned organelles, which contain the green pigment chlorophyll. The outer membrane and inner membrane are separated by an intervening intermembrane space. The inner membrane surrounds the stroma, which is the site of carbohydrate synthesis. Chloroplasts contain a third membrane known as the thylakoid membrane. The thylakoid membrane folds up upon itself to enclose the thylakoid lumen, further forming flattened sacs, or grana, linked together by stromal lamellae (all components labelled in Figure 1.4). This distinct lipid bilayer is the site of photosynthesis and is dynamic in nature, with some species known to structurally re-organise their membranes in response to various light conditions (Moisan et al., 2006).

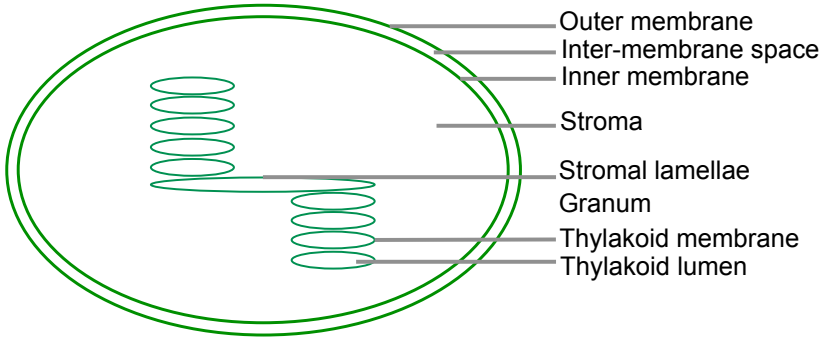

Figure 1.4: Simplified diagram of a chloroplast.

1.4.4 Photosynthesis

Phytoplankton typically perform as oxygenic photoautotrophs, converting sunlight into chemical energy through a complex series of reactions that essentially utilise H_2O and CO_2 to produce O_2 and simple sugars. Chl-*a* is used to catalyse the photooxidation of H_2O, generating molecular O_2. This process serves as one half of oxygenic photosynthesis, termed the light reactions (Eq. 1.1). The second half, the so-called dark reactions or Calvin-Benson-Bassham cycle, do not require light to proceed and involve the reduction of CO_2 to simple carbohydrates (Eq. 1.2).

Light reaction:

$$H_2O + NADP \xrightarrow{\text{sunlight + chlorophyll}} O_2 + NADPH + H^+ \tag{1.1}$$

Dark reaction:

$$CO_2 + NADPH + H^+ \xrightarrow{\text{Rubisco}} [CH_2O]_n + H_2O + NADP \tag{1.2}$$

1.4.4.1 Linear electron transport

Phytoplankton regulate the linear electron transport (LET) from water to the reductant nicotinamide adenine dinucleotide phosphate (NADPH) through PSI and PSII. Central to both photosystems are specialised chlorophyll dimers (P700 in PSI and P680 in PSII), surrounded by an intricate network of pigment-protein complexes forming an energetically efficient LHC. The coupling of these photosystems in a LET chain forms the basis of the Z-scheme, first proposed by Hill and Bendall (1960), which depicts the system in terms of electropotential energy of the various components (Fig. 1.5).

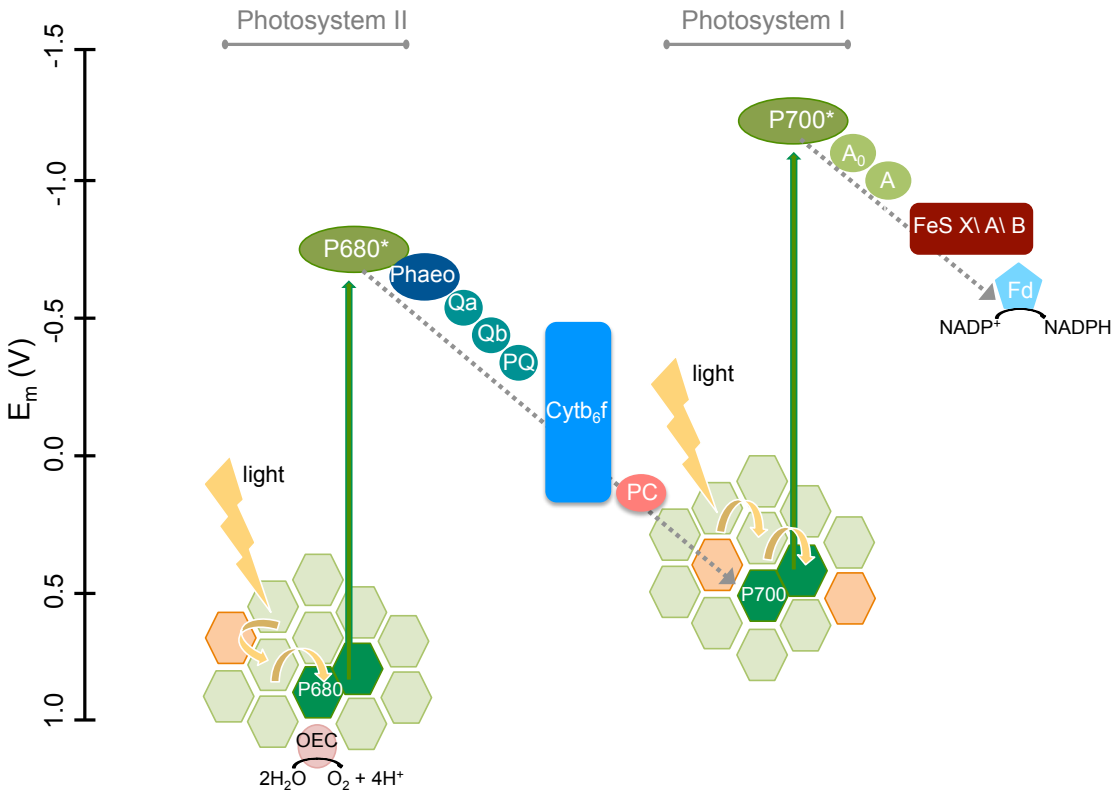

Figure 1.5: The z-scheme of linear electron transport in photosynthesis. Photons of light are received by the chl-*a* dimer P680 in PSII, resulting in excitation to a higher energy level (P680*). Water is electron donor for this reaction, undergoing photolysis in the oxygen evolving centre (OEC) on the donor side of PSII. Pheophytin (Phaeo) is the primary electron acceptor molecule of P680*, transporting electrons to plastoquinone-a (Qa), which subsequently donates to plastoquinone-b (Qb), which in turn passes electrons into the plastoquinone pool (PQ) before reaching cytochrome b_6f (Cyt b_6f). Electrons are then shuttled to oxidised P700 molecules via plastocyanin (PC) on the donor side of PSI. Light received by P700 elevates the molecule (P700*), with chlorophyll-A_0 serving as the primary electron acceptor. Electrons move from A_0 to a phylloquinone, A_1, and subsequently to iron-sulphur (FeS)-containing complexes F_X, F_A, and F_B. The F_B complex reduces ferredoxin (Fd), which in turn reduces $NADP^+$ to NADPH.

Photosystem II is a plastoquinone:water oxidoreductase and a key regulator of LET (Zavafer et al., 2015). When P680 receives sufficient excitation energy, be it directly from sunlight or through the resonance transfer of electrons from antennae pigments, it transfers this energy to the primary-electron acceptor molecule, phaeophytin, through a process known as photoinduced charge separation. Water, the principal electron donor for this process, undergoes photolysis to yield O_2 and four protons (H^+). This process involves the oxygen evolving complex (OEC), located on the donor side of PSII and comprises two redox active tyrosine residues, Y_Z and Y_D (Styring et al., 2012), a metalloenzyme core cluster of Mn_4Ca (Davis and Pushkar, 2015), and the primary electron accepting quinone Q_a (Zavafer et al., 2015). The electron received by phaeophytin is subsequently donated to Q_a before being transferred to another mobile quinone, Q_b, at the acceptor side of PSII. Once Q_b is fully reduced it is protonated from the stroma and released from PSII as plastoquinol (PQH_2) to bind with cytochrome (Cyt) b_6f. From Cyt b_6f the protons are released into the thylakoid lumen and the electrons are shuttled via a copper-containing plastocyanin to PSI (Hope, 2000). The chlorophyll dimer in the reaction centre of PSI (P700) must be oxidised prior to accepting the electrons from plastocyanin. This occurs during a second light reaction in which the absorption of a photon by P700 leads to the transfer of an electron to the PSI's primary-electron acceptor, chlorophyll-A_0. From chlorophyll-A_0 the electron is transferred to phylloquinone A_1 (Itoh and Iwaki, 1989). The secondary electron acceptors are a group of iron-sulphur containing complexes, namely F_X, F_A, and F_B (Vassiliev et al., 2001). It is ultimately F_B that reduces ferredoxin (Fd) (Vassiliev et al., 2001), the soluble protein that reduces $NADP^+$ to NADPH.

The net outcome of LET, when four photons are used by each photosystem, is one O_2, two NADPHs, and an accumulation of 12 H^+ ions in the lumen, the latter of which drives adenosine triphosphate (ATP) synthase (Junge, 1999) to produce approximately three ATP molecules (Behrenfeld and Milligan, 2013). Both ATP and NADPH are utilised during the dark reactions of photosynthesis, as energy and reducing power respectively. Together with a host of enzymes, including Rubisco (ribulose-1,5-bisphosphate carboxylase/oxygenase), they are used to fix CO_2 and convert it to simple sugars to be used in cellular respiration (Falkowski and Raven, 2007).

1.4.4.2 Iron requirements of the photosynthetic apparatus

Iron is a key trace metal component of various compounds and physiological processes, and is an irreplaceable piece of the protein puzzle that constitutes the photosynthetic electron transport chain (Chereskin and Castelfranco, 1982). Nearly every aspect of the thylakoid electron transport is Fe-dependent, with PSI having the highest Fe-requirement

(12 atoms), followed by Cyt b_6f (5 atoms), and PSII (3-4 atoms) (Behrenfeld and Milligan, 2013). Low levels of Fe affect physiological responses in natural phytoplankton assemblages, significantly decreasing their photosynthetic capacity (Cheah et al., 2013; Chereskin and Castelfranco, 1982). The SAZ and PFZ, two regions characterised as HNLC, have reported that Fe plays a key role in limiting phytoplankton growth (de Baar et al., 2005; Martin et al., 1990a), with light modulating the response to Fe supply (Boyd et al., 2001; Cassar et al., 2011; de Baar et al., 2005). Light modulates the response to Fe fertilisation (de Baar et al., 2005), partly because Fe demand increases under low light availability (i.e. Fe-light co-limitation) (Raven, 1990; Strzepek et al., 2012; Strzepek and Price, 2000). Under low light conditions phytoplankton can maximise photosynthesis by either increasing the size or the number of their photosynthetic units, the latter leading to higher requirements due to the increase in Fe-rich PSI reaction centres (Raven, 1990; Strzepek et al., 2012, 2011; Sunda and Huntsman, 1997).

1.4.5 Chl-*a* fluorescence quenching

Light absorption results in singlet-state excitation of a chl-*a* molecule (^{1}Chl*) which can return to the ground state through one of several pathways including (1) photochemistry, (2) de-excitation through thermal dissipation, (3) re-emission as chl-*a* fluorescence or (4) decay via the triplet state (^{3}Chl*) (Muller et al., 2001) (Fig. 1.6). While the triplet pathway can be a significant release of excess energy (4-25% of absorbed photons (Foyer and Harbinson, 1999)), ^{3}Chl* can transfer energy to ground-state O_2 generating highly reactive singlet oxygen ($^1O_2$). Singlet oxygen, although short-lived, can decay to other reactive oxygen species that target various macromolecules including DNA, lipids and proteins (Lesser, 2006). At room temperature, chlorophyll fluorescence is primarily emitted from PSII and typically at low yields (0.6-3% (Krause and Weis, 1991)). The amount of energy dissipated as ^{3}Chl* and fluorescence vary in proportion to the average lifetime of ^{1}Chl*, which is subsequently dependent upon the other de-excitation pathways. The high efficiency of photochemistry in a low light environment results in a reduction, or quenching, of fluorescence that is termed photochemical quenching (qP). The thermal dissipation of excess photon energy in the PSII antennae under high light conditions also decreases chl-*a* fluorescence in a process termed non-photochemical quenching (qN). Phytoplankton are able to maintain a low steady-state fluorescence yield and ^{3}Chl* over a wide spectrum of light conditions due to these quenching pathways, resulting in limited production of $^1O_2$ and decreased potential for free radical damage.

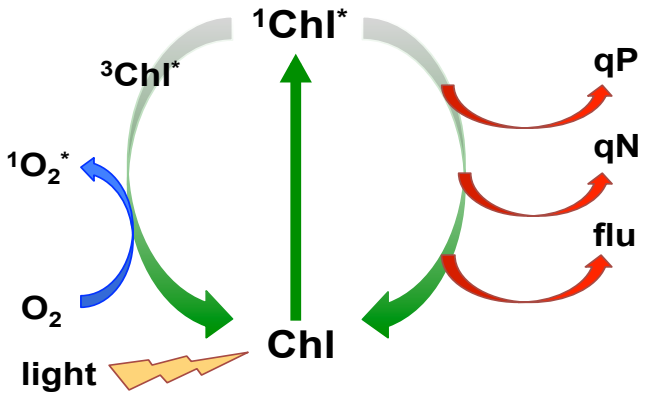

Figure 1.6: The de-excitation pathways of solar stimulated chl-*a*. When chl-*a* absorbs a photon it is elevated to singlet-state chl-*a* (^{1}Chl*), and returns to its ground state through decay via triplet chl-*a* (^{3}Chl*), photochemical quenching (qP), non-photochemical quenching (qN), i.e. heat, or photon re-emission as chl-*a* fluorescence (flu). Figure adapted from Muller et al. (2001).

In addition to the linear flow of electrons in oxygenic photosynthesis where electrons flow from PSII to PSI and $NADP^+$, additional pathways exist, referred to as alternative electron flow, and serve to dissipate excess excitation energy and balance the ATP/ NADPH demands of the cell (Hughes et al., 2018). These pathways include the cyclic flow of electrons around PSII and PSI, and the controlled photoreduction of O_2 at the level of the plastoquinone (PQ) pool (chlororespiration) or the PSI electron acceptor side (Mehler reaction), the latter two processes substituting for CO_2 to maintain electron flow and prevent photoinhibition (Ort and Baker, 2002; Peltier et al., 2010).

1.4.5.1 Alternative electron flow

Cyclic electron flow (CEF) around PSI serves to manufacture additional ATP to maintain the correct ATP/ NADPH ration needed for CO_2 fixation (Joliot and Joliot, 2002; Munekage et al., 2004), and CEF around PSII serves as a photoprotective slip mechanism that short-circuits photosynthetic charge separations when the PQ pool is reduced more rapidly than it can be oxidised (Feikema et al., 2006). The Mehler reaction involves the photoreduction of O_2 to water in PSI, by electrons generated by the photolysis of water in PSII (Asada, 1999, 2000, 2006; Mehler, 1951). The Mehler reaction effectively protects against photoinhibition by rapidly reducing the lifespan of photoproduced active oxygen species through the use of oxygen as an alternative electron acceptor. In addition to safely dissipating excess excitation energy, a pH gradient is maintained across the thylakoid membrane driving ATP production (Asada, 2000). Chlororespiration involves the reduction of the PQ pool by a stromal reductant (NAD(P)H) and the subsequent

oxidation of the PQ pool through the activity of a plastoquinol terminal oxidase (PTOX) located upstream of the Cyt b_6f complex (Cournac et al., 2000; Peltier and Cournac, 2002). It has been proposed that this alternative cycling serves to alleviate an over-reduced PQ pool, thus preventing photoinhibition and subsequent photosystem damage. In addition, under low light or dark conditions, chlororespiration promotes the formation of a pH gradient across the thylakoid lumen, which is essential in ATP synthesis and the photoprotective xanthophyll cycle (XC) (Jakob et al., 1999).

1.4.5.2 Non-photochemical quenching (qN)

The non-photochemical quenching of chl-*a* fluorescence is the term used to describe all thermal processes involved in the dissipation of excess excitation energy. While the principle of qN is the same throughout all phytoplankton, crucial differences exist in its regulation and the mechanisms employed. It encompasses a range of actions that collectively contribute to the reduction in fluorescence; while numerous qN mechanisms exist, the three main processes include the energy-dependent formation of a trans-thylakoid proton gradient (qE), state transitions of photosystem components (qT), and photoinhibition (qI).

Energy dependent quenching (qE)

The XC in chromophytes, including diatoms, dinoflagellates, and haptophytes, was first observed in the 1970s (Hager and Stransky, 1970; Stransky and Hager, 1970). It involves the interconversion of diadinoxanthin (Dd) and diatoxanthin (Dt) in response to changing light conditions (Eq. 1.3) (Demers et al., 1991; Goss and Lepetit, 2015; Liaaen-Jensen, 1978). Under high light conditions, Dd is converted to Dt through a photo-dependent de-epoxidation reaction, trigged by a ΔpH gradient across the thylakoid membrane (Lavaud and Kroth, 2006). The de-epoxidation of Dd to Dt occurs at a higher lumenal pH in diatoms than in higher plants, allowing for the accumulation of Dt in the dark through chlororespiratory electron flow (Grouneva et al., 2009; Jakob et al., 1999, 2001). In the absence of a proton gradient, typically in low light or dark conditions, the epoxy group is reintroduced to Dt via diatoxanthin epoxidase (DEP).

$$\text{Diadinoxanthin} \underset{DDE}{\overset{DEP}{\rightleftharpoons}} \text{Diatoxanthin} \tag{1.3}$$

The conversion of Dd to Dt occurs rapidly, typically on the time scale of seconds to minutes (Lavaud et al., 2002b; Olaizola et al., 1994; Welschmeyer and Hoepffner, 1986; Wu et al., 2012; Zhu and Green, 2010), sometimes up to 1 h (Demers et al., 1991), with the

feasibility of capturing such a rapid reaction *in situ* remaining uncertain (Brunet et al., 1993). Exposure to constant increased growth irradiance leads to increases in both the Dd and Dt pool, occurring over longer time periods (Casper-Lindley and Björkman, 1998; Demers et al., 1991; Lavaud et al., 2002b; Meyer et al., 2000; Moisan et al., 1998).

State transitions (qT)

Photosynthetic organisms are continuously acclimating to a changing light environment and can balance energy input with consumption by reversibly redistributing the energy between the two photosystems through state transitions (qT). In the green algae *Chlamydomonas reinhardtii*, a reduction of the PQ pool leads to activation of the thylakoid-associated serine-threonine kinase (Stt7), which phosphorylates the light-harvesting complex II (LHCII) (Depège et al., 2003). The phosporylated LHCII is then translocated from PSII to PSI (state II), in a Cyt b_6f-dependent manner (Delosme et al., 1996). When the photosystems are in a state II arrangement there is a switch from LEF to CEF around PSI, resulting in oxidation of the PQ pool, and a return to state I (Finazzi et al., 1999, 2002). *C. reinhardtii* is a good model organism to study qT, as its transition from state I to state II is accompanied by a large, detectable drop in fluorescence (Wollman, 1984). While this reversible chromatic adaptation plays a role in balancing the light absorption between PSI and PSII in multiple photosynthetic organisms (Bellafiore et al., 2005), it has yet to be identified in numerous photosynthetic organisms, including diatoms (Owens, 1986). In addition, qT may not be a strict transition between states; energy may not be redirected to another photosystem, and one or other photosystem is simply decoupled to result in high dissipation, creating a high fluorescence state that impacts the quantum yield.

Photoinihibition (qI)

Photoinhibition (qI) is an unavoidable consequence of oxygenic photosynthesis, a feature that phytoplankton try to mitigate through alternative electron flow and thermal quenching mechanisms including qE and qT. In terms of relaxation kinetics in darkness following a period of illumination, qI occurs on a timescale of hours, distinguishable from the faster relaxation kinetics of qE (Alderkamp et al., 2013). Damage to the D1 protein and the loss of functional PSII reaction centres leads to a decrease in photosynthetic activity and subsequent drop in NADPH production, limiting antioxidant activity, resulting in increased ROS and a loss of viability (van de Poll et al., 2006, 2007). Photoinhibition is reversible, with damaged D1 reaction centre protein degraded and replaced with D1 synthesised *de novo* (Hazzard et al., 1997). An active D1 repair cycle is crucial for

maintaining photosynthetic efficiency and cell viability (van de Poll et al., 2007).

1.4.5.3 Non-photochemical quenching in Southern Ocean phytoplankton

In cyanobacteria, the orange carotenoid protein (OCP), which binds the xanthophyll 3'-hydroxyechinenone (Kerfeld et al., 2003), is essential for qN (Wilson et al., 2006). This carotenoid is activated through absorption of blue-green light, which triggers conformational changes that render OCP activated (Wilson et al., 2008). This activated state of OCP is able to bind to the phycobilisomes and quench excess excitation energy (Gwizdala et al., 2011).

Diatoms have hyper-efficient photoprotective responses to fluctuating light environments and often dominate the phytoplankton community in turbulent conditions (Harris, 1986), where vertical mixing continuously exposes them to changing light levels on time scales of minutes to days (Lewis et al., 1984). They have adapted to survive long periods of darkness when carried below the euphotic zone as well as brief periods of full surface sunlight (Lavaud et al., 2002c). Photoprotection of PSII through dissipation of excess excitation energy and the related XC are of particular importance to diatoms (Lavaud et al., 2002a), with the xanthophyll pigment concentration relative to chl-*a* often greater than in higher plants (Wilhelm, 1990). Non-photochemical quenching in diatoms is very important under high light conditions, and generally involves three interacting components, namely (1) the formation of a trans-thylakoid proton gradient during light exposure, (2) the xanthophyll Dt is synthesised from Dd by DDE in the presence of the formed proton gradient, and (3) the Lhcx antenna proteins (Goss and Lepetit, 2015). The acidification of the thylakoid lumen is necessary to activate DDE (Goss et al., 2007), with chlororespiration and CEF around PSI responsible for the establishment of a pH gradient under conditions not conducive to LET (Jakob et al., 2001; Ting and Owens, 1993). Additional qN mechanisms found in diatoms include the regulation of the PQ redox state (Lepetit et al., 2013) and structural rearrangements reminiscent of state transitions (Fujita and Ohki, 2004; Schaller-Laudel et al., 2015). Certain species attempt to mitigate qI through CEF around PSII (Feikema et al., 2006) and/ or through an active D1-repair cycle (Domingues et al., 2012).

P. antarctica is well adapted to low irradiance (Moisan and Mitchell, 1999) and typically responds by increasing the number of thylakoid membranes per cell (Moisan et al., 2006). It is also well adapted to a high light environment, reducing thylakoid stacking (Moisan et al., 2006) and implementing effective qN (Moisan et al., 1998). Moisan et al. (1998) first described the presence of a rapidly induced Dd-Dt cycle in *P. antarctica*, with initial conditions of acclimation determining the size of the xanthophyll pool. How-

ever, photoprotection in *Pheaocystis* appears to be inferior to that of diatoms (Alderkamp et al., 2013; Arrigo et al., 2010; van de Poll et al., 2011). Kropuenske et al. (2010) observed that *P. antarctica* acclimated to changes in irradiance more rapidly than diatoms, but were more sensitive to photoinhibition, with diatoms displaying extensive photoprotection and low photoinhibition, highlighting their adaptations to mixed and stratified environments respectively. van de Poll et al. (2011) showed that populations present in stratified Antarctic coastal waters were dominated by diatoms (∼74%) and *P. antarctica* (∼13%), which is largely due to the higher photoprotective: photosynthetic pigment ratio in diatoms relative to *P. antarctica* (Alderkamp et al., 2013; Arrigo et al., 2010; van de Poll et al., 2011).

Cryptophytes are able to elicit both qT-type quenching (Cheregi et al., 2015) and qE-type quenching (Kana et al., 2012). However, crytophytes do not exhibit a XC nor contain the photoprotective pigments Dd, Dt, and zeaxanthin (Funk et al., 2011; Kana et al., 2012). Non-photochemical quenching is reported to occur at the site of the chl-a/c antennae and not the phycobiliproteins (Kana et al., 2012), and may involve increased amounts of the photoprotective pigment alloxanthin (Funk et al., 2011). Alloxanthin is the dedicated marker pigment for cryptophytes (Jeffrey and Vesk, 1997), and exhibits an abs_{max} at 496 nm (Kana et al., 2009). Under high light conditions the increased concentration of alloxanthin would lead to increased absorption in the blue part of the light spectrum, akin to an increased concentration of Dt in phytoplankton that employ a XC.

1.5 Chlorophyll-a

1.5.1 Chlorophyll-a absorption

Absorption ($a(\lambda)$), an inherent optical property (Preisendorfer, 1976), is best described in terms of its constituent components as in Eq. 1.4, where $a_w(\lambda)$ is absorption by water, $a_p(\lambda)$ is the total particulate absorption and $a_s(\lambda)$ is the absorption by dissolved material in the water. Light absorption by phytoplankton alone is a complex process requiring numerous considerations, as summarised by Eq. 1.5 and Eq. 1.6, where $a_{ph}(\lambda)$ is phytoplankton-specific absorption, $a_d(\lambda)$ is the non-algal, or detrital, absorption, $a_{ps}(\lambda)$ is absorption by photosynthetic pigments in phytoplankton, and $a_{nps}(\lambda)$ is the absorption by non-photosynthetic pigments.

$$\text{a}(\lambda) = a_w(\lambda) + a_p(\lambda) + a_s(\lambda) \tag{1.4}$$

and

$$\mathrm{a}_p(\lambda) = a_{ph}(\lambda) + a_d(\lambda), \tag{1.5}$$

where

$$\mathrm{a}_{ph}(\lambda) = a_{ps}(\lambda) + a_{nps}(\lambda). \tag{1.6}$$

Absorption of light by phytoplankton is governed by complex mechanisms. Through numerous laboratory (Sathyendranath et al., 1987; Sosik and Mitchell, 1991) and field studies (Bricaud et al., 1995, 2004; Bricaud and Stramski, 1990; Hoepffner and Sathyendranath, 1992; Lohrenz et al., 2003; Nelson and Robertson, 1993; Stuart et al., 1998), it has been consistently shown that variation in *in vivo* specific absorption coefficients (400-700 nm) is due to pigment composition and packaging. The absorption spectrum of phytoplankton is representative of the total absorption by all pigments within the cell, including photoprotective pigments. Chlorophyll-*a* absorbs light in the blue and red parts of the visible electromagnetic spectrum, and when dissolved in acetone, the blue band, also known as the B or Soret band, is centred around 430 nm and the red band, or Q band, is centred at 662 nm (Fig. 1.7) (Huot and Babin, 2010). Upon excitation, chl-*a* molecules may return to the ground state through one of four pathways (Fig. 1.6), one of which is through the re-emission of light at a longer wavelength, a process termed fluorescence. Fluorescence emitted by chl-*a*, extracted in acetone, is characterised by a dominant peak centred at 668 nm. As the red chl-*a* absorption band partly overlaps its fluorescence band (Figure 1.7), the fluorescence emission may be partly reabsorbed before leaving the cell (Collins et al., 1985).

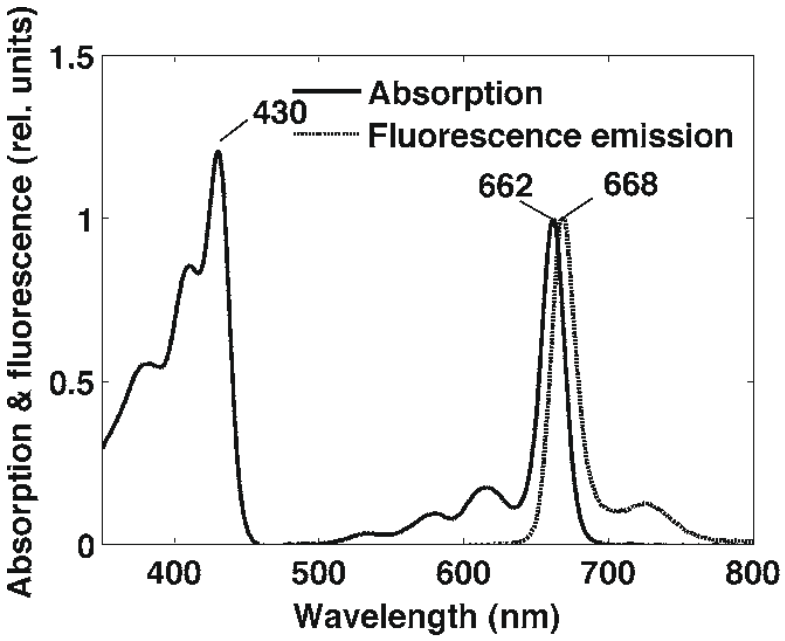

Figure 1.7: Spectra of light absorption and fluorescence emission by pure chl-a dissolved in acetone. Chl-a absorbs in the blue part of the spectrum (centred around 430 nm) and in the red part of the spectrum (centred around 662 nm). The overlap between the red spectral absorption of chl-a and fluorescence emission (centred around 688 nm) is clearly evident, occasionally allowing for re-absorption of fluoresced light by chl-a. Figure reproduced from Huot and Babin (2010).

The $a_{ph}(\lambda)$ of a population is typically calculated by the subtracting $a_d(\lambda)$ from $a_p(\lambda)$, with the total contribution of $a_d(\lambda)$ known to vary (Bricaud et al., 1998). Kishino et al. (1985) presented a methanol extraction method to eliminate phytoplankton pigments from the filtered material so that $a_d(\lambda)$ could be estimated; the efficiency of this treatment was proposed to be 90-95%. The occurrence of incomplete extraction, due to non-pigmented particles and non-extractable pigments (phycobilins), may lead to an overestimation of $a_d(\lambda)$ and should be considered. Other approaches include statistical and numerical modelling techniques to isolate the $a_{ph}(\lambda)$ and $a_d(\lambda)$ components from $a_p(\lambda)$ (Bricaud and Stramski, 1990; Roesler et al., 1989). Babin et al. (1996a) performed both methanol extraction (Kishino et al., 1985) and spectral decomposition (Bricaud and Stramski, 1990) techniques to derive $a_{ph}(\lambda)$, whereby both methods lead to convergent results when applied to the same sample.

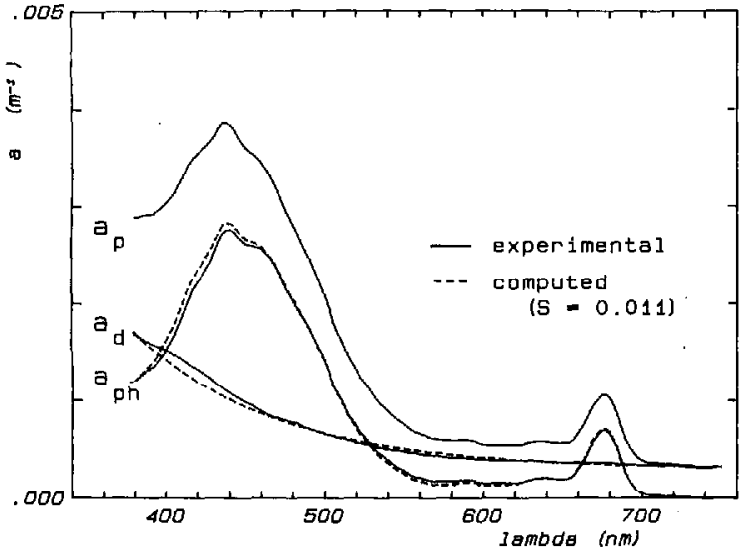

Figure 1.8: Comparison of the spectral values of detrital absorption ($a_d(\lambda)$) and phytoplankton-specific absorption ($a_{ph}(\lambda)$), experimentally obtained with the method of Kishino et al. (1985) (solid lines) and numerically computed through the decomposition method of Bricaud and Stramski (1990) (dashed lines). The exponent value S is 0.011 nm^{-1}. This example of a surface sample in the Sargasso Sea has been reproduced from Bricaud and Stramski (1990)

The numerical decomposition approach designed by Bricaud and Stramski (1990) makes use of the shape of the $a_p(\lambda)$ spectrum. This method is based on a green-to-violet and a yellow-to-red ratio of the $a_p(\lambda)$, where the ratios are typically $\sim$1 for living phytoplankton. The criteria for selecting the wavelengths used in these ratios stipulate that the absorption by accessory pigments must be minimal, the ratios selected must be close to $\sim$1 for living phytoplankton and that the wavelengths in each ratio must be adequately spaced to reliably estimate the $a_d(\lambda)$ slope. Avoiding accessory pigment absorption removes the influence of pigment composition variations, making this approach universal across phytoplankton taxa. Selecting ratios close to $\sim$1 eliminates the effect of pigment packaging and the resultant flattening of the absorption spectrum that occurs due to an increase in cell size or pigment concentration (Morel and Bricaud, 1981). Ratios that best fit these criteria were $a_{ph}(505)$:$a_{ph}(380)$ and $a_{ph}(580)$:$a_{ph}(692.5)$, which were found to be nearly constant, 0.99 and 0.92 respectively, in surface samples in the Sargasso Sea (Bricaud and Stramski, 1990). A station example from Bricaud and Stramski (1990) is illustrated in Figure 1.8, where the value of the slope exponent S was 0.011 nm^{-1}. The spectral dependency of $a_d(\lambda)$ has been shown to vary experimentally, with a varying exponent S ranging from 0.005-0.014 nm^{-1}(Table 1.2). Values that deviate from $\sim$1 may be detected through anomalous S values (close to 0 or $\gtrapprox$0.02). This method

of Bricaud and Stramski (1990) was used to effectively deconvolve $a_p(\lambda)$ into algal and non-algal components by Babin et al. (1993, 1995), demonstrating the reproducibility of this approach.

Table 1.2: Examples of average slope exponent values from previous studies.

Reference	Site	Average S (nm^{-1})
Yentsch (1962)	New Jersey coast	0.007
Okami et al. (1982)	Tokyo Bay	0.005
Kishino et al. (1985)	Shimodo coast	0.006
Iturriaga and Siegel (1989)	Sargasso Sea	0.011
Morrow et al. (1989)	Sargasso Sea	0.009
Roesler et al. (1989)	San Juan Islands	0.011
Bricaud and Stramski (1990)	Sargasso Sea	0.011
	Peruvian upwelling	0.010
Babin et al. (1993)	Gulf of St. Lawrence (1989)	0.011
	Gulf of St. Lawrence (1990)	0.014
Babin et al. (2003)	UK surrounding seas	0.012
Published mean		0.010 $\pm$0.003

1.5.1.1 Phytoplankton accessory pigment absorption

Phytoplankton-specific absorption comprises the total absorption of intracellular pigments (Fig. 1.9), including those that effectively transfer excitation energy to the photochemical reaction centres (photosynthetic pigments) and those that function as photoprotective accessory pigments or other cell components not coupled to photochemistry (non-photosynthetic pigments) (Eq. 1.6). It should be noted that all pigments transfer energy to other pigments or reaction centres, but they do so with either high or less than high transfer efficiency (Suggett et al., 2004). Accessory pigments, such as the carotenoids zeaxanthin and β-carotene, function in photoprotection and do not transfer received photon energy to the reaction centre cores, yet still contribute to the a_{ph} (Bidigare et al., 1989; Sosik and Mitchell, 1995). Carotenoids are capable of quenching triplet state molecules, singlet oxygen, and free radical intermediates, all of which are potentially destructive to phytoplankton (Rau, 1988). Attempts have been made to separate the photosynthetic (a_{ps}) and non-photosynthetic (a_{nps}) pigments through pigment reconstruction methods (Bidigare et al., 1989; Letelier et al., 2017), spectral decomposition techniques (Allali et al., 1997; Babin et al., 1996a) and through fluorescence excitation spectra analyses (Johnsen et al., 1997; Lutz and Sathyendaranath, 2001; Sakshaug et al., 1991; Sosik and Mitchell, 1995). It has been conclusively shown that the majority of variation in a_{ph}, in the upper layers of the water column, is due to changes in the contributions of photo-

protective pigments relative to chl-a (Allali et al., 1997; Letelier et al., 2017; Sosik and Mitchell, 1995).

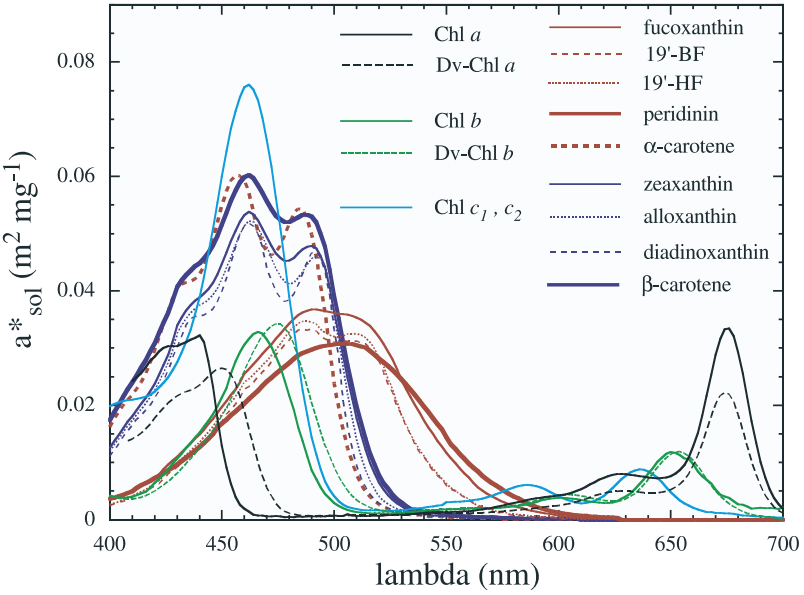

Figure 1.9: Weight-specific absorption spectra of key pigments, a^*_{sol} (m^2 mg^{-1}), as derived from absorption spectra of individual pigments in solvent. The absorption spectra of photosynthetic and non-photosynthetic carotenoids are shown in blue and red respectively. Figure reproduced from Bricaud et al. (2004)

.

1.5.1.2 The package effect

Increasing intracellular pigment concentration or enlarging cell size diminishes the absorption efficiency of a cell (Q_a). The absorption efficiency refers to the ratio of light absorbed by a cell relative to the total incident light on that cell (Morel and Bricaud, 1981). This non-linearity is due to the "package effect", the reduction of the light absorbed by intact phytoplankton relative to the same amount of pigment in solution (Kirk, 2011). The package effect occurs due to the fact pigments are not uniformLy distributed and are arranged within chloroplasts, which themselves are arranged within the cell. The effect of pigment packaging on the absorption spectra of algal suspensions was first described by Duysens (1956), in a pioneering study that showed the package effect varies with the size, shape, and optical density of the particles. Further pivotal studies were undertaken, including work done by Kirk (1975a,b, 1976), who considered the impact of cell size, shape, and pigment content on packaging and the subsequent effect on light attenuation within natural waters. While Duysens (1956) and Kirk (1975a,b, 1976) examined particles of various shape, Morel and Bricaud (1981) described the same flattening of the

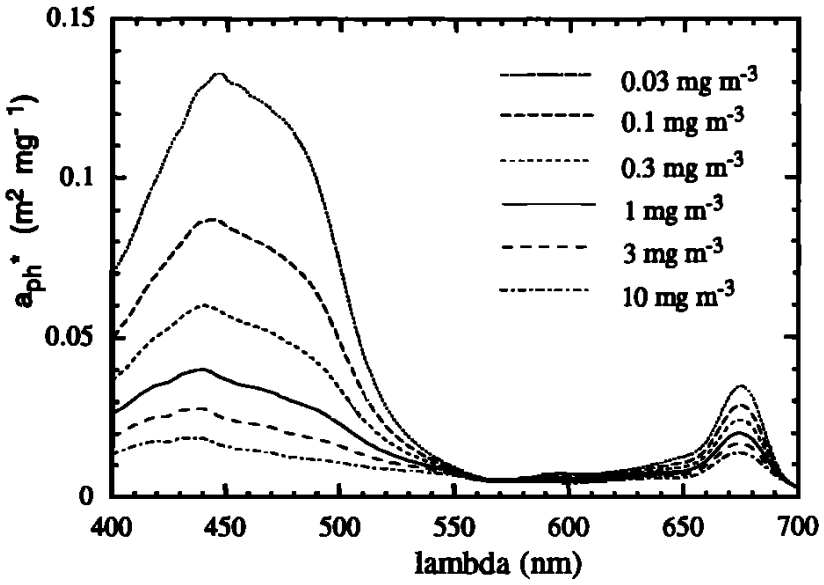

Figure 1.10: Chl-a-specific absorption spectra of living phytoplankton for various values of [chl-a], clearly illustrating spectral flattening as a result of increasing [chl-a] and the subsequent package effect. Figure reproduced from Bricaud et al. (1995).

absorption spectrum through the Mie theory of scattering. Pigment packaging reduces the capacity to effectively capture light from the surrounding environment, contributing to the reabsorption of chl-a fluorescence (Babin et al., 1993), lowering a^*_{ph}, and flattening the resulting spectra (Fig. 1.10).

Chl-a-specific absorption in the red absorption maximum peak is negligibly influenced by pigment packaging. Johnsen et al. (1994) established the maximum, unpackaged $a^*_{ph}(675)$ to be 0.027 m^2 mg chl-a^{-1} in two dinoflagellate species. Stuart et al. (1998) found that the mean $a^*_{ph}(676)$, with HPLC-derived [chl-a], varied widely (∼0.028-0.039 m^2 mg chl-a^{-1}) across different environments. Organelli et al. (2017) recorded $a^*_{ph}(675)$ values up to 0.057 m^2 mg chl-a^{-1} for mixed assemblages in culture studies, surpassing those of 0.038 m^2 mg chl-a^{-1} observed for simulated mixed assemblages (Bricaud et al., 1995; Organelli et al., 2016), suggesting a weaker pigment packaging effect of chl-a in natural assemblages.

1.5.2 Chlorophyll-a fluorescence

The phenomenon of the re-emission of absorbed radiation, known as fluorescence, was first observed and detailed by Sir George Stokes in 1852 (Stokes, 1852). Fluorescence is more recently described as the re-emission of energy as a photon, observed when excited singlet-state molecules return to the ground state. When a chl-a molecule absorbs a photon of light less than 670 nm (Bolhàr-Nordenkampf and Öquist, 1993), either in the

blue Soret bands or red Q-bands of the visible electromagnetic spectrum, the molecule will be elevated to an excited singlet-state. The return of chl-*a* to the ground state occurs through photochemistry, resonance-energy transfer, non-radiative decay, or re-emission of light, i.e. fluorescence (Mathis and Pailloton, 1981). When chl-*a* absorbs light in the Q-bands, the molecule is raised to the first excited state, S_1, which rapidly returns to ground state through energy dissipation as heat and fluorescence. When chl-*a* absorbs a photon in the higher-energy Soret bands, the chl-*a* molecule is elevated to the second excited state, S_2, which thermally decays to S_1, before returning to ground state as heat and fluorescence (Figure 1.11).

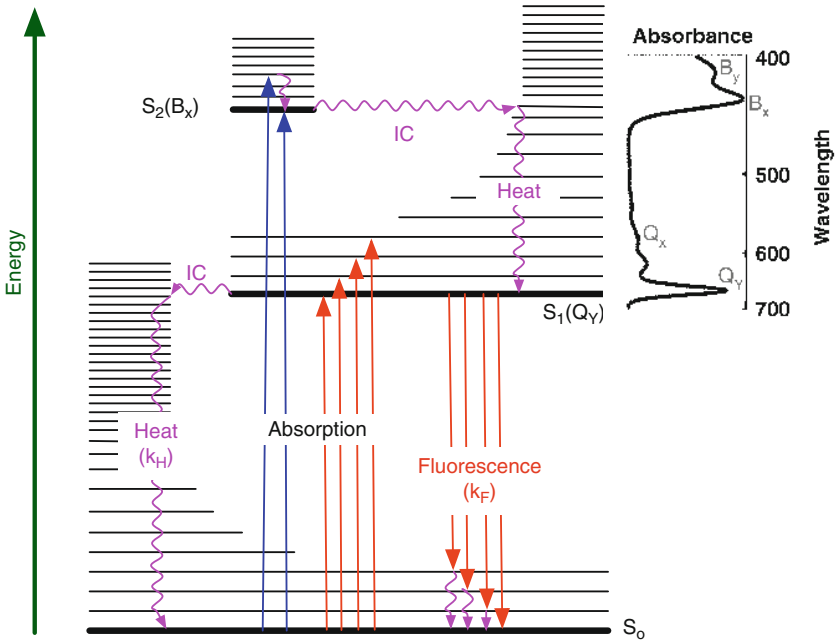

Figure 1.11: Jablonski diagram depicting the relationships between excited states, absorption bands and fluorescence in chl-*a* (figure reproduced from Huot and Babin (2010)). The higher excitation states achieved by Soret band photon absorption (B_x and B_y), rapidly decay to lower excitation states (Q_x and Q_y) through heat dissipation. The Q_y band, centred around 678 nm *in vivo*, is the lowest singlet excited state. Decay from the lowest excited state to the ground state occurs through thermal and fluorescence emission. In algae, the peak wavelength of the lower-energy fluorescence band is centred around 685 nm *in vivo* (Krause and Weis, 1991).

At room temperature, chl-*a* fluorescence is predominantly emitted by PSII (Falkowski and Kiefer, 1985; Vredenberg and Slooten, 1967) as a typically conserved distribution around 685 nm (Krause and Weis, 1991). While phytoplankton absorption spectra describe total absorption by all pigments within a cell, the fluorescence excitation spectra, at room temperature, are derived exclusively from the re-emission of light reaching chl-*a* of PSII. The fixed waveband of fluorescence varies with incident light as a function of wave-

length. The shape of excitation spectra can appear very different to absorption spectra as the contribution from a_{nps} is removed, and can be more meaningful when examining how light absorption contributes to LEF (Suggett et al., 2004).

1.5.2.1 Chlorophyll-a fluorescence applications

In 1931, Kautsky and Hirsch were the first to report on the chl-a fluorescence induction kinetics in dark-adapted leaves following light exposure (Kautsky and Hirsch, 1931). This phenomenon is referred to as the Kautsky effect, also termed variable fluorescence, and forms the premise of many modern fluorescence studies. In the 1960s, the use of *in vitro* (Yentsch and Menzel, 1963) and *in vivo* (Lorenzen, 1966) chl-a fluorescence to determine chl-a concentration ([chl a]) was introduced to biological oceanography. The use of variable fluorescent techniques for *in vitro* and *in vivo* studies has proven valuable in understanding the fundamentals of phytoplankton photophysiology. Interestingly, recent attempts have been made to account for the package effect through fluorescence reabsorption corrections derived from variable fluorescence measurements (Boatman et al., 2019). However, while variable fluorescence measurements offer insight into light utilisation, they do not provide full closure on the fate of absorbed photons (Lin et al., 2016), and are not easily related to satellite observations. During the daytime, phytoplankton emit low but detectable levels of chl-a fluorescence, referred to as natural fluorescence, also known as passive, solar or sun-induced chlorophyll fluorescence (SICF). Natural fluorescence can be detected *in situ* using radiometers mounted on moorings (Dickey et al., 1993, 1998), profilers or drifters (Letelier et al., 1997; Schallenberg et al., 2008), ships (Dandonneau and Neveux, 1997; Kiefer et al., 1989), aircraft (Neville and Gower, 1977), or satellites (Babin et al., 1996b; Huot et al., 2005). Satellite-derived ocean colour products are desirable, providing cost-effective, routine measurements on a global scale. The launch of the Moderate Resolution Imaging Spectroradiometer (MODIS)-Aqua sensor (National Aeronautics and Space Administration (NASA)), with a dedicated chl-a fluorescence waveband, has expanded ocean colour opportunities (Esaias et al., 1998).

1.5.3 Chlorophyll-a fluorescence quantum yield

The fluorescence quantum yield of chl-a (Φ_F) of acetone-extracted chl-a *in vitro*, i.e. the ratio of photons emitted as fluorescence to those absorbed by chl-a (the absolute Φ_F), is $\sim$30%, with the remaining $\sim$70% of photons being dissipated as heat (Huot and Babin, 2010). The absorption of excitation energy by chl-a of intact phytoplankton is largely dependent upon pigment composition and the package effect. The *in situ* Φ_F, often

termed apparent Φ_F, is defined as the ratio of light fluoresced by chl-*a* to total light absorbed by phytoplankton (Browning et al., 2014a), which accounts for the absorption by chromophores that do not participate in the fluorescence emission (Miller et al., 2002). The derivation of Φ_F requires, in addition to the accurate quantification of fluorescence, the spectral composition of the excitation energy and the spectral absorption capacity of the phytoplankton present. Variability in Φ_F will be discussed in depth throughout this thesis. Previous studies examining Φ_F, both through *in situ* and remotely sensing investigations, have reported Φ_F values between 0.001-0.15 (Table 1.3).

Table 1.3: Examples of chl-*a* fluorescence quantum yield values and proxies thereof from previous studies (Φ_F, quanta emitted (quanta absorbed)$^{-1}$).

Reference	Site	Φ_F
***In situ* studies**		
Roesler and Perry (1995)	Misc. environments	∼0.008-0.09
Letelier et al. (1997)	Drake Passage	∼0.001-0.003
Ostrowska et al. (1997)	Baltic Sea	∼0.001-0.03
Maritorena et al. (2000)	Tropical Pacific & Peru upwelling	∼0.01-0.06
Morrison (2003)	NE coast of the UK	∼0.004-0.063
Westberry and Siegel (2003)	Sargasso Sea	∼0.01-0.05
Schallenberg et al. (2008)	Bering Sea	∼0.003-0.1
Ostrowska (2012)	Baltic Sea & Atlantic Ocean	∼0.002-0.1
Ostrowska et al. (2012)	Global waters (modelled study)	∼0.001-0.1
Remote sensing studies		
Babin et al. (1996b)	Global oceans	∼0.01-0.05
Huot et al. (2005)	Arabian Sea	∼0.01-0.035
Behrenfeld et al. (2009)	Global oceans	∼0.00-0.028
Morrison and Goodwin (2010)	Gulf of Maine	∼0.003-0.018
Westberry et al. (2013)	Pacific Southern Ocean	∼0.01-0.04
Browning et al. (2014a)	Atlantic Southern Ocean	∼0.01-0.10
Lin et al. (2016)	Global oceans	∼0.02-0.15

1.6 Satellite Remote Sensing of Ocean Colour

1.6.1 Light in the ocean and bio-optical principles

Light that enters the ocean can either be absorbed or scattered by the material in the water. The amount of absorption and scattering are dependent on the concentration and characteristics of the seawater constituents and are independent of the radiant light field; these are known as the inherent optical properties (IOPs). The IOPs of seawater include the absorption (a), scattering (b), and attenuation coefficients (c, where $c = a +$

b) (Preisendorfer, 1976). The scattering coefficient, b, is divided into forward (b_f) and backward (b_b) components. While both b_f and b_b are representative of the scattering by water and particulate material, a is affected by the absorption of numerous optically active components, including water, coloured dissolved organic material (CDOM), algal and non-algal components. The apparent optical properties (AOPs) are reliant on both the IOPs and the geometric structure of the light field and include radiance and/ or irradiance ratios, i.e. reflectances, as well as diffuse attenuation coefficients (Mobley, 1994).

The processes of scattering and absorption by dissolved and particulate matter in the ocean affect the spectrum and light field of the water-leaving reflectance and are crucial to explicating remote sensing data, with Gordon et al. (1975) describing the relationship between such bio-optical features and the remote sensing reflectance (R_{rs}) as follows:

$$R_{rs} \propto \frac{b_b}{a + b_b} \tag{1.7}$$

Both algal and non-algal particulate biological material dominate the optical variability of the open ocean (Bricaud and Stramski, 1990). The most significant, optically active constituents can be separated into three categories (Lapucci et al., 2012): phytoplankton and other microscopic organisms (e.g. zooplankton, heterotrophic bacteria and viruses); non-algal particles (NAP), suspended detrital material of organic and inorganic matter; and CDOM, dissolved compounds derived from the disruption of organic matter (IOCCG, 2000; Morel and Prieur, 1977). Chlorophyll-a, serving as a marker for phytoplankton, has an absorption maxima in the blue and red wavelengths (Bidigare et al., 1989). Phytoplankton-related b_b coefficients are generally very low at the relatively low concentrations of biomass found in the open ocean (Bricaud et al., 1983). NAP absorption follows a decreasing exponential function of wavelength, with an absorption maximum in the blue (Bricaud et al., 1998). NAP b_b is remarkable, and considered a major source of ocean b_b (Stramski et al., 2001). CDOM absorption is also notable and follows a decreasing trend with wavelength (Prieur and Sathyendranath, 1981), while its contribution to b_b is negligible. The partly common absorption and scattering properties of the three main constituents tend to create ambiguous spectral situations, particularly when present in similar low concentrations (Mobley, 1994). A broad optical classification scheme was introduced by Morel and Prieur (1977), partitioning seawater types into Case 1 and Case 2 waters. In Case 1 waters, phytoplankton and their accompanying biogenous material are primarily responsible for variation in the optical properties of the water. Case 2 waters are not only influenced by phytoplankton and related particles, but also by NAP and

CDOM that vary independently of the phytoplankton (IOCCG, 2000).

Bio-optical characterisation can provide qualitative and quantitative information pertaining to variability in phytoplankton biomass, species composition, and physiological responses. Measurements of ocean colour and the fate of solar radiation in the ocean have long since been exploited as effective indicators of the biological activity in surface waters (Lorenzen, 1972; Yentsch, 1960). The principal approach to obtaining information on phytoplankton dynamics, over a wide range of spatial and temporal scales, has been through the estimation of chl-*a* from satellite-derived water-leaving radiance or equivalents such as R_{rs}. A satellite ocean-colour sensor measures spectral radiance (L_{sat}, W m^{-2} nm^{-1} sr^{-1}), which is dependent upon solar irradiance, atmospheric transmission and scattering, sea-surface reflection and the optical properties of the water (Cullen et al., 1997). The removal of surface reflection and various atmospheric factors results in the water-leaving radiance ($L_w(\lambda)$), the spectral variation of which defines ocean colour (Gordon et al., 1988). Variation in $L_w(\lambda)$ is largely driven by changes in the downwelling solar irradiance ($E_d(\lambda)$, W m^{-2} nm^{-1}), with R_{rs} representing the ratio of $L_w(\lambda)$ to $E_d(\lambda)$.

1.6.2 Satellite-derived [chl-*a*] and fluorescence

As the biomass of phytoplankton in the surface water of the ocean increases, the colour of the water changes from violet-blue to green-olive. This shift in colour is the result of the strong absorption of blue wavelengths by phytoplankton as well as their weaker absorption of green wavelengths (Morel, 1988; Yentsch, 1960), reducing the amount of blue light backscattered out of the ocean relative to green light. These shifts in hues of water are quantifiable through remote sensing measurements of the spectra of light leaving the ocean surface and can be used to infer the phytoplankton biomass (Clarke et al., 1970). Such empirical algorithms were first developed by functionally relating the ratio of blue-to-green reflectance (blue light near 440 or 490 nm, green light near 550 nm) leaving the ocean surface to the phytoplankton [chl-*a*] measured *in situ*. The launch of the Nimbus-7 satellite (NASA) saw the first ever dedicated ocean colour sensor being sent into space, the CZCS (1978-1986), for which an empirical blue-to-green ratio algorithm was successfully developed to estimate [chl-*a*] (Gordon et al., 1983). These blue-green algorithms are still used today as the default method of deriving [chl-*a*] from ocean colour sensors (O'Reilly et al., 2000). Whilst the empirical approaches used to derive [chl-*a*] are generally robust (Morel, 2009), it has been established that second order variability, such as assemblage composition, can affect [chl-*a*] retrieval by up to 50% (Alvain et al., 2006). This may be accounted for and exploited to provide a more holistic description of

the in-water constituents, through the development of model-based approaches such as semi-analytical algorithms (Brown et al., 2008; Sauer et al., 2012). These models apply inversion techniques to the satellite-retrieved AOPs, such as R_{rs}, in order to derive the IOPs of seawater, and have the advantage of simultaneously retrieving several bio-optical markers from a single set of R_{rs} data (Hoge and Lyon, 1996; Lee et al., 2002; Maritorena et al., 2002; Roesler and Perry, 1995).

Satellite-detected SICF has been utilised as an indicator of [chl-*a*] and subsequent proxy for phytoplankton biomass (Hu et al., 2005), in addition to being used to provide insight into the photophysiological status of phytoplankton (Abbott et al., 2001; Behrenfeld et al., 2009; Huot et al., 2005, 2013; Laney et al., 2005; Letelier et al., 1997; Morrison and Goodwin, 2010; Schallenberg et al., 2008; Westberry et al., 2013). The *in vivo* fluorescence of chl-*a* in phytoplankton was first described as a red peak centred around 685 nm in subsurface reflectance (Morel and Prieur, 1977) and nadir radiance signal (Neville and Gower, 1977). This characteristic red peak has since been exploited to examine variations in phytoplankton biomass, and is detected in both in-water (Babin et al., 1996b; Gordon, 1979; Kiefer et al., 1989; Maritorena et al., 2000; Morrison, 2003; Roesler and Perry, 1995) and water-leaving (Doerffer, 1981; Gower, 1980; Neville and Gower, 1977) radiance spectra. The MODIS sensor, launched into orbit by NASA onboard the Terra (1999) and Aqua (2002) satellites (Savtchenko et al., 2004), comprises wavebands necessary for SICF extraction. Compared to the traditional blue-green algorithms, SICF retrievals are less likely to be contaminated by coloured dissolved and detrital organic material absorption or by highly scattering mineral particles (Hoge et al., 2003). It is representative of chl-*a* fluorescence, incident irradiance, and the optical and fluorescence traits of the resident phytoplankton (Babin et al., 1996b), and has been used in estimates of satellite-derived Φ_F (Φ_{sat}), providing a useful tool for evaluating physiological responses to various environmental forces i.e. light and Fe conditions (Babin et al., 1996b; Behrenfeld et al., 2009; Browning et al., 2014a; Huot et al., 2005, 2013; Laney et al., 2005; Letelier et al., 1997; Lin et al., 2016; Morrison and Goodwin, 2010; Schallenberg et al., 2008).

1.7 Thesis Outline

The Southern Ocean is a highly productive region and yet little is known about its variance, what drives it over space and time, and how it affects global carbon cycling. Exploiting Φ_F serves as a unique and novel opportunity to expand on current understanding. This thesis serves to derive *in situ* Φ_F, to investigate the drivers of variability, and to validate existing satellite ocean colour Φ_{sat} algorithms, with the overall aim of increasing insight into phytoplankton dynamics in this climate-relevant ocean.

The thesis objectives are threefold:

1. Develop an existing multi-excitation fluorometer for use in *in situ* Φ_F determination.
2. Investigate the drivers of *in situ* Φ_F variability.
3. Validate existing satellite Φ_{sat} algorithms with *in situ* Φ_F.

Chapter 2 details the general oceanographic methods followed, the materials used, and the data quality control techniques employed in this study. Chapter 3 is a technical chapter, describing the radiometric characterisation and calibration of a multi-excitation fluorometer identified for use in *in situ* Φ_F determination. A Multi-Exciter Fluorometer (JFE Advantech, Co., Ltd.) undergoes a full instrument characterisation prior to being subjected to two different calibration approaches. Chapter 4 explores the potential drivers of *in situ* Φ_F variability. Wavelength-specific Φ_F measurements are derived for various stations sampled in the Atlantic sector of the Southern Ocean during the austral winter of 2012 and summer of 2013/ 2014. Potential drivers investigated include community structure, light history, and surrounding macronutrient conditions. Chapter 5 uses the *in situ* Φ_F measurements of Chapter 4 to validate three existing Φ_{sat} algorithms. Chapter 6 provides a synthesis of all the work contributing to this study and details the key findings of the individual chapters.

Chapter 2

General Methods and Data Quality Control

2.1 Research Cruise Participation

Data were obtained over five cruises destined to various Southern Ocean latitudes over a course of three years, as listed in Table 2.1. Certain cruises were affected by rust contamination in the underway scientific seawater supply, which occurred due to rouging, a form of stainless steel corrosion; the Winter Cruise and South African National Antarctic Expedition 53 (SANAE53) cruise were the only two cruises free from such contamination. Nonetheless, full sampling occurred across all 5 cruises, followed by subsequent attempts at data recovery from the contaminated cruises. The influence of rust on various underway measurements was too great to accurately account for, specifically regarding the absorbance samples where the influence of rust in the visible spectrum (up to 450 nm) rendered data unusable.

Table 2.1: Summary of research cruise participation. The Winter Cruise and SANAE53 cruises were the only rust-free cruises, the rest having a rust-contaminated underway water supply (grey). SOSCEx: Southern Ocean Seasonal Cycle Experiment; SANAE53: South African National Antarctic Expedition 53; No. und: number of underway stations; No. dis: number of discrete stations.

Cruise name	Date	Marine vessel	No. und	No. dis
Winter Cruise	9 Jul - 1 Aug 2012	*S.A. Agulhas II*	90	32
Expedition Cruise	7 Jul - 11 Feb 2013	*S.A. Agulhas I*	119	-
SOSCEx I	15 Feb to 11 Mar 2013	*S.A. Agulhas I*[1]	107	16
SANAE53	28 Nov 2013 - 13 Feb 2014	*S.A. Agulhas II*	149	5
SOSCEx III	20 Jul - 15 Aug 2015	*S.A. Agulhas II*[2]	83	29

The historic GoodHope Line monitoring programme was implemented in 2004, serving as a region of ongoing physical and biogeochemical sampling (Swart et al., 2012). The Winter Cruise sampling track spans a portion of the GoodHope Line as well as the coast of Marion Island (Fig.2.1 (a)). The SANAE53 summer cruise was separated into three legs effectively capturing the different regions in advancing stages of the summer. Leg 1 is the GoodHope-South leg from Cape Town to Antarctica (early summer); leg 2, the Buoy Run from Antarctica to South Georgia, return (mid-summer); and leg 3, the GoodHope-North leg from Antarctica to Cape Town (late summer) (Fig.2.1 (b)). The position of the fronts was determined using sea surface height data from maps of absolute dynamic topography (MADT) from the CLS/AVISO product (Rio et al., 2011; Swart et al., 2010).

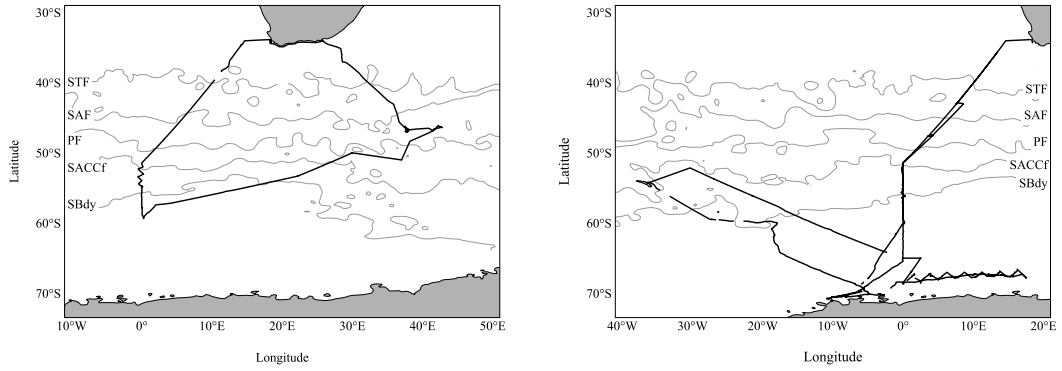

(a) The Winter cruise.

(b) The summer SANAE53 cruise.

Figure 2.1: The Winter Cruise (winter 2012) and SANAE53 voyage (summer 2013/ 2014) *S.A. Agulhas II* cruise tracks.

2.2 Pigment Extraction and Analysis

2.2.1 High performance liquid chromatography

High-performance liquid chromatography (HPLC) separates phytoplankton pigments in order of polarity upon passage through a reverse phase column (Ras et al., 2008), allowing for the quantification of a wide range of carotenoids, chlorophylls, and their degradation

[1]The SOSCEx I cruise was the final scientific research voyage of the *S.A. Agulhas*, which has since been commissioned as a maritime training vessel.

[2]The SOSCEx III cruise was the only voyage to date that has seen the *S.A. Agulhas II* underway water supply contaminated with rust; this dedicated polar research vessel has since been refurbished with epoxy coated stainless steel inflow pipes to mitigate future rust contamination.

products. Pigment samples collected for this project were personally processed through HPLC at the Laboratoire d'Oceanographie de Villefranche (LOV, Villefranche-sur-Mer, France, July 2014), following the procedure described by Ras et al. (2008). All [chl-*a*] values used in this study constitute HPLC-derived total [chl-*a*] measurements (the sum of chl-*a*, divinyl-chl-*a* and chlorophillide-*a*), apart from the total [chl-*a*] less divinyl-chl-*a* used in CHEMTAX analysis (see Section 2.2.2).

Approximately 2 L of seawater was filtered through 0.7 μm Whatman GF/F glass-fibre filters (25 mm) under less than 10 mmHg. The filters were folded in half and placed within labelled cryovials before being immediately stored in liquid nitrogen or at -80°C (cruise dependent). Upon arrival at LOV samples were sorted, on ice, and transferred to labelled, 14 mL Falcon tubes (Corning). Pigments were then extracted using methanol. Acetone is typically used for pigment extraction as it is less toxic and allows for a longer storage time at -80°C, however, methanol extraction allows for the rapid degradation of pigments, has a higher extraction efficiency and greater injection volume. Three millilitres of extraction solvent, containing vitamin E acetate as an internal standard, was added prior to incubation at -20°C for 1 h (extraction stock solution: 250 mg DL-α-tocopherol acetate (Sigma-Aldrich Fluka) + 100 mL methanol; extraction working solution: 3 mL stock solution + 1000 mL methanol, stored at -20°C in the dark). Inclusion of an internal standard allows for the monitoring of instrument drift.

Samples were then sonicated, on ice, for 10 s, before a further incubation period of 1 h at -20°C. The sonicator (Bandelin SONOPULS HD 2070) was thoroughly cleaned with ethanol between samples. Samples were clarified by filtration through 0.7 μm Whatman GF/Fs placed on a Millipore filtration rig. A glass pestle was used to ensure all sample was released from the GF/F slurry. Clarified samples were immediately transferred to HPLC glass vials (Agilent Technologies) using pasteur pipettes (VWR International).

The HPLC (Agilent Technologies 1200 series) consists of multiple units, including the de-gasser, binary pump, injection unit and refrigerated sample compartment, Pelletier refrigeration unit, thermostatted column compartment, and DAD detector unit. The column used was an Agilent Technologies Zorbax Eclipse XBD-C8 (150 $\times$ 3 mm, 3.5 μm, PN 963954-306). Samples, standards and methanol were loaded in a specific sequence. Following every ten samples the internal standard was measured to assess the overall stability of the run, with methanol used to clean the injection needle between every sample. The elution time for one sample was 28 min, with 30 samples being analysed in one run.

Analysis of samples was performed using ChemStation software (Agilent Technologies). Sample signals were detected at 450 nm (carotenoids, chl-*c* and -*b*), 667 nm (chl-*a* and

related allomers and epimers, chlorophyllide-*a*, pheophorbide-*a* and pheophytin-*a*), 770 nm (bacteriochlorophyll-*a*), and at 222 nm (internal standard). Peaks were identified using a library constructed from various pigment standards, which are run on an annual basis and at varying concentrations to determine the detection threshold of the HPLC system. The integration values of sample peaks were multiplied by the unique extinction co-efficient of each pigment and divided by the original volume of seawater filtered to give the resultant concentrations.

2.2.2 CHEMTAX analysis

The relative abundance of phytoplankton groups was determined using CHEMTAX, a mathematical tool that allows for the taxonomic interpretation of pigment data (Mackey et al., 1996). The CHEMTAX software (v1.95, run in Microsoft Excel), requires the user to define an initial matrix of pigment ratios representative of the taxonomic classes anticipated in the study area. The program can adjust these ratios, within boundaries set by the user, to better match the ratios present in the community. It involves an iterative process of matrix factorisation to optimise pigment ratios to estimate the contribution of phytoplankton groups to total chl-*a*. Starting ratios are important and have a large influence on the final output. The software may not discover the best solution if it encounters local minima in the process, which is circumvented by using multiple starting points (Wright et al., 2009). Sixty additional pigment ratio tables were generated by multiplying each cell with a randomLy determined factor F, where

$$F = 1 + s \cdot (\mathrm{R} - 0.5) \tag{2.1}$$

The scaling factor s is 0.7 and the random number R is generated between 0 and 1 using the Microsoft Excel RAND function. Each of the sixty ratio matrices was used as the starting point for a CHEMTAX optimisation, with the solution with the smallest residual favoured as the most reliable.

As there was no microscopy data available to pre-determine the taxa selected for this study, functional types were chosen based on work done by Gibberd et al. (2013), who followed a similar cruise track (SANAE48) to the SANAE53 summer cruise. These authors defined ten taxonomic groups of phytoplankton: Prasinophytes, chlorophytes, cryptophytes, diatoms-subtype A (containing Chls c_1, c_2, fucoxanthin, and diadinoxanthin), diatoms-B (chl-*b* replaces chl-c_1, typified by *Pseudonitzschia* sp.), dinoflagellates, haptophytes-subtype 6 (coccolithophores), haptophytes-subtype 8 (*Phaeocystis* sp.), *Synechoccocus* sp. and *Prochlorococcus* sp. The seed ratio of pigments defined by Gibberd

et al. (2013) was used for both clusters of SANAE53 and Winter Cruise data (Table 2.2.2).

The CHEMTAX software was set up for all runs as per DiTullio et al. (2003). The pigment ratios were allowed to vary up to a maximum limit of 500%, i.e. 1/ 6 to 6 times the initial value. Other settings included the iteration limit (500), epsilon (residual) limit (0.005), initial step size (10), step ratio (1.3), cutoff step (1000), elements varied (5), subiterations (5), weighting (3), and weight bound (30). The optimised ratios obtained for each of the cruises were comparable to those obtained for other Southern Ocean studies (Table 2.2.2) (DiTullio et al., 2003; Higgins et al., 2011; Wright et al., 2010).

The CHEMTAX outputs are the fraction of total chl-*a* contained in each algal group specified in the matrix. Through HPLC pigment extraction, 5 derivatives of chl-*a* are isolated, namely monovinyl-*a*, a chl-*a* allomer, a chl-*a* epimer, chlorophyllide-*a*, and divinyl-chl-*a*. For this study, the sum of the first 4 chl-*a* subtypes constitute total chl-*a*, with divinyl-chl-*a* being exclusively allocated to *Prochlorococcus*. All final CHEMTAX output was subjected, per cruise, to K-means clustering, to assign similar phytoplankton populations to groups for an optimised assessment (Section 2.7.2).

Table 2.2: Table depicting the initial seed matrix used and the final optimised matrices for SANAE53 and Winter Cruise cluster groups 1 and 2, denoted S(G1), S(G2), W(G1) and W(G2) respectively. The seed ratios were obtained from Gibberd et al. (2013), as their region of interest was almost identical to this study. Final optimised matrices were selected based on the lowest residual of the original seed matrix following factorisation. The phytoplankton classes for this region of this study include Prasinophytes (Prasin.), Chlorophytes (Chlor.), Cryptophytes (Crypt.), Diatom-subtype A (Dia.-A), Diatom-subtype B (Dia.-B), Dinoflagellate (Dino.), Haptophyte-subtype 6 (representing coccolithophores, Hap.-6), Haptophyte-subtype 8 (representing *Phaeocystis*, Hap.-8), *Synechococcus* (Syn), and *Prochlorococcus* (Pro). Pigments used to characterise the phytoplankton types included Chlorophyll-*a* (Chl*a*), Divinyl-Chl-*a* (Dv-Chl*a*), Chlorophyll-*b* (Chl*b*), Chlorophyll-$_{c3}$ (Chl$_{3c}$), Peridinin (Per), Fucoxanthin (Fuco), Violaxanthin (Viol), Prasinoxanthin (Pras), 19'Hexanoyloxyfucoxanthin (19'HF), Alloxanthin (Allo), Lutein (Lut), Zeaxanthin (Zea), and Chlorophyll-$_{c1c2}$ (Chl$_{c1c2}$).

Seed													
Class	Chl*a*	Dv-Chl*a*	Chl*b*	Chlc_3	Per	Fuco	Viol	Pras	19'HF	Allo	Lut	Zea	Chl c_1c_2
Prasin.	1	0	1.114	0	0	0	0.104	0.096	0	0	0.011	0.062	0
Chlor.	1	0	0.451	0	0	0	0.183	0	0	0	0.062	0.039	0
Crypt.	1	0	0	0	0	0	0	0	0	0.274	0	0	0.134
Dia.-A	1	0	0	0	0	0.732	0.001	0	0	0	0	0.002	0.317
Dia.-B	1	0	0	0.109	0	1.144	0	0	0	0	0	0	0.235
Dino.	1	0	0	0	0.848	0	0	0	0	0	0	0	0.258
Hap.-6	1	0	0	0.133	0	0.142	0	0	1.092	0	0	0	0.135
Hap.-8	1	0	0	0.286	0	0.249	0	0	0.763	0	0	0	0.368
Syn.	1	0	0	0	0	0	0	0	0	0	0	0.882	0
Pro.	0	1	0.322	0	0	0	0	0	0	0	0	0.287	0

S(G1)											RMSE	=	0.045
Class	Chl*a*	Dv-Chl*a*	Chl*b*	Chlc_3	Per	Fuco	Viol	Pras	19'HF	Allo	Lut	Zea	Chl c_1c_2
Prasin.	1	0	0.444	0	0	0	0.077	0.122	0	0	0.010	0.079	0
Chlor.	1	0	0.560	0	0	0	0.074	0	0	0	0.096	0.043	0
Crypt.	1	0	0	0	0	0	0	0	0	0.344	0	0	0.130
Dia.-A	1	0	0	0	0	0.389	0.001	0	0	0	0	0.001	0.097
Dia.-B	1	0	0	0.130	0	0.830	0	0	0	0	0	0	0.246
Dino.	1	0	0	0	1.139	0	0	0	0	0	0	0	0.234
Hap.-6	1	0	0	0.089	0	0.093	0	0	1.131	0	0	0	0.090
Hap.-8	1	0	0	0.271	0	0.136	0	0	0.708	0	0	0	0.294
Syn.	1	0	0	0	0	0	0	0	0	0	0	0.918	0
Pro.	0	1	0.244	0	0	0	0	0	0	0	0	0.472	0

S(G2)											RMSE	=	0.024
Class	Chl*a*	Dv-Chl*a*	Chl*b*	Chlc_3	Per	Fuco	Viol	Pras	19'HF	Allo	Lut	Zea	Chl c_1c_2
Prasin.	1	0	0.400	0	0	0	0.077	0.128	0	0	0.015	0.045	0
Chlor.	1	0	0.597	0	0	0	0.201	0	0	0	0.079	0.048	0
Crypt.	1	0	0	0	0	0	0	0	0	0.184	0	0	0.089
Dia.-A	1	0	0	0	0	0.867	0.001	0	0	0	0	0.001	0.326
Dia.-B	1	0	0	0.052	0	0.512	0	0	0	0	0	0	0.102
Dino.	1	0	0	0	1.074	0	0	0	0	0	0	0	0.346
Hap.-6	1	0	0	0.090	0	0.113	0	0	0.788	0	0	0	0.117
Hap.-8	1	0	0	0.402	0	0.274	0	0	0.299	0	0	0	0.497
Syn.	1	0	0	0	0	0	0	0	0	0	0	0.985	0
Pro.	0	1	0.428	0	0	0	0	0	0	0	0	0.339	0

W(G1)											RMSE	=	0.014
Class	Chl*a*	Dv-Chl*a*	Chl*b*	Chlc_3	Per	Fuco	Viol	Pras	19'HF	Allo	Lut	Zea	Chl c_1c_2
Prasin.	1	0	0.789	0	0	0	0.136	0.269	0	0	0.008	0.033	0
Chlor.	1	0	1.004	0	0	0	0.095	0	0	0	0.041	0.027	0
Crypt.	1	0	0	0	0	0	0	0	0	0.111	0	0	0.151
Dia.-A	1	0	0	0	0	0.489	0.001	0	0	0	0	0.002	0.373
Dia.-B	1	0	0	0.182	0	0.491	0	0	0	0	0	0	0.101
Dino.	1	0	0	0	1.004	0	0	0	0	0	0	0	0.176
Hap.-6	1	0	0	0.105	0	0.161	0	0	1.427	0	0	0	0.124
Hap.-8	1	0	0	0.283	0	0.261	0	0	0.860	0	0	0	0.400
Syn.	1	0	0	0	0	0	0	0	0	0	0	0.652	0
Pro.	0	1	0.504	0	0	0	0	0	0	0	0	0.292	0

W(G2)											RMSE	=	0.031
Class	Chl*a*	Dv-Chl*a*	Chl*b*	Chlc_3	Per	Fuco	Viol	Pras	19'HF	Allo	Lut	Zea	Chl c_1c_2
Prasin.	1	0	0.438	0	0	0	0.058	0.155	0	0	0.006	0.030	0
Chlor.	1	0	0.700	0	0	0	0.083	0	0	0	0.092	0.028	0
Crypt.	1	0	0	0	0	0	0	0	0	0.185	0	0	0.151
Dia.-A	1	0	0	0	0	0.489	0.001	0	0	0	0	0.002	0.373
Dia.-B	1	0	0	0.136	0	1.094	0	0	0	0	0	0	0.175
Dino.	1	0	0	0	1.004	0	0	0	0	0	0	0	0.176
Hap.-6	1	0	0	0.099	0	0.151	0	0	1.337	0	0	0	0.116

Hap.-8	1	0	0	0.261	0	0.125	0	0	0.563	0	0	0	0.209
Syn.	1	0	0	0	0	0	0	0	0	0	0	0.309	0
Pro.	0	1	0.504	0	0	0	0	0	0	0	0	0.292	0

2.2.3 Diagnostic pigment analysis

Uitz et al. (2006) described a method of using weighted diagnostic phytoplankton pigments to estimate the size class of phytoplankton in a mixed population; this group assessed 2419 pigment profiles taken from Case 1 waters of various trophic states (0.03-6 mg Chl$a$ m^{-3}), including the Southern Ocean. The seven marker pigments and respective weightings are illustrated in the equations below. HPLC-extracted pigment data was used to determine the size classes for all stations.

$$\%\ \text{picoplankton} = 100 * (0.86[\text{zeaxanthin}] + 1.01[\text{chl-}b + \text{divinyl-chl-}b])/\ \text{DP} \tag{2.2}$$

$$\%\ \text{nanoplankton} = 100 * (0.60[\text{alloxanthin}] + 0.35[\text{19'-BF}] + 1.27[\text{19'-HF}])/\ \text{DP} \tag{2.3}$$

$$\%\ \text{microplankton} = 100 * (1.41[\text{fucoxanthin}] + 1.41[\text{peridinin}])/\ \text{DP}\ , \tag{2.4}$$

where DP is the sum of the weighted concentrations of all diagnostic pigments:

$$\begin{aligned} \text{DP} \ &= (0.86[\text{zeaxanthin}] + 1.01[\text{chl}-b+\text{divinyl-chl}-b] \\ &\quad + 0.60[\text{alloxanthin}] + 0.35[\text{19'-BF}] + 1.27[\text{19'-HF}] \\ &\quad + 1.41[\text{fucoxanthin}] + 1.41[\text{peridinin}]). \end{aligned} \tag{2.5}$$

2.3 Macronutrient Sampling

Underway macronutrient samples were collected directly from the ship's uncontaminated scientific seawater supply into 50 mL Falcon tubes, every 2 h. These samples were stored at -20°C until analysis on land. Nitrate and silicate were measured using a Lachat Flow Injection Analyser (FIA) (Egan, 2008; Wolters, 2002). All NO_3^- and $Si(OH)_4$ concentrations used in this study are listed in Appendix B.1.

2.4 Light History

2.4.1 Assessment of available PAR data

The Scientific Data System (SDS) on board the *S.A. Agulhas II* reported photosynthetically active radiation (PAR, 400-700 nm) through a Biospherical 2π PAR sensor (μmol m^{-2} s^{-1}). It was imperative to validate the data from this sensor, as it was last calibrated prior to 2012. In 2015, subsequent to data collection for this thesis, the *S.A. Agulhas II* was fitted with a newly-calibrated CMP 21 pyranometer to measure incoming short wavelength radiation (W m^{-2}). The new sensor was fitted in parallel to the existing SDS PAR sensor, allowing for a comparison between the two; data recorded over the SANAE55 cruise (austral summer 2015/ 2016) was selected for inter-sensor comparison. The PAR measurements recorded by the SDS PAR sensor and the pyranometer, were compared through an analysis of time-averaged rolling mean observations over the austral summer of 2015/ 2016 (Fig. 2.2), and regression analysis of time-averaged PAR measurements (Fig. 2.3). The 95% confidence intervals for the regressions at 20 min, 6 h, 12 h, and 24 h are (0.63, 0.67), (0.64, 0.77), (0.56, 0.83), and (0.58, 0.85), respectively. The degree of similarity between the two PAR sensors, $p < 0.001$ for all binned time points, validated the use of the SDS PAR data for light history analysis on the Winter and SANAE53 cruises. All cumulative PAR values, over 20 min, 6, 12, and 24 h, used in this study, are listed in Appendix B.1.

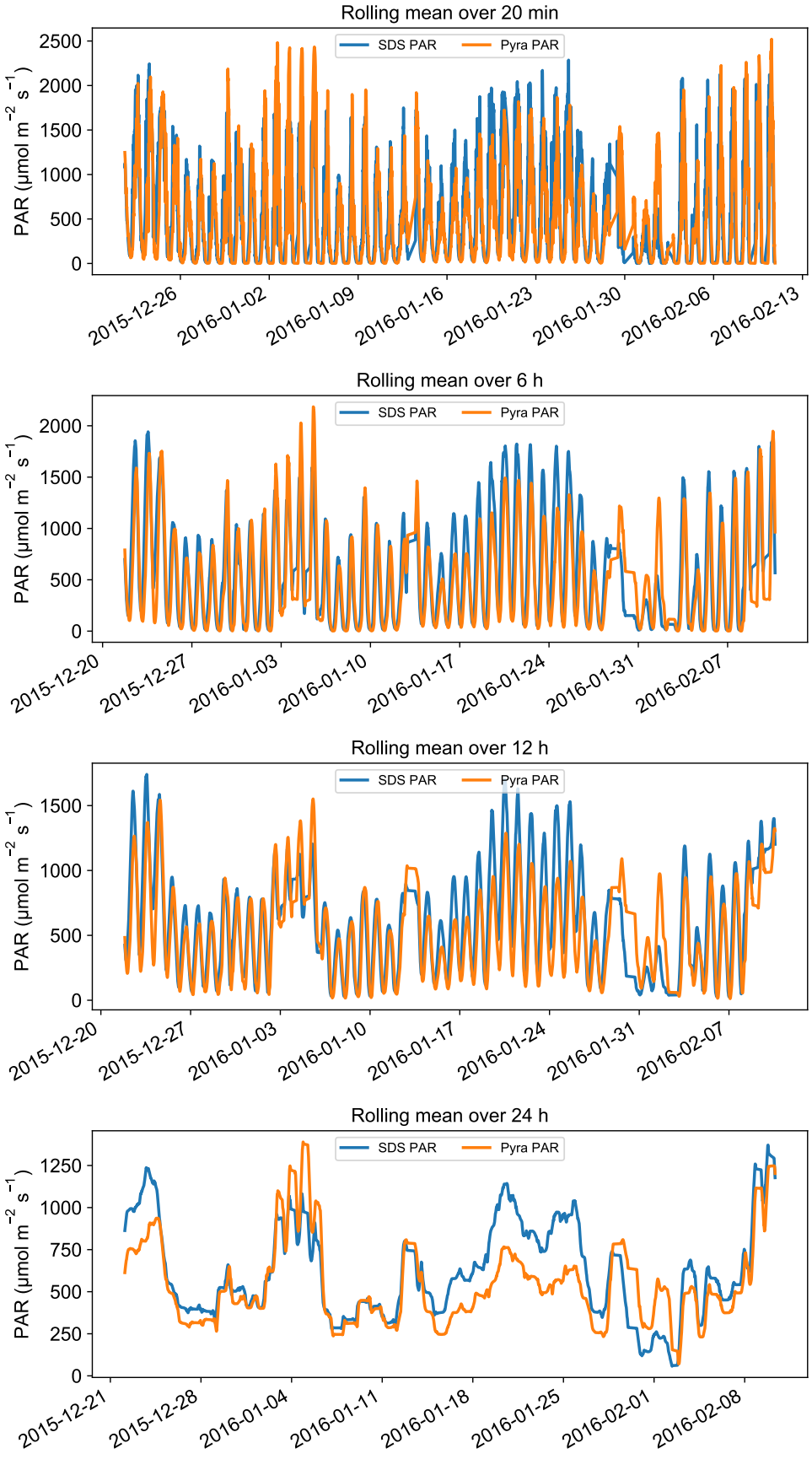

Figure 2.2: Rolling mean comparison for SDS and pyranometer (Pyra) PAR data, over different temporal ranges (20 min, 6 h, 12 h, and 24 h).

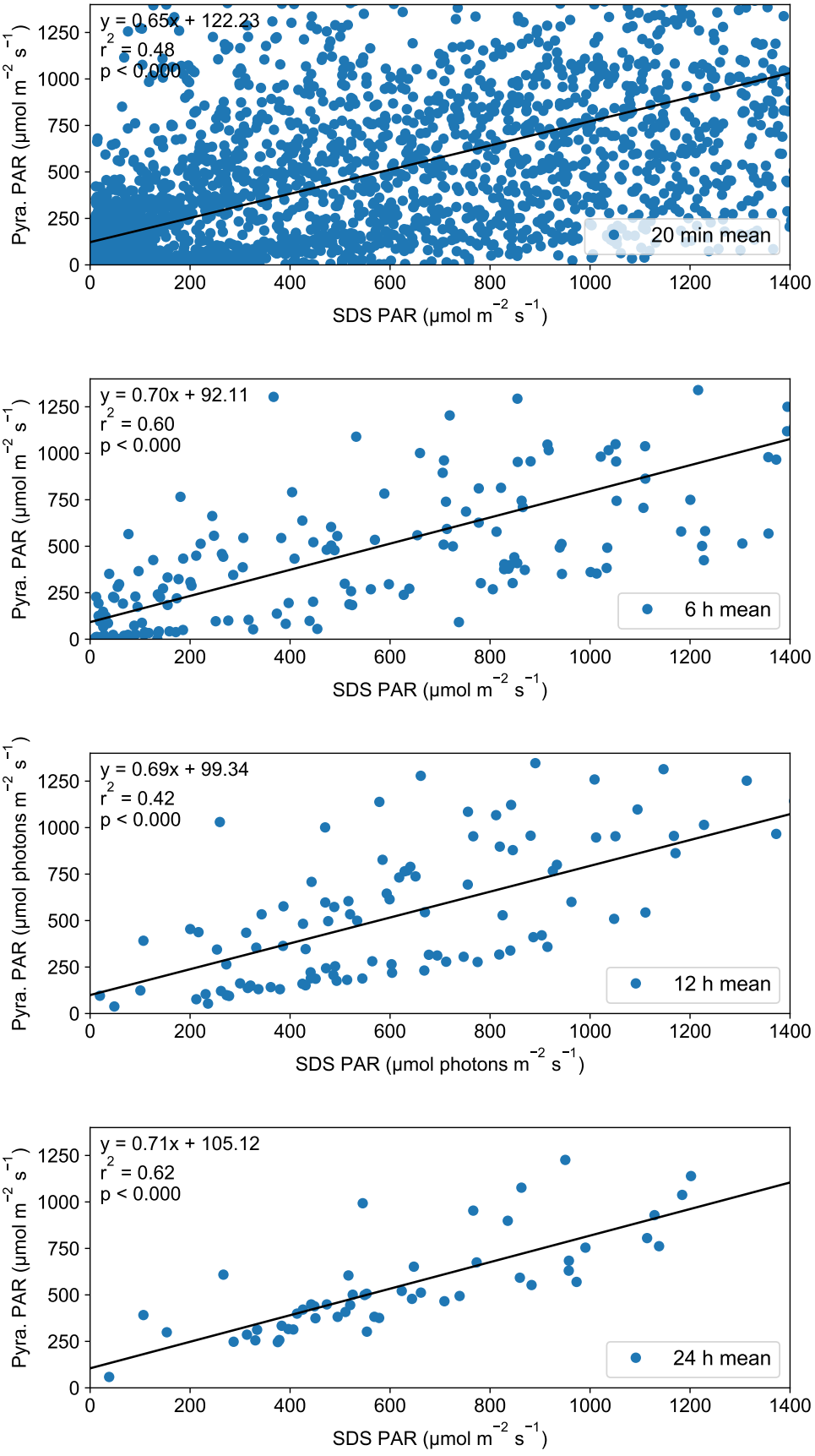

Figure 2.3: Regression analysis of SDS and pyranometer (Pyra) PAR data, over different temporal ranges (20 min, 6 h, 12 h, and 24 h).

2.5 Absorbance Measurements

Total particulate absorption was measured following the quantitative filter technique (Yentsch, 1962), whereby approximately 2 L of seawater was filtered through 0.7 μm Whatman GF/F glass-fibre filters (25 mm) under less than 10 mmHg. Total particulate absorbance of the filters was determined spectrophotometrically (Shimadzu UV-2501 PC, ISR-2200 internal integrating sphere) over a wavelength range of 350-750 nm, in 1 nm increments. To determine the detrital absorbance, filters were subsequently soaked in methanol for 24 h to extract phytoplankton pigments (Kishino et al., 1985). Excess methanol was removed through filtration prior to spectral analysis. One litre of deionised water (Milli-Q) was perfused through an identical filter to serve as the blank.

Absorption coefficients were calculated from the absorbance data using Eq. 2.6, where λ denotes wavelength, 2.303 is the coefficient representing the transformation from log_{10} to log_e, $D_f^{'}(\lambda)$ is the measured optical density of the particles on the filter, $D_{750}^{'}$ is the null point correction (set at 750 nm), $B^{'}$ is the path-length amplification factor, set at 2 (Roesler, 1998), and l is the ratio of the volume filtered to the effective area of the filter pad.

$$\mathrm{a}(\lambda) = 2.303 \frac{D_f^{'}(\lambda) - D_{750}^{'}}{B^{'} l} \tag{2.6}$$

Phytoplankton-specific absorption is typically calculated by subtracting $a_d(\lambda)$ from $a_p(\lambda)$. In this instance, the methanol extraction method of Kishino et al. (1985) proved unfavourable for accurate quantification of $a_d(\lambda)$. At higher biomass stations ([chl-a] > 1 mg.m^{-3}) the extractions were incomplete and residual phytoplanton-specific features remained, notably between 400-540 nm and at the 676 nm peak (Fig. 2.4). The incomplete extraction of pigments resulted in an underestimation of $a_{ph}(\lambda)$, such that the Bricaud and Stramski (1990) spectral decomposition technique was used to derive $a_d(\lambda)$ for all stations. The exponential slope values (S) generated through the Bricaud and Stramski (1990) method were individually determined through an iterative, best-fit approach. The a_{ph}^{*} was derived by normalising the a_{ph} to the HPLC-derived total [chl-a].

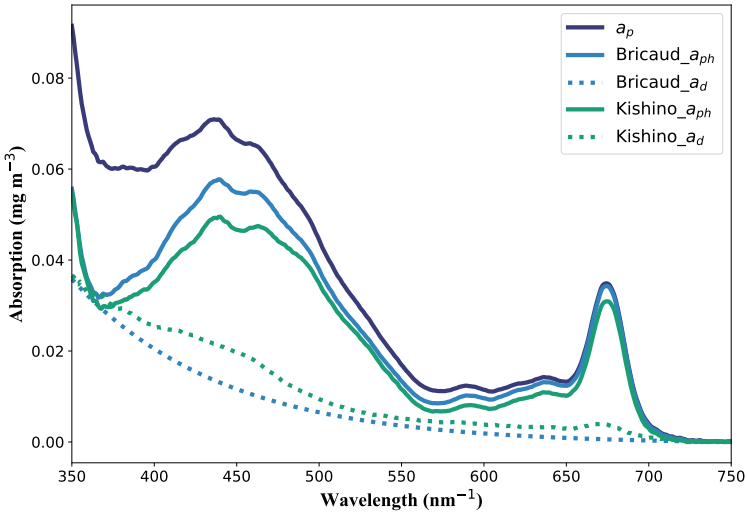

Figure 2.4: Comparison of deriving the non-algal component (a_d) of total particulate absorption (a_p) from either methanol extraction (Kishino_a_d) (Kishino et al., 1985) or spectral decomposition (Bricaud_a_d) (Bricaud and Stramski, 1990). Phytoplankton-specific absorption (a_{ph}) is determined by subtracting a_d from a_p. Incomplete methanol extraction of phytoplankton pigments is evidenced by spectral features present in the Kishino_a_d between 400-450 nm and around 676 nm. These features are removed through spectral decomposition (Bricaud_a_d), with an exponential slope value of $S = 0.011$ nm^{-1}. In this example, [Chl-a] = 1.1862 mg m^{-3} and $a^*_{ph}(676) = 0.029$ m^2 mg chl-a^{-1}.

2.5.1 Quality control of absorption data

Two quality control checks were applied to the absorption data; the first made use of the $a_{ph}(440)$:$a_{ph}(675)$ ratio, which, in line with published literature, was allowed to vary between 1-4 (Bricaud and Stramski, 1990; Lohrenz et al., 2003; Nelson and Robertson, 1993; Neukermans et al., 2016; Roesler et al., 1989; Sosik and Mitchell, 1995). The second quality control check looked at a^*_{ph} at 675 nm, where chl-a absorption at this wavelength is fairly constrained and the effects of pigment packaging are considered minimal (Nelson and Robertson, 1993; Stuart et al., 1998). The present study allowed $a^*_{ph}(675)$ to vary between 0.014 and 0.045 m^2 mg TChl-a^{-1}, to account for differences in taxonomy, cell size and [chl-a] (Johnsen et al., 1994; Meler et al., 2017; Organelli et al., 2017; Stuart et al., 1998). All $a_{ph}(440)$:$a_{ph}(675)$ and $a^*_{ph}(675)$ values are listed in Appendix A.1.

2.5.1.1 Results of absorption quality control

The average the $a_{ph}(440)$:$a_{ph}(675)$ ratio across all stations was 1.922±0.276, and demonstrated is a strongly positive, linear relationship between $a_{ph}(440)$ and $a_{ph}(675)$ ($r_s = 0.97$, $p < 0.001$) (Fig. 2.5). Regarding the second quality control measure, measurements of

$a^*_{ph}(675)$, the summer $a^*_{ph}(675)$ data, as a collective, shows a significant negative relationship with increasing [chl-a] (r_s = -0.78, p < 0.001). During winter, the biomass remained relatively similar across stations, with an average [chl-a] of 0.22±0.06 mg m^{-3}, yet the $a^*_{ph}(675)$ ranged from 0.014-0.040 m^2 mg chl-a^{-1}.

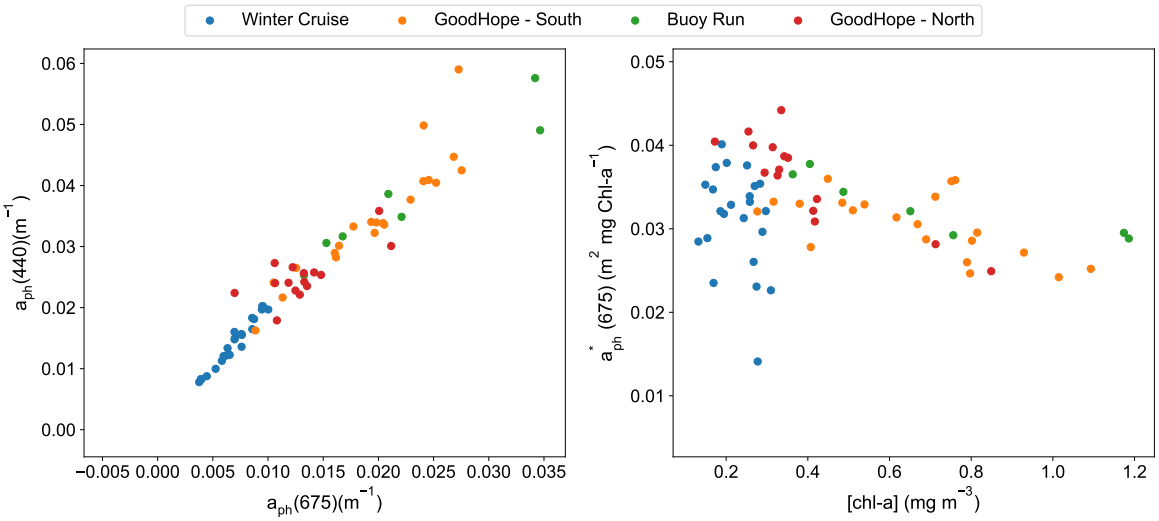

Figure 2.5: Quality assessments of absorption data. The lefthand panel depicts $a_{ph}(440)$ (m^{-1}) versus $a_{ph}(675)$ (m^{-1}), and the righthand panel $a^*_{ph}(675)$ (m^2 mg chl-a^{-1}) relative to HPLC-derived [chl-a] (mg m^{-3}).

2.5.1.2 Discussion of absorption quality control

The first quality control of absorption data examined the $a_{ph}(440)$:$a_{ph}(675)$ ratio. An average the $a_{ph}(440)$:$a_{ph}(675)$ of 1.92±0.28, across all stations, was slightly below the range obtained in a previous study by Sosik and Mitchell (1995), which was 2-4.5. Sosik and Mitchell (1995) reported the higher the ratio, the more likely the population was to be dominated by small phytoplankton, including prokaryotes; this would mean the populations examined in this study had an appreciable amount of larger species.

The second approach to investigating the quality of absorption data was to calculate a$^*_{ph}(675)$. A pioneering study by Johnsen et al. (1994), established the maximum, unpackaged $a^*_{ph}(675)$ to be 0.027 m^2 mg chl-a^{-1} in two dinoflagellate species. While this value has often been the benchmark for $a^*_{ph}(675)$ measurements, other studies have demonstrated a wider range of measured values. Culture studies have reported a range of 0.013-0.057 m^2 mg chl-a^{-1} (Mitchell and Kiefer, 1988b; Organelli et al., 2017). *In situ* studies, such as that by Meler et al. (2017), have reported values, in the Baltic Sea, of 0.067 m^2 mg chl-a^{-1} for [chl-a] of 0.8 mg m^{-3}. Ferreira et al. (2017) measured $a^*_{ph}(675)$ up to 0.045 m^2 mg chl-a^{-1} off the Antarctic Peninsula, which was attributed to small cell size, low

pigment concentration and/ or the presence of chl-*b*. All $a^*_{ph}(675)$ values for this study were between 0.014 and 0.045 m^2 mg chl-a^{-1}. All summer cruise values for $a^*_{ph}(675)$ and their respective [chl-*a*] values behaved in a typical manner, i.e. the smaller the value of $a^*_{ph}(675)$ the higher the [chl-*a*] and/ or larger the cell volume, due to the greater the effect of pigment packaging (Fig. 2.5). All Winter Cruise $a^*_{ph}(675)$ values varied widely from 0.014-0.040 m^2 mg chl-a^{-1}, for a relatively consistent [chl-*a*] of an average of 0.22±0.06 mg m^{-3}. As the [chl-*a*] remains constant, this range in $a^*_{ph}(675)$ would indicate a change in cell size and/ or taxonomy, which is feasible as the Winter Cruise covers a latitude of approximately 20 degrees and a longitude of approximately 40 degrees (Fig. 2.12), encompassing a variable range of community characteristics and species dominance.

2.6 Fluorescence Measurements

2.6.1 MFL setup and data collection

The Multi-Exciter Fluorometer (MFL, JFE Advantech, Co., Ltd.) was positioned in parallel with multiple optical instruments as part of an on-board, flow-through optics suite (Fig. 2.6). The MFL was orientated with the optical-window facing down, in a non-fluorescent, black perspex bucket, with light-excluding inflow and outflow tubing, at a distance $z \approx 60$ mm from the bottom. The scientific seawater supply used to sustain the suite was taken from the ship's intake system, located approximately 7 m below the sea surface. The seawater supply was passed through a debubbler, which limited the influence of bubbles on all optical measurements. However, this system was not completely failsafe due to occasional periods of rough seas where the bow intake rose above the sea level or was high enough to draw in highly aerated seawater. In addition, the possibility of shear caused by the ship's pump, plumbing, debubblers, and the MFL setup, as well as bio-fouling of both the plumbing and the MFL, were taken into consideration.

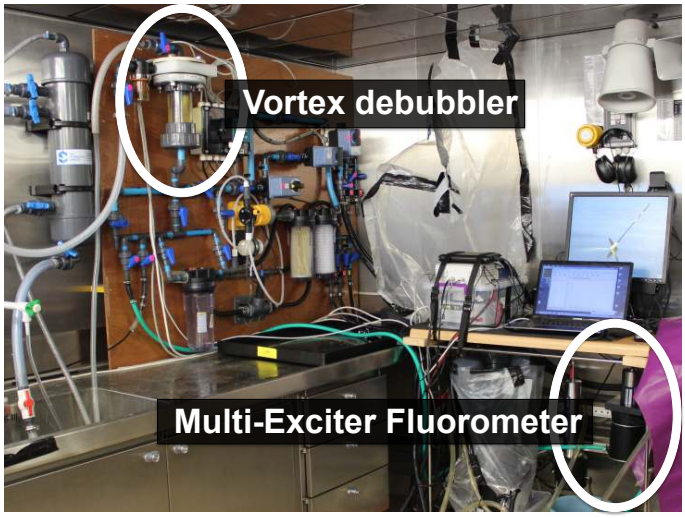

Figure 2.6: The underway seawater flowboard and MFL set-up on the *S.A. Agulhas II*.

The MFL was directly connected to a laptop loaded with the MFL software (supplied by the manufacturers). Measurements were continuously recorded for 10 sec every 1 min. Post-processing saw the measurements averaged into 20 min bins (station ±10 min), in order to capture the same population present in overlapping station measurements, including absorbance and HPLC. The standard deviations (SD) of data binned over different temporal ranges were compared; bins with an average time of 10 min had an average SD of 0.017, while bins averaged over 20 min had an average SD of 0.027 and 30 min an average of 0.038 (Fig. 2.7). The sampling window of 20 min averaged over the station time was considered ideal, allowing for minor inconsistencies in station sampling time without covering too much travel distance.

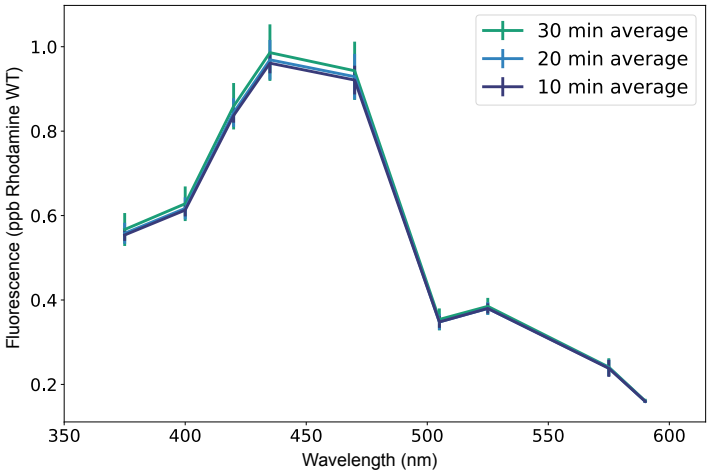

Figure 2.7: Time-averaged measurements of raw MFL output.

2.6.2 Instrument drift

Intermittent dark measurements were performed to monitor the MFL for potential instrument drift. The values for two nominal dark measurements are presented in Table 2.3. As evident, there are negligible differences in dark readings between 2014 and 2018, demonstrating that instrument drift is of minor importance when processing current MFL data. However, the use of a suitable fluorescence standard may be employed to monitor instrument drift in the future. In addition, frequent baseline measurements of filtered seawater would allow for a more robust assessment of the influence of biofouling, such as measurements performed by Bibby et al. (2008).

Table 2.3: Values for two nominal dark readings (ppb Rhodamine WT).

MFL LED	June 2014	2014 SD	February 2018	2018 SD
375 nm	-0.007	±0.007	-0.010	±0.006
400 nm	0.003	±0.007	0.001	±0.004
420 nm	-0.004	±0.005	-0.005	±0.004
435 nm	-0.007	±0.006	-0.007	±0.005
470 nm	0.006	±0.006	0.006	±0.004
505 nm	-0.003	±0.004	-0.004	±0.004
525 nm	0.068	±0.006	0.068	±0.005
570 nm	-0.082	±0.031	-0.087	±0.019
590 nm	-0.003	±0.005	-0.004	±0.004
880 nm	-0.023	±0.005	-0.032	±0.005

2.6.3 Quality control of MFL fluorescence data

MFL fluorescence data underwent multiple steps of rigorous quality control. From the outset, the manual inspection of the data recorded over the 20 min sampling period for each individual station was performed. Outliers were detected and removed with an upper and lower outlier limit of the mean ± SD×3. An example of acceptable raw fluorescence data is shown in Fig. 2.8, where relative consistency in spectral shape was retained between channels.

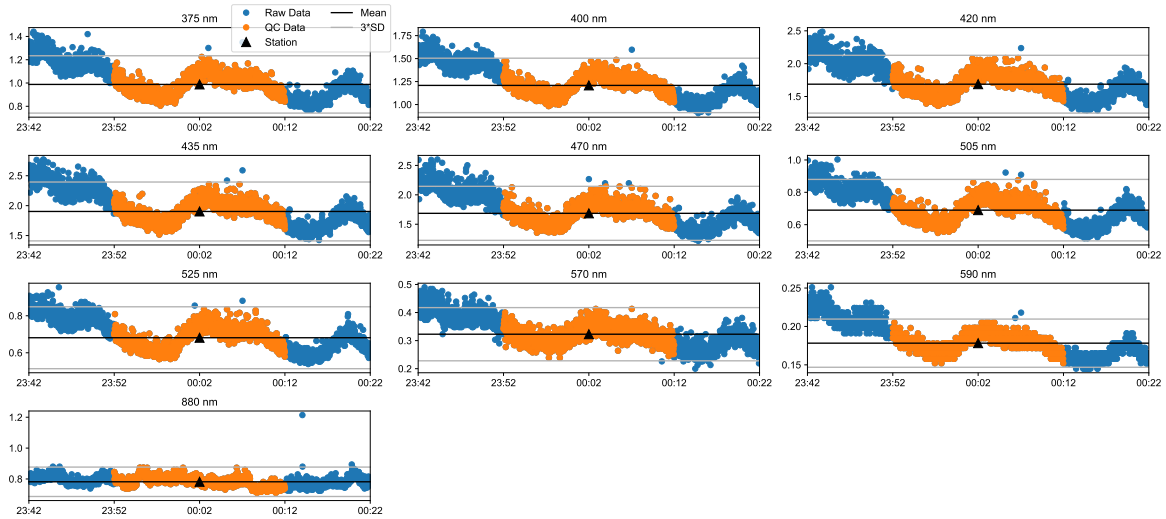

Figure 2.8: These data represent an acceptable MFL fluorescence recording (station GHN05). Of the 20 min time period sample, the blue points represent data lying outside of the chosen SD and time constraints, while orange points represent usable data that lies within the specified limits.

Manual inspection of the data collected for each of the stations identified spectral anomalies. The influence of bubbles was clearly visible (Fig. 2.9), affecting the MFL LED channels differently. Such stations were omitted from further processing.

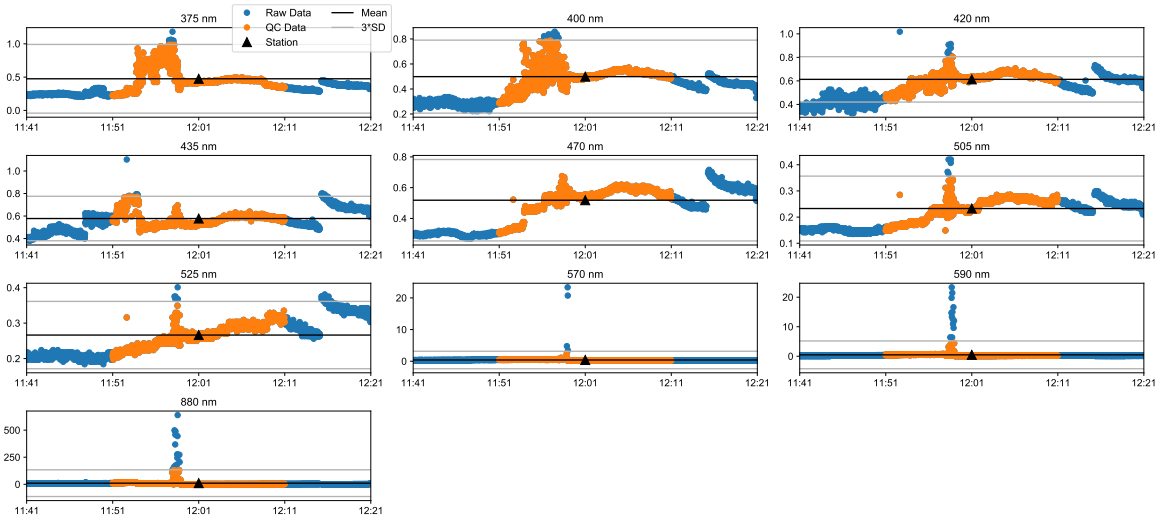

Figure 2.9: An example of an MFL raw fluorescence measurement influenced by the presence of bubbles on the optical window.

Another observed anomaly was an unexpected instrument surge that occurred every 59:30 min (Fig. 2.10). The spike was not observed in any of the other instrument detectors (i.e. temperature, depth and turbidity), demonstrating the surge was not due to the ship's power supply but rather due to a possible instrument flaw. This feature was apparent in both SANAE53 and Winter Cruise data. Stations influenced by instrument surges were similarly omitted from further processing.

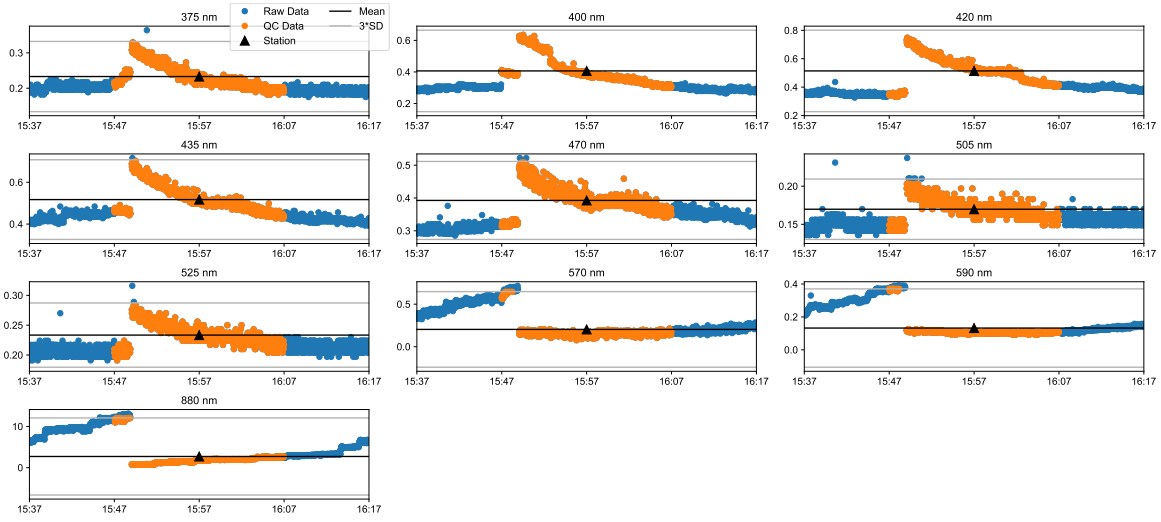

Figure 2.10: An example of an MFL raw fluorescence measurement situated over the observed spiking of the MFL. It is apparent, in this instance, that the 570, 590, and 880 nm channels behave in an inverse manner to the other channels.

The 880 nm MFL LED was identified as a flag for highly scattering environments and proved to be significantly ($p < 0.001$) related to the 570 nm LED fluorescence output (Fig. 2.11); the 95% confidence interval for the slope is (11.88, 16.88). The 570 nm channel is the most sensitive to noise and turbidity, caused by, for example, bubbles. The validity of both of the MFL calibration models (Chapter 3) are contingent upon deployment in a low scattering environment. Fluorescence samples considered to be contaminated with scattering elements were excluded i.e. stations with a turbidity value greater than 10 Formazine Turbidity Units (FTU).

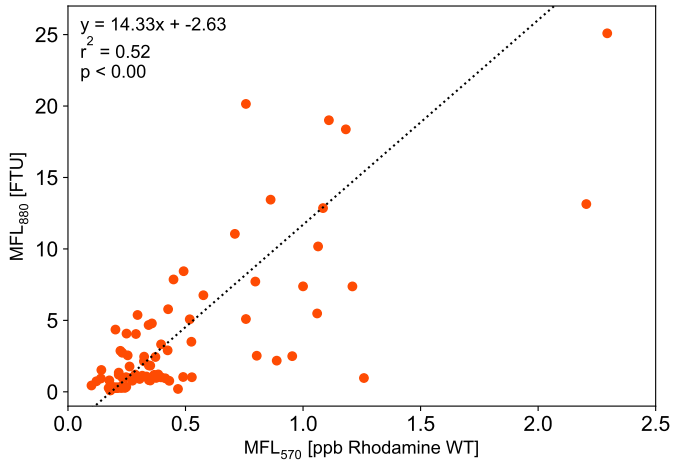

Figure 2.11: The MFL 570 nm output is positively, significantly ($p < 0.001$) correlated to the 880 nm turbidity output; FTU: formazine turbidity units.

The application of these MFL fluorescence quality control saw the loss of approximately 50% of measured stations that had previously passed the absorption quality control. The remaining stations, where both the absorption and MFL-fluorescence passed the quality control checks, were used to derive $\Phi_F(\lambda)$ in Chapter 3, and can be seen on the cruise maps in Figure 2.12.

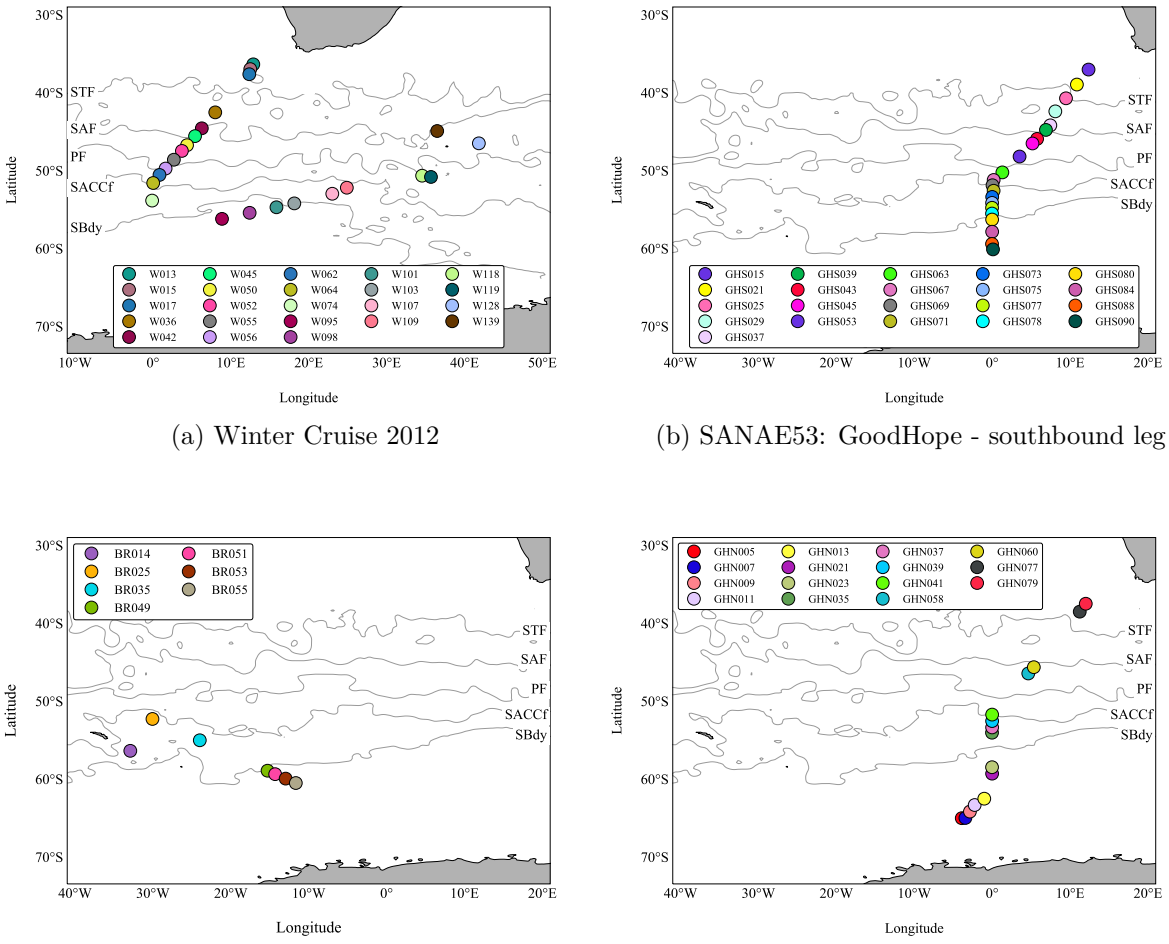

(a) Winter Cruise 2012

(b) SANAE53: GoodHope - southbound leg

(c) SANAE53: Buoy run

(d) SANAE53: GoodHope - northbound leg

Figure 2.12: Quality-controlled stations selected for work in this thesis on (a) the Winter Cruise during the austral winter of 2012, (b) the GoodHope-South transect of the SANAE53 cruise during the austral summer of 2013/ 2014, (c) the Buoy Run transect of SANAE53, and (d) the GoodHope-North transect of SANAE53. Frontal positions, Sub-Tropical Front (STF), the Sub-Antarctic Front (SAF), the Polar Front (PF), the Southern Antarctic Circumpolar Current Front (SACCf), and the Southern Boundary (SBdy) of the ACC, were determined through Maps of Absolute Dynamic Topography (MADT). The position of the fronts was determined using sea surface height data from maps of absolute dynamic topography (MADT) from the CLS/AVISO product (Rio et al., 2011; Swart et al., 2010).

2.7 Data Clustering

Clustering is the unsupervised classification of unlabelled patterns into meaningful groups, or clusters. This is an important tool in exploratory data analysis, whereby the appropriate algorithm, parameter setting and number of clusters depends upon the nature of input data as well as the intended use of the outcome (Jain et al., 1999). K-means clustering partitions a given dataset, of n data points, into a user-specified number of clusters, k. This hard clustering algorithm allocates each pattern to a single cluster during its operation and in its output. This approach was followed for both $\Phi_F(\lambda)$ spectra and pigment data for CHEMTAX analysis, using the Python Scikit-learn package (sklearn.cluster.KMeans algorithm).

2.7.1 K-means clustering of $\Phi_F(\lambda)$ spectra

With a small total sample size of n = 66, the ideal number of clusters was needed to be as low as possible, to maintain statistical integrity for further analysis. Visually, four was the lowest number of clusters to satisfactorily separate $\Phi_F(\lambda)$ spectra, isolating the three stations with exceptionally large $\Phi_F(570)$ values (GHS78, GHS80, and GHS90), which may have skewed subsequent interpretation (Appendix B.3). Silhouette analysis was performed on the total dataset to validate the choice in cluster number, where cluster numbers 2-5 were 0.56, 0.38, 0.41, and 0.44 respectively. The silhouette value is a measure of how similar each spectrum is to its own cluster compared to other clusters. This value lies between + 1 and - 1, the former being optimal and the latter being suboptimal, with values close to zero indicating overlap between clusters. The distance metric used in this study was Euclidean distance. The silhouette score for 2 clusters was the highest (0.56), however, two clusters severely limited the range of spectral separation. Based on sample/ cluster size, visual separation of spectra and with an acceptable silhouette score of 0.41, four was selected as the optimum number of clusters.

2.7.2 K-means clustering of pigment data for CHEMTAX

Clustering of the entire dataset into similar pigment groups allowed for a more directed application of CHEMTAX. Extracted pigments, quantified by HPLC, were normalised to total [chl-a], prior to root square transformation. Multi-dimensional scaling was then used to cluster out similar samples, and silhouette analysis was used to examine the separation distance between resulting clusters. The highest silhouette coefficients obtained were used to identify the optimum number of clusters for all data, which in this instance proved to

be 2 clusters per cruise.

2.8 Empirical Orthogonal Function Analysis

Empirical orthogonal function (EOF) analysis was used to assess the variance of $\Phi_F(\lambda)$ spectral structure within the cluster datasets. Intra-cluster $\Phi_F(\lambda)$ spectra were separated into a set of geometrically independent (orthogonal) modes of oscillation, which represented all the variance in the data (Craig et al., 2012). The modes, generated by computation of the eigenvectors of the covariance matrix of the dataset, were selected to be different from each other and to account for as much variance as possible. The first mode captured the largest portion of total variance and subsequent modes captured progressively less. The first three modes were used for analysis of the $\Phi_F(\lambda)$ dataset. All data were non-normally distributed (Shapiro-Wilk test), necessitating the use of Spearman's *rho* (r_s) to investigate statistical significance. The analysis was only performed on cluster numbers 1-3, as the sample size of cluster number 4 was statistically unreliable (n = 3). All data were standardised using the Python Scikit-learn package (sklearn.preprocessing.StandardScaler) and all statistical analyses were performed using the Python SciPy library.

Chapter 3

Calibration of a Multi-Excitation Fluorometer for use in Apparent Fluorescence Quantum Yield Determination

The radiometric calibration of a Multi-Exciter Fluorometer (JFE Advantech, Co., Ltd.) for use in fluorescence quantum yield determination forms content published in Griffith et al. (2018): *Griffith, D.J., Bone, E.L., Thomalla, S.J., and Bernard, S. (2018). Calibration of an in-water multi-excitation fluorometer for the measurement of phytoplankton chlorophyll-a fluorescence quantum yield. Optics Express, 26(15):18863-18877.*

3.1 Introduction

3.1.1 Background

The derivation of Φ_F requires, besides accurate quantification of the fluorescence signal, that the spectral composition of excitation energy and the spectral absorption properties of phytoplankton be known. Not all received excitation energy is transferred to chl-*a* in intact phytoplankton, with light absorption largely influenced by a combination of pigment composition, concentration, and packaging (Bricaud et al., 1998; Hoepffner and Sathyendranath, 1991; Lohrenz et al., 2003; Nelson and Robertson, 1993; Sathyendranath et al., 1987). As such, *in situ* Φ_F is considered an apparent Φ_F, as opposed to an absolute Φ_F. *In situ* studies investigating Φ_F are limited, both in the Southern Ocean and globally, with existing studies typically making use of SICF near the ocean surface

(Table 1.3). SICF can be detected as red peaks in both in-water (Babin et al., 1996b) and water-leaving radiance spectra (Neville and Gower, 1977). Derivation of *in situ* Φ_F requires knowledge of a_{ph} together with a fully characterised light field. The downwelling irradiance and upwelling radiance are typically quantified through the use of spectroradiometers. Examples used in existing studies include a PRR-600 underwater radiometer (Biospherical Instruments) (Morrison, 2003), a LI-1800 UW spectroradiometer (LI-COR Instruments) (Maritorena et al., 2000), and a MER-2040 spectroradiometer (Biospherical Instruments) (Ostrowska et al., 1997; Westberry and Siegel, 2003). A different approach to deriving *in situ* Φ_F, involving linear parameterisation, has been utilised in various Lagrangian studies. For example, Letelier et al. (1997) defined an apparent Φ_F as the slope of the relationship between FLH/ chl-*a* (fluorescence line height normalised to the concentration of chlorophyll, as estimated using ocean colour measurements from a drifter) and the incident irradiance at 490 nm; this same approach was followed by Abbott et al. (2001). Schallenberg et al. (2008) performed a similar study, however, instead of normalising fluorescence to chl-*a*, they normalised fluorescence to absorption. All three studies made use of METOCEAN Data Systems optical drifters, equipped with a 7-channel upwelling radiance sensor (412, 443, 490, 510, 555, 670, and 683 nm) and a downwelling irradiance sensor (490 nm). A third approach to deriving *in situ* Φ_F was put forward by Ostrowska (2011), who made use of a BBE Moldaenke FluoroProbe multi-excitation fluorometer. Multi-excitation fluorometers exploit fluorescence excitation spectra to define phytoplankton taxonomic groups based on signature accessory pigment composition (Johnsen et al., 1997; Sosik and Mitchell, 1995; Yentsch and Yentsch, 1979), which are typically used to discriminate between phytoplankton species in mixed assemblages (Beutler et al., 2003, 1998, 2002; Cowles, 1993; Desiderio et al., 1997; Kolbowski and Schreiber, 1995; Yoshida et al., 2011). While Ostrowska (2011) did not radiometrically characterise the excitation LEDs, nor the emission detector of the instrument, they still derived an apparent, wavelength-specific Φ_F. If such an instrument was accurately calibrated for Φ_F measurements, routine deployments would increase the number of global Φ_F observations, which would in turn improve current understanding of the drivers of variability of Φ_F, and play a crucial role in validating existing satellite-derived Φ_F algorithms.

3.1.2 Chapter objectives

This chapter sees the calibration of a Multi-Exciter Fluorometer (MFL, JFE Advantech Co., Ltd.), for use in wavelength-specific, apparent Φ_F determination. The MFL undergoes an extensive characterisation to investigate instrument functionality, and a subse-

quent radiometric calibration for use in Φ_F derivation. Two distinct calibration models are employed, the first of which incorporates the use of fluorescent dye solutions with known quantum yield and spectral traits. The second model adds a degree of complexity to the calibration, making use of fluorescent acrylic plaques and films to determine the MFL response as a function of distance.

3.2 Radiometric Calibration of the Multi-Exciter Fluorometer

Please refer to the List of Notation (p.iv) for specific symbols and units used throughout this chapter.

3.2.1 The Multi-Exciter Fluorometer

A MFL, was originally designed to discriminate between phytoplankton species in population, through exploitation of signature accessory pigments (Yoshida et al., 2011), was purchased from JFE Advantech, Co., Ltd. (MFL10W-CAD model, serial number 0013). The instrument consists of nine excitation LEDs, centred at 375, 400, 420, 435, 470, 505, 525, 570, and 590 nm. The LEDs at 375 and 590 nm are present in duplicate, and 570 nm in triplicate, to account for differences in LED intensity (Fig. 3.1). In addition, the MFL also contains a turbidity LED at 880 nm, and temperature and pressure sensors. The MFL detector, fitted with a cut-on filter at 640 nm, receives emitted light in the 640-1000 nm region.

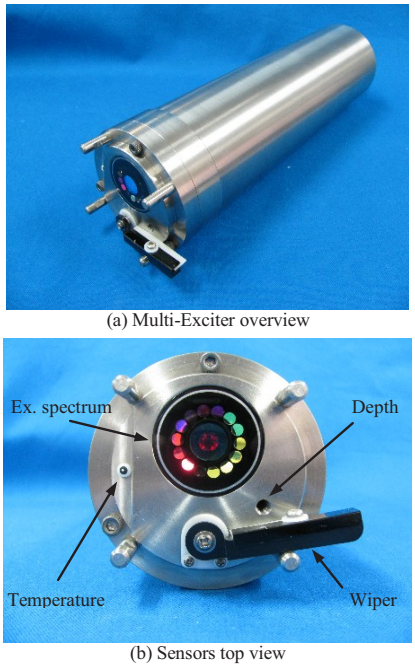

(a) Multi-Exciter overview

(b) Sensors top view

(a) The Multi-Exciter Fluorometer

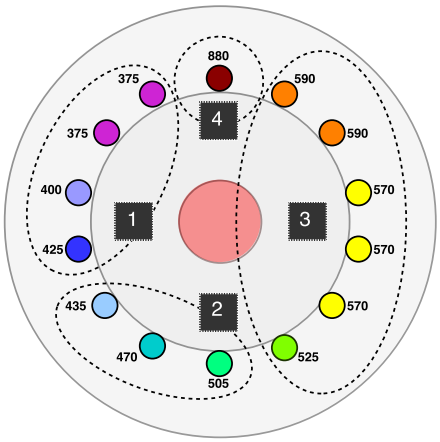

(b) LED positions and groupings

Figure 3.1: (a) The JFE Advantech, Co., Ltd, Multi-Exciter Fluorometer (Yoshida et al., 2011). (b) Depicts the MFL LED layout and grouping for the flashlet sequence (1-4).

3.2.2 Characterisation of the Multi-Exciter Fluorometer

Prior to the calibration of the MFL, the instrument required a full optical characterisation. A thorough investigation, including characterisation of the LED spectral bandwidths, LED temporal cycles, detector field-of-view (FOV), and bias over temperature, was performed.

3.2.2.1 LED temporal cycle

The MFL was initially placed in an integrating sphere, where it was discovered that an ambient background reading is automatically subtracted from the measured signal prior to output. The grouping and sequence in which the LEDs flash was determined through the use of a Tektronix oscilloscope. Each group (1-4) flashes sequentially, with each group measuring the stimulated signal for 2 ms followed by an ambient background measurement for another 2 ms, making each group flashlet last a total of 4 ms. The ambient measurement is automatically subtracted from the stimulated measurement. One complete LED measurement is 16 ms (Fig. 3.1).

3.2.2.2 Spectral distribution of the LEDs

It was necessary to determine the spectral distribution of the LEDs for weighting of both the MFL signal response and absorption measurements. The absolute irradiance of the individual LEDs was measured with a B&W Tek, Inc. SpectraRad irradiance meter (Fig. 3.2).

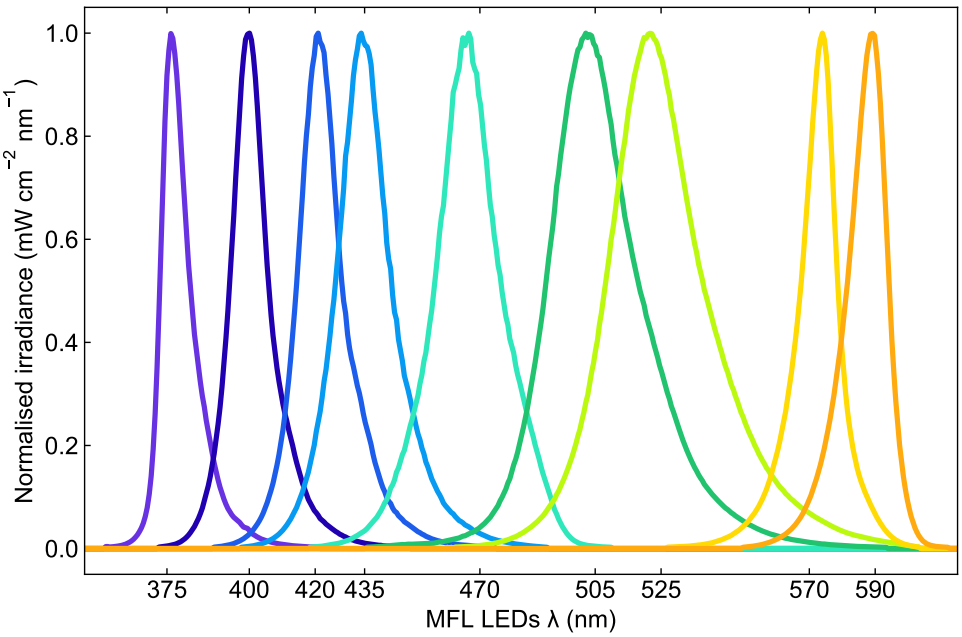

Figure 3.2: MFL LED spectral bandwidths (nm).

3.2.2.3 Detector field of view

The MFL distance response calibration (Section 3.2.5) is contingent upon the assumption that the MFL has a relatively narrow FOV. To assess the FOV, a small rectangle of strongly fluorescing film was placed on an opaque, black substrate and submerged in distilled water (dH_2O). The lateral response of the MFL was measured, in two perpendicular orientations, at various distances above the film. The "full-width at half maximum" refers to the total field of view determined by finding angles at which the signal from the instrument drops to half the peak signal established when the piece of film was near the centre of the FOV. The full-width at half maximum was established to be 16 mm at a distance $z = 40$ mm and 24.3 mm at $z = 60$ mm. The half-width at half maximum of the angular FOV was hence estimated to be 11.4°.

3.2.2.4 Negligible bias over temperature

The stability of the MFL over time and temperature was investigated. Black, non-fluorescent tape was placed over the optical face of the MFL, until no visible LED excitation radiation was observed. The instrument was positioned in a black, plastic bucket, and filled with H_2O and ice. The temperature increased from 2-21℃ over a period of 24 h, with the results presented in Fig. 3.3. While almost all LEDs remain close to zero throughout the 24 h period, 570 and 525 nm are consistently lower and higher, respectively, over time. It is evident from the output that the 570 nm channel is very sensitive to noise. In addition to the 570 nm LED being the only LED present in triplicate (Fig. 3.1), the internal gain factor has also been set higher than other LEDs to increase signal detection, which is typically low at this wavelength.

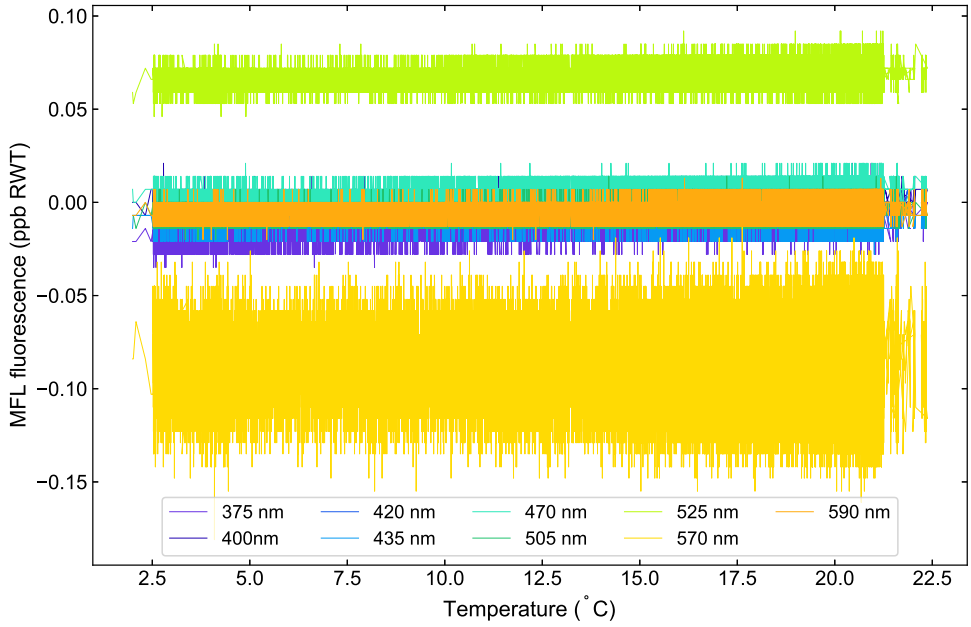

Figure 3.3: Fluorescence output per LED over a temporal range of 24 h and temperature range of 2-21℃.

3.2.3 Absolute radiometric calibration of the Multi-Exciter Fluorometer

The MFL was originally factory calibrated against Rhodamine-WT (RWT) fluorescent dye, with the raw instrument output in parts-per-billion (ppb) RWT. Limited quantitative information on the fluorescence characteristics of RWT meant this calibration could not be exploited in the quest to derive Φ_F from the MFL. This led to the development of two novel calibration techniques. The first method was the most direct and involved the

use of fluorescent dyes of known quantum yields and spectral traits. The second method made use of fluorescent acrylic plaques and plastic films to determine the MFL response as a function of distance.

3.2.4 Fluorescent dye calibration

Ideal quantum yield standards should have minimal overlap between absorption and emission, i.e. a large Stoke's Shift, be soluble in the same solvent as the compound being investigated, and have high photostability. The excitation and emission spectra should also be similar to the compound being studied, and most importantly have an accurately known quantum yield (Demas and Crosby, 1971). As such, water-soluble, photostable dyes were obtained with a similar emission spectrum as chl-*a* and excitation spectrum covering the full excitation range of the MFL (350-610 nm). The carboxy-derivatives of two suitable ATTO-TEC (ATTO Technology, Inc.) dyes with dissimilar spectral traits were selected, namely ATTO655 and ATTO490LS. ATTO490LS has an exceptionally large Stoke's shift, which is preferential when avoiding second order excitation light field effects. Both dyes have a specified quantum yield of 0.3, however, uncertainty data were not available from the manufacturer.

3.2.4.1 Fluorescent dye model

The linear calibration model for the MFL output signal response to a fluorescent solution with index i was defined as

$$R_{ij} = k_{ij} a_{ij} p_i \Phi_i \tag{3.1}$$

where

- R_{ij} is the MFL signal response to the fluorescent solution i exposed to the spectral distribution of LED wavelength j,
- k_{ij} is a calibration constant for solution i, LED j, expected to be independent of solution i, leaving k_j,
- a_{ij} is the absorption coefficient of solution i, a mean value weighted by the spectral photon distribution of LED j,
- p_i is the MFL-relative partial quantum yield factor for the fluorophore in solution i and
- Φ_i is the total fluorescence quantum yield (FQY) for the fluorophore in solution i.

Calibration constants k_{ij} were determined through the rearrangement of Eq. 3.1:

$$k_{ij} = \frac{R_{ij}}{a_{ij} p_i \Phi_i} \tag{3.2}$$

3.2.4.2 Derivation of dye calibration constants

The fluorescent dye calibration comprised five key components, the first of which was to determine the spectral molar absorptivity of the fluorescent dye stock solutions. A Varian (now Agilent) Cary 500 spectrophotometer, with long pathlength cuvettes (10 cm), was used to determine the spectral molar absorptivity of the dyes (Fig. 3.4), and as such the spectral molar absorption coefficient of any dye solutions used during the calibration.

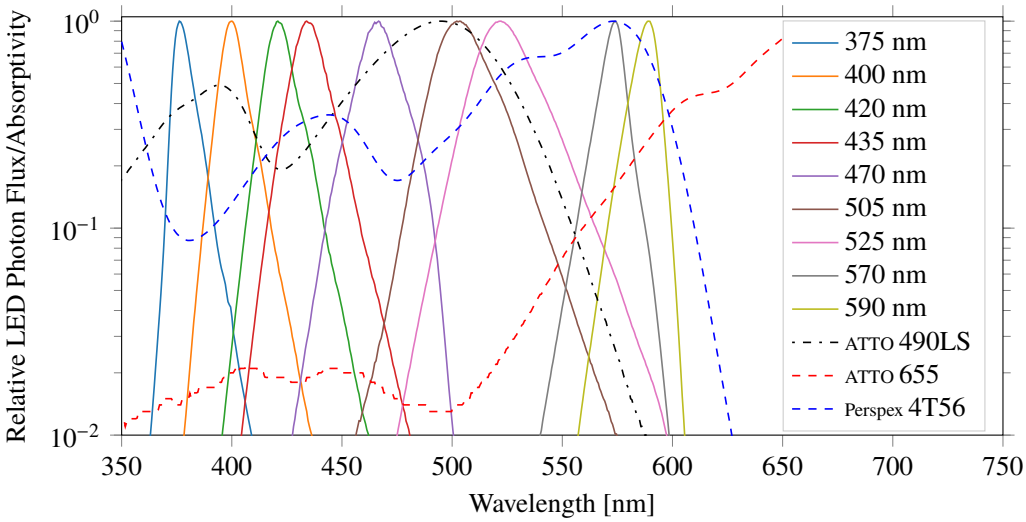

Figure 3.4: Derived MFL LED normalised photon spectra, plotted on a log scale with the relative spectral absorptivity of fluorophores used in the various calibration approaches.

Next, the MFL was immersed in solutions of the working stock at known dilution ratios under the premise that the absorption coefficients were linearly related to the concentration. The ATTO490LS and ATTO655 fluorescent dyes were dissolved in dH_2O to yield fluorescent solutions with index i. The MFL response (R_{ij}) values were established by placing the MFL in the solutions, where the equivalent absorption coefficient (a_{ij}) for each LED spectral photon distribution had been established; R_{ij} was thence determined for each LED.

The LED-specific absorption coefficients of the dye solutions were calculated using spectral weighted averaging. Various concentrations of the dye solutions were used to ensure good signal on all channels of the MFL. A stock dye solution with a known spectral

absorption coefficient was made up, from which a_{ij} for any dilution of the stock could be calculated.

As part of the dye emission spectrum is filtered out by the MFL detector cut-on filter, derivation of the MFL-relative partial quantum yield was required. The MFL-relative partial quantum yield lies between 0 and 1 and takes into account the spectral response of the MFL detector channel. If the relative spectral quantum response of the MFL is denoted $\Gamma(\lambda)$ and the emission spectrum of fluorescent solution i is $S_i(\lambda)$, then the MFL-relative partial quantum yield factors over depth $\mathrm{d}\lambda$ can be defined as

$$p_i \equiv \frac{\int S_i(\lambda)\Gamma(\lambda)d\lambda}{\int S_i(\lambda)d\lambda}. \tag{3.3}$$

The quantum response of the MFL ($\Gamma(\lambda)$) and the dye emission spectra ($S_i(\lambda)$) were provided by the manufacturers, as shown in Fig. 3.5. The MFL-relative partial quantum yield factors calculated this way and used in the calibration are listed in Table 3.1. For chl-a, the MFL-relative partial quantum yield factor comprised the mean values for chl-a in ether and methanol, that is $p_c = 0.851$.

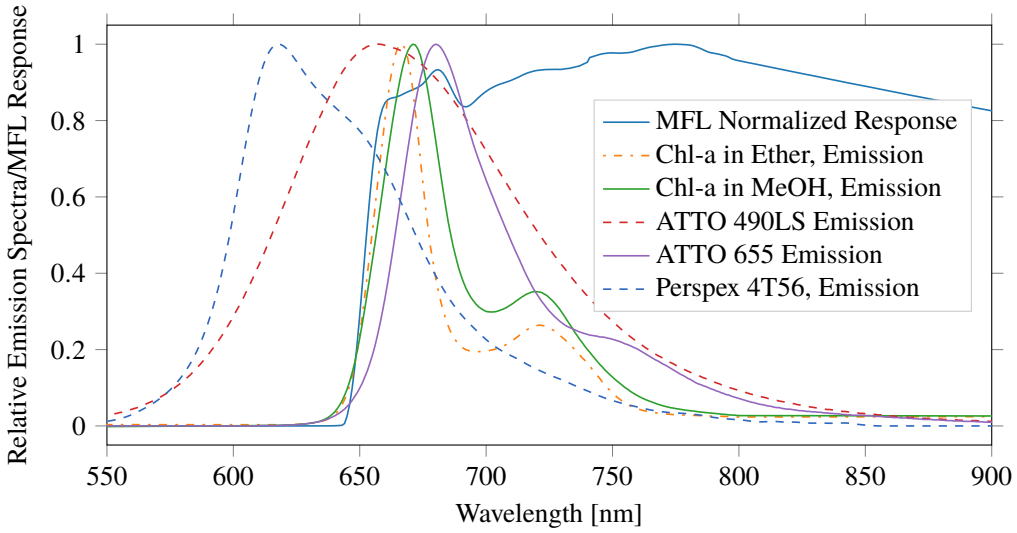

Figure 3.5: Fluorophore normalised emission photon spectra plotted together with the MFL normalised effective quantum detection efficiency.

Table 3.1: MFL-relative partial quantum yield factors. The mean factor for chl-a in ether and in methanol was used in Eq. 3.4, where $p_c = 0.851$

Fluorophore	p_i Photon-based
ATTO 490LS	0.624
ATTO 655	0.893
Perspex 4T56	0.319
Chl-a in ether	0.827
Chl-a in methanol	0.875

As the fluorescence quantum yield of the dyes, Φ_i, was supplied by the manufacturer, the final step was to determine the calibration coefficient for each LED wavelength using Eq. 3.2.

3.2.4.3 Fluorescent dye calibration: Field application

Field measurements require that Φ be solved through manipulation of Eq. 3.2. *In situ* raw MFL output was recorded for 10 sec every 1 min, for a total of 20 min over the station time (Section 2.6.1). These data were time-averaged (R_j) and input into Eq. 3.2. The LED channel phytoplankton-specific absorption coefficients (a_j^*) were determined spectrophotometrically as per the quantitative filterpad technique (Yentsch, 1962) (Section 2.5). The calibration factor (k_j) and partial yield factor for chl-a (p_c) were experimentally determined. As the fluorescence quantum yield was no longer expected to be wavelength-independent, the field application equation was defined by

$$\Phi_j = \frac{R_j}{k_j a_j^* p_c}. \tag{3.4}$$

3.2.5 Fluorescent acrylic plaque calibration

The MFL fluorescent acrylic plaque calibration, also referred to as the distance-response calibration, added another dimension of complexity to the fluorescent dye calibration model. While the dyes were regarded as isotropic and homogeneous, the MFL stimulating radiation and returned fluorescence from elementary plane-parallel layers of the fluorescent plaque was now considered (Fig. 3.6).

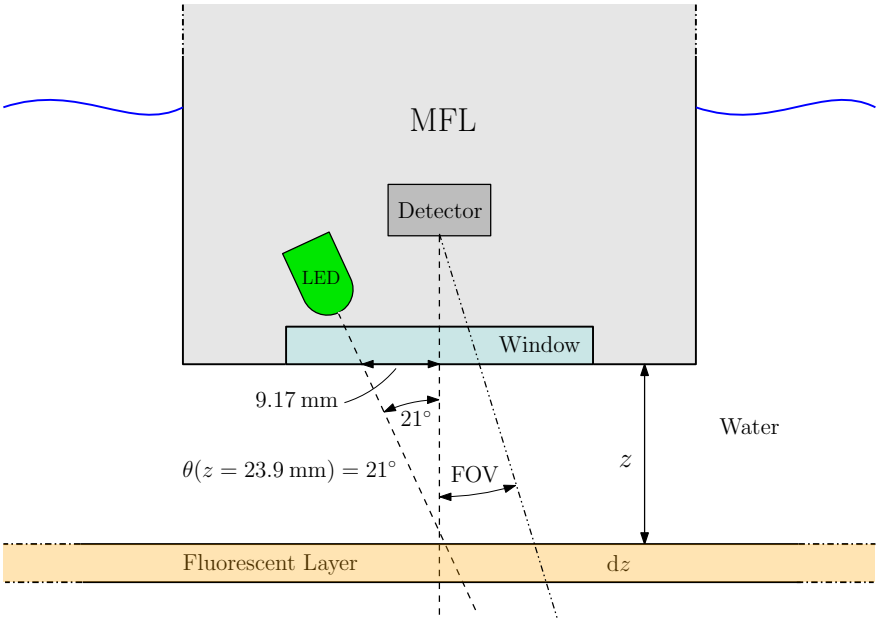

Figure 3.6: MFL LED and detector viewing geometry, supplied from personal communication with JFE Advantech Co., Ltd. The angle at which the LED illumination intersects the fluorescent layer at distance z at the centre of the MFL FOV is θ. The thickness of the fluorescent plaque is denoted dz.

As in the case of the fluorescent dye calibration, an indexing scheme was used to denote different fluorophores (i) and different LED illumination spectra (j). It followed that the differential response of the MFL to a plane parallel layer of thickness dz at distance z was defined as

$$\mathrm{d}R_{ij} = \mathrm{a}_{ij} p_i \Phi_i g_j(z) \mathrm{d}z \tag{3.5}$$

where

- $\mathbf{d}R_{ij}$ is the differential MFL signal response to the fluorescent plaque i exposed to the spectral distribution of LED wavelength j,
- a_{ij} is the absorption coefficient of the fluorescent plaque i, a mean value weighted by the spectral photon distribution of LED j,
- p_i is the MFL-relative partial quantum yield factor for the fluorescent plaque i,
- Φ_i is the total FQY for the fluorescent plaque i,
- $g_j(z)$ is the calibration function of distance z from the MFL window, for LED j,

The geometric calibration function $g_j(z)$ subsumes all geometrical aspects of LED illumination and detector FOV, including the variation in illumination with distance. It

was assumed that $g_j(z)$ was independent of the characteristics of the fluorescent plaque. This would hold true for an isolated layer of fluorescent material in an otherwise uncontaminated, transparent and infinite body of water. The distance calibration was set up to closely mimic this ideal scenario. Attenuation of the excitation radiation in the layers preceding the layer under consideration must be accounted for, as well as the attenuation of the return path of emitted fluorescence radiation. If scattering is neglected, on the outward path, the transmittance of the stimulation radiation is

$$T_{ij}(z) = \exp[-a_{ij} z \sec\theta(z)] \tag{3.6}$$

and the return path is

$$T_i^{'}(z) = \exp[-a_i^{'} z] \tag{3.7}$$

where $a_i^{'}$ is the absorption coefficient of the medium at the fluorophore emission wavelength. Taking the outward and return light attenuation into account, the differential MFL response becomes

$$\begin{aligned} \mathrm{d}R_{ij} &= a_{ij} p_i \Phi_i g_j(z) T_{ij}(z) T_i^{'}(z) \mathrm{d}z \\ &= a_{ij} p_i \Phi_i g_j(z) \exp[-a_{ij} z \sec\theta(z)] \exp[-a_i^{'} z] \mathrm{d}z \\ &= a_{ij} p_i \Phi_i g_j(z) \exp[-(a_{ij} \sec\theta(z) + a_i^{'}) z] \mathrm{d}z. \end{aligned} \tag{3.8}$$

Integrating to derive the total signal for a fluorescent medium layer of finite thickness t provides

$$R_{ij} = \mathrm{a}_{ij} p_i \Phi_i \int_0^t g_j(z) \exp[-(a_{ij} \sec\theta(z) + a_i^{'}) z] \mathrm{d}z. \tag{3.9}$$

A red-orange fluorescent acrylic (Perspex 4T56) plaque, given index $i = 0$ and physical thickness = 3 mm, formed the basis of the distance calibration. The spectral absorption coefficient of the plaque, a_0, was measured on a Varian Cary 500 spectrophotometer (Fig. 3.4) and the emission spectrum and quantum yield of the plaque, Φ_0, and MFL-relative partial quantum yield factor, p_0, were determined as described below in Section 3.2.5.1. The fluorescent plaque was found to saturate one or more MFL channels, necessitating the use of a neutral absorption filter, free from fluorescence, to attenuate excess radiation departing from and returning to the MFL (Fig. 3.7).

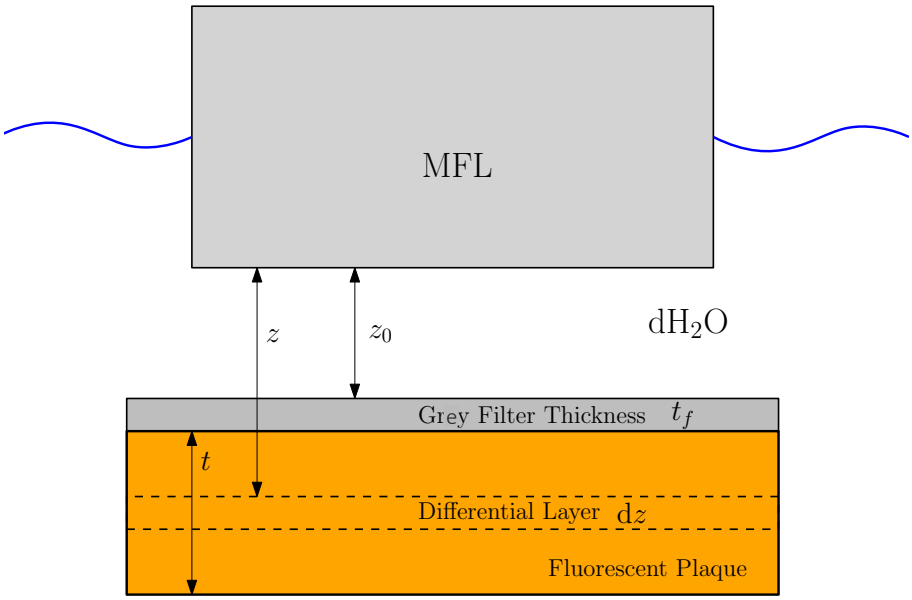

Figure 3.7: Calibration setup using a fluorescent acrylic plaque and neutral grey filter.

The absorption filter, of thickness t_f and transmission, T_{fj}, respectively $T_f^{'}$, was placed over the fluorescent plaque, as illustrated in Fig. 3.7. The outward signal was reduced by $T_{fj}^{sec\theta(z)}$ and the return signal by $T_f^{'}$, providing

$$\mathrm{R}_{0j}(z) = \mathrm{a}_{0j} p_0 \Phi_0 T_f^{'} \int_{z_0+t_f}^{z_0+t_f+t} g_j(z) T_{fj}^{sec\theta(z)} \exp[-(a_{0j} sec\theta(z) + a_i^{'})(z - z_0 - t_f)]\mathrm{d}z. \qquad (3.10)$$

The spectral transmittance of this grey filter was measured using a Varian Cary 500 spectrophotometer, allowing for the calculation of T_{fj} and $T_f^{'}$ by weighted averaging. The MFL response to the fluorescent plaque, R_{0j}, with the grey filter, was measured, leaving $g_j(z)$ as the only unknown.

3.2.5.1 Derivation of distance calibration constants

Derivation of $g_j(z)$

The calibration functions $g_j(z)$ were calculated to within a scaling constant d_i by using a thin film of fluorescent plastic bonded onto a flat, black, opaque, solid substrate. The experiment was performed in dH_2O, where the response of the MFL was recorded as a function of distance z between the fluorescent film and the optical window of the MFL using a z-axis mechanical motion stage (Fig. 3.8).

Figure 3.8: MFL setup for $g_j(z)$ determination. The MFL was positioned on a z-axis translation stage and submerged in dH_2O. The response of the MFL to a weakly fluorescent plastic film fixed onto a black, solid substrate was recorded as a function of distance between the film and the optical window of the MFL.

Two weakly fluorescent plastics films, one pink and one yellow, were compared to verify independence of $g_j(z)$ from the fluorophore. The weakly fluorescent films were optically thin enough for the total fluorescence signal to be considered arising at a single distance z of the film from the MFL. The first film was given index $i = 1$, the second $i = 2$, so that

$$R_{1j} = d_{1j} g_j(z) \tag{3.11}$$

and

$$R_{2j} = d_{2j} g_j(z) \tag{3.12}$$

where d_{1j} and d_{2j} are proportionality constants. Therefore

$$g_j(z) = \frac{R_{1j}(z)}{d_{1j}} = \frac{R_{2j}(z)}{d_{2j}}. \tag{3.13}$$

The typical shape of the $g_j(z)$ functions were considered log-normal, starting at zero for $z = 0$ mm, with the majority of channels peaking at $z \approx 15$ mm before dropping off exponentially (Fig. 3.9). The 570 and 590 nm channels comprised a notable peak at $z \approx 6$ mm, with the LED output displaying a bimodal shape in response to the dull pink film and a single 6 mm peak in response to the dull yellow film. The geometric arrangement of the LEDs and detector shown in Fig. 3.6 imply that the $g_j(z)$ should peak at $z \approx 23.9$

mm, where the LED axes intercept the detector axis. However, while the distance of peak response depends on this geometry, the reduced z maximum may be a result of dilution of LED energy over distance, as per the inverse-square law.

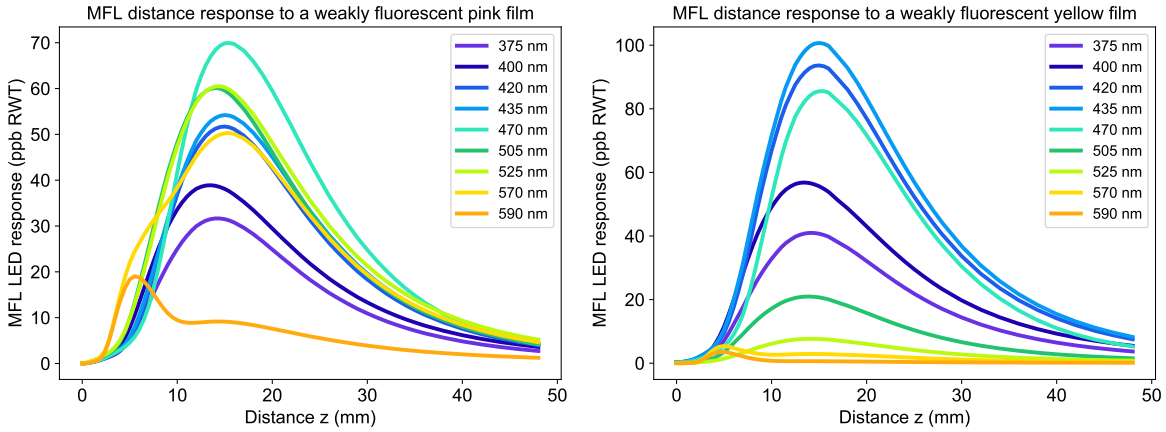

Figure 3.9: The calibration functions $g_j(z)$ were established to within a scaling constant using a thin film of weakly fluorescing film bonded to a flat, black, solid substrate. The MFL LED responses peak at ∼15 mm aside from the 570 and 590 nm channels, which display a notable peak at ∼ 6 mm.

By measuring the MFL response to the fluorescent plaque (with grey filter), at different distances z_0, it is possible to derive the unknown scaling constant d_i by substituting an option from Eq. 3.13 into Eq. 3.10, written as

$$d_{1j} = \frac{a_{0j} p_0 \Phi_0 T_f^{'}}{R_{0j}(z_0)} \int_{z_0+t_f}^{z_0+t_f+t} R_{1j}(z) T_{f_j}^{sec\theta(z)} \exp[-(a_{0j} sec\theta(z) + a_i^{'})(z - z_0 - t_f)] \mathrm{d}z. \tag{3.14}$$

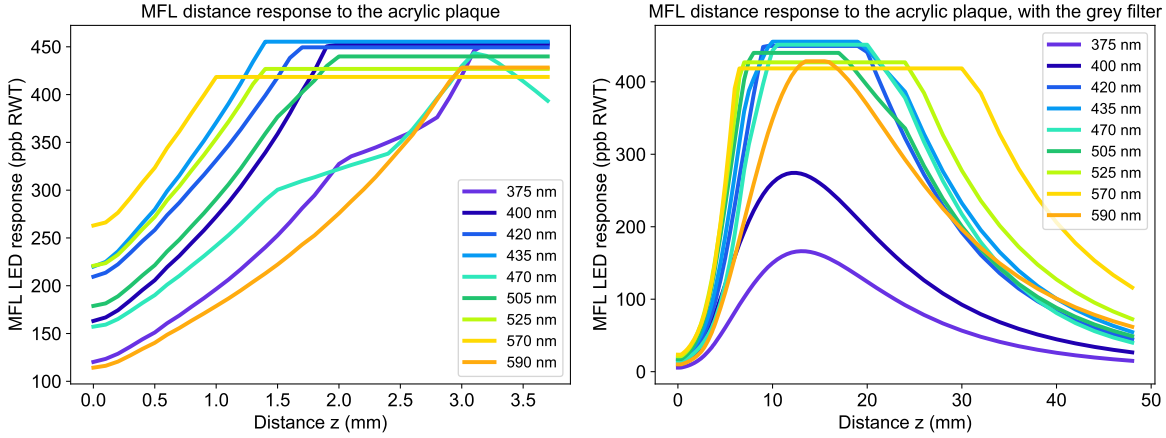

Figure 3.10: The MFL response over distance z to the exposed fluorescent acrylic plaque (left) and with the addition of a neutral, grey filter (right).

The MFL LED response to the weakly fluorescing films was only considered reliable after $z \approx 1.5$-2 mm (Fig. 3.9), due to low signal and potential back-reflections of stimulating radiation from the MFL. However, the instrument response to the fluorescent plaque allowed for good separation of signal at these distances, up to $z \approx 1$ mm without the grey filter (Fig. 3.10). The limiting factor in the plaque response is that the 570 nm channel saturates very quickly ($z \approx 1$ mm). As the MFL detector is common to all LEDs it is feasible that any LED measurements near or beyond saturation may impact the integrity of the other LEDs. To derive the highest resolution $g_j(z)$, the fluorescent plaque measurements were used from 0-1 mm, the fluorescent plaque with the grey filter from 1-6 mm and the weakly fluorescing films for distances greater than 6 mm.

Derivation of Φ_i and p_i

Unlike the dye calibration model, where the quantum yields of ATTO490LS and ATTO655 were provided by the manufacturer, the emission spectrum and quantum yield of the fluorescent plaque needed to be derived experimentally. The photon emission spectrum and quantum yield (Φ_i) were measured by irradiating the plaque with quasi-monochromatic light in the excitation region and subsequently measuring the spectral radiance of the plaque with a spectroradiometer (Fig. 3.11). While the MFL was easily saturated at moderate light intensities, the spectroradiometers used in this exercise required a very high intensity light source to produce a detectable response. Two appropriate light sources were selected, the first was a high intensity blue LED (Osram OSTAR LE B Q8WP), with peak emission centred around 455 nm, and the second was a high intensity green LED (Osram OSLON LT CP7P) with an emission peak centred around 521 nm. The spectral irradiance ($E(\lambda), s^{-1}$ cm^{-2} nm^{-1}) from the Osram LEDs on the plaque were measured with a B&W Tek SpectraRad spectral irradiance metre. Fresnel reflectance, the phenomenon that occurs when changing between media of different refractive indices, was effectively accounted for when performing these measurements, as detailed by Griffith et al. (2018). The emergent photon radiance (L, s^{-1} sr^{-1} cm^{-2}) was measured using an ASD Inc. FieldSpec 3 spectroradiometer. The photon emission spectrum of the fluorescent plaque is plotted in Fig. 3.5.

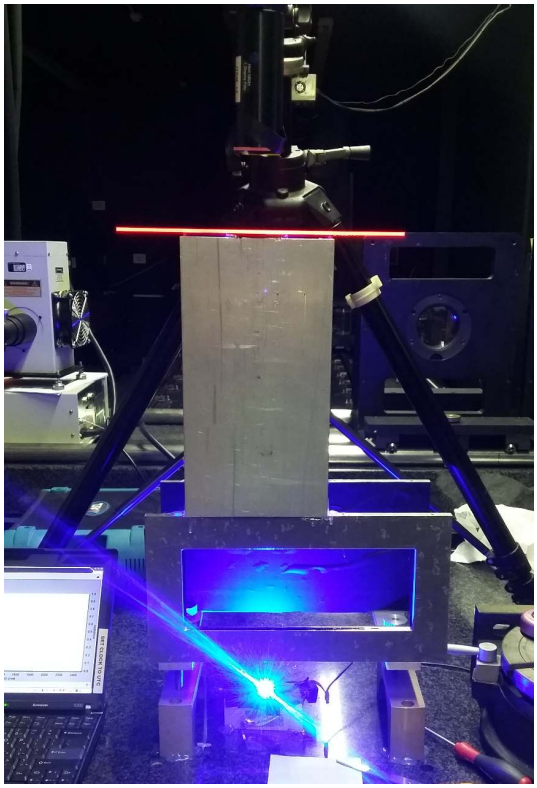

Figure 3.11: The MFL-setup for derivation of the photon emission spectrum of the fluorescent plaque. The plaque response to the high intensity blue LED was measured with an ASD Inc. FieldSpec 3 spectroradiometer.

The fluorescence emitted from the plaque at the known blue and green stimulation wavebands, and the spectral absorption coefficient of the plaque, allowed for derivation of Φ_i. The quantum yield was calculated to be 0.50 for the blue LED and 0.54 for the green LED. The slight discrepancy between FQYs may have arisen due to the presence of more than one fluorophore in the acrylic plaque, a slight wavelength dependence, or simply due to technical error. An average value of 0.52 was used in further calculations.

The MFL-relative partial quantum yield of the fluorescent plaque, p_i, was determined as per Eq. 3.3, where the $S_i(\lambda)$ represents the plaque, illustrated in Fig. 3.5 and listed in Table 3.1.

3.2.5.2 Fluorescent plaque calibration: Field application

The distance calibration process was used to establish data for $g_j(z)$ through application of Eq. 3.14 and then returning to Eq. 3.13. In the field, the calculated MFL-relative partial quantum yield factor for chl-a (p_c) and measured absorption (a_j), made it possible to apply the calibration to MFL field measurements (R_j), and derive the chl-a fluorescence quantum yield (Φ_j). The instrument calibration factors are computed using a_j from each

field station, as follows

$$\mathrm{G}_j = \int_0^\infty g_j(z)\exp[-(a_j \sec\theta(z) + a^{'})z]\mathrm{d}z. \tag{3.15}$$

The unknown Φ_j was determined by solving Eq. 3.9, arriving at

$$\Phi_j = \frac{R_j}{G_j a_j^* p_c} \tag{3.16}$$

where a_j^* is the phytoplankton-specific absorption.

3.3 Results

Two distinct calibration models were applied to the MFL, for use in *in situ* apparent Φ_F determination. The first approach made use of fluorescent dye solutions of known quantum yields and the second utilised fluorescent plastic plaques and films. At low attenuation, the dye calibration factors k_j are related to plaque calibration factors $g_j(z)$ as

$$\mathrm{k}_j = \int_0^\infty g_j(z)\mathrm{d}z. \tag{3.17}$$

The $\Phi_F(\lambda)$ derived through both calibration approaches were in good agreement, particularly for the ATTO490LS dye and the fluorescent plaque methods (Fig. 3.12). All methods display a similar output up until 525 nm, and display the largest standard deviation of MFL measurements at 570 nm. The ATTO655 calibration output increases exponentially after 525 nm, and the ATTO490LS and fluorescent plaque outputs diverge at 570 nm.

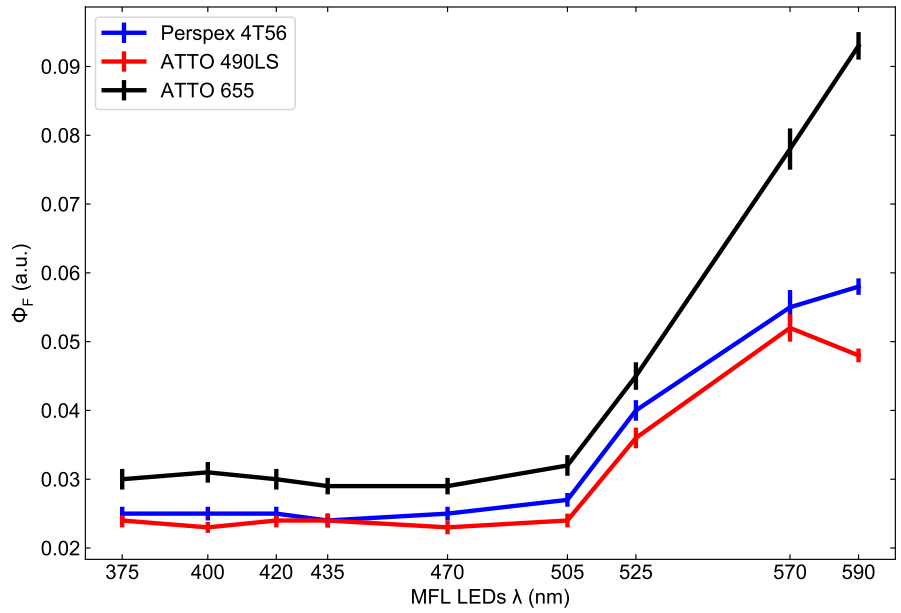

Figure 3.12: Derived $\Phi_F(\lambda)$ for field station GHS21, as per the fluorescent dye and plaque calibration models. The error bars represent the standard deviation of the time-averaged MFL measurements, accounting for temporal variability.

3.4 Discussion

3.4.1 Calibration comparison

Field sample GHS21 (Appendix A.1) was selected as a proof-of-concept dataset to compare the output of the two calibration approaches. Uncertainty in the quantum yield of the reference dyes and acrylic plaque, as well as other direct inputs to the calibration, feed directly into *in situ* Φ_F output. It is thus imperative to ascertain the most accurate approach available. Both calibration approaches displayed congruent results up until 525 nm (Fig. 3.12), whereafter the ATTO655 calibration output increased exponentially. This was likely due to the strong absorptivity of this dye over this region (Fig. 3.4), increasing the fluorescence response and overestimating of Φ_F at these wavelengths. The low absorptivity of ATTO490LS over the 590 nm LED was likely responsible for the downward trend from 570 nm to 590 nm, compared to the plaque calibration output (Fig. 3.12). A negative component to the fluorescent plaque calibration is that the plaque has a high optical depth resulting in strong spectral variation, causing a failure of the Beer-Lambert Law. The Beer-Lambert Law relates the transmittance of a substance to its optical depth and its absorbance, and fails at high concentrations and/ or when the substance is highly scattering, leading to changes in attenuation. This was of particular

concern when the plaque was used in close proximity to the optical window of the MFL. The ATTO490LS dye calibration was ultimately selected as the most reliable calibration for *in situ* Φ_F derivation. Motivating factors included the large Stoke's shift of the dye, compliance with the Beer-Lambert Law, and the similar instrument set-up during the calibration and when deployed at sea.

3.4.2 Calibration considerations

While both calibration approaches are assumed to be valid in low scattering environments, they may be potentially compromised if field samples have high optical attenuation or scattering. An important consideration when quantifying chl-*a* fluorescence is that of Raman scattering by water (Maritorena et al., 2000; Morrison, 2003; Westberry and Siegel, 2003). Scattering of light, both elastic and inelastic, is responsible for redirecting incident photons into the upwelling light stream (Mobley, 1994). Elastic scattering reflects ambient solar radiation, whereas inelastic scattering involves a shift in wavelength and includes chl-*a* fluorescence and Raman scattering by water (excitation wavelength around 550 nm). To obtain the upwelling radiance from fluorescence, it is necessary to quantify the amount of elastic scattering of ambient solar radiation and inelastic Raman scattering, so these may be subtracted from the total upwelling radiance. Excitation wavelengths of importance to scattering to the range of chl-*a* fluorescence output lie between 510 and 600 nm. In this study, Raman scattering was not accounted for, possibly resulting in an overestimation of chl-*a* fluorescence, notably in the 525, 570, and 590 nm channels. Anomalously high chl-*a* fluorescence will be carried through to Φ_F, leading to the exaggeration of signal. In an attempt to minimise the number of stations that displayed high scattering, from Raman, bubbles, or otherwise, the MFL 880 nm turbidity LED was used as a flag for highly scattering environments. Stations displaying an MFL_{880} value above 10 FTU were discarded (Section 2.6.3). The extensive quality control of the MFL data ensured that samples subjected to highly scattering environments were omitted. Furthermore, the MFL recordings for individual stations were visually examined and the presence of bubbles (Section 2.9) or instrument artefacts (Section 2.10) led to further station elimination. Another concern is that of fluorescence reabsorption. When the absorption spectrum and the emission spectrum of a fluorophore overlap, there is a chance the emitted light will be reabsorbed by the fluorophore. All fluorophores used in this study were potentially susceptible to fluorescence reabsorption, with ATTO490LS being the least affected due to its large Stoke's shift.

3.5 Conclusion

The MFL, originally designed to discriminate between phytoplankton species within a population by exploiting accessory pigment composition, was redirected for use in apparent Φ_F determination. The instrument underwent an in-depth optical characterisation of all relevant components. In order to derive Φ_F, it was vital to have detailed knowledge of the incident irradiance and returned fluorescence, as well as the absorption properties of the medium being examined. Two calibration approaches were implemented in this study, the first made use of fluorescent dyes and the second of a fluorescent perspex plaque.

The first approach utilised two fluorescent dyes with different spectral properties and known quantum yields (ATTO655 and ATTO490LS). All other components necessary for $\Phi_F(\lambda)$ derivation were determined experimentally, and a series of wavelength-specific calibration factors were generated. The second approach, also known as the distance-response calibration, made use, primarily, of a fluorescent perspex plaque. While the dyes were regarded as homogenous solutions, the MFL stimulating radiation and returned fluorescence from elementary plane-parallel layers was investigated in this process. Wavelength-specific calibration factors were derived for both calibration approaches. The respective calibration factors were applied to an *in situ* field sample, and the resultant outputs demonstrated satisfactory agreement, apart from at 570 and 590 nm. The green-to-orange LEDs are highly sensitive and susceptible to anomalous outputs in highly scattering and/or low signal-to-noise environments, which may have been the case in the field sample. The dye calibration, through use of ATTO490LS, was selected as the optimal calibration to apply to *in situ* Southern Ocean samples for derivation of $\Phi_F(\lambda)$.

The greater aim of expanding the functionality of the MFL was to allow for increased *in situ* Φ_F observations in the under-sampled Southern Ocean. The routine deployment of the MFL and subsequent implementation of the novel dye calibration, will allow for more *in situ* Φ_F measurements in this ecologically significant region. Furthermore, in principle, other spectrally-resolved fluorometers could be employed to derive Φ_F following the calibration approaches detailed in this chapter. This important physiological index serves as a proxy of the health of the surrounding environment. An increase in *in situ* Φ_F measurements will lead to an improved understanding of the mechanisms governing the variability in signal, which will ultimately aid in the validation and improvement of existing satellite Φ_F algorithms.

Chapter 4

Investigation of *in situ* Fluorescence Quantum Yield Variability in the Southern Ocean

4.1 Introduction

4.1.1 Overview

Variability in Φ_F is due to changes in energy distribution within the photosynthetic apparatus, through changes in light absorption and fluorescence emission. These physiological responses to environmental variability are adaptive features that can primarily be attributed to three principal drivers, namely the light environment, nutrient availability, and community structure (Babin et al., 1996b; Behrenfeld et al., 2009; Browning et al., 2014a; Huot et al., 2005; Letelier et al., 1997; Maritorena et al., 2000; Morrison, 2003; Morrison and Goodwin, 2010; Schallenberg et al., 2008). The Southern Ocean seasonal cycle has been established as the dominant mode of variability that couples the physical mechanisms of climate forcing to ecosystem response in production, diversity, and carbon export (Monteiro et al., 2011; Thomalla et al., 2011). The seasonal evolution of phytoplankton biomass has typically been ascribed to the seasonal cycle of solar radiation, impacting vertical stability through net heat flux, influencing vertical light and nutrient distribution (Arrigo et al., 2008; Boyd, 2002; Sverdrup, 1953). Resident phytoplankton display characteristic photophysiological responses to changes in incident irradiance and Fe availability, which is detectable through Φ_F observations (Letelier et al., 1997; Lin et al., 2016; Schallenberg et al., 2008).

4.1.2 The light environment as a driver of Φ_F variability

Phytoplankton fluorescence *in vivo* is derived almost entirely from PSII (Falkowski and Kiefer, 1985), with a number of processes acting to alter Φ_F. A brief recap of Section 1.4.5 is as follows; photochemical quenching (qP) occurs at low irradiance levels and decreases as light levels increase, with reaction centres progressively closing due to photochemistry (Kiefer and Reynolds, 1992). Under high light conditions, a variety of mechanisms, collectively known as non-photochemical quenching (qN), act to regulate exciton energy transfer to PSII reaction centres by balancing photochemical utilisation and excess energy dissipation (Horton and Ruban, 2005; Krause and Weis, 1991). Antenna quenching (qE) is a rapid (seconds to minutes), energy-dependent mechanism that typically dissipates excess energy through the xanthophyll cycle (XC) (Demmig-Adams, 1990; Lavaud et al., 2002b). Implementation of reaction centre quenching (qI) occurs over a longer timescale, through the reversible down-regulation of PSII reaction centres (Morrison, 2003). Under high irradiance levels Φ_F is typically low, due to qN, and under low light conditions Φ_F is typically high, subject to qP (Behrenfeld et al., 2009; Laney et al., 2005; Maritorena et al., 2000; Morrison, 2003; Morrison and Goodwin, 2010; Ostrowska, 2012; Schallenberg et al., 2008; Westberry and Siegel, 2003). This pattern is observed at both diel (Babin et al., 1996b; Dandonneau and Neveux, 1997) and seasonal scales (Babin et al., 1996b; Morrison and Goodwin, 2010), and over depth when sampling vertically through the water column (Maritorena et al., 2000; Morrison, 2003).

For example, work by Maritorena et al. (2000) showed a minimum Φ_F in surface, sunlit waters (1-2%, $<$ 10 m) and a maximum at depth (5-6%, $>$ 50 m). This light-related discrepancy in Φ_F was corroborated by Morrison (2003), who derived *in situ* Φ_F measurements through a_{ph}(400-700 nm) and an underwater, bi-directional radiometer, and reported surface values ranging from 0.027 under low light conditions, to 0.004 under high light conditions (Fig. 4.1). Two distinct patterns were observed in the variation of Φ_F with depth, and thus irradiance; an increase in Φ_F from the surface to a subsurface maximum, and a subsequent decrease with increasing depth. The increase in Φ_F to the subsurface maximum was ascribed to a decrease in qN, whereas the decrease below the subsurface maximum was indicative of increasing qP.

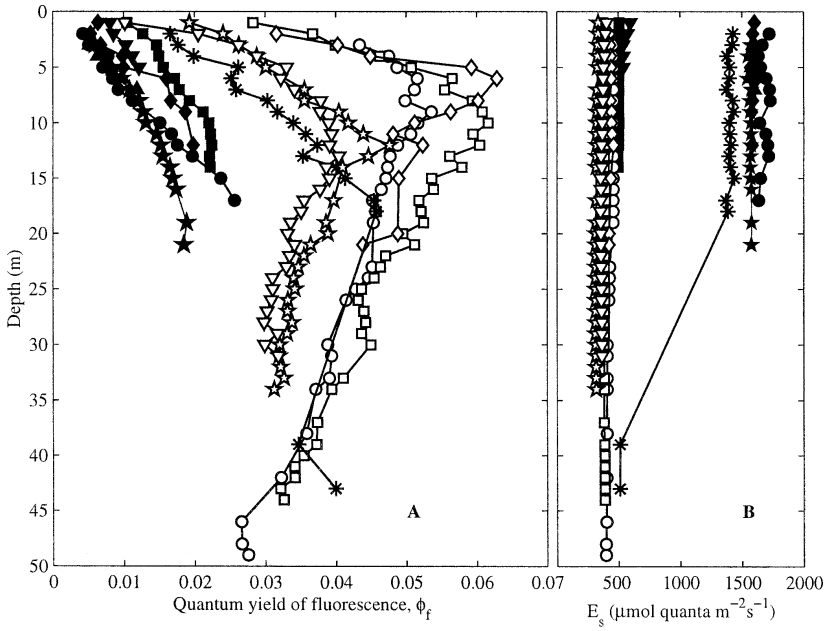

Figure 4.1: Variation in the quantum yield of fluorescence with depth and surface irradiance. Two distinct regimes were apparent in the variation of Φ_F with depth (panel A), an initial increase from low surface values to a subsurface maximum, followed by a decrease with depth. This was observed only in station casts that were performed before 10:00 am (open symbols), which had typically low surface irradiance (panel B). Casts sampled after 10:00 am (closed symbols) had comparably depressed Φ_F values, irrespective of surface irradiance. Figure reproduced from Morrison (2003).

The XC in phytoplankton mediates the interconversion of diadinoxanthin (Dd) and diatoxanthin (Dt) in response to changing light conditions (Demers et al., 1991). The amount of Dt present is linearly related to the amount of qE taking place (Alderkamp et al., 2010; Lavaud et al., 2004), and is often expressed as a de-epoxidation state ratio, i.e. Dt/ Dd + Dt (Brunet et al., 1993; Demers et al., 1991; Grouneva et al., 2009; van de Poll et al., 2011). While this is measurable in the laboratory setting (Arrigo et al., 2010; Demers et al., 1991; Kropuenske et al., 2010, 2009; Lavaud et al., 2004, 2007; Olaizola et al., 1994; Wu et al., 2012), the possibility of accurately capturing such a rapid reaction *in situ* is yet to be effectively achieved. The time lag between sample collection and shipboard measurements, as well as the preconditioning of the sample, must be considered. In addition, it is difficult to measure the concentration of Dt at sea unless the biomass is sufficiently high (Olaizola et al., 1992). Previous studies have alternatively looked at the combined total concentration of Dd and Dt (Brunet et al., 1993; Cheah et al., 2013), as an indicator of qE levels. In addition to qN, the photoacclimation state of phytoplankton to their ambient surroundings must be considered when investigating the light response of a population. The influence of photoacclimation on qN is likely to be species-specific

(Kropuenske et al., 2009; van de Poll et al., 2011, 2007), with studies reporting high-light acclimated cells to have superior qN responses (Lavaud et al., 2002b; Ragni et al., 2008; van de Poll et al., 2006), and others reporting the same result for low light acclimated cells (Milligan et al., 2012). Irrespective of the underlying photoacclimation status of a community, fluorescence quenching corrections for Φ_F measurements have been proposed, in an attempt to resolve additional physiological information, for example, Fe-limitation (Behrenfeld et al., 2009; Browning et al., 2014a).

4.1.3 Nutrient availability as a driver of Φ_F variability

The highly productive Southern Ocean is driven in part by the high macronutrient availability, with phytoplankton growth and productivity constrained by the availability of light and Fe (de Baar et al., 1990; Martin et al., 1990b). While the macronutrients NO_3^- and phosphate (PO_4^{3-}) are not considered limiting in the Southern Ocean (Dafner and Mordasova, 1994; Tréguer and Jacques, 1992), any potential fluctuations in their concentrations would have negligible effect on Φ_F, as Φ_F is not considered an ideal proxy for macronutrient limitation, particularly in the surface ocean where the influence of light is the dominant driver of variability (Schallenberg et al., 2008). Macronutrient availability sets a limit on phytoplankton standing stocks, with intracellular chl-*a* to carbon (chl:C_{phyto}) scaling linearly with growth rate (Laws and Bannister, 1980), reflecting a balance between light harvesting capacity and metabolic demand; i.e. there is no change in fluorescence properties across growth rates under steady-state limiting conditions (Behrenfeld et al., 2006; Moore et al., 2008; Parkhill et al., 2001; Schrader et al., 2011). Behrenfeld et al. (2009) conducted a global analysis study on MODIS-derived Φ_{sat} and found no significant relationship between Φ_{sat} and NO_3^- and PO_4^{3-} concentrations. They instead attributed 82% of the elevated Φ_{sat} (0.015-0.028) to limitation of the micronutrient Fe.

Southern Ocean phytoplankton populations are broadly regulated by an interplay of $Si(OH)_4$, Fe, and light levels (Boyd et al., 2001, 1999; Hutchins et al., 2001; Le Moigne et al., 2013; Martin et al., 2013; Ryan-Keogh et al., 2018). Silicate concentrations regulate the distribution of diatoms, and is not specifically linked to a characteristic Φ_F response. Dissolved $Si(OH)_4$ concentrations, ranging from 1-15 μM north of the PFZ to 40-60 μM south of the PFZ (Coale et al., 2004; Franck et al., 2000; Tréguer and Jacques, 1992), regulates local diatom populations, which display high inter-species variability in response to varying Fe, $Si(OH)_4$ and light regimes (Hoffmann et al., 2008; Timmermans et al., 2001). The fluctuating Fe levels in the Southern Ocean, in part, also affects phytoplankton community composition, with different phytoplankton exhibiting species-specific photoadap-

tive traits (Arrigo et al., 2010; Kropuenske et al., 2009) that impact the local Φ_F. For example, in terms of photoacclimation, Fe-light co-limited diatoms typically favour an increase in the antenna size of PSII rather than the number of reaction centres, allowing for the maximum capture of light energy with the minimal Fe requirement, resulting in a reduced Φ_F (Strzepek et al., 2012). Understanding the seasonal Fe-cycling dynamics over the different Southern Ocean provinces is imperative to isolating its contribution to Φ_F variability.

4.1.4 Taxonomy as a driver of Φ_F variability

Phytoplankton speciation and growth in the Southern Ocean is regulated by a multitude of factors (Abbott et al., 2000; Boyd et al., 2001, 1999; de Baar et al., 1990; Strzepek et al., 2012), with different species exhibiting specific nutrient requirements and employing characteristic photoadaptive strategies to changing light conditions, which mechanistically affect Φ_F. Phytoplankton that employ xanthophyll cycling as their first defence to increasing light levels will see a reduction in Φ_F, due to the rapid de-epoxidation of Dd to Dt, operating in the blue part of the light spectrum (Kropuenske et al., 2009). As such, both diatoms (Lavaud et al., 2002c) and *P. antarctica* (Moisan et al., 1998), which are known to employ an effective XC, typically exhibit reduced Φ_F under high light conditions. In the Southern Ocean MIZ, diatoms prefer stable environments with shallow mixed layers, coping with high light by maintaining low levels of photosynthetic pigments and high levels of photoprotective pigments, rendering them less susceptible to photoinhibition than *P. antarctica*. *P. antarctica* focuses more on the repair of photodamage and thrives in areas characterised by deep mixed layers (Arrigo et al., 2010).

4.1.5 Chapter objectives

Given the preceding evidence, it is expected that *in situ* Φ_F will show a strong seasonal variance as a result of changes in both the community structure and the surrounding environment. The novel calibration of the MFL (Chapter 3) is employed to derive $\Phi_F(\lambda)$ for 66 *in situ* field stations located in the Atlantic sector of the Southern Ocean. These stations were sampled during the austral winter of 2012 and the austral summer of 2013/ 2014. Spectral cluster analysis is performed on all derived $\Phi_F(\lambda)$, to collate similar spectra into groups for statistical analysis, such that potential relationships between $\Phi_F(\lambda)$ and the possible drivers of variability can be determined.

4.2 Results

Please refer to the List of Notation (p.iv) for specific symbols and units used throughout this chapter.

4.2.1 Pigment analysis

4.2.1.1 Chl-*a* concentrations

Chl-*a* concentrations were derived through HPLC extraction (Section 2.2.1) and are displayed in Fig. 4.2. Stations sampled during the Winter Cruise (0.23±0.05 mg m^{-3}) had the lowest average [chl-*a*], while stations sampled in the early summer (GoodHope South, 0.66±0.22 mg m^{-3}) and mid-summer (Buoy Run, 0.72±0.34 mg m^{-3}) had higher average [chl-*a*] than those sampled in the late summer (GoodHope-North, 0.39±0.17 mg m^{-3}).

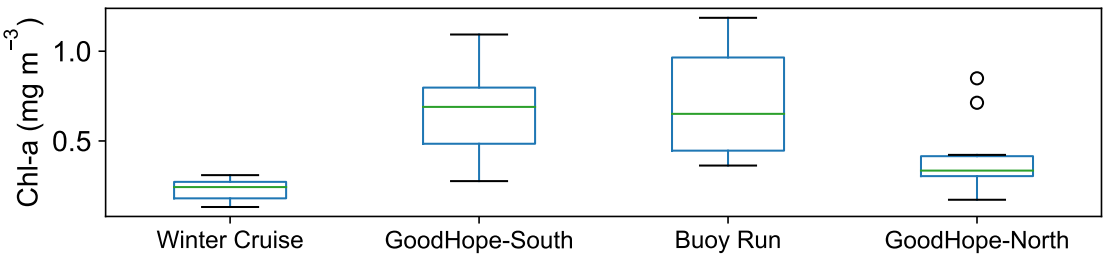

Figure 4.2: Boxplots showing HPLC-derived median [chl-*a*] per cruise leg (mg m^{-3}). Minimum outlier (5%), first quartile (Q1, 25%), median, third quartile (Q3, 75%), and maximum outlier (95%).

4.2.1.2 CHEMTAX

Output from the CHEMTAX analysis of various phytoplankton pigments is shown in Fig. 4.3, subdivided into the various cruise legs. Diatom-subtypes A and B, and Haptophyte-subtypes 6 and 8, were grouped together for better visualisation of the overall phytoplankton taxa. The percentages of the different phytoplankton groups for each station are listed in Appendix B.2.

The Winter Cruise comprised a mix of phytoplankton assemblages, dominated by haptophytes north of the SACCf and diatoms to the south. The largest diatom population was at station W101 (65.7%). Populations of prasinophytes and *Synechoccocus* were observed towards the northern latitudes. Cryptophytes were present in varying amounts at all stations, with a small increase in the prevalence towards the south. The GoodHope-South cruise leg (early summer) was dominated by diatoms, followed by haptophytes, across all latitudes. The station with the largest diatom population was GHS78 (78.4%) and

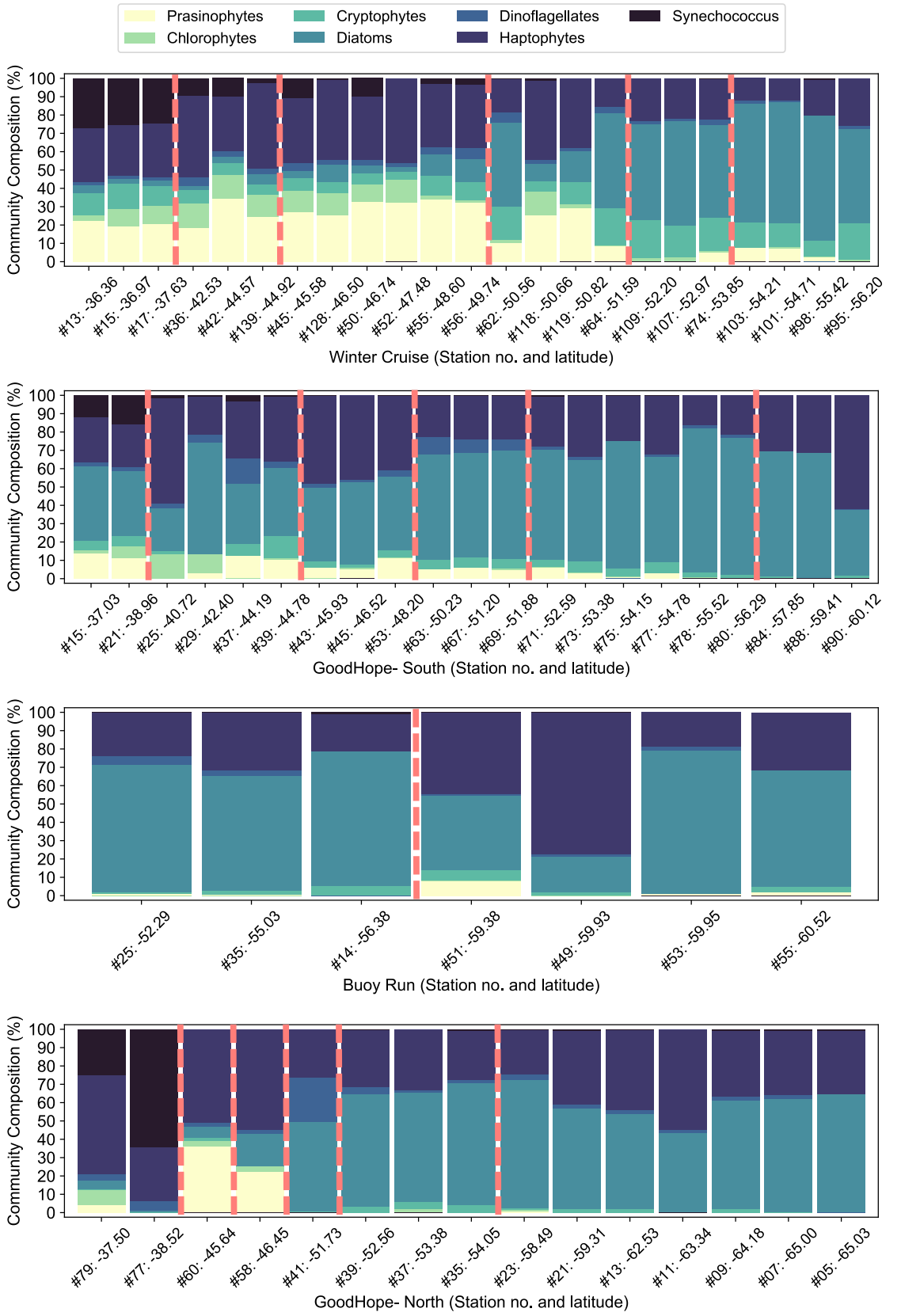
Prasinophytes
Chlorophytes
Cryptophytes
Diatoms
Dinoflagellates
Haptophytes
Synechococcus
Community Composition (%)
#13: -36.36
#15: -36.97
#17: -37.63
#36: -42.53
#42: -44.57
#139: -44.92
#45: -45.58
#128: -46.50
#50: -46.74
#52: -47.48
#55: -48.60
#56: -49.74
#62: -50.56
#118: -50.66
#119: -50.82
#64: -51.59
#109: -52.20
#107: -52.97
#74: -53.85
#103: -54.21
#101: -54.71
#98: -55.42
#95: -56.20
Winter Cruise (Station no. and latitude)
#15: -37.03
#21: -38.96
#25: -40.72
#29: -42.40
#37: -44.19
#39: -44.78
#43: -45.93
#45: -46.52
#53: -48.20
#63: -50.23
#67: -51.20
#69: -51.88
#71: -52.59
#73: -53.38
#75: -54.15
#77: -54.78
#78: -55.52
#80: -56.29
#84: -57.85
#88: -59.41
#90: -60.12
GoodHope- South (Station no. and latitude)
#25: -52.29
#35: -55.03
#14: -56.38
#51: -59.38
#49: -59.93
#53: -59.95
#55: -60.52
Buoy Run (Station no. and latitude)
#79: -37.50
#77: -38.52
#60: -45.64
#58: -46.45
#41: -51.73
#39: -52.56
#37: -53.38
#35: -54.05
#23: -58.49
#21: -59.31
#13: -62.53
#11: -63.34
#09: -64.18
#07: -65.00
#05: -65.03
GoodHope- North (Station no. and latitude)

Figure 4.3: CHEMTAX analysis of all stations sampled. Stations are grouped into cruise legs, the station numbers and latitudes of which are specified, and are arranged in order of increasing latitude, moving poleward from left to right. Approximate positions of the fronts are indicated by the red dashed line; From left to right: For Winter, STF (38°S), SAF (45°S), PF (50°S), SACCf (52°S), SBdy (54°S), For summer, STF (39°S), SAF (45°S), PF (49°S), SACCf (52°S), SBdy (57°S).The position of the fronts was determined using sea surface height data from maps of absolute dynamic topography (MADT) from the CLS/AVISO product (Rio et al., 2011; Swart et al., 2010).

that with the largest haptophyte population was GHS90 (62.1%), two adjacent stations. Small populations of *Synechoccocus* were found north of the STF, and there was a decreasing population of prasinophytes from north to south. There were small populations of chlorophytes present at GHS21, GHS25, and GHS29, north of the STF. Small populations of cryptophytes existed at most stations, with negligible quantities at the four stations south of the SBdy. The six stations of the Buoy Run (mid summer) were largely dominated by diatoms and haptophytes, with the largest populations of each found at BR53 (78.2%) and BR49 (77.3%) respectively. Interestingly, there was no correlation between haptophytes and highly scattering stations, as might be expected with an abundance of reflective coccolithophores. A small population of prasinophytes was present at BR51 (4.6%). Mixed populations dominated the GoodHope-North leg (late summer) north of the PF, with *Synechoccocus* featuring north of the STF (64.4% for station GHN77), and prasinophytes near the SAF (36% for station GHN60). Station GHN41, located on the SACCf, contained a dinoflagellate component (24.4%). All stations south of the PF were primarily governed by haptophyte and diatom populations.

4.2.1.3 Diagnostic pigment ratios

The use of weighted diagnostic pigment ratios to estimate the size classes present within stations was performed as per Uitz et al. (2006), the results of which are shown in Fig. 4.4. The percentages of the different phytoplankton size classes for each station are listed in Appendix B.2.

All stations across the summer cruise legs appeared to be dominated by micro- and nanoplankton populations (Fig. 4.4), with picoplankton being consistently present during the Winter Cruise, but still only occupying a small percentage of each station. The GoodHope-South leg had the largest populations of picoplankton present north of the STF (GHS15 and GHS21), decreasing in number before becoming obsolete south of the SBdy (GHS78), where microplankton dominated. The Buoy Run comprised only micro and nanoplankton, apart from a small population of picoplankton at BR51 (4.6%).

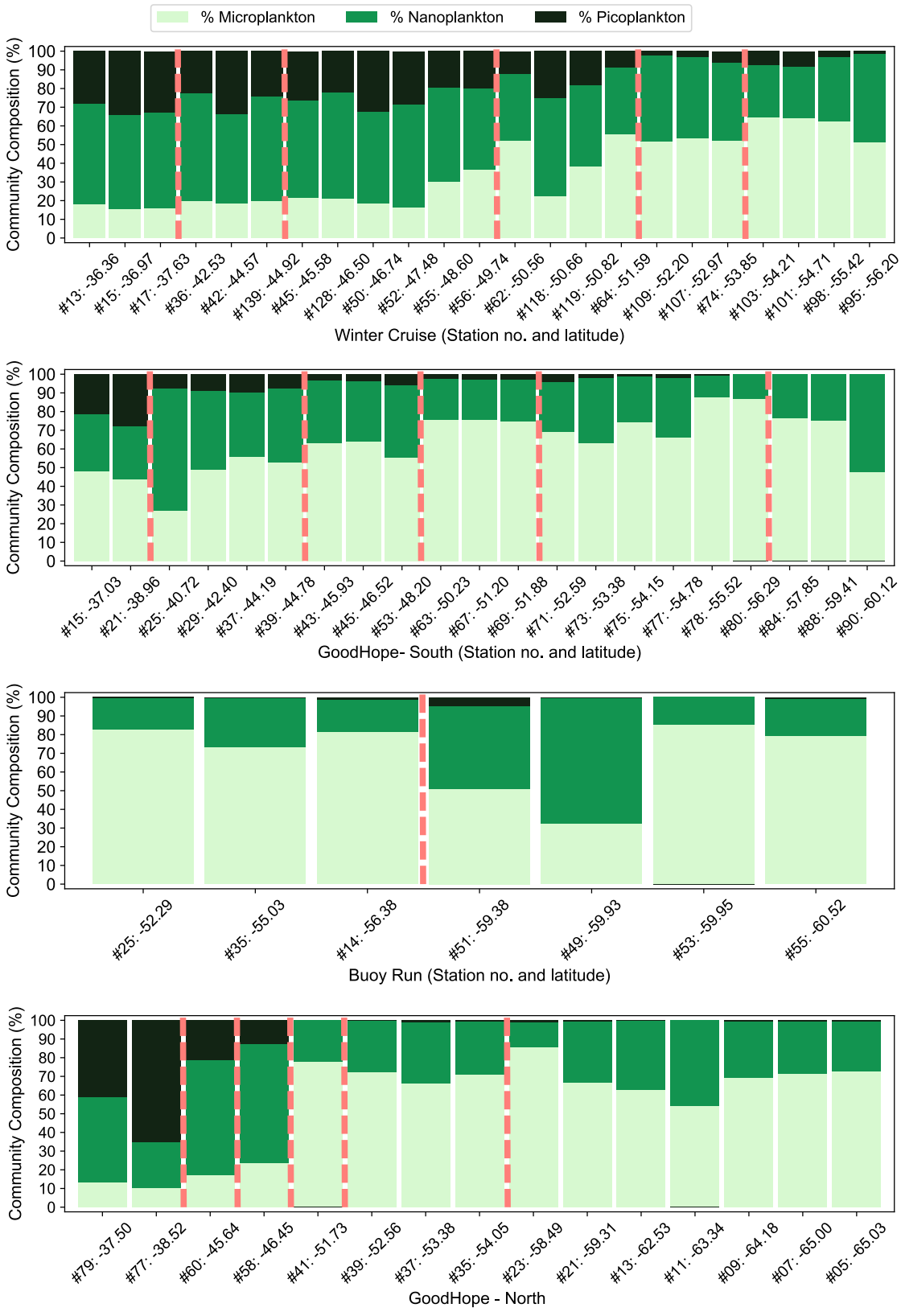
% Microplankton
% Nanoplankton
% Picoplankton
Community Composition (%)
#13: -36.36
#15: -36.97
#17: -37.63
#36: -42.53
#42: -44.57
#139: -44.92
#45: -45.58
#128: -46.50
#50: -46.74
#52: -47.48
#55: -48.60
#56: -49.74
#62: -50.56
#118: -50.66
#119: -50.82
#64: -51.59
#109: -52.20
#107: -52.97
#74: -53.85
#103: -54.21
#101: -54.71
#98: -55.42
#95: -56.20
Winter Cruise (Station no. and latitude)
#15: -37.03
#21: -38.96
#25: -40.72
#29: -42.40
#37: -44.19
#39: -44.78
#43: -45.93
#45: -46.52
#53: -48.20
#63: -50.23
#67: -51.20
#69: -51.88
#71: -52.59
#73: -53.38
#75: -54.15
#77: -54.78
#78: -55.52
#80: -56.29
#84: -57.85
#88: -59.41
#90: -60.12
GoodHope- South (Station no. and latitude)
#25: -52.29
#35: -55.03
#14: -56.38
#51: -59.38
#49: -59.93
#53: -59.95
#55: -60.52
Buoy Run (Station no. and latitude)
#79: -37.50
#77: -38.52
#60: -45.64
#58: -46.45
#41: -51.73
#39: -52.56
#37: -53.38
#35: -54.05
#23: -58.49
#21: -59.31
#13: -62.53
#11: -63.34
#09: -64.18
#07: -65.00
#05: -65.03
GoodHope - North

Figure 4.4: Weighted diagnostic pigment ratios, following the method of Uitz et al. (2006). The size classes are represented as a percentage of the total population for each station. Stations are grouped into cruise legs, the station numbers and latitudes of which are specified, and are arranged in order of increasing latitude, moving poleward from left to right. Approximate positions of the fronts are indicated by the red dashed lines; From left to right: For Winter, STF (38°S), SAF (45°S), PF (50°S), SACCf (52°S), SBdy (54°S), For summer, STF (39°S), SAF (45°S), PF (49°S), SACCf (52°S), SBdy (57°S). The position of the fronts was determined using sea surface height data from maps of absolute dynamic topography (MADT) from the CLS/AVISO product (Rio et al., 2011; Swart et al., 2010).

Stations BR49 and BR51, with prominent populations of nanoplankton, were positioned over the frontal position of the SBdy, with subsequent stations positioned directly to the south (BR53 and BR55) demonstrating a size transition to larger microplankton. Station GHN77 displayed a dominant population of picophytoplankton (65%), which may be representative of *Synechoccocus* known to exist in the STZ. On the GoodHope-North leg, stations GHN58 and GHN60 were indicative of the smaller species that occurs in the late summer. Stations south of the SACCf front (GHN41), were notably dominated by microplankton.

4.2.2 Absorption, fluorescence, and $\Phi_F(\lambda)$

4.2.2.1 Absorption

While a_{ph} is used in the derivation of $\Phi_F(\lambda)$, presenting the a^*_{ph} data removed biomass-related variance across time and stations, to better resolve physiological differences (Fig. 4.5). The fact that both the Winter Cruise and SANAE53 were dominated by haptophytes and diatoms (Fig. 4.3) is evidenced in the similar a^*_{ph} spectral shapes. However, a difference in phytoplankton size is apparent between the Winter Cruise and the Buoy Run; the Buoy Run phytoplankton are of a much larger size than those present in Winter 2012, as observed by the spectral flattening of the 400-500 nm region (Ciotti et al., 2002), and verified by the diagnostic pigment size classifications (Fig. 4.4). All individual station S values, [chl-a], and absorption quality control data are found in Appendix A.1.

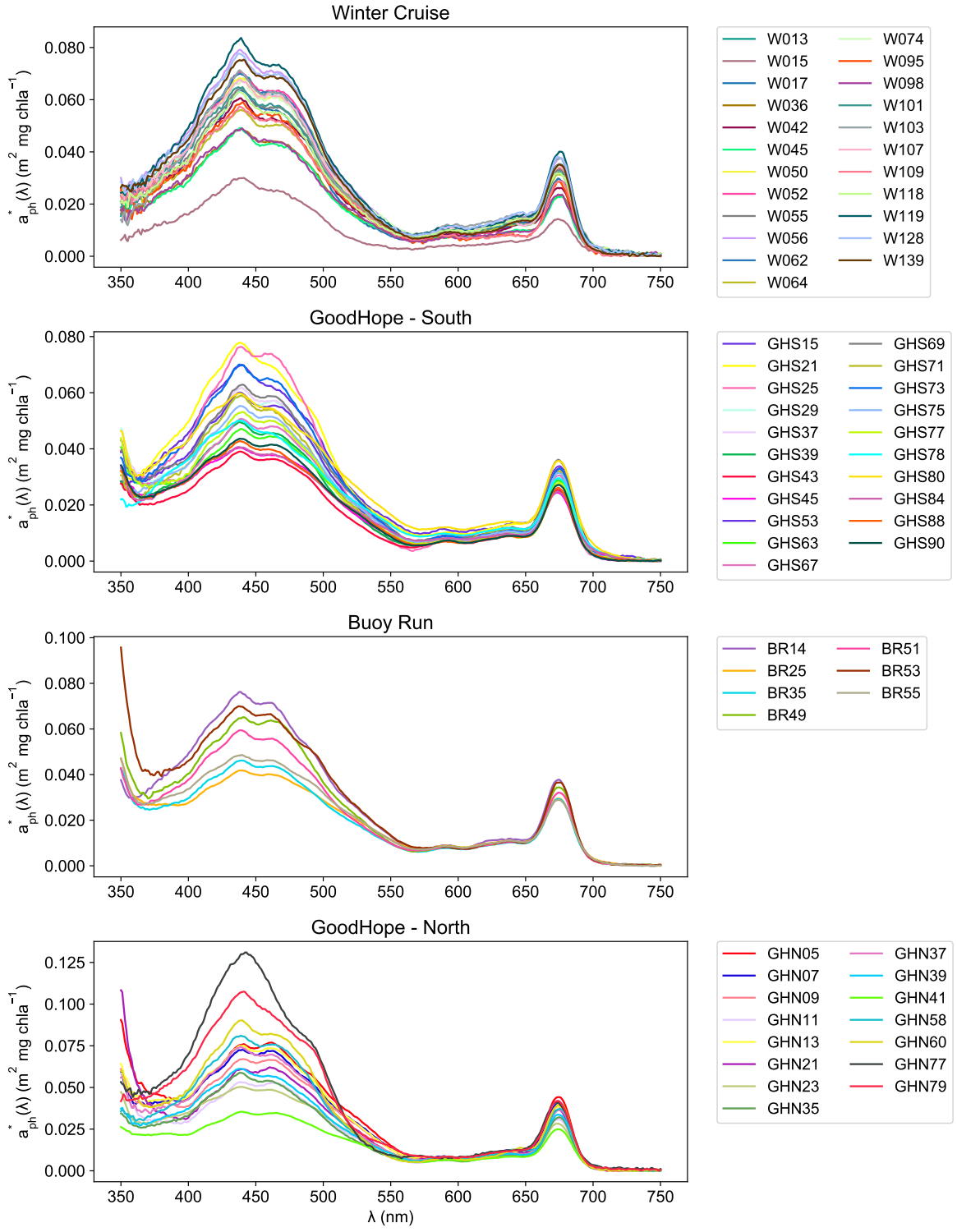

Figure 4.5: Chl-a-specific absorption (a^*_{ph}) for all field stations sampled, measured in m^2 mg chl-a^{-1}. Note the difference in magnitude between plots.

4.2.2.2 Fluorescence measurements

The raw MFL fluorescence measurements were subjected to quality control (Section 2.6.3), with any sub-standard output discarded. Furthermore, due to the presence of unexplained spectral artefacts in some samples, it was important to confirm with the manufacturers that the raw fluorescence data was of an acceptable quality; the MFL raw fluorescence output was deemed satisfactory through personal communication with the manufacturers (JFE Advantech, Co. Ltd., date of communication: 21/05/2014).The spectral diversity between the various stations sampled is apparent in the fluorescence data measured across various cruise legs (Fig. 4.6). The magnitude of the MFL fluorescence measurements for the Winter Cruise were low relative to summer stations. The effect of the chl-*a* Soret absorption wavebands was observed by the higher fluorescence values achieved in the blue part of the spectrum, notably at 435 nm.

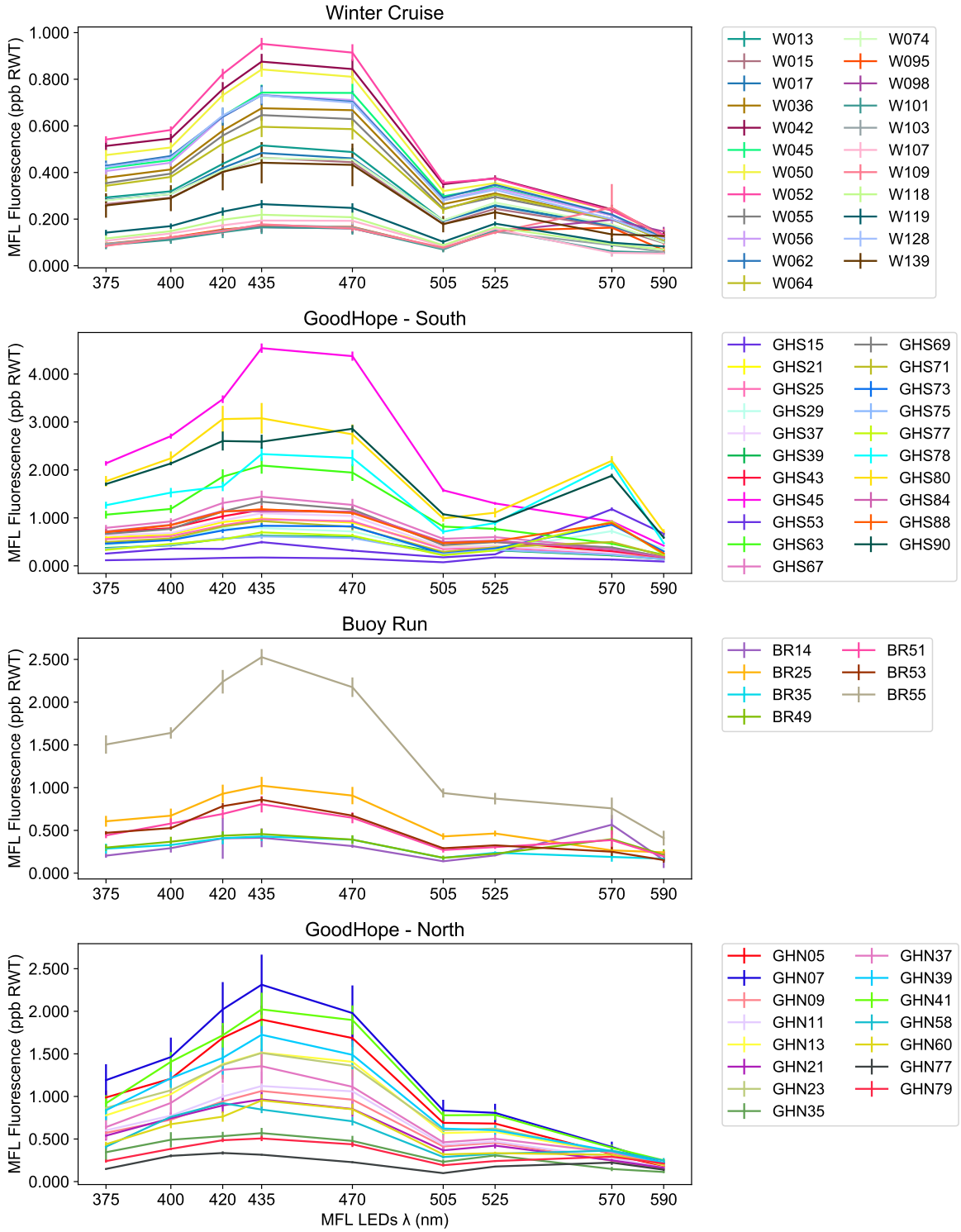

Figure 4.6: Raw MFL fluorescence measurements for all stations sampled. Note the difference in magnitude between plots.

4.2.2.3 Apparent fluorescence quantum yield of chl-*a*

Apparent $\Phi_F(\lambda)$ was derived for each of the MFL excitation wavelengths (Fig. 4.7), using wavelength-specific fluorescence, spectrally-averaged *in situ* a_{ph} measurements, and the MFL calibration coefficients obtained from the ATTO490LS dye calibration (Chapter 3).

Values of $\Phi_F(\lambda)$ ranged from the overall lowest station at GHS15 ($\Phi_F(435)$ = 0.006±0.0002, $\Phi_F(570)$ = 0.021±0.003) to the overall highest station at GHS80 ($\Phi_F(435)$ = 0.101±0.009, $\Phi_F(570)$ = 0.351±0.015). Both stations were sampled in the early summer, with GHS15 located in the STZ and GHS80 in the MIZ. The GoodHope-North leg, i.e. late summer, displayed the largest average $\Phi_F(\lambda)$ values ($\Phi_F(435)$ = 0.061±0.029, $\Phi_F(570)$ = 0.120±0.027), followed by the GoodHope-South leg (early summer, $\Phi_F(435)$ = 0.046±0.034, $\Phi_F(570)$ = 0.118±0.101), the Winter Cruise ($\Phi_F(435)$ = 0.033±0.017, $\Phi_F(570)$ = 0.077±0.026), and the Buoy Run (mid summer, $\Phi_F(435)$ = 0.021±0.017, $\Phi_F(570)$ = 0.039±0.020). The standard deviations were high for the average $\Phi_F(\lambda)$ per cruise leg, emphasising the high degree of variability between stations. All MFL-derived $\Phi_F(\lambda)$ measurements are listed in Appendix A.2.

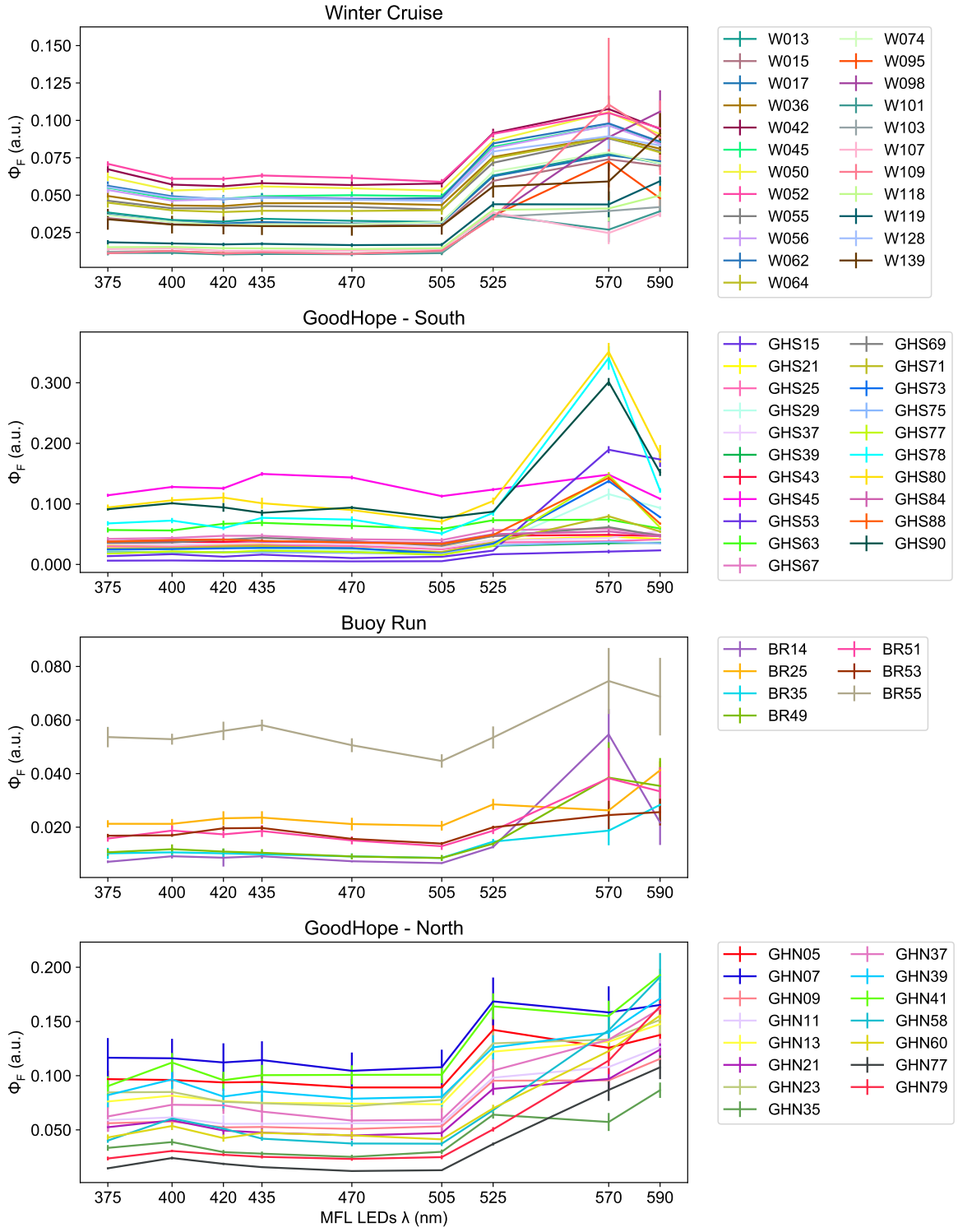

Figure 4.7: Wavelength-specific apparent fluorescence quantum yields ($\Phi_F(\lambda)$). Note the difference in magnitude between plots.

4.2.3 Statistical analysis of the drivers of $\Phi_F(\lambda)$ variability

4.2.3.1 K-means clustering $\Phi_F(\lambda)$ spectra

The variability in $\Phi_F(\lambda)$ spectral shape between individual stations required a more dynamic approach than grouping data according to cruise legs. Numerous background analyses were initially performed in an attempt to assign $\Phi_F(\lambda)$ spectra/ values into taxonomic-relevant groups (taxonomic/ size groups); further attempts were made to assign $\Phi_F(\lambda)$ spectra/ values to Southern Ocean zones (latitude), nutrient regimes (high vs. low silicate), light conditions (day vs. night), and season (summer vs. winter). However, no clear cluster assignments/ relationships were apparent; this may be improved by a larger study cohort. As such, k-means spectral clustering of all stations was employed (Section 2.7.1) to resolve the drivers of $\Phi_F(\lambda)$ variability. The mean spectral shapes of cluster 1-3 were similar (represented by the black dashed lines in Fig. 4.8), with the clusters being largely distinguishable by different orders of magnitude. This was separation by magnitude was further evidenced in the boxplot analysis (Fig. 4.9). The shape of the Φ_F spectra across all clusters was uniform for 375-505 nm, with the average ranging from 0.0 to 0.1, before increasing after 525 nm. The anomalous $\Phi_F(570)$ of cluster 4 (0.331 ± 0.026) was clearly apparent.

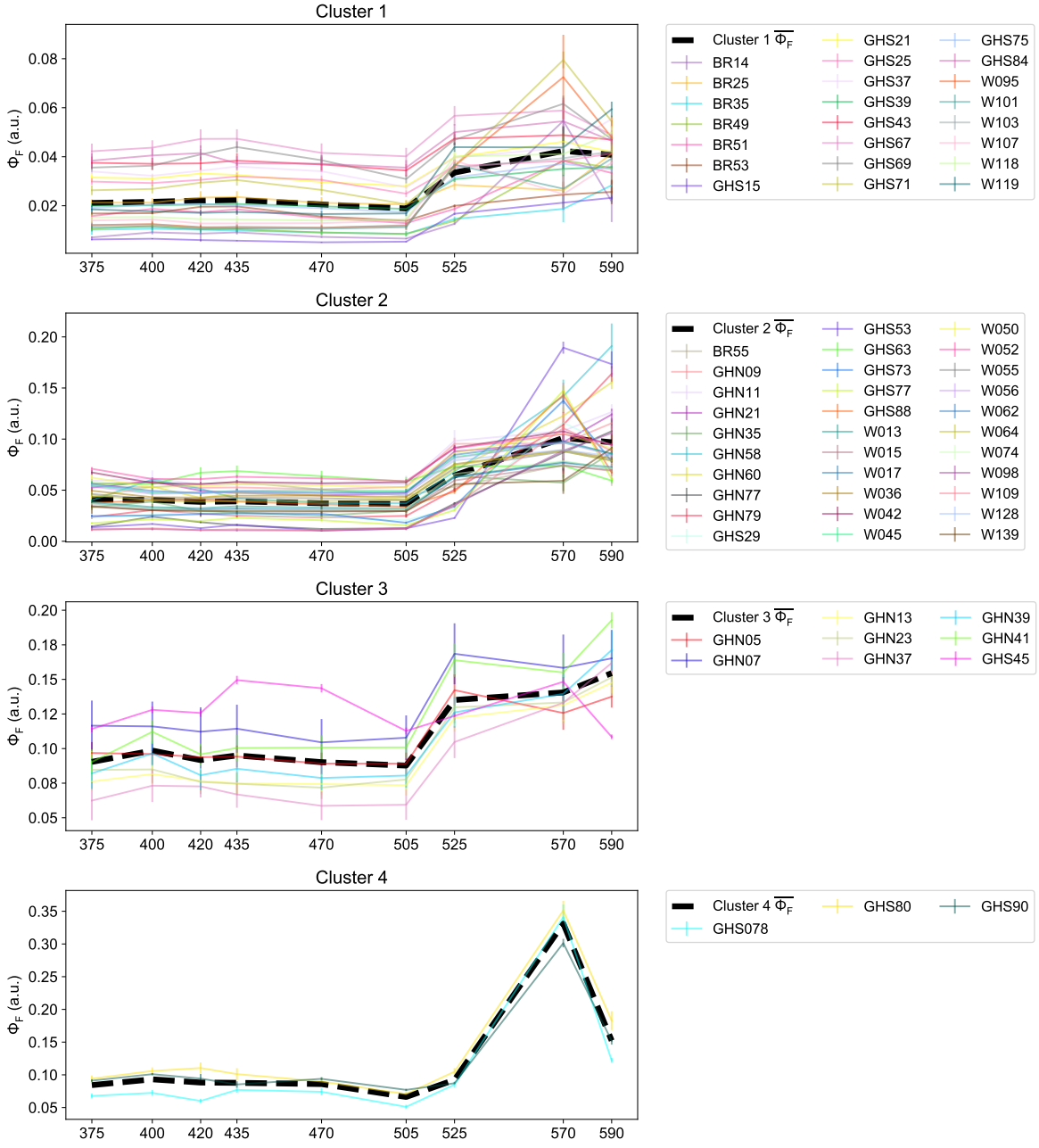

Figure 4.8: Wavelength-specific apparent fluorescence quantum yields $\Phi_F(\lambda)$. The black dashed lines represents the mean spectral shape for each cluster. Note the difference in magnitude between plots.

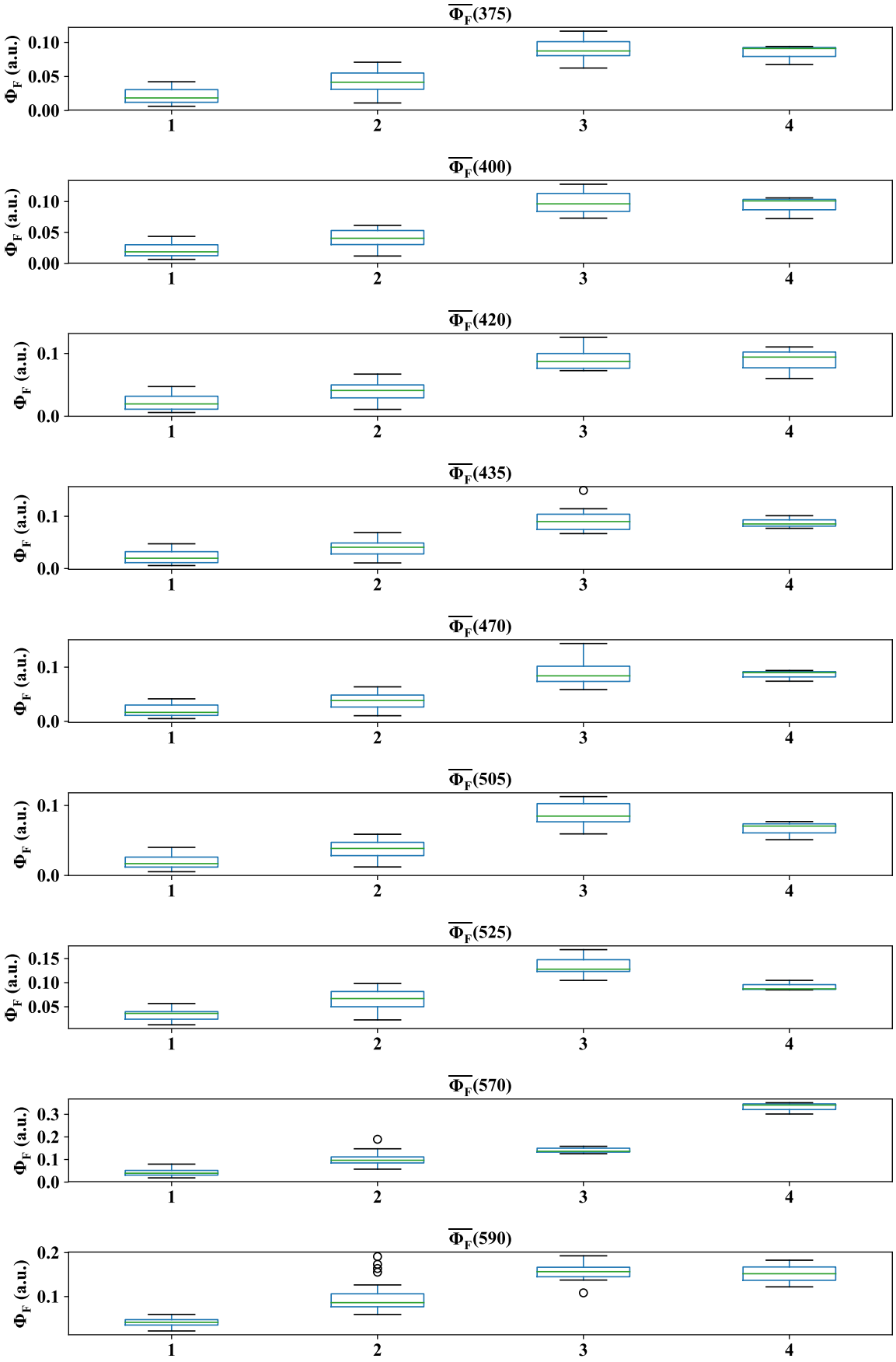

Figure 4.9: Cluster means of individual $\Phi_F(\lambda)$. Note the difference in magnitude between plots. Minimum outlier (5%), first quartile (Q1, 25%), median, third quartile (Q3, 75%), and maximum outlier (95%).

4.2.3.2 Boxplots of possible drivers of $\Phi_F(\lambda)$ variability

Inter-cluster boxplot analysis of the median values of potential drivers of variability are presented in Figs. 4.10, 4.11 and 4.12. Cluster 1 had the highest average macronutrient concentrations (NO_3^- = 21.68±14.34 μM, $Si(OH)_4$ = 27.27±30.80 μM), despite large intra-cluster variability. In addition, this cluster was dominated by microplankton (59.2±18.2%) and displayed the highest Dt/ Dd + Dt ratio out of all clusters (0.10±0.042). Cluster 2 was characterised by populations of mixed size (microplankton = 41.2±23.2%, nanoplankton = 42.7±12%, picoplankton = 16.3±15.6%), with an even distribution between phytoplankton type and taxonomic marker pigments. Cluster 3 had a large microplankton component (79.7±7.6%) dominated by diatoms (57.9±8.5%), corroborated with a high fucoxanthin content (0.5±0.1%). This cluster had the highest pool of photoprotective pigments (Dd + Dt) (0.2±0.02%). Cluster 4 was characterised by a high biomass (0.83±0.09 mg m^{-3}), microplankton dominated population (74±22.8%), with high fucoxanthin concentrations (0.51±0.14) and corresponding diatom levels (63.1±23.6%). This cluster showed a high degree of photoacclimation (Dd + Dt) (0.16±0.01), possibly to the high cumulative PAR over 12 h prior to the stations (0.357±0.038 mol m^{-2} s^{-1}).

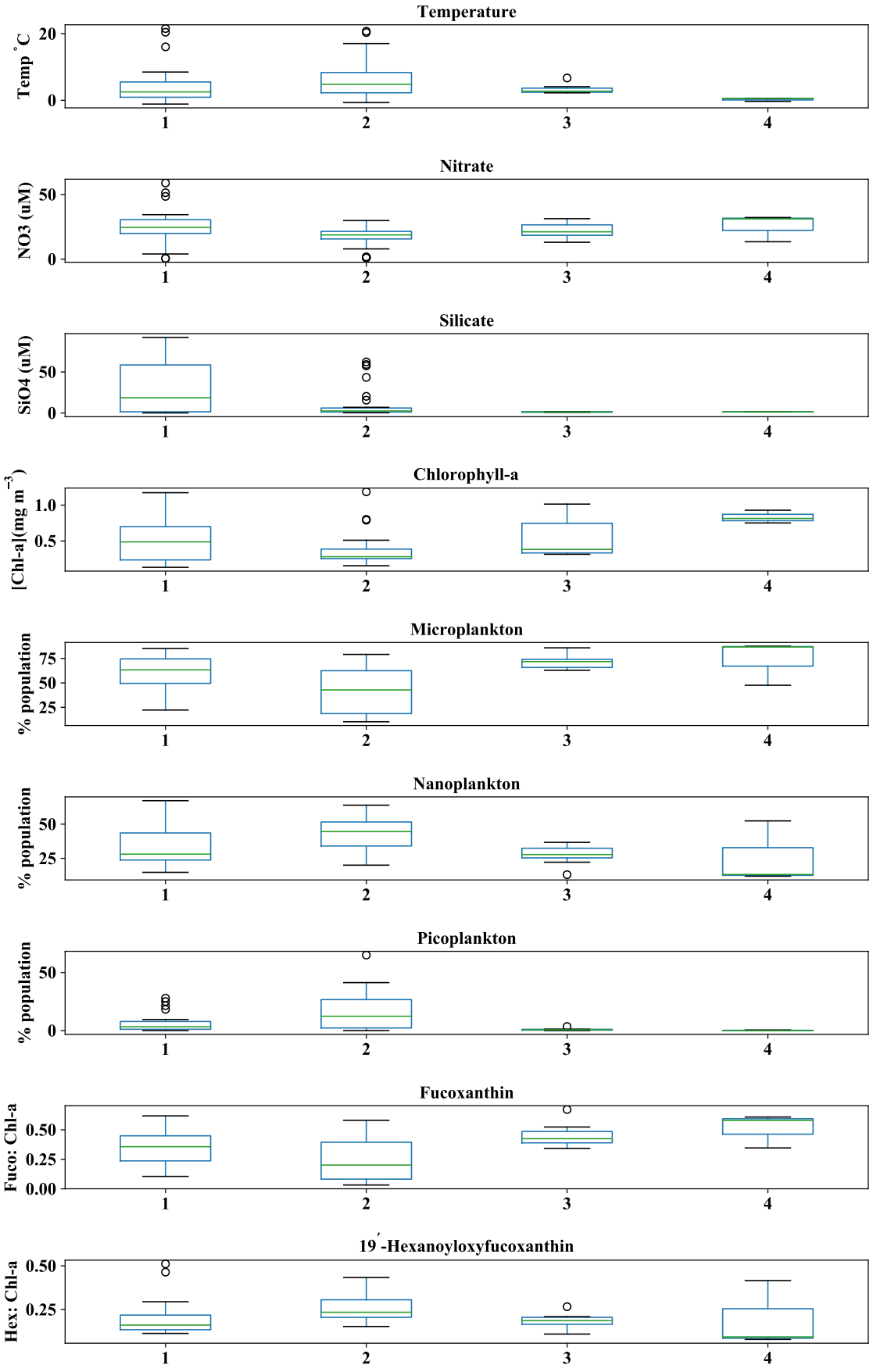

Figure 4.10: Boxplot analysis of the median values of possible environmental and taxonomy-related drivers of $\Phi_F(\lambda)$ variability. Minimum outlier (5%), first quartile (Q1, 25%), median, third quartile (Q3, 75%), and maximum outlier (95%).

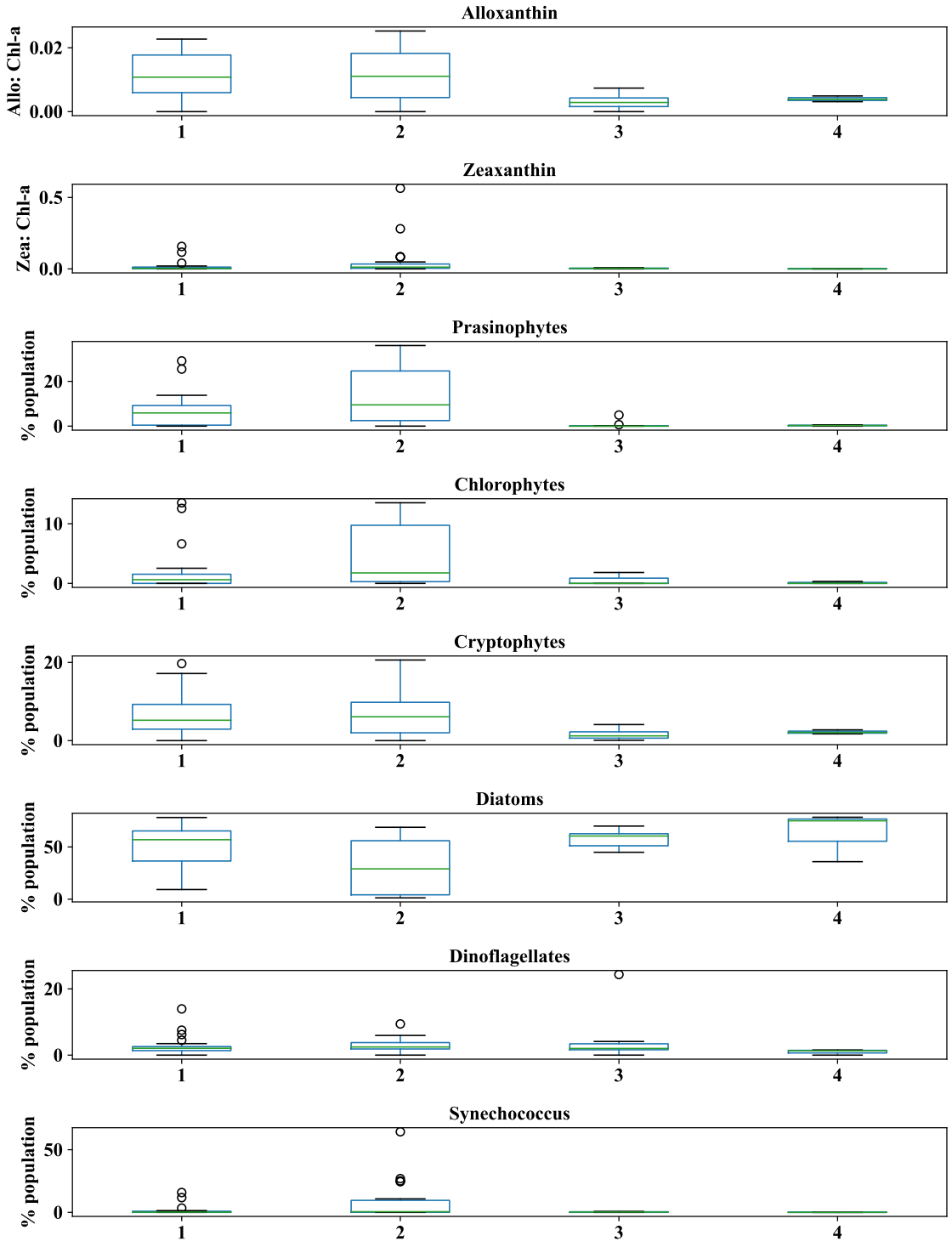

Figure 4.11: Boxplot analysis of the median values of possible taxonomy-related drivers of $\Phi_F(\lambda)$ variability. Minimum outlier (5%), first quartile (Q1, 25%), median, third quartile (Q3, 75%), and maximum outlier (95%).

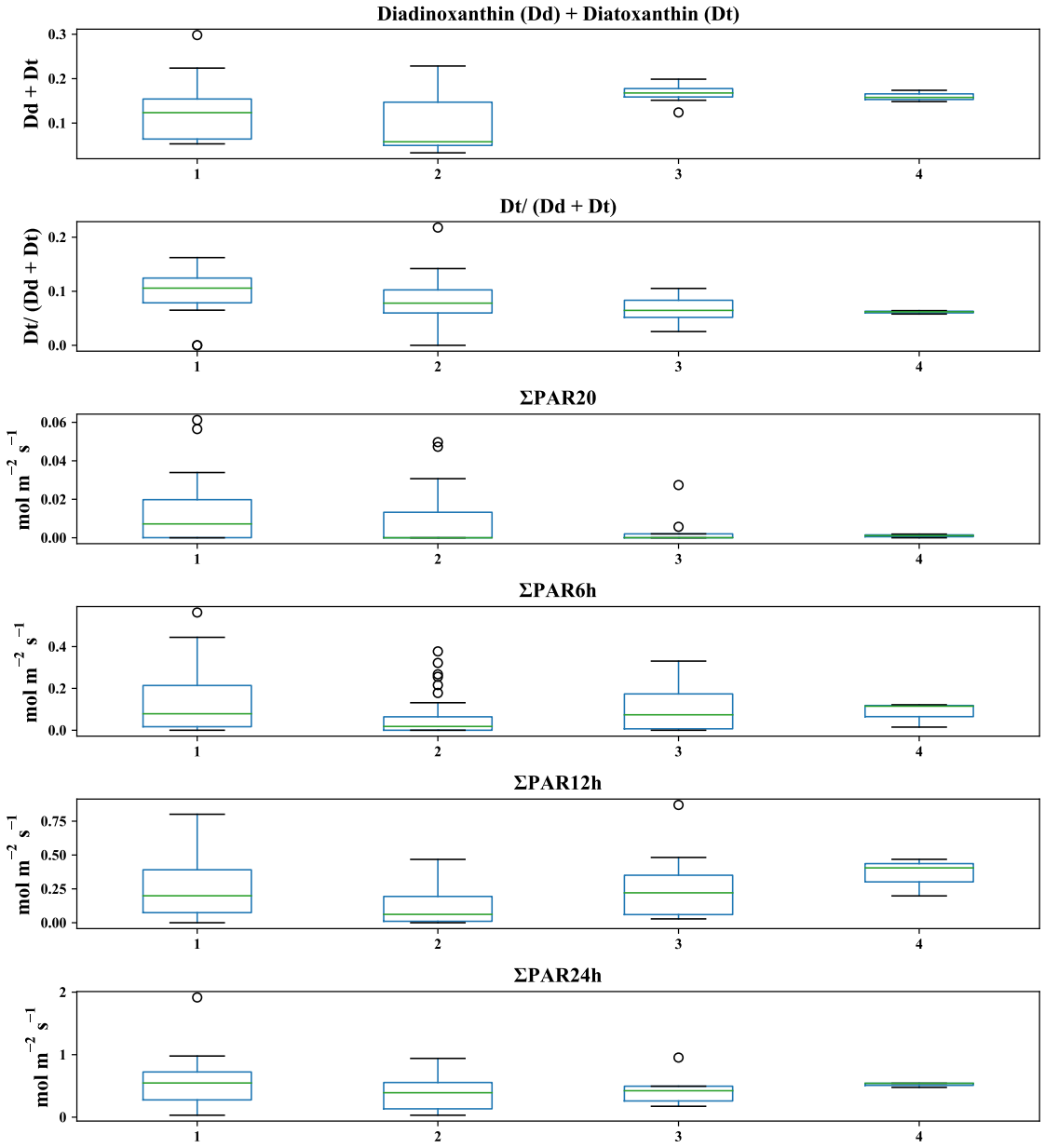

Figure 4.12: Boxplot analysis of the median values of possible light environment-related drivers of $\Phi_F(\lambda)$ variability. Minimum outlier (5%), first quartile (Q1, 25%), median, third quartile (Q3, 75%), and maximum outlier (95%).

4.2.3.3 Empirical orthogonal function analysis

Empirical orthogonal function (EOF) analysis was used to assess the variance of $\Phi_F(\lambda)$ spectral structure within the cluster datasets (Section 2.8). The first three modes of spectral variance were assessed. The significance of the Spearman's *rho* (r_s) values generated were evaluated using a Spearman Rank significance table (Ramsey, 1989), where the critical values were set at the 95% confidence level. EOF analysis was not performed

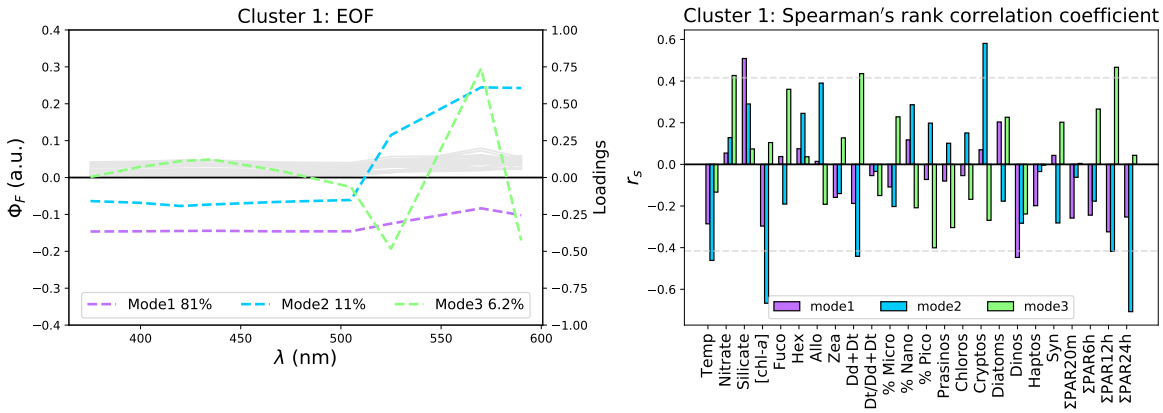

Figure 4.13: EOF analysis of $\Phi_F(\lambda)$ for cluster number 1 (n = 23). The grey $\Phi_F(\lambda)$ spectra plotted on the left are overlaid with the top three modes of the analysis. The correlation coefficients (Spearman's *rho* (r_s)), calculated between the EOF amplitude factors and a selection of possible drivers of $\Phi_F(\lambda)$ variability, are displayed on the right; The dashed, grey horizontal lines represent the 95% confidence level.

on cluster 4, due to the low sample number (n = 3) and limited statistical viability.

For cluster 1 (Fig. 4.13), where n = 23, the critical value was determined to be 0.416 (Ramsey, 1989). Mode 1 described 81% of the variance in the dataset, which appeared to be an amplitude effect, where silicate concentration had a significant positive relationship (r_s = 0.509, p < 0.05), and dinoflagellates (Dinos) a significant negative relationship (r_s = -0.447, p < 0.05). Mode 2 explained 11% of the variance in spectral shape, showing the spectral shift between the shorter and longer wavelengths, with significant negative drivers including temperature (Temp)(r_s = -0.461, p < 0.05), [chl-*a*] (r_s = -0.667, p < 0.05), the photoprotective pigments Dd + Dt (r_s = -0.442, p < 0.05), and the cumulative sum of PAR over 12 h and 24 h (ΣPAR12h and ΣPAR24h) (r_s = -0.418 and -0.708 respectively, p < 0.05). The presence of cryptophytes (Cryptos) was significantly positively related to mode 2 (r_s = 0.581, p < 0.05). Mode 3 accounted for 6.2% of the variance and explains the 570 to 525 and 590 ratio change, with significant positive drivers including nitrate (r_s = 0.427, p < 0.05), Dd + Dt (r_s = 0.436, p < 0.05), and ΣPAR12h (r_s = 0.466, p < 0.05).

For cluster 2 (Fig. 4.14), where n = 32, the critical value was determined to be 0.350. Mode 1 described 74% of the variance in the dataset, showing the spectral shift between the shorter and longer wavelengths; however, there were no significant drivers of the variance for this mode. Mode 2 accounted for 17% of the variance in spectral shape, reflecting the magnitude changes in the long wavelengths, with significant positive drivers including silicate (r_s = 0.471, p < 0.05), alloxanthin (Allo) (r_s = 0.592, p < 0.05), and cryptophytes (r_s = 0.597, p < 0.05). Significant negative drivers included 19'-

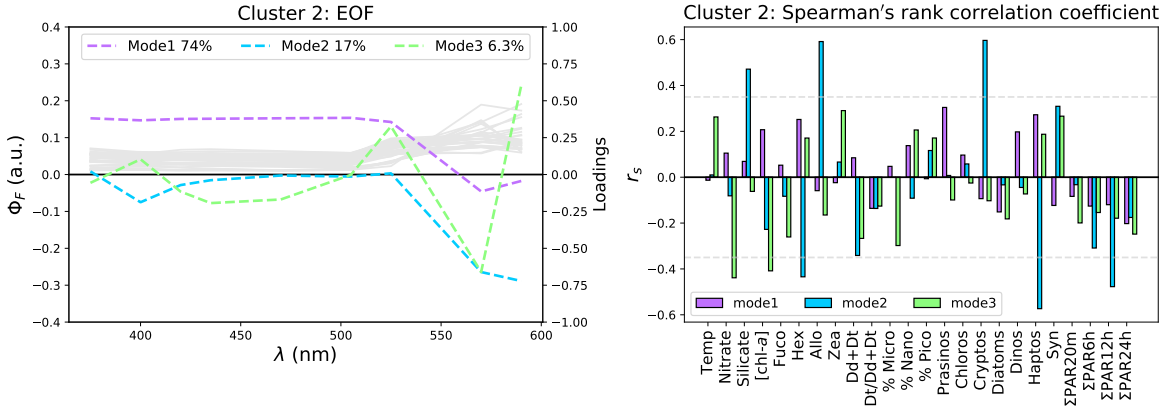

Figure 4.14: EOF analysis of $\Phi_F(\lambda)$ for cluster number 2 (n = 32). The grey $\Phi_F(\lambda)$ spectra plotted on the left are overlaid with the top three modes of the analysis. The correlation coefficients (Spearman's *rho* (r_s)), calculated between the EOF amplitude factors and a selection of possible drivers of $\Phi_F(\lambda)$ variability, are displayed on the right; The dashed, grey horizontal lines represent the 95% confidence level.

hexanoyloxyfucoxanthin (Hex) (r_s = -0.434, p < 0.05), haptophytes (Haptos) (r_s = -0.573, p < 0.05), and ΣPAR12h (r_s = -0.477, p < 0.05). Mode 3 described 6.3% of the spectral variance and explains the 570 to 525 and 590 ratio change, with nitrate (r_s = -0.439, p < 0.05) and [chl-*a*] (r_s = -0.408, p < 0.05) being significantly negatively correlated to the spectral shape.

For cluster 3 (Fig. 4.15), where n = 8, the critical value was set at 0.738. Mode 1 described 74% of the spectral variance in the dataset, with Allo (r_s = -0.743, p < 0.05) and Dt/ (Dd + Dt) (r_s = -0.881, p < 0.05) being significantly negatively correlated. Mode 2 explained 20% of the variance in spectral shape, with ΣPAR6h (r_s = 0.738, p < 0.05) being significantly positively related. Mode 3 accounted for 4.7% of the variance in the spectral shape, with significant positive relationships to Hex (r_s = 0.762, p < 0.05) and to *Synechococcus* (Syn) (r_s = 0.756, p < 0.05), and significant negative relationships to silicate (r_s = -0.833, p < 0.05), Cryptos (r_s = -0.786, p < 0.05), and ΣPAR24h (r_s = -0.905, p < 0.05). The shape of Mode 1 is driven by the changes in amplitude at wavelengths < 525 nm, while Mode 2 is related to changes in magnitude > 525 nm, and Mode 3 once again describes the 570 to 525 and 590 ratio change.

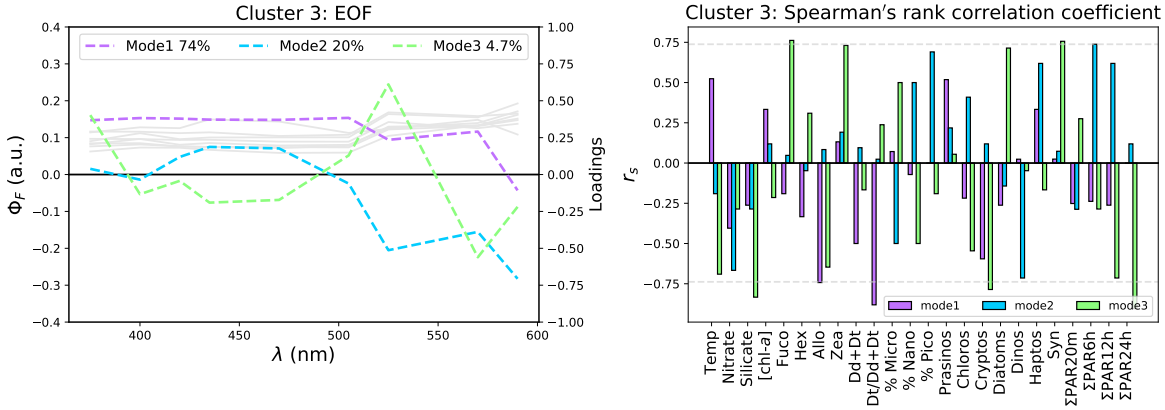

Figure 4.15: EOF analysis of $\Phi_F(\lambda)$ for cluster number 3 (n = 8). The grey $\Phi_F(\lambda)$ spectra plotted on the left are overlaid with the top three modes of the analysis. The correlation coefficients (Spearman's *rho* (r_s)), calculated between the EOF amplitude factors and a selection of possible drivers of $\Phi_F(\lambda)$ variability, are displayed on the right; The dashed, grey horizontal lines represent the 95% confidence level.

4.2.3.4 Correlation matrices of clustered $\Phi_F(\lambda)$ and drivers of variability

From Fig. 4.8, it was apparent the Φ_F values obtained from LEDs 375-505 nm were fairly constrained, whereas Φ_F values of 525-590 nm showed greater variability. For the majority of stations, the fluorescence emission peaked at 435 nm, with a small fraction of stations displaying 570 nm peaks (Fig. 4.6). The 435 nm fluorescence peak is likely due to the maximum a_{ph} absorption at 435 nm (Fig. 4.5). For correlation matrix analyses, $\Phi_F(435)$ was selected as a suitable representative of the MFL 375-505 nm LEDs, and $\Phi_F(570)$ as a representative of the 525-590 nm LEDs. In addition, $\Phi_F(435)$ will be used for future remote sensing application (Chapter 5). The mean $\Phi_F(435)$ and $\Phi_F(570)$ values for each cluster are listed in Table 4.1.

Table 4.1: Mean $\Phi_F(435)$ and $\Phi_F(570)$ values for all cluster numbers.

Cluster No.	Mean $\Phi_F(435)$	Mean $\Phi_F(570)$
1	0.022±0.012	0.042±0.016
2	0.039±0.015	0.101±0.028
3	0.095±0.027	0.141±0.012
4	0.088±0.012	0.331±0.026

The data were determined to be non-normally distributed, as confirmed by the Shapiro-Wilk test of normality. As such, the nonparametric approach of Spearman's *rho* (r_s) was used for statistical analysis. A Spearman's rank correlation matrix was calculated for $\Phi_F(435)$ and $\Phi_F(570)$, against possible drivers of Φ_F variability. Twenty-four potential drivers of Φ_F variability were selected, the same as those examined in Section

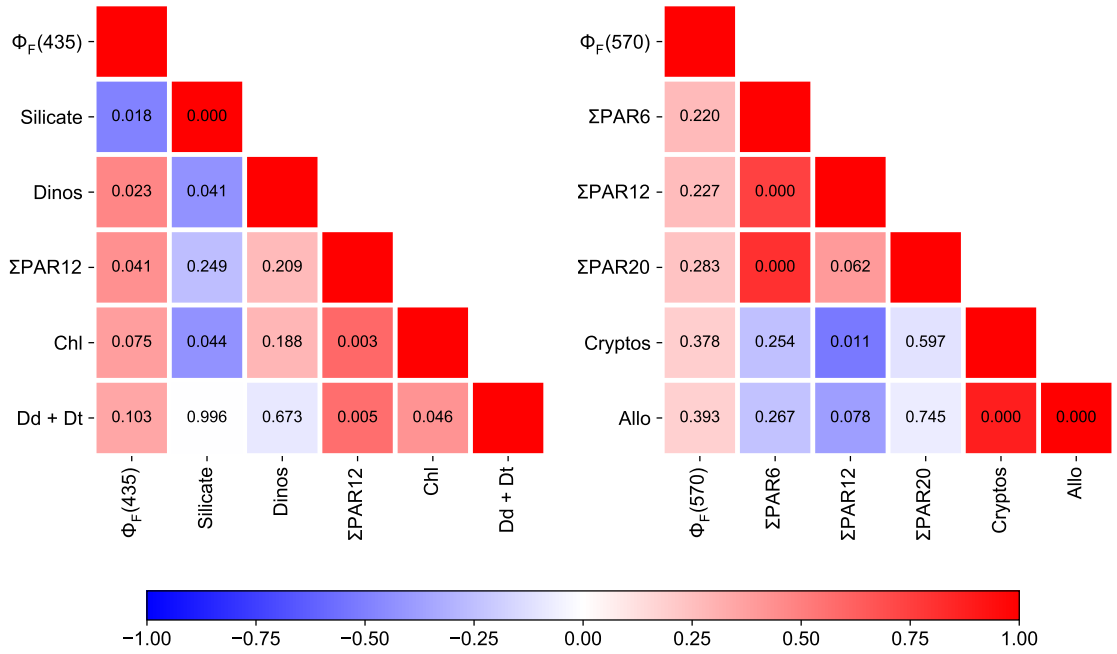

Figure 4.16: Spearman's correlation matrix of $\Phi_F(435)$ (left) and $\Phi_F(570)$ (right) versus potential drivers of variability, for cluster 1. The matrices display the five drivers of variability that exhibit the highest correlation to $\Phi_F(435)$ and to $\Phi_F(570)$. Dinos- dinoflagellates, Cryptos- cryptophytes, Allo- alloxanthin, Chl- chl-*a* concentration, ΣPAR20/ 6/ 12 (20 min/ 6 h/ 12 h)- cumulative sum of photosynthetically available radiation for the time period stipulated prior to the station, Dd + Dt- sum of photoprotective pigments Dd and Dt. Colours of the blocks represent negative and positive r_s values, with the p-values for each variable listed within.

4.2.3.3. The matrices presented are representative of the top five drivers of variability that exhibited the lowest p-values (Figs. 4.16, 4.17, and 4.18). Figure 4.16 shows the correlation matrices of cluster 1, $\Phi_F(435)$ and $\Phi_F(570)$ against possible drivers of Φ_F variability. From this plot it is apparent that silicate (p = 0.018) was significantly negatively correlated to $\Phi_F(435)$ variability, with dinoflagellates (p = 0.023) and ΣPAR12h (p = 0.041) being significantly positively correlated. There were no statistically significant correlations for $\Phi_F(570)$ in this cluster. The output from cluster 2 is shown in Fig. 4.17. The only significantly correlated driver of $\Phi_F(435)$ variability was the presence of prasinophytes (p = 0.043). Alloxanthin (p = 0.038), Dd + Dt (p = 0.033), cryptophytes (p = 0.034), haptophytes (p = 0.053), *Synechococcus* (p = 0.033), ΣPAR6h (p = 0.030), and ΣPAR12h (p = 0.002) were all significantly correlated to $\Phi_F(570)$ signal. The cluster 3 matrix is displayed in Fig. 4.18. In this cluster, significantly correlated drivers of signal variability for $\Phi_F(435)$ included alloxanthin (p = 0.045) and the Dt/ Dd + Dt ratio (p = 0.002), with no significantly correlated drivers of $\Phi_F(570)$ observed.

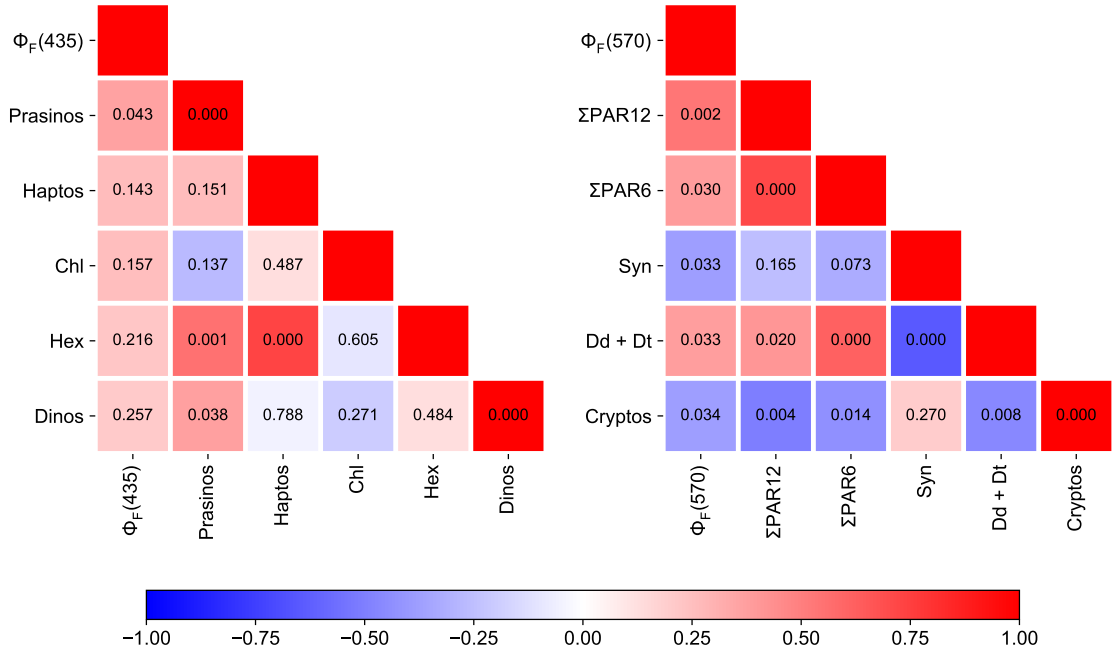

Figure 4.17: Spearman's correlation matrix of $\Phi_F(435)$ (left) and $\Phi_F(570)$ (right) versus potential drivers of variability, for cluster 2. The matrices display the five drivers of variability that exhibit the highest correlation to $\Phi_F(435)$ and to $\Phi_F(570)$. Prasinos- prasinophytes, Haptos- haptophytes, Dinos- dinoflagellates, Cryptos- cryptophytes, Syn- *Synechococcus*, Hex- 19' hexanoyloxyfucoxanthin, Chl- chl-*a* concentration, ΣPAR6/ 12 (6/ 12 h) - cumulative sum of photosynthetically available radiation for the time period stipulated prior to the station, Dd + Dt- sum of photoprotective pigments Dd and Dt. Colours of the blocks represent negative and positive r_s values, with the p-values for each variable listed within.

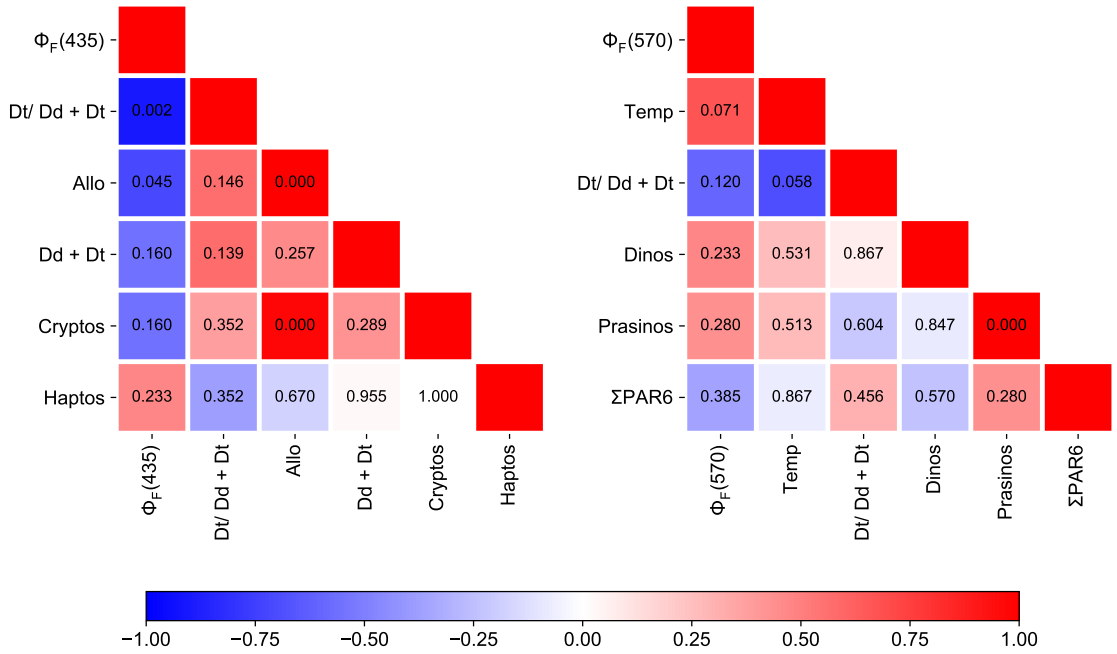

Figure 4.18: Spearman's correlation matrix of $\Phi_F(435)$ (left) and $\Phi_F(570)$ (right) versus potential drivers of variability, for cluster 3. The matrices display the five drivers of variability that exhibit the highest correlation to $\Phi_F(435)$ and to $\Phi_F(570)$. Cryptos- cryptophytes, Haptos- haptophytes, Dinos- dinoflagellates, Prasinos- prasinophytes, Allo- alloxanthin, Temp- temperature, ΣPAR6h- cumulative sum of photosynthetically available radiation over 6 h prior to the station, Dd + Dt- sum of photoprotective pigments Dd and Dt, Dt/ Dd + Dt- ratio of Dt to the sum of Dd and Dt. Colours of the blocks represent negative and positive r_s values, with the p-values for each variable listed within.

4.3 Discussion

4.3.1 Interpretation of MFL-fluorescence spectral shape

Chlorophyll-*a* absorbs maximally in the blue Soret bands, resulting in peak fluorescence emission, subject to other de-excitation pathways (Huot and Babin, 2010; Muller et al., 2001). This is apparent for the MFL fluorescence at 435 nm, where the maximum peaks are observed (Fig. 4.6). Fluorescence values for the Winter Cruise are notably lower than those of the summer stations (Fig. 4.6), a likely effect of the low [chl-*a*] conditions that exist in the Southern Ocean during the winter months (Thomalla et al., 2011). This is due to phytoplankton growth being primarily limited by light during this time of the year (Boyd et al., 1999), as a result of low solar zenith angle and deep mixed layers. The majority of stations sampled on the Buoy Run are also of lower magnitude than the other summer stations (Fig. 4.6). All Buoy Run $\Phi_F(\lambda)$ spectra, apart from BR55, were separated out into cluster 1 (Fig. 4.8), which was representative of microplankton dominance (59.2±18.2%) and high amounts of Dt/ Dd + Dt (0.10±0.042). As such, the low fluorescence values for this cruise leg are likely due to qN, specifically the XC, which is present in local microplankton species such as diatoms (Alderkamp et al., 2013).

Throughout this study, the occurrence of fluorescence peaks at 570 nm is more challenging to understand. Below are a number proposed possible explanations:

[1] The increased gain settings of the MFL 570 nm LEDs. The instrument gain settings at this wavelength are enhanced to account for low absorption in the green-orange region, where absorption by phytoplankton is minimal (Mitchell and Kiefer, 1988a). In addition to having heightened sensitivity, this is the only LED to exist in triplicate (Fig. 3.1). Furthermore, the MFL 570 nm LEDs are incredibly sensitive to noise relative to the other wavebands (Fig. 3.3), which is problematic when the phytoplankton signal is low.

[2] Fluorescence contamination by the Raman scattering of water. Raman scattering, which displays peak excitation at 550 nm, should be considered when quantifying chl-*a* fluorescence (Maritorena et al., 2000; Morrison, 2003). Scattering of light, both elastic and inelastic, is responsible for redirecting incident photons into the upwelling light stream (Mobley, 1994). Elastic scattering reflects ambient solar radiation, whereas inelastic scattering involves a shift in wavelength and includes chl-*a* fluorescence and Raman scattering by water. To obtain the upwelling radiance from fluorescence, it is necessary to quantify the amount of elastic scattering of ambient solar radiation and inelastic Raman scattering, so these may be subtracted from the total upwelling radiance. Excitation wavelengths of importance to scattering to the range of chl-*a* fluorescence lie between 510 and 600 nm; in this study, as Raman scattering was not accounted for, it is possible that fluorescence in

the 525-590 nm range is overestimated by the MFL. Anomalously high chl-*a* fluorescence will be propagated to Φ_F, leading to an exaggeration of signal.

[3] The presence of phycobiliprotein-containing cyanobacteria (Yoshida et al., 2011) or cryptophytes (Doust et al., 2004, 2006). Cyanobacteria, including *Synechococcus* (Gibberd et al., 2013), and cryptophytes (Garibotti et al., 2005; Mendes et al., 2013), are known to occupy various Southern Ocean provinces throughout the year. Phycoerythrin absorbs strongly in the green-orange part of the spectrum (Ting et al., 2002), which would lead to subsequent increase in Φ_F at these wavelengths.

4.3.2 MFL-Derived $\Phi_F(\lambda)$

Whilst phytoplankton absorption and fluorescence provide insight into photophysiology and the surrounding light levels, they paint a far greater picture when investigated as Φ_F, which serves as an important ecological proxy for various environmental conditions. While the use of SICF in the derivation of Φ_{sat} is fairly well established (for example, Behrenfeld et al. (2009); Browning et al. (2014a); Huot et al. (2005)), *in situ* studies remain limited globally. This may in part be due to a lack of dedicated instrumentation and/ or the requirement of multiple instruments to accurately record the incident and return light levels in the field. In this study, the PAR values used to determine $\Phi_F(\lambda)$ represent the spectral bandwidth of the individual excitation LEDs on the MFL. While this adds a layer of complexity when interpreting the output, wavelength specific-Φ_F provides a more detailed overview on the fate of absorbed photons. $\Phi_F(435)$ and $\Phi_F(570)$ were selected as the representative wavelengths for investigation during this study, representing the effects of both blue and green-orange stimulating radiation.

Summer stations as a collective displayed a higher average $\Phi_F(435)$ and $\Phi_F(570)$ than winter stations; summer $\Phi_F(435) = 0.047\pm0.032$ and $\Phi_F(570) = 0.110\pm0.078$, and winter $\Phi_F(435) = 0.033\pm0.017$ and $\Phi_F(570) = 0.077\pm0.026$. The lower $\Phi_F(\lambda)$ estimates quantified in winter are possibly due to the low ambient light levels leading phytoplankton to direct all available light energy to photosynthesis, i.e. qP is reducing the $\Phi_F(\lambda)$ signal. As the stations sampled in the summer months are unlikely to be light limited, the higher $\Phi_F(\lambda)$ may be due to photoinhibition, or indicative of Fe-limitation (Behrenfeld et al., 2009; Browning et al., 2014b); 40% of summer stations in NO_3^--replete waters (> 10 μM) had a relatively low biomass (< 0.5 mg.m^{-3}), suggesting potential Fe-limitation (all [NO_3^-] and [chl-*a*] values are listed in Appendix B.1).

While the majority of stations fall within an acceptable range of published Φ_F values (approximately 0.001 to 0.15 (Table 1.3)), the outliers may be a result of a particular

environmental cue, a sampling artefact or a combination of both. It is apparent, regardless of season, that $\Phi_F(570)$ is substantially larger than $\Phi_F(435)$, with a greater standard deviation ($\Phi_F(570) = 0.096 \pm 0.066$, $\Phi_F(435) = 0.042 \pm 0.029$). This is likely due to a combination of reasons discussed in Section 4.3.1. A similar study by Ostrowska (2011) showed a relatable result, using a BBE Moldaenke FluoroProbe multi-excitation fluorometer to derive $\Phi_F(\lambda)$ from 5 different excitation LEDs. While they did not radiometrically characterise the multi-excitation fluorometer, there was a similar increase in $\Phi_F(\lambda)$ from 470-610 nm.

4.3.3 Variability in $\Phi_F(\lambda)$ spectral shape: Cluster analysis

This is the first study investigating *in situ*, wavelength-specific $\Phi_F(\lambda)$ variability. All derived $\Phi_F(\lambda)$ spectra were subjected to k-means clustering, statistically separating data into clusters to assist in the investigation of potential drivers of variability.

Cluster 1 comprises 23 stations from the GHS, BR, and the Winter Cruise (Fig. 4.8). This cluster encompasses a range of seasons and regions, including the GoodHope Line and regions south of South Georgia and the Prince Edward Islands. Across all statistical analyses, $Si(OH)_4$, dinoflagellate populations, and ΣPAR12h appeared to be significant influencers of the $\Phi_F(\lambda)$ spectral shape (Fig. 4.13), as well as the $\Phi_F(435)$ signal (Fig. 4.16). Boxplot analysis of cluster 1 visually corroborates the importance of $Si(OH)_4$ within this cluster (Fig. 4.10), which has an expected inverse relationship to $\Phi_F(\lambda)$ spectral shape (Fig. 4.13), as well as $\Phi_F(435)$ (Fig. 4.16). While the macronutrient $Si(OH)_4$ is not considered essential to all phytoplankton (Redfield, 1934), it is fundamental for the growth of diatoms (Martin-Jézéquel et al., 2000). Silicate levels can be used to infer diatom abundance in specific Southern Ocean provinces, with concentrations closely linked to natural assemblage composition (de Salas et al., 2011; Salter et al., 2007). As such, any relationship derived between $Si(OH)_4$ and Φ_F is likely to be representative of the underlying community structure rather than physiology. High $[Si(OH)_4]$ may be indicative of large diatom cells, which would exhibit a low Φ_F due to pigment packaging. However, the same can be said for low $[Si(OH)_4]$, having been recently consumed by large diatoms, and soon to be surpassed by another community with little to no $Si(OH)_4$ demand. Ultimately, Φ_F is not a good proxy for $[Si(OH)_4]$. An interplay between micro and nanoplankton occurred across all stations, with populations of picoplankton present in the STZ and two winter stations (W118 and W119). The latter two stations lie to the south-west of the Prince Edward Islands, a region identified as having low [chl-*a*] and a large picoplankton component during the austral autumn (Pakhomov and Froneman,

1999; Perissinotto et al., 2000). The mixed sized classes of the stations within this cluster make it difficult to interpret the influence of taxonomy on $\Phi_F(\lambda)$ spectral shape. Whilst dinoflagellates have been shown to be positively significantly correlated to $\Phi_F(435)$, their abundance remained fairly low throughout all stations, with an average of 2.3±1.8% (excluding GHS37 which was 14%) (Fig. 4.3). Boxplot analysis showed that the Dt/ Dd + Dt ratio was the highest for cluster 1 relative to other clusters (Fig. 4.12), which would indicate a high level of qN resulting in a reduced Φ_F. This may, in part, explain why this cluster has the lowest Φ_F values relative to the other clusters.

Cluster 2 comprises 32 stations from both summer and winter (Fig. 4.8). The segregation of $\Phi_F(\lambda)$ spectra into cluster 2 appeared to be based upon the mixed phytoplankton assemblage that dominates the dataset. While mode 1 in the EOF analysis failed to yield any significant drivers of spectral shape, mode 2, accounting for 17% of the variance, was significantly influenced by $Si(OH)_4$, alloxanthin, 19-hex, cryptophytes, haptophytes, and ΣPAR12h (Fig. 4.14). The Spearman's rank correlation matrix identified prasinophytes as being significantly positively correlated to $\Phi_F(435)$, along with ΣPAR12h, ΣPAR6h, and Dd + Dt, and Syn and Cryptos being significantly negatively correlated to $\Phi_F(570)$ (Fig. 4.17). Boxplot analysis of cluster 2 further highlights the probability of this cluster having a highly mixed population assemblage, as evidenced by size class, pigment concentrations and species composition means (Figs. 4.10, 4.11 and 4.12). Silicate concentrations were low for all GHS, GHN, and Winter Cruise (north of the PF) stations (2.02±1.39 μM), whilst stations south of the SBdy were considered $Si(OH)_4$-replete (54.35±8.34 μM). This region north of PF is known for being periodically $Si(OH)_4$ limited, allowing smaller phytoplankton species to propagate (de Salas et al., 2011). Stations in both cluster 1 and cluster 2 have mixed assemblages, variable $Si(OH)_4$ concentrations, and are correlated to ΣPAR12. One distinguishing feature between these two clusters is the larger picoplankton component present in cluster 2 (16.3±15.6%, versus 6.9±8.3% for cluster 1), which includes small prasinophytes (13.8±13.6%). These smaller cells would exhibit a greater Φ_F than a population comprised of larger species, which is apparent when comparing the magnitude of cluster 1 Φ_F to that of cluster 2 (Fig. 4.8).

Cluster 3 has a limited number of stations (n = 8) and is composed almost entirely of GHN stations, apart from GHS45 (Fig. 4.8). Boxplot analysis revealed that stations in cluster 3 are exposed to moderate light levels (ΣPAR6h and ΣPAR12h), and may be photoacclimated to their surrounding environment based on the fairly high Dd + Dt value (Fig. 4.11). Some studies have reported a greater qN capacity in high-light acclimated cells, which typically involves an increase in the Dd and Dt pool size (Ragni et al., 2008; van de Poll et al., 2006). While stations in cluster 3 appear to be high-light acclimated,

it is unlikely they are experiencing qN. Upon exposure to increased light, Dd is rapidly de-epoxidised to Dt on the timescale of seconds to minutes, and it is Dt that is believed to have the fluorescence quenching effect (Olaizola et al., 1994). Boxplot analysis revealed a small amount of Dt/ Dd + Dt relative to other the clusters (Fig. 4.11), indicating that qN is possibly acting at a low level. However, the correlation matrix showed Dt/ Dd + Dt to be significantly positively correlated to $\Phi_F(435)$ ($p = 0.043$, Fig. 4.18). This result is doubtful, and the small sample size of this cluster, together with the rapid timescale of the XC and the feasibility of accurately capturing the individual pigment components *in situ* must be considered. Mode 1 of the EOF analysis, accounting for 74% of the $\Phi_F(\lambda)$ spectral variance, has a significantly inverse correlation to alloxanthin and Dt/ Dd + Dt (r_s = -0.743 and -0.881 respectively, $p < 0.05$, Fig. 4.15), i.e. a low concentration of photoprotective pigments would result in an increase in Φ_F. This relationship has been reported previously (Maritorena et al., 2000; Morrison, 2003). In addition to the fairly low amount of Dt/ Dd + Dt, boxplot analysis revealed that the mean alloxanthin concentration was the lowest across all clusters (0.003±0.003, Fig. 4.11). The low concentration of alloxanthin and Dt suggests a low activity of qN, which may, in part, be the reason for the high magnitude of $\Phi_F(\lambda)$ in this cluster.

Cluster 4 comprises three GHS stations with anomalous $\Phi_F(570)$ values of 0.331±0.026 (Fig. 4.8). No statistical analyses were performed on this cluster due to the small sample size, and as such only relative relationships derived from boxplot analysis are reported. While a Φ_F of approximately 35% has never been reported, the result should be investigated regardless, as all data used for these three stations underwent strict quality control and were deemed to be acceptable. Trends in boxplot analysis (Figs. 4.10, 4.11, and 4.12) reveal that cluster 4 is characterised, relative to the other three clusters, by a high biomass (0.83±0.09 mg m^{-3}), largely microplankton dominated population (74±22.8%), with high fucoxanthin concentrations (0.51±0.14) and corresponding diatom levels (63.1±23.6%). This cluster shows a high degree of photoacclimation (Dd + Dt) (0.16±0.01), possibly due to the high ΣPAR12h (0.357±0.038 mol m^{-2} s^{-1}). For all three stations, while the Φ_F(375- 525) portion of the spectra are relatively low compared to the high $\Phi_F(570)$, they still average a substantial Φ_F(375-525) of 0.085±0.010. The overall high $\Phi_F(\lambda)$ response is likely a result of a large seasonal bloom of photoadapted phytoplankton. It would seem that the bloom event at the position of the SBdy front (GHS78 and GHS80) was separate to that of GHS90, which was positioned in the southern MIZ (Fig. 2.12). GHS78 and GHS80 are dominated by microplankton (87.2±0.5%), specifically diatoms (76.7±2.4%), while GHS90 is located in the MIZ and dominated by nanoplankton (52.4%), likely haptophytes (62.1%), specifically *Phaeocystis* (Arrigo, 1999; Arrigo et al., 2000; Arrigo and

McClain, 1994). There is a clear absence of PE-containing cryptophytes or *Synechococcus* at all three stations, which could partially explain the high $\Phi_F(570)$ values. This community structure is typical of the diatom/ *P. antarctica* ice-edge interplay that occurs during the austral summer (Alderkamp et al., 2013; Arrigo, 1999; Arrigo et al., 2010). All three stations exhibit near-identical spectral shapes (Fig. 4.8), hinting at the likelihood of the $\Phi_F(\lambda)$ being controlled by a similar feature. These stations would have been grouped into cluster 3 had it not been for the outlier $\Phi_F(570)$ values (Fig. B.1). Boxplot analysis shows a similar, fairly low amount of Dt/ Dd + Dt to that of cluster 3. This would imply at low levels of qN and higher $\Phi_F(\lambda)$, barring other electron dissipation pathways. Boyd et al. (2001) reported stations south of 54°S to be Fe/ light co-limited in the early summer, which would contribute to the high $\Phi_F(\lambda)$. The community composition, bloom progression and high $\Phi_F(\lambda)$ values obtained in this region are likely due to an interplay between sea ice, light and nutrient conditions. However, this is still not reason enough to explain the exorbitant $\Phi_F(570)$ values specifically, which are likely a result of a combination of the factors described above, as well as those in Section 4.3.1. If the sample number were higher for this cluster, the reason for the high $\Phi_F(570)$ would likely be more apparent, highlighting the benefits of increased sampling resolution for improved understanding of the drivers of Φ_F variability, not just in this study but on a global scale.

It is apparent that the drivers of both spectral and discrete $\Phi_F(\lambda)$ variability are extensive. A larger overall dataset would potentially provide more reliable insight and allow for more definitive conclusions to be made; a broad-brush summary of the main drivers of cluster assignment are listed in Table 4.2.

Table 4.2: The drivers of cluster assignment

Cluster No.	Dominant driver
1	Silicate
2	Mixed species composition
3	Light and qE
4	High biomass and large microplankton

4.4 Conclusion and future recommendations

Application of the MFL-calibration (Chapter 3) to *in situ* data has allowed for the derivation of wavelength-specific $\Phi_F(\lambda)$. This is the first time such a calibration has been performed, and subsequently applied to *in situ* samples.

Absorption and MFL fluorescence measurements underwent extensive quality control to limit the propagation of errors when deriving $\Phi_F(\lambda)$. The result was 66 *in situ* mea-

surements, obtained from the Atlantic sector of the Southern Ocean over the austral winter of 2012 and austral summer of 2013/ 2014. Statistically clustering the wavelength-specific $\Phi_F(\lambda)$ spectra was considered a strong starting point for identification of drivers of spectral variability. $\Phi_F(\lambda)$ spectra provided high resolution detail of the phytoplankton response to different excitation wavelengths. While $\Phi_F(570)$ was anticipated to provide new insight into the photosynthetic efficiency of populations comprising PE-containing cryptophytes and cyanobacteria, this waveband was fraught with background noise and possible Raman scattering contamination, masking any potential species-specific signal.

The effect of light levels and fluorescence quenching on $\Phi_F(\lambda)$ were distinguishable between clusters, with high light exposure being related to a reduced $\Phi_F(\lambda)$ due to qN, depending on the photoacclimation state of the resident phytoplankton population. Reduced $\Phi_F(\lambda)$ under moderate to low light levels may be indicative of qP, where all available photons are devoted to photochemistry. The possibility of constraining the effects of fluorescence quenching to extract information of additional physiological drivers, e.g. Fe availability, is complicated by the fact that there is no accurate way to account for the photoacclimation state of the local phytoplankton, without drastically narrowing the spatial and temporal range of sampling.

While $\Phi_F(\lambda)$ is not considered a good proxy for macronutrient limitation, the relationship between $\Phi_F(\lambda)$ and $Si(OH)_4$ was briefly explored to investigate possible taxonomic relationships, specifically relating to diatoms. $Si(OH)_4$ concentrations were typically low to north of the PFZ and replete to the south. These two distinct regions are influenced by different environmental conditions and physical processes, and as the dataset presented in this study was a combination of these regions, it was not possible to accurately infer the underlying mechanisms driving any relationships between $Si(OH)_4$ and $\Phi_F(\lambda)$.

While the results of this chapter emphasise the important role of taxonomy and light levels on $\Phi_F(\lambda)$ measurements, a larger sample size and measurements of dissolved Fe (DFe) would have added a far greater depth of understanding to the observed $\Phi_F(\lambda)$ responses, considering the two key drivers of photophysiological regulation in Southern Ocean phytoplankton, irrespective of community structure, are light and Fe (Cassar et al., 2011; Lin et al., 2016; Strzepek et al., 2012). In addition, while the spectral clustering of data was a good initial approach to investigating drivers of variability, future approaches will need to better define ways of grouping data if this work is to be expanded for routine use with potential remote sensing application. The comparison of $\Phi_F(435)$ and $\Phi_F(570)$ to possible drivers of variability was a good bridge in moving from broad spectral analysis to key waveband determinants.

To conclude, the newly calibrated MFL was deployed in the Southern Ocean and used

to successfully derive wavelength-specific $\Phi_F(\lambda)$ measurements, with the majority of values falling within the range of previous studies (0.001-0.15, Table 1.3). Outlier values were typically obtained in the green-orange excitation LEDs, notably at 570 nm, due to increased instrument sensitivity, a low signal-to-noise ratio, and possible Raman contamination; it is a possibility that the 525-590 nm wavebands may be omitted from future analyses if reliable constraints cannot be developed. Both taxonomy and light were found to impact $\Phi_F(\lambda)$ in characteristic ways, which were largely dependent on the photoacclimation state of the phytoplankton community. The potential routine deployment of the MFL will provide unprecedented insight into processes governing *in situ* $\Phi_F(\lambda)$, expediting the investigation into the interplay between taxonomy, light levels, and Fe-availability, and their influences on associated phytoplankton photophysiology. Through increased sampling frequency and generation of a larger *in situ* $\Phi_F(\lambda)$ database, improved understanding of signal variability will facilitate Φ_F satellite ocean colour algorithm development, and allow for improved monitoring capabilities in the globally important Southern Ocean.

Recommendations for future work are listed below:

- The implementation of a Raman scattering correction. Studies have stressed the importance of such a correction (Maritorena et al., 2000; Morrison, 2003), with Raman scattering known to account for approximately 20% of the upwelling radiance in the red part of the spectrum, leading to an overestimation of chl-*a* fluorescence.

- Account for chl-*a* fluorescence reabsorption. As the red chl-*a* absorption band partly overlaps its fluorescence band, the fluorescence emission may be partly reabsorbed before leaving the cell (Collins et al., 1985). This would result in diminished chl-*a* fluorescence and Φ_F (Babin et al., 1996b).

- Measure local DFe concentrations. As this micronutrient is a key regulator of Southern Ocean phytoplankton dynamics (Boyd, 2002), it is imperative for future studies to account for Fe-availability when examining Φ_F values and the drivers of its variability.

- *In situ* sampling should include depth measurements. In the Southern Ocean, the mixed layer depth is an important physical feature, regulating the amount of light and nutrients supplied to resident phytoplankton. Sampling over a range of depths will capture potential deep chl-*a* maxima and species transitions that may have been overlooked with exclusive surface sampling (Bathmann et al., 1997; Detmer and Bathmann, 1997; Gervais et al., 2016; Holm-Hansen and Hewes, 2004).

- Apply additional taxonomic methods when examining community structure. While the use of diagnostic pigment ratios (Uitz et al., 2006) and CHEMTAX analysis (Mackey et al., 1996) have their advantages and dis-advantages, the incorporation of additional enumeration techniques would improve the taxonomic resolution of natural assemblages. For example, size-fractionated chl-*a* analysis would aid in size structure determination (Rozema et al., 2017) and microscopy analysis in species identification (Patil et al., 2013).

- One approach to disentangling the influence of individual phytoplankton species on $\Phi_F(\lambda)$, would be through the use of nutrient and light-regulated mono-specific phytoplankton cultures. Submerging the MFL in pure cultures of known conditions, would allow for the derivation of species-specific $\Phi_F(\lambda)$. Further manipulation would allow for the effects of light and nutrient levels on phytoplankton-specific $\Phi_F(\lambda)$ to be examined.

- Separate photosynthetic and non-photosynthetic absorption components to examine their individual contributions to the shape of the quantum yield spectra.

Chapter 5

Remote Sensing of Fluorescence Quantum Yield in the Southern Ocean

5.1 Introduction

5.1.1 Overview of satellite-derived Φ_F

The advent of satellite remote sensing has proven to be especially useful in remote areas, such as the high-latitude polar regions, where traditional data collection methods are logistically difficult. The launch of remote sensors such as MODIS and the Medium Resolution Imaging Spectrometer (MERIS, European Space Agency), with spectral bands in the red-wavelengths, has allowed for the estimation of SICF (Gower et al., 2004; Letelier and Abbott, 1996). Algorithms have been proposed (Abbott and Letelier, 1999; Babin et al., 1996b) and applied, to interpret this measurement in terms of phytoplankton biomass or satellite-derived estimates of Φ_{sat} (Behrenfeld et al., 2009; Browning et al., 2014a; Huot et al., 2005, 2013; Laney et al., 2005; Lin et al., 2016; Morrison and Goodwin, 2010). Observations of SICF near the sea surface reveal substantial variability in space and time that may reflect environmental controls on the photosynthetic and physiological status of phytoplankton (Abbott et al., 2001; Letelier et al., 1997; Schallenberg et al., 2008). Laboratory and field experiments, using passive and stimulated measurements of fluorescence, have reported that metrics or proxies of Φ_F are influenced by the nutritional state of the phytoplankton (Abbott et al., 2000; Cleveland and Perry, 1987; Laney et al., 2005; Timmermans et al., 2008). The use of satellite-derived fluorescence as a diagnostic for nutrient stress is complicated by the fact phytoplankton near the ocean surface

can experience physiological stress due to excess irradiance as well as nutrient limitation (Babin et al., 1996b; Behrenfeld et al., 2009; Browning et al., 2014a; Huot et al., 2005, 2013; Schallenberg et al., 2008). The combined effect of these stressors on Φ_F is poorly understood (Cullen et al., 1997; Cullen and Lewis, 1995; Laney et al., 2005). It has been shown that under high light levels near the ocean surface, Φ_F is subject to qN (Maritorena et al., 2000; Morrison, 2003; Schallenberg et al., 2008). Variability in qP and qN is a crucial consideration when deriving Φ_{sat} under ambient light conditions (Falkowski and Kiefer, 1985), as satellite ocean colour products are typically generated from surface waters at times near local noon (Savtchenko et al., 2004), when Φ_{sat} values are significantly impacted by qN (Behrenfeld et al., 2009; Browning et al., 2014a; Morrison and Goodwin, 2010).

The interplay between nutrient limitation and excess-irradiance dissipation is yet to be properly elucidated (Laney et al., 2005). Attempts have been made to parameterise the effects of qN in order to elucidate surrounding nutrient conditions; for example, qE-corrections were implemented by Behrenfeld et al. (2009) using iPAR, and Browning et al. (2014a) using SST. The development of a suitable qN-correction for Φ_{sat} is a complex task, further complicated by the strong dependence of qN on the phytoplankton community structure and the photoacclimation state of the population (Graff and Behrenfeld, 2018; Milligan et al., 2012). Phytoplankton-specific photoacclimation strategies, including altering the size of the absorption cross-section of PSII and adjusting the amount of PSII reaction centres (Falkowski and Owens, 1980), affect Φ_{sat} and have been shown to be responsible for up to 89% of Φ_{sat} variability in certain regions (Morrison and Goodwin, 2010). Photoprotective mechanisms employed by phytoplankton are further influenced by upper ocean turbulence affecting the surrounding light field (Alderkamp et al., 2010) and nutrient distribution (Moore et al., 2013; Strzepek et al., 2012).

A major obstacle for remote sensing at high latitudes is the need for acquisition of appropriate validation data sets, particularly for ocean colour applications. Current attempts to validate Φ_{sat} algorithms remain limited, predominantly as there is a shortage of *in situ* Φ_F measurements; instruments that measure a continuous fluorescence yields, for example, the MFL, provide more relatable outputs to satellite-derived SICF than those derived from variable fluorescence measurements. While instruments that measure variable fluorescence have provided unprecedented information on the photochemical conversion in phytoplankton *in situ*, they are unable to measure absolute quantum yields of fluorescence. Browning et al. (2014a) derived relative Φ_F from variable fluorescence measurements, and compared their *in situ* values to remotely sensed Φ_{sat} in the Atlantic sector of the Southern Ocean. However, there are limitations to using variable fluorescence to

reliably derive Φ_F. Kuzminov and Gorbunov (2016) constructed a custom picosecond fluorescence lifetime fluorometer to quantify picosecond fluorescence decay kinetics; such measurements are quantitatively relatable to Φ_F (Falkowski et al., 2017; Lakowicz and Masters, 2008). Long fluorescence lifetimes, i.e. high Φ_F, have been observed in the Southern Ocean, and attributed to Fe-limitation (Lin et al., 2016; Park et al., 2017).

5.1.2 Chapter objectives

Detection of Φ_F from satellite ocean colour products will provide routine, synoptic observations and, as such, improve understanding of phytoplankton dynamics and offer insight into surrounding environmental conditions. The *in situ* measurements of $\Phi_F(435)$, calculated in Chapter 4, are used to validate three existing Φ_{sat} algorithms. From an available *in situ* dataset of 66 stations, there are six MODIS level 2 match-ups, all occurring in the austral summer of 2013/ 2014. A sensitivity analysis, over varying ranges of [chl-a] and irradiance, is undertaken to assess algorithm performance. A preliminary, optimised hybrid Φ_{sat} algorithm is used to investigate the influence of [DFe] on Φ_{sat}. The algorithm is also used to perform a decadal study in the Atlantic Southern Ocean, as an initial demonstration of the value of the validated Φ_{sat} product.

5.2 Methods

Please refer to the List of Notation (p.iv) for specific symbols and units used throughout this chapter.

5.2.1 Spectral correction of MFL-derived $\Phi_F(\lambda)$

To account for differences in the spectral distribution of MFL LEDs, all $\Phi_F(\lambda)$ values were multiplied by a spectral correction factor (SCF), making the output more comparable to Φ_{sat}, which comprises an integrated iPAR measurement. A solar irradiance spectrum resembling typical Southern Ocean, noon-day, conditions was generated using a solar spectrum calculator (https://www2.pvlighthouse.com.au/), to create a range of irradiance values over 350-700 nm (1 nm intervals); conditions selected were 12:00 GMT, 2 December 2013, at 50°S. All spectra used in the derivation of the SCF, i.e. the solar irradiance, the MFL LED response and the phytoplankton-specific absorption (for each station), were normalised to their respective highest values. A unique SCF was generated for each MFL LED, for every field station (Eq. 5.1).

$$\mathrm{SCF} = \frac{\sum_{350}^{700} a_{ph}^{*} E_{insitu} \cdot \sum_{350}^{700} E_{LED}}{\sum_{350}^{700} a_{ph}^{*} E_{LED} \cdot \sum_{350}^{700} E_{insitu}} \tag{5.1}$$

Equation 5.1 is an adaptation of that used by Suggett et al. (2001), where E_{insitu} specifies the normalised solar irradiance, E_{LED} the normalised MFL LED response and a_{ph}^{*} ($\mathrm{m^2}$ mg $\mathrm{chl^{-1}}$) the chl-*a*-specific phytoplankton absorption for each station.

5.2.2 MODIS-Aqua ocean colour products

All ocean colour products were obtained from the NASA MODIS-Aqua R2018.0 archive (https://oceancolor.gsfc.nasa.gov/). MODIS-Aqua level 2 data (daily, 1 km) were used for the *in situ* match-ups, with the applied level 2 flags listed in Table 5.1. Data were assessed in 3×3 megapixel grids over a period of 24 h (station time ±12 h) for the match-ups. All stations had a minimum of 8 valid pixels, with the megapixel mean used in further calculations. All level 2 product means and standard deviations used for the match-up analysis are listed in Appendix C.1. For the derivation of Φ_{sat} at stations with co-located *in situ* DFe measurements (obtained from the GEOTRACES Intermediate Data Product (IDP) 2017 database, http://www.geotraces.org/dp/idp2017, Schlitzer et al. (2018)), MODIS-Aqua level 2 data (daily, 1 km) was used. Slightly less demanding criteria, i.e. the use of 5×5 megapixel boxes over a period of 24 h, were implemented. All stations had a minimum of 15 valid pixels, with the megapixel mean used in further analyses. All level 2 product means, standard deviations, Φ_{sat} values, and [DFe] are listed in Appendix C.3. MODIS-Aqua level 3 data (monthly, 4 km) data was used for Φ_{sat} derivation in the decadal analysis.

Table 5.1: MODIS-Aqua level 2 flags.

Bit	Flag name	Description
01	LAND	Pixel is over land
04	HILT	Observed radiance very high or saturated
05	HISATZEN	Sensor view zenith angle exceeds threshold
09	CLDICE	Probable cloud or ice contamination

5.2.2.1 Chl-*a* concentration

The near-surface concentration of chl-*a* (chlor_a) in mg $\mathrm{m^{-3}}$, is calculated through an empirical relationship derived from *in situ* measurements of chl-*a* and R_{rs} in the blue-green visible spectrum. The chlor_a product combines two algorithms, the O'Reilly band ratio OCx algorithm (O'Reilly et al., 1998, 2000) and the Hu et al. (2012) colour index

(CI) algorithm (https://oceancolor.gsfc.nasa.gov/atbd/chlor_a/). The CI algorithm is a three-band reflectance difference algorithm employing the difference between R_{rs} in the green band (547 nm) and a reference formed linearly between R_{rs} in the blue (443 nm) and red (667 nm) bands (Eq. 5.2). The OCx algorithm, referred to as OC3M, is a fourth-order polynomial relationship between a ratio of R_{rs} and chlor_a (Eq. 5.3).

$$\text{CI} = R_{rs}(547) \text{ - } [R_{rs}(443) + \frac{(547-443)}{(667-443)} \cdot (R_{rs}(667) \text{ - } R_{rs}(443))] \tag{5.2}$$

$$log_{10}(\text{chlor\_a}) = a_0 + \sum_{i=1}^{4} a_i \left(log_{10} \left(\frac{R_{rs}(blue)}{R_{rs}(547)} \right) \right)^i \tag{5.3}$$

The coefficients a0-a4 (Table 5.2) were derived specifically for MODIS using version 2 of the NASA bio-Optical Marine Algorithm Data set (NOMAD) (Werdell and Bailey, 2005). For chl-*a* retrievals below 0.15 mg m^{-3} the CI algorithm is used, for CI retrievals above 0.2 mg m^{-3} the OC3M algorithm is used, and in between these values the algorithms are blended using a weighted approach.

Table 5.2: MODIS-specific chlor_a and Kd_490 algorithm coefficients.

MODIS product	Algorithm	Blue λ	Green λ	a0	a1	a2	a3	a4
chlor_a	OC3M	443>488	547	0.2424	-2.7423	1.8017	0.0015	-1.2280
Kd_490	KD2M	488	547	-0.8813	-2.0584	2.5878	-3.4885	-1.5061

5.2.2.2 Diffuse attenuation coefficient

Kd_490 refers to the diffuse attenuation coefficient for downwelling irradiance at 490 nm (m^{-1}). NASA's standard algorithm (KD2M) takes the format of a fourth-order polynomial relationship between a blue-green ratio of R_{rs} and Kd_490 (Eq. 5.4, https://oceancolor.gsfc.nasa.gov/atbd/kd_490/).

$$log_{10}(K_{bio}(490)) = a_0 + \sum_{i=1}^{4} a_i \left(log_{10} \left(\frac{R_{rs}(443)}{R_{rs}(547)} \right) \right)^i \tag{5.4}$$

where

$$\text{Kd\_490} = \text{K}_{bio}(490) + 0.0166 \tag{5.5}$$

The coefficients a0-a4, listed in Table 5.2, were derived specifically for MODIS using version 2 of the NOMAD (Werdell and Bailey, 2005).

5.2.2.3 Normalised fluorescence line height

The normalised fluorescence line height (nflh, W m^{-2} μm^{-1} sr^{-1}) is calculated as the difference between the observed normalised water-leaving radiance (nL_w) at 678 nm and a linearly interpolated $nL_w(678)$ between $nL_w(667)$ and $nL_w(748)$ (https://oceancolor.gsfc.nasa.gov/atbd/nflh/). The theoretical basis of nflh is explained in detail by Abbott and Letelier (1999) and implemented in work by Behrenfeld et al. (2009) (Eq. A2), and is generically described as follows:

$$\text{nflh} = nL_w(678) \text{ - } nL_w(667) \text{ - } \left[(nL_w(748) \text{ - } nL_w(667)) \cdot \left(\frac{678-667}{748-667}\right) \right] \tag{5.6}$$

5.2.2.4 Instantaneous photosynthetically available radiation

The instantaneous photosynthetically available radiation (iPAR, Einstein m^{-2} s^{-1}), represents the total PAR incident on the ocean surface at the time of the satellite observation (https://oceancolor.gsfc.nasa.gov/atbd/ipar/). The theoretical basis of iPAR is explained in detail by Carder et al. (2003), and the algorithm is generically defined as:

$$\text{iPAR} = \frac{1}{hc} \int_{700}^{400} \lambda E_d(\lambda, 0^-) d\lambda, \tag{5.7}$$

where h = 6.63e^{-34} (Planck's constant), c = 3e^{8} (speed of light) and $E_d(\lambda, 0^-)$ is the spectral downwelling irradiance just below the sea surface.

5.2.3 General considerations

The MODIS-Aqua products chlor_a, Kd_490, and nflh are denoted as Chl$a$, $K_d(490)$, and FLH, respectively, hereforth. The satellite products Chl$a$, iPAR, and $K_d(490)$ are standardly processed to lie just below the sea surface (as per their respective NetCDF metadata), whereas FLH is processed just above the sea surface and had to be converted to subsurface values ($E_0(0^-)$,λ). This was performed by multiplying FLH by $t/\ n_w^2$, where t is the transmission of nadir radiance across the sea surface (t = 0.97, (Mobley, 1994)) and n_w is the index of refraction of sea water (n_w = 1.34). In some instances, i.e. for the Babin et al. (1996b) and Huot et al. (2005) equations, FLH radiance units were converted to moles of photons by multiplying FLH by λ (m^{-1})/ hc, and subsequently dividing by Avogadro's number (6.02e^{23}).

Huot et al. (2013) determined the detection limit for FLH at the top of the atmosphere (TOA) to be 0.003 mW cm^{-2} μm^{-1} sr^{-1}, and warned the integrity of satellite-detected

chl-a may be compromised at values of [chl-a] < 0.1 mg m^{-3}. The positioning of the MODIS FLH detection bands mean FLH is estimated to be 0.6 (Gower et al., 2004) and 0.7 (Huot et al., 2005) of the actual emission at 685 nm. MODIS band 15 is positioned more than 60 nm from the fluorescence emission maximum, leading to the baseline being slightly overestimated at low [chl-a], which results in negative FLH values (Letelier and Abbott, 1996). For this study, all stations had [chl-a] > 0.1 mg m^{-3} and positive FLH pixels well above the detection limit proposed by Huot et al. (2013).

5.2.4 Φ_{sat} Algorithms

The three algorithms used in this study were considered best suited to our *in situ* dataset and included relevant factors thought to be of importance, particularly in the high latitude, low [chl-a] Southern Ocean. The first algorithm used to derive Φ_{sat} from SICF measurements was that of Babin et al. (1996b):

$$\Phi_{Bab} = \frac{FLH}{iPAR \cdot Chla \cdot \overline{a}^{*}_{\phi} \cdot Q^{*}_{a}(685) \cdot dz} \tag{5.8}$$

where

- Φ_{Bab} is Φ_{sat} derived using the algorithm of Babin et al. (1996b),
- FLH is the MODIS fluorescence line height product (mol m^{-2} s^{-1} nm^{-1} sr^{-1}) emitted by a thin seawater layer of thickness dz(m),
- $iPAR$ is the instantaneous scalar PAR irradiance just below the sea surface (mol m^{-2} s^{-1}),
- $Chla$ is the MODIS OC3M estimate of [chl-a] (mg m^{-3}),
- $\overline{a}^{*}_{\phi}$ is the mean chl-a-specific absorption coefficient, and is calculated as $\overline{a}^{*}_{\phi} = 0.0161 \cdot Chla^{-0.257}$ (m^2 mg chl^{-1}), and
- $Q^{*}_{a}(685)$ is a dimensionless factor accounting for intracellular reabsorption of fluorescence within the spectral emission band centred at 685 nm and is calculated as $Q^{*}_{a}(685) = 0.549 \cdot Chla^{-0.173}$.

Babin et al. (1996b) originally made use of PAR (mol m^{-2} s^{-1}), the scalar irradiance ($\overset{0}{E}(\lambda)$) integrated between 400 and 700 nm. The MODIS PAR product is measured just above the sea surface ($E_0(0^+)$, λ), in units of mol m^{-2} d^{-1}. The MODIS iPAR product is taken from just below the sea surface ($E_0(0^-)$, λ), and is in mol m^{-2}

s^{-1}. In this study, the iPAR product satisfied the requirements for Φ_{sat} derivation.

The Φ_{sat} algorithm of Huot et al. (2005) was selected as the second algorithm to be investigated. While the author proclaims the Φ_{sat} algorithm developed in Huot et al. (2013) should supersede the 2005 version, the earlier version was better suited to this study; the Huot et al. (2013) algorithm did not provide quantum yields in absolute values, which was necessary for the comparison to the *in situ* absolute Φ_F values. Furthermore, the Huot et al. (2013) algorithm was developed using level 3 data, which does not provide the sensor angle of observation ($\theta^{'}$), an important consideration in Φ_{sat} retrieval. The Huot et al. (2005) algorithm is as follows:

$$\Phi_{Huo} = \frac{FLH \cdot \beta_{\Phi}}{iPAR \cdot Chla} \tag{5.9}$$

where

- Φ_{Huo} is Φ_{sat} derived using the algorithm of Huot et al. (2005),
- FLH is the MODIS fluorescence line height product (mol m^{-2} s^{-1} nm^{-1} sr^{-1}),
- $iPAR$ is the instantaneous scalar PAR irradiance just below the sea surface (mol m^{-2} s^{-1}),
- $Chla$ is the MODIS OC3M estimate of [chl-a] (mg m^{-3}), and
- β_{Φ} is a correction factor that accounts for the viewing geometry and optical properties associated with FLH, and is described in Eq. 5.10.

To retrieve Φ_{sat}, the surface fluorescence was corrected for bio-optical sources of variability through the derivation of the β_{Φ} factor:

$$\beta_{\Phi} = \frac{4\pi \cdot C_f \cdot [K_{abs}^{\tau_f} + (a_f / cos\theta^{'})]}{\overline{a}_{\phi}^{*} \cdot Q_a^{*}} \ , \tag{5.10}$$

where

- 4π converts isotropic fluorescence field to radiance (sr),
- C_f is the proportionality factor for MODIS bands, converting fluorescence measurements made at 678 nm to the whole fluorescence band (43.38 nm),
- $K_{abs}^{\tau_f}$ is the attenuation coefficient for downwelling absorbed irradiance at 490 nm, evaluated to depth (z_{90}), above which 90% of the fluorescence radiance at the surface originates, and is calculated as $K_{abs}^{\tau_f}$ = -0.00831 + 0.908 $\cdot K_d(490)^{0.781}$ (m^{-1}),

- a_f is the attenuation of upwelling fluorescence radiance, $a_f = a_w(678) + a_\Phi(678)$, with a_f and a_Φ being the absorption coefficients for water and phytoplankton respectively. $a_w(678) = 0.461$ m^{-1} (Pope and Fry, 1997) and $a_\Phi(678) = 0.4762 \cdot(\mathrm{K}_d(490)-0.016)^{1.22}$ m^{-1},

- $\theta^{'}$ is the zenith angle of observation in water, provided by the MODIS MYD03 product (radians),

- $\overline{a}^*_\phi$ is the irradiance-weighted chl-*a*-specific absorption coefficient, and is calculated as $\overline{a}^*_\phi = 0.00663 \cdot(\mathrm{K}_d(490)$ - $0.016)^{-0.3611}$ (m^2 mg chl^{-1}), and

- Q^*_a is a parameter accounting for the fraction of emitted radiation at λ_{em} not reabsorbed within the cell. Q^*_a is set to 1 (unitless) for $K_d(490) < 0.11$ m^{-1}.

The Φ_{sat} algorithm of Huot et al. (2005) inspired subsequent variations (Behrenfeld et al., 2009; Morrison and Goodwin, 2010). The final equation selected for derivation of Φ_{sat} from SICF was that of Behrenfeld et al. (2009), adapted from Huot et al. (2005) as follows:

$$\Phi_{Beh} = \frac{FLH}{Chla \cdot < a^*_{ph} > \cdot S_{beh}} \tag{5.11}$$

where

- Φ_{Beh} is Φ_{sat} derived using the algorithm of Behrenfeld et al. (2009),

- FLH is the satellite-derived surface chl-*a* fluorescence (mW cm^{-2} μm^{-1} sr^{-1}),

- $Chla$ is the MODIS OC3M estimate of [chl-*a*] (mg m^{-3}),

- $< a^*_{ph} >$ is the spectrally-weighted chl-*a*-specific absorption coefficient, and is calculated as $< a^*_{ph} > = 0.0147 \cdot Chla^{0.684}(m^2$ mg chl$^{-1})$, and

- S_{beh} is a correction factor of 100 mW cm^{-2} μm^{-1} sr^{-1}.

Behrenfeld et al. (2009) included an inverse-light function to describe qN, specifically qE. The quenching correction, which used an iPAR/$\overline{iPAR}$ ratio (where $\overline{iPAR}$ is the global average iPAR for MODIS, 1590 μmol m^{-2} s^{-1}), was found to be appropriate for phytoplankton acclimated to a single light level, however, the actual reduction in Φ_{sat} due to qN expressed at any given saturating iPAR differs between phytoplankton acclimated to different light levels. As Southern Ocean phytoplankton experience vastly different light regimes across the latitudinal provinces, the photo-acclimation states of resident phytoplankton are too varied to employ this type of qN-correction. For consistency between all

three algorithms, the Behrenfeld et al. (2009) equation used in this study did not include their qN-correction. (When the qN-correction was included in the Φ_{sat} calculation the difference was negligible (Appendix C.2)).

5.2.4.1 FLH constants

Huot et al. (2005) add a small value, FLH_0, to FLH to avoid negative radiances encountered. This constant, $FLH_0 = 0.05$ W m^{-2} μm^{-1} sr^{-1}, corresponds to the minimum amount of fluorescence expected based on historical measurements (Abbott and Letelier, 1999). In contrast, Behrenfeld et al. (2009) subtract a small value (0.001 mW cm^{-2} μm^{-1} sr^{-1}) from the FLH product, to further separate out negative values, before completely removing any negative pixels from their dataset. Their justification of this treatment was that the negative pixels only represented 0.2% of their MODIS data, they were randomly distributed globally and likely represented pixels with unflagged atmospheric correction problems.

5.2.5 Statistical metrics

While both r and regression slopes, representative of goodness of fit, have their merits, they do not provide a full description of algorithm performance, including accuracy and bias (Seegers et al., 2018). As such, a full suite of statistical metrics were applied to the satellite-derived chl-a and Φ_{sat} data. The statistical descriptors included the bias (the average difference), the mean absolute relative difference (MARD) and the root-mean-square difference (RMSD). The bias is determined for logarithmically transformed (base 10) data, an accepted approach considering chl-a follows a lognormal distribution (Campbell, 1995). The bias is computed as per Seegers et al. (2018):

$$\text{Bias} = 10^{\left(\frac{\sum_{i=1}^{N} log_{10}S_i - log_{10}I_i}{N}\right)} \tag{5.12}$$

the mean absolute relative difference (MARD), expressed in percentage, as per Gerbi et al. (2016):

$$\text{MARD } (\%) = 100 \cdot \frac{1}{N} \sum_{i=1}^{N} \frac{\mid S_i - I_i \mid}{I_i} \tag{5.13}$$

and the root-mean-square difference (RMSD) as per Gerbi et al. (2016):

$$\text{RMSD} = \sqrt{\frac{1}{N} \sum_{i=1}^{N} (S_i - I_i)^2} \tag{5.14}$$

where N is the sample size, S_i are the satellite derived values and I_i are the *in situ* measured values. Note, the bias calculated through Eq. 5.12 is centred at a value of 1, e.g. if the bias = 1, the satellite is unbiased, if the bias = 0.5, there is a negative bias/ underestimate of 50% etc.

5.3 Results

5.3.1 Φ_{sat} Algorithm evaluation

Three existing Φ_{sat} algorithms, namely that of Babin et al. (1996b), Huot et al. (2005), and Behrenfeld et al. (2009), were used to derive Φ_{sat} (Φ_{Bab}, Φ_{Huo}, and Φ_{Beh}, respectively) for stations that matched the *in situ* MFL-derived $\Phi_F(435)$. As chl-*a* absorbs maximally in the blue, the 435 nm MFL waveband was specifically selected to provide the maximal signal and most relatable Φ_F values to that derived from satellites. $\Phi_F(435)$ data were spectrally corrected to further improve the relationship to Φ_{sat} (Section 5.2.1), with Φ_F(sc) values listed in Table 5.3.

Table 5.3: *In situ* MFL-derived $\Phi_F(435)$ and spectrally corrected Φ_F(sc) values.

Φ_F	GHS39	GHS43	GHS45	GHN09	GHN35	GHN41
$\Phi_F(435)$	0.0207	0.0384	0.1495	0.0527	0.0281	0.1005
Φ_F(sc)	0.0089	0.0173	0.0719	0.0235	0.0114	0.0489

The *in situ* Φ_F(sc) of the 6 satellite match-up stations were regressed against Φ_{sat} derived through the three selected algorithms and variations thereof (Fig. 5.0, Table 5.4). For all algorithms and their variants, the *in situ* Φ_F(sc) measurements were higher than their respective Φ_{sat} estimates. The original algorithms, with treatment of the data followed verbatim, did not show any significant relationships to the *in situ* Φ_F(sc) (row 1). In row 2, the FLH used in all algorithms was kept the same, i.e. the constants used by Huot et al. (2005) and (Behrenfeld et al., 2009) were omitted, and the $\overline{a}^*_\phi$ and Q^*_a terms of Babin et al. (1996b) were substituted in to the Huot et al. (2005) and (Behrenfeld et al., 2009) equations, where applicable. This led to a minor improvement between Φ_{Beh} and Φ_F(sc), and a more substantial improvement between Φ_{Huo} and Φ_F(sc); this change to the original Huot et al. (2005) algorithm decreased the bias, MARD and r from 0.38, 52.1% and 0.11, respectively, to 0.65, 50.8% and 0.47, with an improvement in p from 0.83 to 0.35. This is the version of the Huot et al. (2005) algorithm (Fig. 2b) that forms the hybrid Φ_{Huo}/ Φ_{Bab} (Φ_{HB}) algorithm in Section 5.5. Up until this point, all results are congruent. Row 3 incorporates the same algorithms used in row 2 Φ_{sat} derivation, with

the exception of substituting the satellite chl-a with that of *in situ* chl-a. This led to an improvement in relationships across the full suite of stats for Φ_{Bab} and Φ_{Huo}, yet increased the bias and uncertainty for that of Φ_{Beh}. The Φ_{sat} algorithms, with the same treatment of FLH, the Q_a^* term of Babin et al. (1996b) and *in situ* chl-a, were further manipulated through substitution of the Babin et al. (1996b) $\overline{a}_\phi^*$ term with *in situ* $\overline{a}_\phi^*$, averaged over the visible spectrum (400-700 nm) (row 4). This improved the r and p values for all algorithms, however, there was an increase in bias and uncertainty for Φ_{Huo} and Φ_{Beh}. This strengthening of the linear relationship between all Φ_{sat} and *in situ* Φ_F(sc) r and p values continued when the waveband range of the *in situ* $\overline{a}_\phi^*$ was narrowed to 415-455 nm (row 5); Φ_{Bab} r = 0.90, p = 0.01, Φ_{Huo} r = 0.88, p = 0.02 and Φ_{Beh} r = 0.87, p = 0.02. This version of the Babin et al. (1996b) algorithm further resulted in the least bias and lowest uncertainty out of all versions, with a bias of 0.58 and an MARD of 37.4%. This version of the Huot et al. (2005) algorithm resulted in the largest negative bias (0.21) and uncertainty (76.4%) out of all their versions, likewise for the Behrenfeld et al. (2009) algorithm, which underestimated Φ_{Beh} by approximately 90%.

In summary; in case of the Babin et al. (1996b) model, adding the *in situ* chl-a and $\overline{a}_\phi^*$(415-455) decreased the overall uncertainty, and incrementally brought down the bias from a severe overestimation to a moderate underestimation. For Huot et al. (2005) equation, adding the $\overline{a}_\phi^*$ and Q_a^* terms of Babin et al. (1996b) improved the bias, MARD, and RMSD, whereas adding the *in situ* $\overline{a}_\phi^*$ tended to increase the negative bias and generally increase the uncertainty. For the Behrenfeld et al. (2009) equation, the addition of the $\overline{a}_\phi^*$ and Q_a^* terms of Babin et al. (1996b) improved the bias and MARD, and the addition of *in situ* chl-a and $\overline{a}_\phi^*$ increased the negative bias, the uncertainty, and the RMSD. Overall, almost all algorithms returned good linear agreement but poor accuracy compared to the *in situ* Φ_F(sc); Φ_{sat} derived through the Babin et al. (1996b) model, with *in situ* chl-a and $\overline{a}_\phi^*$(415- 455 nm), showed the strongest overall statistical relationship to *in situ* Φ_F(sc) (r = 0.90, p = 0.01), with bias = 0.58, MARD = 37.6%, and RMSD = 0.026. All Φ_{sat} values are listed in Appendix C.2.

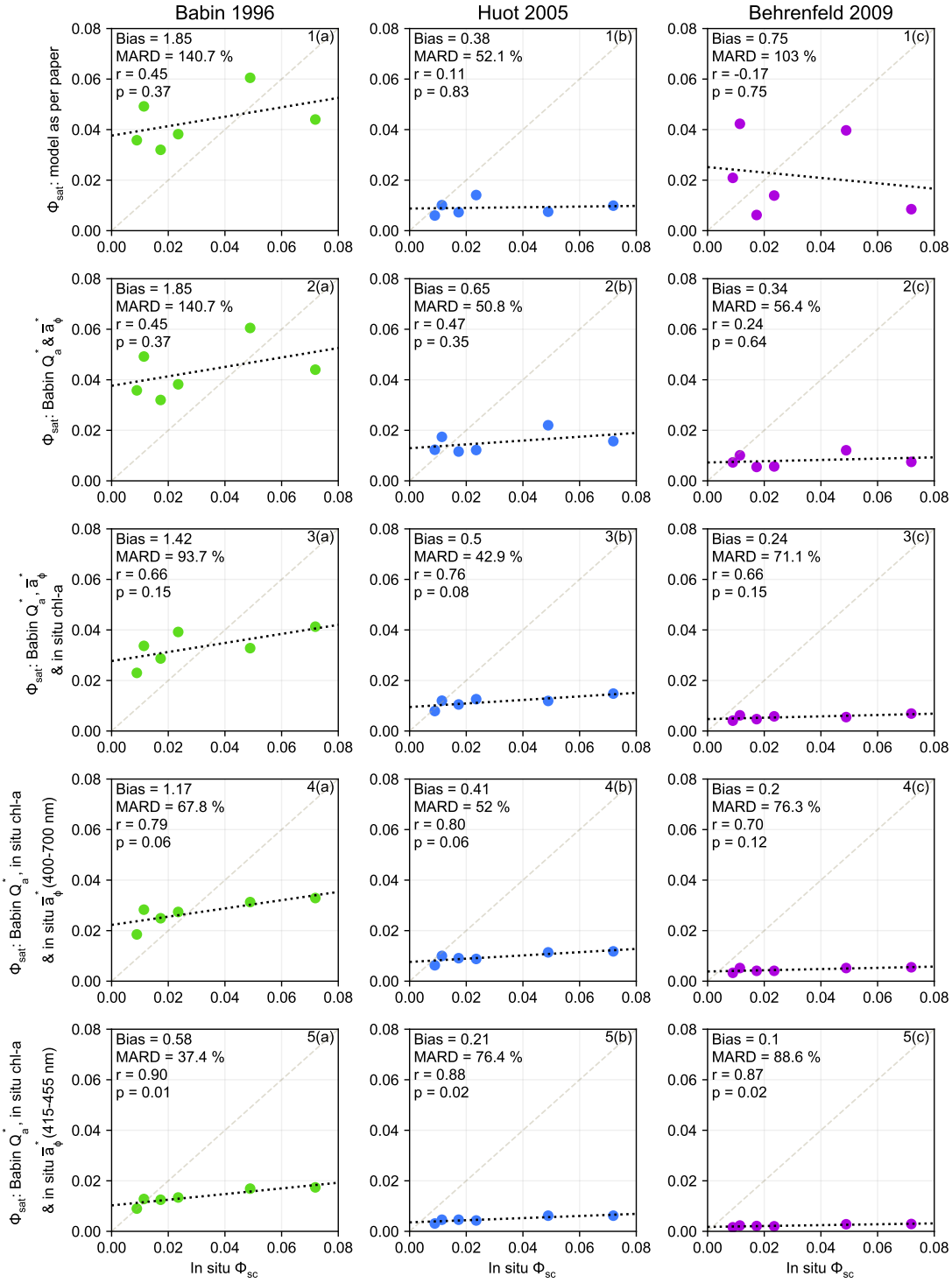
Babin 1996
Huot 2005
Behrenfeld 2009
Φsat: model as per paper
Φsat: Babin Q*a & a*ϕ
Φsat: Babin Q*a, a*ϕ & in situ chl-a
Φsat: Babin Q*a, in situ chl-a & in situ a*ϕ (400-700 nm)
Φsat: Babin Q*a, in situ chl-a & in situ a*ϕ (415-455 nm)
In situ Φsc
Bias = 1.85
MARD = 140.7 %
r = 0.45
p = 0.37
1(a)
Bias = 0.38
MARD = 52.1 %
r = 0.11
p = 0.83
1(b)
Bias = 0.75
MARD = 103 %
r = -0.17
p = 0.75
1(c)
Bias = 1.85
MARD = 140.7 %
r = 0.45
p = 0.37
2(a)
Bias = 0.65
MARD = 50.8 %
r = 0.47
p = 0.35
2(b)
Bias = 0.34
MARD = 56.4 %
r = 0.24
p = 0.64
2(c)
Bias = 1.42
MARD = 93.7 %
r = 0.66
p = 0.15
3(a)
Bias = 0.5
MARD = 42.9 %
r = 0.76
p = 0.08
3(b)
Bias = 0.24
MARD = 71.1 %
r = 0.66
p = 0.15
3(c)
Bias = 1.17
MARD = 67.8 %
r = 0.79
p = 0.06
4(a)
Bias = 0.41
MARD = 52 %
r = 0.80
p = 0.06
4(b)
Bias = 0.2
MARD = 76.3 %
r = 0.70
p = 0.12
4(c)
Bias = 0.58
MARD = 37.4 %
r = 0.90
p = 0.01
5(a)
Bias = 0.21
MARD = 76.4 %
r = 0.88
p = 0.02
5(b)
Bias = 0.1
MARD = 88.6 %
r = 0.87
p = 0.02
5(c)
0.00
0.02
0.04
0.06
0.08

Figure 5.0: Algorithm comparison for Φ_{sat} derivation. Algorithms from Babin et al. (1996b), Huot et al. (2005) and Behrenfeld et al. (2009) were used to derive Φ_{sat}, for 6 satellite match-up points for the spectrally corrected *in situ* $\Phi_F(435)$. Φ_{sat} in row 1 was derived through the original algorithms, with treatment of the data followed verbatim. Φ_{sat} in row 2 was derived using all algorithms with no additional FLH constants, and the $\overline{a}^*_\phi$ and Q^*_a terms of Babin et al. (1996b). Φ_{sat} in row 3 is derived as previous, with satellite chl-*a* substituted for *in situ* chl-*a*. Φ_{sat} in row 4 is derived as that reported in row 3, with $\overline{a}^*_\phi$ replaced with *in situ* $\overline{a}^*_\phi$, over 400-700 nm. Row 5 shows Φ_{sat} derived as above, with *in situ* $\overline{a}^*_\phi$(400- 700 nm) replaced with *in situ* $\overline{a}^*_\phi$, over 415-755 nm. The grey, dashed 1:1 line is inserted to illustrate satellite bias, with the black, dotted line representing the regression slope between satellite and *in situ* Φ_F.

Table 5.4: Statistical metrics used to compare MODIS-derived Φ_{sat} and *in situ* Φ_F(sc). Reference to the sub-plots in Fig. 5.0 and the statistical metrics employed are shown. The Φ_{sat} *original* values are derived through the original algorithms, with treatment of the data followed verbatim; Φ_{sat} *& is chl-a* values make use of *in situ* chl-*a* measurements; Φ_{sat} *& Bab* $\overline{a}^*_\phi$, Q^*_a values include the Babin et al. (1996b) $\overline{a}^*_\phi$ and Q^*_a terms; Φ_{sat} *& Bab* $\overline{a}^*_\phi$ *& is chl-a,* $\overline{a}^*_\phi$*(400-700)* are the values derived through the original algorithms, with the Babin et al. (1996b) Q^*_a term, *in situ* chl-*a* and *in situ* $\overline{a}^*_\phi$ over 400-700 nm; Φ_{sat} *&* *Bab* $\overline{a}^*_\phi$ *& is chl-a,* $\overline{a}^*_\phi$*(415-455)* is as previous, apart from the inclusion of *in situ* $\overline{a}^*_\phi$ over 415-455 nm instead of the entire visible spectrum.

Φ_{sat} algorithm	Fig.	Bias	MARD	RMSD	r	p
Φ_{Bab} original	1/2(a)	1.85	140.7	0.024	0.45	0.37
Φ_{Bab} & *is* chl-*a*	3(a)	1.42	93.7	0.019	0.66	0.15
Φ_{Bab} & *is* chl-*a*, $\overline{a}^*_\phi$(400-700)	4(a)	1.17	67.8	0.020	0.79	0.06
Φ_{Bab} & *is* chl-*a*, $\overline{a}^*_\phi$(415-455)	5(a)	0.58	37.6	0.026	0.90	0.01
Φ_{Huo} original	1(b)	0.38	52.11	0.031	0.11	0.83
Φ_{Huo} & Bab $\overline{a}^*_\phi$, Q^*_a	2(b)	0.65	50.8	0.026	0.47	0.35
Φ_{Huo} & Bab $\overline{a}^*_\phi$, Q^*_a & *is* chl-*a*	3(b)	0.5	42.9	0.028	0.76	0.08
Φ_{Huo} & Bab $\overline{a}^*_\phi$ & *is* chl-*a*, $\overline{a}^*_\phi$(400-700)	4(b)	0.41	52.0	0.030	0.80	0.06
Φ_{Huo} & Bab $\overline{a}^*_\phi$ & *is* chl-*a*, $\overline{a}^*_\phi$(415-455)	5(b)	0.21	76.4	0.034	0.88	0.02
Φ_{Beh} original	1(c)	0.75	102.98	0.03	-0.17	0.75
Φ_{Beh} & Bab $\overline{a}^*_\phi$, Q^*_a	2(c)	0.34	56.4	0.032	0.24	0.64
Φ_{Beh} & Bab $\overline{a}^*_\phi$, Q^*_a & *is* chl-*a*	3(c)	0.24	71.1	0.033	0.66	0.15
Φ_{Beh} & Bab $\overline{a}^*_\phi$ & *is* chl-*a*, $\overline{a}^*_\phi$(400-700)	4(c)	0.2	76.3	0.034	0.70	0.12
Φ_{Beh} & Bab $\overline{a}^*_\phi$ & *is* chl-*a*, $\overline{a}^*_\phi$(415-455)	5(c)	0.1	88.6	0.036	0.87	0.02

5.3.2 Φ_{sat} Algorithm sensitivity analysis

A sensitivity analysis of the original three Φ_{sat} algorithms was performed (Fig. 5.1). An average $K_d(490)$ value of 0.07±0.02 m^{-1} was applied, and the FLH values were allowed to scale linearly with [chl-a], in that FLH = 0.2 × [chl-a] (W m^{-2} μm^{-1} sr^{-1}), as a rough approximation derived through linear regression of FLH and [chl-a]. Chl-a concentrations ranged from 0.05 to 10 mg m^{-3} and iPAR values were selected to represent high (1590 μmol m^{-2} s^{-1}), medium (795 μmol m^{-2} s^{-1}), and low (397 μmol m^{-2} s^{-1}) light conditions. The Φ_{Beh} values decreased with increasing [chl-a], and remain identical across all three light levels, as there is no iPAR term used in Φ_{Beh} derivation (at [chl-a] = 1 mg m^{-3}, Φ_{Beh} = 0.073 across all light regimes). The Φ_{Bab} and Φ_{Huo} overall spectra were lowest under high light and increased as light decreased; at [chl-a] = 1 mg m^{-3}, under high light, Φ_{Bab} = 0.433 and Φ_{Huo} = 0.078, medium light Φ_{Bab} = 0.866 and Φ_{Huo} = 0.156 and low light Φ_{Bab} = 1.734 and Φ_{Huo} = 0.313. Φ_{Bab} values were consistently higher than Φ_{Huo}, with the largest difference between the two observed at high [chl-a].

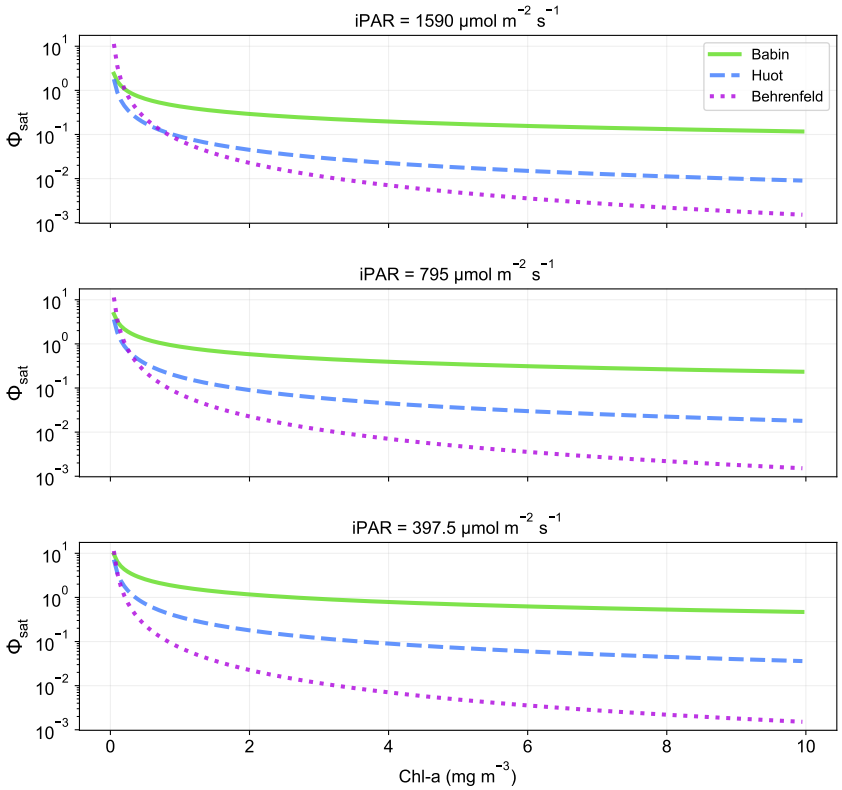

Figure 5.1: Performance analysis of the original Babin et al. (1996b), Huot et al. (2005) and Behrenfeld et al. (2009) Φ_{sat} algorithms. An average $K_d(490)$ value of 0.07±0.02 m^{-1} was applied, FLH values varied with [chl-a], in that FLH = 0.2 × [chl-a] (W m^{-2} μm^{-1} sr^{-1}), and [chl-a] ranged between 0.005-10 mg m^{-3} and iPAR values were selected to represent high (1590 μmol m^{-2} s^{-1}), medium (795 μmol m^{-2} s^{-1}), and low (397 μmol m^{-2} s^{-1}) light conditions.

5.3.3 Uncertainty introduced by θ' in Φ_{Huo}

Huot et al. (2005) incorporates θ' in their β_Φ term, which represents the sensor viewing angle of observation. In this study, θ' is obtained from MODIS level 1A MYD03 products (https://ladsweb.modaps.eosdis.nasa.gov/), for all *in situ* match-up stations and those co-located to *in situ* [DFe]. A sensitivity study is performed to determine the percent error introduced to Φ_{Huo} over a range of θ' values (Fig. 5.2). Φ_{Huo} was calculated over a [chl-*a*] range of 0.1-2 mg m^{-3}, over a constant light level of 795 μmol m^{-2} s^{-1}, an average $K_d(490)$ value of 0.07±0.02 m^{-1}, and FLH values that varied with [chl-*a*], according to FLH = 0.2 × [chl-*a*] (W m^{-2} μm^{-1} sr^{-1}). Different values of θ' were applied (0-60°). Results show the percent difference in Φ_{Huo} generated between nadir ($\theta'(0°)$) and the various angles are as follows: $\theta'(10°) = 1\%$, $\theta'(20°) = 5\%$, $\theta'(30°) = 13\%$, $\theta'(40°) = 25\%$, $\theta'(50°) = 45\%$, and $\theta'(60°) = 81\%$. For example, there is an 81% difference between Φ_{Huo} derived from a nadir viewing angle to that positioned at the edge of the swath ($\theta'(60°)$). This has impact on the use of composite MODIS level 3 products used in Φ_{sat} derivation, and emphasises the need to produce Φ_{sat} from level 2 products with appropriate per-pixel θ' values. In addition, this discrepancy is exaggerated at very low [chl-*a*] (< 0.25 mg m^{-3}, Fig. 5.2), which are typical of the Southern Ocean.

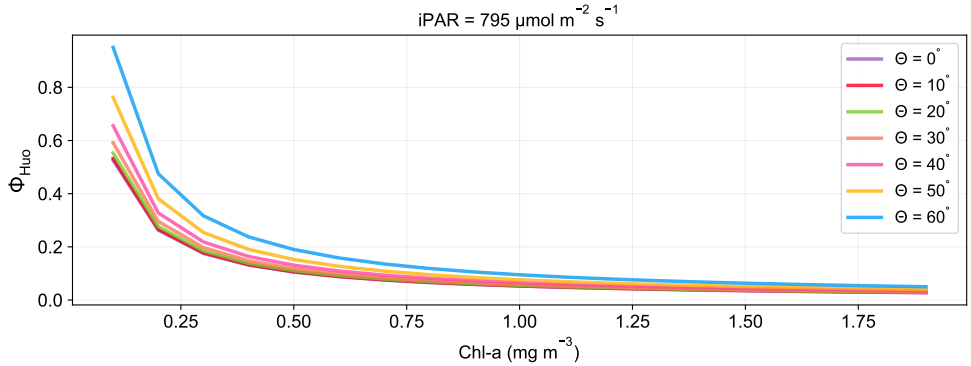

Figure 5.2: Sensitivity analysis of θ' in Φ_{Huo}. An average $K_d(490)$ value of 0.07±0.02 m^{-1} and constant light level of 795 μmol m^{-2} s^{-1} were applied, FLH values varied with [chl-*a*], in that FLH = 0.2 × [chl-*a*] (W m^{-2} μm^{-1} sr^{-1}), and [chl-*a*] ranged between 0.1-2 mg m^{-3}.

5.3.4 Comparison of satellite- and *in situ*-derived chl-*a*

Chl-*a* validation is not the key focus of this study, and the small size of the dataset precludes highly quantitative conclusions. This investigation was performed to better understand why the inclusion of *in situ* chl-*a* in the Φ_{sat} models improved the fit of the satellite derived estimates to the that of *in situ* Φ_F (Section 5.3.1). The comparison

between satellite- and *in situ*-derived [chl-*a*] is shown in Fig. 5.3. While the linear relationship between the two [chl-*a*] values was relatively strong (r = 0.79, p = 0.06), with a good uncertainty estimate (MARD = 33.4%, RMSD = 0.230), the MODIS OC3M algorithm was shown to underestimate [chl-*a*] (bias = 0.63). Satellite estimates are coloured according to the time difference between the overpass and the *in situ* station time. Station GHN09 was the only station to fall on the grey 1:1 line, and had the largest Δtime (approx.17 h prior to the station time) of all stations. All Δtime values are listed in Appendix C.1.

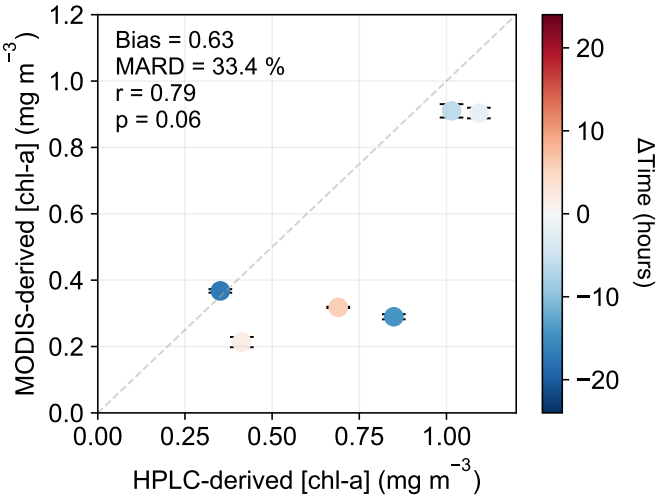

Figure 5.3: Comparison between MODIS OC3M-derived and *in situ* HPLC-derived chl-*a*. Satellite estimates are coloured according to the time difference between the overpass and the *in situ* station time.

5.4 Discussion

5.4.1 Φ_{sat} Algorithm validation and performance

Studies that seek to validate Φ_{sat} algorithms typically make use of relative Φ_F proxies derived from, for example, passive fluorescence measurements (Letelier et al., 1997; Schallenberg et al., 2008), variable fluorescence measurements (Browning et al., 2014a), or through investigation of fluorescence lifetimes (Lin et al., 2016). This is the first study to use *in situ* Φ_F data to validate Φ_{sat} measurements and evaluate existing algorithm performance. To account for differences in the spectral distribution of the MFL LEDs and *in situ* light, the $\Phi_F(435)$ values were multiplied by a spectral correction factor (Section 5.2.1), which allowed for the comparison of *in situ* $\Phi_F(435)$ to Φ_{sat}. The spectral correction of *in situ* $\Phi_F(435)$ led to minor changes in the data distribution and an appropriate

scaling of the magnitude (Table 5.3).

The lower magnitude of all Φ_{sat} values, compared to *in situ* Φ_F(sc), were likely a result of qN on the satellite-retrieved signal. Satellite ocean colour measurements are typically obtained under local noon day conditions (Savtchenko et al., 2004), and fluorescence measurements are reduced as a result of increased heat dissipation processes employed by resident phytoplankton, i.e. qN (Behrenfeld et al., 2009; Browning et al., 2014a; Morrison and Goodwin, 2010). In this study, the *in situ* measurement of MFL fluorescence involved sampling seawater from the ship's underway supply, with an inflow at ∼7 m below the surface, before being fed through black tubing into a sealed, black bucket where measurements were recorded (Chapter 2, Section 2.6.1). The match-up Φ_{sat} values were estimated from surface phytoplankton, which experience much higher PAR levels than those at any depth deeper than a few centimetres from the surface (Gerbi et al., 2016; Zhai et al., 2018). A study by Zhai et al. (2018) used radiative transfer modelling to simulate phytoplankton fluorescence over a range of known drivers of variability. The group performed a sensitivity analysis on iPAR and Φ_F as a function of depth for a set [chl-*a*]; at [chl-*a*] = 1 mg m^{-3}, surface iPAR = 1500 μmol m^{-2} s^{-1} and at ∼7 m iPAR < 500 μmol m^{-2} s^{-1}, with Φ_F increasing from surface to ∼7 m depth, from approximately 0.005 to 0.024. This difference between Φ_F at the surface and Φ_F at ∼7 m depth effectively explains the values reported in the current study. The approximate 40% underestimation in Φ_{HB} relative to Φ_F(sc) is likely due to the difference in iPAR levels (Fig. 5.0(2b)).

The three Φ_{sat} algorithms under investigation, were manipulated in an effort to, firstly, use as similar terms as possible for accurate comparison, and secondly, to assess whether the cumulative inclusion of *in situ* data (with much lower uncertainties that satellite-derived products) substantially improved performance. Both Huot et al. (2005) and Behrenfeld et al. (2009) use constants to mitigate negative FLH pixels (Section 5.2.4.1). The six *in situ* Φ_F(sc) match-up points did not comprise any negative FLH pixels, and the first step in normalising the data was to eliminate these constants. Secondly, while Babin et al. (1996b) and Behrenfeld et al. (2009) use chl-*a*-weighted $\overline{a}^*_\phi$ terms, Huot et al. (2005) estimates $\overline{a}^*_\phi$ through $K_d(490)$. As the Behrenfeld et al. (2009) $\overline{a}^*_\phi$ derivation was based upon that of Babin et al. (1996b), the $\overline{a}^*_\phi$ term of Babin et al. (1996b) was selected to be used for all algorithms. Regarding the chl-*a* reabsorption factor, Q^*_a, Behrenfeld et al. (2009) omitted it and Huot et al. (2005) constrained it to 1 at $K_d(490) < 0.11$ m^{-1} (which was the instance in all *in situ* match-ups in this study). This dimensionless factor accounts for the reabsorption of chl-*a* fluorescence within the cell, and ranges from 0-1 (Collins et al., 1985; Morel and Bricaud, 1981). MODIS measures the upwelling radiance at 676.7 nm (bandwidth 673-683 nm, referred to as the 678 nm waveband), whereas

the maximum emission of fluorescence is around 683-685 nm. This offset was selected to avoid an atmospheric oxygen absorption band at 687 nm (Abbott and Letelier, 1999; Gower et al., 2004; Letelier and Abbott, 1996). However, this offset reduces the sensitivity and places the measurement closer to the chl-*a* absorption peak at approximately 676 nm, which may reduce measured fluorescence by up to 40% due to intracellular re-absorption (Babin et al., 1996b). Babin et al. (1996b) include a $Q_a^*(685)$ term in their Φ_{sat} equation, that is dynamically scaled to [chl-*a*]; for example if chl-*a* = 0.1 mg m^{-3} then $Q_a^* = 0.818$, and if chl-*a* = 1 mg m^{-3} then $Q_a^* = 0.549$ (Section 5.2.4, Eq. 5.8). This variable Q_a^* term was substituted in to the Φ_{sat} equation of Huot et al. (2005). All of these changes led to improvements in the relationships between both Φ_{Huo} and Φ_{Beh}, and the *in situ* Φ_F(sc) (Fig. 5.0).

To compare the performance of the three algorithms, a sensitivity analysis was carried out over a range of [chl-*a*] and light levels (Fig. 5.1). Due to the absence of an iPAR term in the Φ_{Beh} equation, no change was observed over the different light levels, which revealed the strong influence of pigment packaging on Φ_{Beh}, with an increase in chl-*a* leading to an increase in packaging and an expected decrease in Φ_{Beh}. Pigment packaging is driven by changes in intracellular pigment concentration or cell size, and is a key contributor to variation in specific absorption coefficients (from 400-700 nm). Changes in intracellular pigment concentration can be triggered by species-specific photoadaptation strategies. The algorithms of Babin et al. (1996b) and Huot et al. (2005) both demonstrated decreasing Φ_{sat} with increasing light, which is in accordance with Schallenberg et al. (2008) who reported high light-derived Φ_F to be approximately threefold lower than low light-derived Φ_F. The difference between the performance of the algorithms developed by Babin et al. (1996b) and Huot et al. (2005) appears to be due to the different processing of light absorption variables, specifically through the β_Φ term described by Huot et al. (2005) (Section 5.2.4, Eq. 5.10). While both Babin et al. (1996b) and Huot et al. (2005) account for $\overline{a}_\phi^*$ and Q_a^*, Huot et al. (2005) expands this to accommodate sensor viewing geometry, the absorption of light by water and phytoplankton, and the attenuation coefficient for absorbed radiance. These combined attributes contribute to a lower Φ_{sat} than that derived through the Babin et al. (1996b) equation.

The substitution of satellite-derived chl-*a* and $\overline{a}_\phi^*$ with *in situ* values greatly improved the relationships between *in situ* Φ_F(sc) and that of Φ_{Huo} and Φ_{Bab}, suggesting a discrepancy between satellite-derived chl-*a* and the *in situ*, HPLC-derived chl-*a*. There is naturally larger uncertainty in the satellite-derived chl-*a* and any absorption terms derived from it, so the result is not surprising. However, there may also be systematic bias for satellite algorithms in high latitude regions such as the Southern Ocean (IOCCG,

2015). It has been reported, that in the Southern Ocean, the globally derived empirical chl-*a* algorithms are biased. Mitchell and Holm-Hansen (1991) and Sullivan et al. (1993) reported an underestimate, by a factor of 2.4, of Southern Ocean chl-*a* derived from the CZCS algorithm, and Dierssen and Smith (2000) reported a similar bias with the SeaWiFS algorithm for [chl-*a*] $>$ 1 mg m^{-3}. These studies were based on a large dataset of fluorometrically extracted chl-*a*. Further investigations have corroborated this finding through MODIS-derived chl-*a* (Guinet et al., 2013; Johnson et al., 2013; Pereira and Garcia, 2018). In contrast, Haëntjens et al. (2017) found no statistically significant bias between HPLC-derived chl-*a* and that of MODIS-derived chl-*a* (apart from an overestimation in the SIZ), which was in agreement with Moutier et al. (2019) (*in press*). Although the dataset was limited to 6 points, a comparison of the relationship between MODIS OC3M-derived chl-*a* and *in situ* HPLC-derived chl-*a* data used in this study was performed (Fig. 5.3), where it was found the MODIS OC3M underestimated [chl-*a*] by approximately 40% (bias = 0.63, MARD = 33.4%, RMSD = 0.23). As such, the improved relationships between Φ_{sat} and Φ_F(sc) was due to the higher *in situ* chl-*a* concentrations bringing the data closer together.

Φ_{Bab} combined with *in situ* chl-*a* and $\overline{a}^*_\phi$(415-455) reported the strongest statistical relationship (bias = 0.58, MARD = 37.6%, RMSD = 0.026, r = 0.90, p = 0.01). However, with the intention of applying an existing Φ_{sat} algorithm to various Southern Ocean data, as a provisional proof-of-concept, the inclusion of *in situ* data was not feasible. While both the original and modified Huot et al. (2005) algorithms did not display a strong linear relationship to the *in situ* data (r = 0.11, p = 0.83 and r = 0.47, p = 0.35, respectively), they did report acceptable algorithm performance metrics; the original Huot et al. (2005) algorithm reported a bias of 0.38, a MARD of 52.1% and a RMSD of 0.031, and the Huot et al. (2005) algorithm, with the omitted FLH constant and included Babin et al. (1996b) $\overline{a}^*_\phi$ and Q^*_a terms, reported a bias of 0.65, a MARD of 50.8%, and a RMSD of 0.026, when compared to *in situ* Φ_F(sc) (Table 5.4). While the MARD was relatively high, at approximately 50% for both versions of the Huot et al. (2005) algorithm, previous studies with similar MARD values and smaller sample size have been performed (Smith and Pitcher, 2015). As such, it was decided to put forward a combined Huot et al. (2005)/ Babin et al. (1996b) algorithm to demonstrate possible downstream applications of Φ_{sat}. The Huot et al. (2005) Φ_{sat} together with the Babin et al. (1996b) $\overline{a}^*_\phi$ and Q^*_a terms, was used to calculate $\Phi_{Huo/Bab}$ (Φ_{HB}) for stations co-located to *in situ* DFe measurements, as well as for a time series analysis, in the Atlantic Southern Ocean.

5.5 Preliminary Φ_{sat} Application

5.5.1 The relationship between Φ_{HB} and [DFe]

To demonstrate the potential use of optimal Φ_{sat} products for first order examination of Fe stress, the preliminary hybrid Φ_{HB} algorithm (Section 5.4.1) was used to derive Φ_{HB} for various points in the Southern Ocean that were co-located to *in situ* DFe measurements obtained from the Geotraces IDP 2017 database. The relationship between Φ_{HB} and [DFe] in austral summer was investigated (n = 26), with respect to light levels (iPAR, μmol m^{-2} s^{-1}) (Fig. 5.4). While there is no obvious relationship to the light environment, there is a small, statistically significant negative relationship between Φ_{HB} and [DFe] (r = -0.39, p $<$ 0.05). The [DFe] ranged from 0.06-0.74 nM, and the Φ_{HB} ranged from 0.001-0.037 (Appendix C.3).

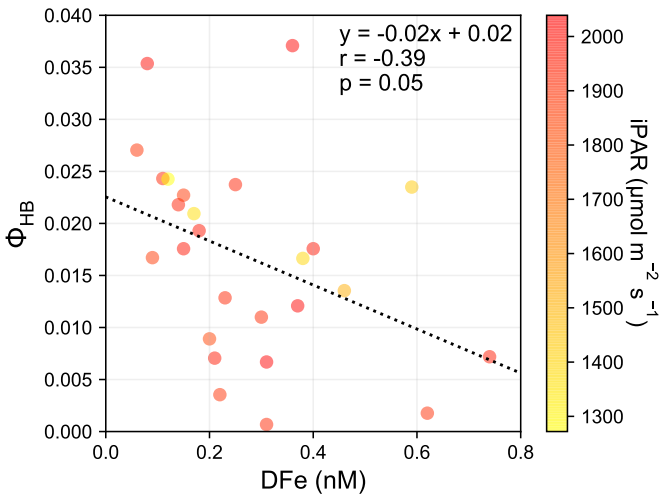

Figure 5.4: Regression analysis of Φ_{HB} and [DFe] in the austral summer, with respect to light levels (iPAR, μmol m^{-2} s^{-1}).

The relationship between Fe availability and chl-*a* fluorescence is well established (Behrenfeld and Milligan, 2013), with laboratory and field experiments demonstrating that phytoplankton living under Fe-deplete conditions exhibit higher chl-*a* fluorescence relative to those in Fe-replete environments (Behrenfeld et al., 1996, 2006; Boyd and Abraham, 2001; Greene et al., 1994; Schrader et al., 2011). With this in mind, satellite SICF has been investigated as an indicator of the photophysiological status of phytoplankton (Abbott et al., 2001; Huot et al., 2013; Morrison, 2003; Morrison and Goodwin, 2010; Schallenberg et al., 2008; Westberry et al., 2013), with multiple studies proposing the use of Φ_{sat} as a proxy for phytoplankton nutrient stress (Huot et al., 2005; Letelier et al., 1997), particularly under Fe-limiting conditions (Behrenfeld et al., 2009; Browning et al.,

2014a; Westberry et al., 2013). In accordance with prior investigations, this study reported a significant, inverse relationship (r = -0.39, p = 0.05) between *in situ* [DFe] and remotely sensed Φ_{HB}, for stations located in the STZ and SAZ of the Atlantic Southern Ocean (Fig. 5.4). Bearing in mind that with only 26 stations the range of DFe variability was low, such that an improved relationship would be expected with more data spanning a greater range of ambient [DFe]. While this study demonstrated a clear inverse relationship between Φ_{sat} and *in situ* DFe, the influence of light and related fluorescence quenching cannot be disentangled. Attempts have been made to correct for the influence of light and related fluorescence quenching on Φ_{sat}, in an effort to resolve Fe-related signal (Behrenfeld et al., 2009; Browning et al., 2014a). The dynamic seasonal and zonal mixing regimes of the Southern Ocean makes the possibility of a one-size-fits-all fluorescence quenching correction unlikely. Future development of regionally targeted quenching corrections may lead to improved retrieval of the specific Fe-related signal, however, the extent of the influence of community structure, i.e. pigment composition, concentration, and arrangement, and the photoacclimation state of resident phytoplankton on Φ_{sat} remains uncertain, implying the use of Φ_{sat} as a direct proxy for any one driver will remain a challenge.

5.5.2 Decadal study of Φ_{HB}

A decadal study of Φ_{HB} was undertaken along the GoodHope line for the period of 2008-2018 (latitude 35-65°S, longitude 5°W to 5°E). The $\theta^{'}$ angle incorporated in the algorithm was an average $\theta^{'}$ angle obtained from all MODIS level 1A ocean colour data used to obtain Φ_{Huo} in this study ($\theta^{'} \approx 26°$, or 0.45 radians). The Φ_{HB} was averaged longitudinally and plotted over time using MODIS level 3 (monthly, 4 km) ocean colour products. The resulting Hovmöller diagram is displayed in Fig. 5.5. A clear seasonal cycle is apparent, with Φ_{HB} showing increased values over austral winter, and minima in summer. Peak values of Φ_{HB} are observed south of ∼52°S, typically in autumn.

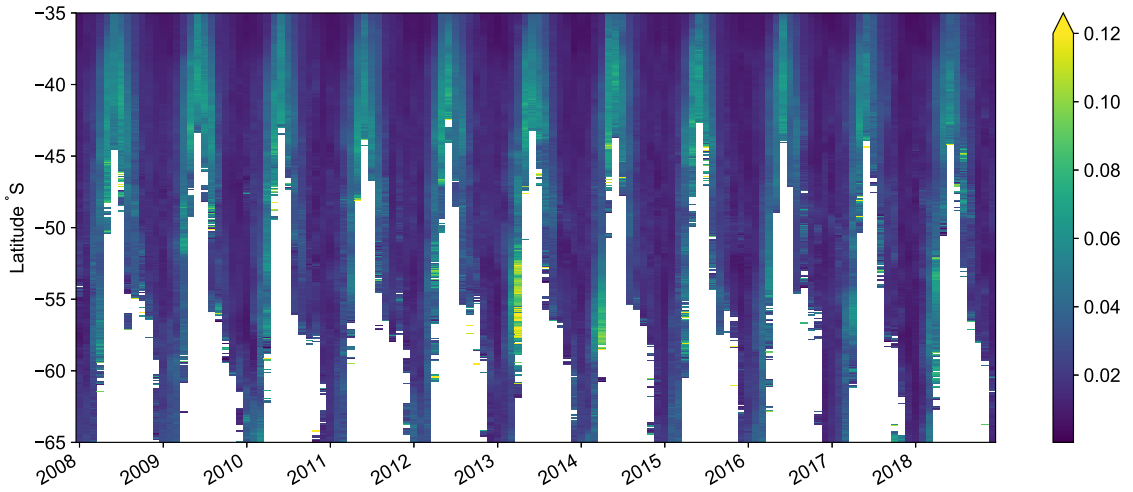

Figure 5.5: A decadal study of Φ_{HB} (2008-2018, latitude 35-65°S, longitude 5°W to 5°E), compiled using MODIS level 3 (monthly, 4 km) ocean colour products.

The decadal Φ_{HB} dataset was divided into Southern Ocean zones separated by the dominant fronts, namely the STZ (40-45°S), SAZ (45-50°S), PFZ (50-55°S), and AZ (55-70°S) (Fig. 5.6). The overall annual cycle of Φ_{HB} is fairly consistent, notably in the STZ, where winter data were limited to, due to the seasonal sea ice coverage. Peak Φ_{HB} was observed in the PFZ (summer 2013) and in the AZ, in the autumn of 2013 and 2014 and the spring 2016. Variability in summer minima in the SAZ and the PFZ are similar, but higher the AZ, representative of high intra-seasonal summer variability in Φ_{HB}.

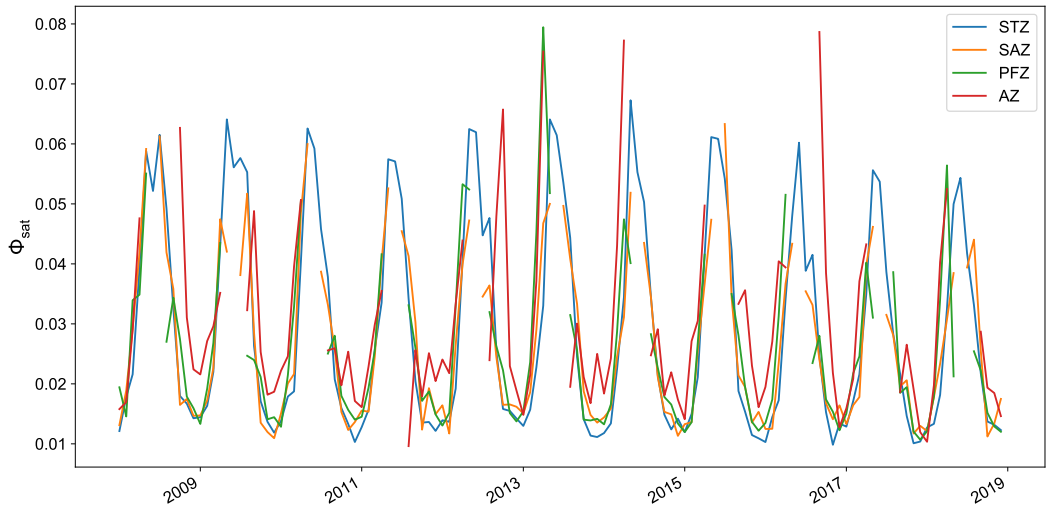

Figure 5.6: Inter-annual variability in Φ_{HB} across different Southern Ocean zones (STZ, SAZ, PFZ and AZ), between 2008 and 2018. Φ_{HB} was generated using MODIS level 3 monthly 4km ocean colour products.

The derivation of Φ_{sat} from monthly MODIS level 3 data should be seen as a first

order demonstration of application rather than an in-depth study, bearing in mind that uncertainty is being introduced from satellite-derived [chl-a] (Fig. 5.3) and through the use of an average $\theta^{'}$ value (Fig. 5.2). However, there is currently no way of obtaining $\theta^{'}$ from level 3 data, and its importance having been realised, a recommendation would be to focus on derivation of Φ_{sat} from level 2 data, with exact sensor viewing angles obtained from the associated level 1A products. Furthermore, it is important to note that as MODIS is not tilted, its maximum scan angle is about 50° as opposed to 60° (Zibordi et al., 2014), which implies an uncertainty maximum of approximately 45% (Section 5.3.3).

Monthly Φ_{HB} observations, over the period of 2008-2018, revealed a clear seasonal cycle of Φ_{HB} (Fig. 5.5), similar to that of Lin et al. (2016). In the Southern Ocean, the seasonal cycle is an established mode of variability, coupling physical mechanisms of climate forcing to ecosystem response in production, diversity and carbon export (Monteiro et al., 2011). Observations of Φ_{HB} in the SAZ displayed higher values over the austral winter than the summer. The seasonal evolution of phytoplankton biomass in the Southern Ocean has typically been ascribed to the seasonal cycle of solar radiation, impacting vertical stability through net heat flux, influencing vertical light and nutrient distribution (Arrigo et al., 2008; Boyd, 2002; Sverdrup, 1953). The amount of incident irradiance reaching the ocean surface is substantially greater in summer than winter, resulting in higher levels of qN employed by the resident phytoplankton and a lower Φ_{HB}. The effect of qN on Φ_F is well established (Maritorena et al., 2000; Morrison, 2003; Schallenberg et al., 2008), with research being undertaken to parameterise the influence of qN on Φ_{sat} in order to resolve remaining physiological information (Behrenfeld et al., 2009; Browning et al., 2014a). For example, in the Atlantic Southern Ocean, DFe levels are considered deplete during the summer and replete in the winter (Mtshali et al., 2019), however, due to the intense levels of qN experienced by summer populations, the anticipated low DFe/ high Φ_{sat} response is completely masked. As there is no current way to account for the photoacclimation state of the resident phytoplankton, which affects qN in a species-specific manner (Graff and Behrenfeld, 2018), a reliable qN-correction remains to be elucidated.

While there is a seasonal bias in satellite ocean colour observations over certain Southern Ocean zones, for example, due to limited coverage in the winter months as a result of increased ice and/or cloud cover, a good separation of inter-zonal variability was achieved (Fig. 5.6). The STZ, SAZ, and PFZ showed minor inter-annual variability, apart from a peak in the PFZ in the autumn of 2013. The MLD is known to control phytoplankton biomass over the summer months in the SAZ, through regulation of light and nutrient levels (Swart et al., 2015). Due to the impact of qN on Φ_{sat} during the summer months, fine scale events such as submesoscale features (du Plessis et al., 2017) or subseasonal

storms (Nicholson et al., 2016), deepening the MLD and leading to nutrient entrainment from depth (Ryan-Keogh et al., 2018), are not resolved. During the autumn months, peaks of Φ_{sat} are observed in the PFZ and AZ, which may in part be due to a reduction in light levels and alleviation of fluorescence quenching. This may also be reminiscent of late summer blooms, associated with highly stratified waters and diatom dominance (Arrigo et al., 2000; Arrigo and McClain, 1994; Arrigo et al., 1998; Goffart et al., 2000). In general, years characterised by heavy sea-ice coverage are associated with increased cloudiness, delayed phytoplankton blooms and lower annual production than years with lighter sea ice (Arrigo and van Dijken, 2004). The community composition, bloom progression and high Φ_{HB} values obtained for the Atlantic Southern Ocean AZ are likely due to an interplay between the sea ice, light, and nutrient conditions.

5.6 Conclusion and future recommendations

In situ MFL-derived $\Phi_F(435)$ (Chapter 4) was used to validate three existing Φ_{sat} algorithms, developed by Babin et al. (1996b), Huot et al. (2005), and Behrenfeld et al. (2009). The Φ_{sat} algorithms, and their associated variants, highlighted two important features that need to be addressed in future Φ_{sat} algorithm development, the first being the need for a dynamic Q_a^* factor (Babin et al., 1996b); if Φ_{sat} is to be obtained accurately, careful corrections are required to account for the absorption of the emitted radiation both inside the cell and within the water column. The behaviour of light absorption and attenuation in the water column was accounted for through the inclusion of the β_Φ term by Huot et al. (2005) (and during processing by (Behrenfeld et al., 2009)). An inclusive Φ_{sat} algorithm would ideally comprise both of these factors. Furthermore, an increase in *in situ* Φ_F(sc) sampling frequency would afford the possibility of more satellite match-ups, providing much needed insight into the development and improvement of existing Φ_{sat} algorithms. Increased *in situ* sampling in general would aid in the advancement of additional standard ocean colour algorithms, particularly with those that lose accuracy at high latitudes.

The sensitivity analysis revealed that the Φ_{sat} of all three algorithms decreased with increasing chl-*a*, a likely result of the package effect. While it is apparent from the sensitivity study that light levels are inversely related to Φ_{sat}, changes in magnitude of Φ_{sat} detected in the field can not solely be attributed to fluorescence quenching. Specifically, a reduction in Φ_{sat} from qN expressed at any given saturating iPAR differs between phytoplankton acclimated to different light environments. Photoacclimation plays an important role as the physical environment changes (e.g. incident light, mixing depth), as well as

in response to self-shading that occurs under bloom conditions. While attempts have been made to constrain qN, in order to extract additional photophysiological signals such as Fe limitation (Behrenfeld et al., 2009; Browning et al., 2014a), it is not yet possible to account for species-specific acclimation. The significant inverse relationship observed between Fe and Φ_{HB} in this study was in accordance with previous studies, however, before Φ_{sat} can be used to identify Fe-limited regions, the effects of incident irradiance on resident phytoplankton, in terms of photoacclimation and qN, needs to be properly characterised. Future work would include the development of a photoacclimation-dependent qN-correction for satellite fluorescence data, which will involve narrowing the spatial and temporal range of Φ_{sat} measurements.

While serving as a proof-of-concept study, the decadal analysis of Φ_{HB} (derived from MODIS monthly level 3 products), over the GoodHope Line in the Atlantic Southern Ocean, revealed a strong seasonal cycle of Φ_{HB}. The lower Φ_{HB} values reported over the austral summer are likely related to the solar seasonal cycle, with qN suppressing the summer signal in response to high incident irradiance. The MIZ showed the greatest variability in Φ_{HB} out of all the Southern Ocean provinces, potentially due to inter-annual variation in sea ice extent and associated release of bioavailable Fe. As the cryosphere is implicit to seasonal dynamics, climate-mediated changes to Fe supply will thus influence the overall extent of phytoplankton growth, macronutrient drawdown and ultimately the strength and efficiency of the biological carbon pump. While the routine derivation of Φ_{sat} will allow for consistent monitoring of this globally important region, it is recommended that future Φ_{sat} algorithms in the region stem from well characterised level 2 ocean colour data, with particular emphasis on accounting for $\theta^{'}$ at the time of measurement.

To conclude, for the first time, *in situ* Φ_F measurements were used to validate three existing Φ_{sat} algorithms. While only a limited number of match-ups were retrieved (n = 6), results indicate a combined Babin et al. (1996b)/ Huot et al. (2005) approach would be well suited to the Southern Ocean. There is a critical need for overall increased *in situ* sampling in the region, to better understand the processes governing phytoplankton photophysiology and ultimately improve regional Φ_{sat} algorithms. The possibility of a global solution to deriving accurate Φ_{sat} measurements seems unlikely as the temporal and spatial variability in Φ_{sat} appears to be sufficiently large to preclude SICF-based investigations of phytoplankton dynamics over all but the smallest time and space windows.

Chapter 6

Thesis Summary

This study presents the novel calibration of a multi-excitation fluorometer for use in apparent Φ_F determination, the subsequent derivation of *in situ* Φ_F, and finally the validation of existing Φ_{sat} algorithms (Fig. 6.1).

Chapter 3 reported the re-direction of a Multi-Exciter Fluorometer (MFL, JFE Advantech Co., Ltd.) for use in *in situ* Φ_F derivation. The MFL, comprising 9 excitation LEDs (375, 400, 420, 435, 470, 505, 525, 570, and 590 nm), was originally designed to discriminate between phytoplankton species within a population based on their accessory pigment composition. The MFL was selected as a suitable option to obtain wavelength-specific Φ_F, and initially underwent an extensive radiometric characterisation to assess its precise functioning. The LEDs at waveband 570 nm, present in triplicate, were very sensitive to noise as they had intrinsically high internal gain settings to account for typically low absorption by phytoplankton at this wavelength. Two novel calibration approaches were applied to the the MFL, the first made use of fluorescent dyes of known quantum yields and spectral traits (ATTO665 and ATTO490LS), the second method made use of fluorescent plaques (Perspex 4T56) and plastic films to determine the MFL response as a function of distance. The apparent $\Phi_F(\lambda)$ derived through both approaches were in good agreement, with the dye calibration of ATTO490LS ultimately providing the most reliable results. Concerns were raised over the influence of scattering of light, both through elastic and inelastic processes. Contamination of the fluorescence signal by Raman scattering by water, particularly in the 525, 570, and 590 nm wavebands, will need to be accounted for in future studies.

Chapter 4 saw the derivation of *in situ* Φ_F from 66 stations in the Atlantic sector of the Southern Ocean, during the austral winter of 2012 and summer of 2013/ 2014. Both MFL-derived fluorescence measurements and processed absorption data underwent rigorous quality control before being utilised, together with the dye calibration factors ob-

tained in Chapter 3, in Φ_F derivation. All raw fluorescence and absorbance measurements were collected alongside a range of useful parameters that were used to investigate potential drivers of Φ_F variability, including pigment, macronutrient, and light measurements. The wavelength-specific $\Phi_F(\lambda)$ obtained for all stations were initially subjected to cluster analysis to identify statistically related spectral shapes and possible drivers of variability. While the influence of light and taxonomy on Φ_F was apparent, due to the limited dataset, it was not possible to ascertain the contribution of each component to variation in spectral shape. A similar conclusion was deduced from a statistical examination of the drivers of two representative Φ_F wavebands, namely $\Phi_F(435)$ and $\Phi_F(570)$. This is the first time *in situ*, wavelength-specific $\Phi_F(\lambda)$ has been derived in absolute units; the prospect of routine deployment of the MFL, combined with increased sampling frequency and inclusion of additional biogeochemical measurements (for example, [DFe]), will facilitate future investigations into a more comprehensive understanding of the drivers of Φ_F variability.

Chapter 5 detailed the validation of existing Φ_{sat} algorithms with *in situ* Φ_F measurements. Different versions of the Φ_{sat} algorithms were employed, to varying degrees of success. It was apparent that accounting for chl-*a* fluorescence reabsorption, the IOPs in the surrounding water column, and the sensor angle of observation was imperative to obtaining reliable Φ_{sat} measurements. A hybrid algorithm comprising these components was used to derive Φ_{sat} for stations co-located to *in situ* [DFe] measurements, revealing a significant negative relationship between the two. While the current focus is on utilising Φ_{sat} measurements as a proxy for Fe-limitation, separating the effects of light conditions on surface phytoplankton, which is dependent on the species composition and photoacclimation state of the population, remains to be fully elucidated. A proof-of-concept decadal study on MODIS level 3 data, using the hybrid Φ_{sat} algorithm, depicted a clear seasonal Φ_{sat} cycle in the Southern Ocean. To properly explore this observation, the effects of photoacclimation and fluorescence quenching need to be better characterised.

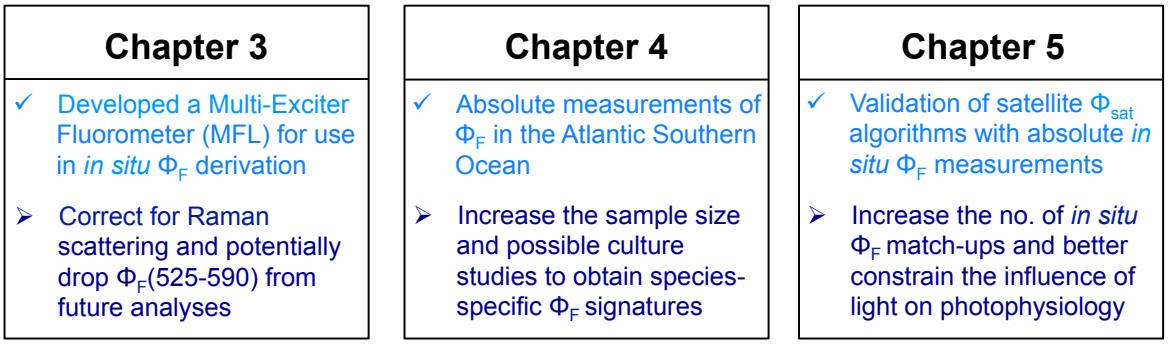

Figure 6.1: Thesis summary showing the novel output of each chapter (light blue) and examples of future considerations (dark blue).

This thesis reports a new capability for *in situ* Φ_F derivation. The MFL can be routinely deployed to increase the amount of *in situ* measurements, which will enhance the understanding of causal variability. The development of improved satellite products and more effective ecological, physiological and biogeochemical interpretation of satellite-observed phytoplankton fluorescence, will prove vastly beneficial to typically undersampled regions such as the climate relevant Southern Ocean.

Appendix A

Chapter 3 & 4

A.1 Station locations and absorption ancillary data

Table A.1: The date, time (GMT), specific co-ordinates, and ancillary absorption data of all stations used in this study are listed below. All measurements were collected from the ship's uncontaminated underway seawater supply (∼7 m below the surface). [chl-a] is in mg m^{-3} and $a^*_{ph}(675)$ is in m^2 mg chl^{-1}.

Station	Date & Time	Lat	Lon	[chl-a]	S-value	$a_{ph}(440)/a_{ph}(675)$	$a^*_{ph}(675)$
W013	12/07/11 04:58	-36.362	12.888	0.212	0.008	2.125	0.033
W015	12/07/11 08:56	-36.972	12.499	0.277	0.006	2.121	0.014
W017	12/07/11 12:57	-37.631	12.374	0.289	0.006	2.139	0.030
W036	12/07/13 07:59	-42.526	8.003	0.274	0.003	2.109	0.023
W042	12/07/14 01:50	-44.573	6.277	0.267	0.003	2.303	0.026
W045	12/07/14 08:57	-45.576	5.408	0.310	0.004	2.146	0.023
W050	12/07/14 20:04	-46.739	4.381	0.297	0.008	2.119	0.032
W052	12/07/15 01:59	-47.475	3.721	0.258	0.004	2.075	0.034
W055	12/07/15 08:57	-48.604	2.689	0.258	0.008	1.922	0.033
W056	12/07/15 20:07	-49.739	1.628	0.251	0.008	2.086	0.038
W062	12/07/16 02:00	-50.559	0.845	0.283	0.008	1.965	0.035
W064	12/07/16 08:57	-51.594	0.035	0.243	0.007	1.788	0.031
W074	12/07/17 06:58	-53.851	-0.101	0.168	0.007	1.940	0.035
W095	12/07/20 18:01	-56.198	8.871	0.132	0.006	2.073	0.028
W098	12/07/21 03:00	-55.421	12.417	0.169	0.005	2.085	0.024
W101	12/07/21 12:00	-54.711	15.859	0.186	0.008	2.020	0.032
W103	12/07/21 18:00	-54.211	18.152	0.175	0.011	1.879	0.037
W107	12/07/22 06:00	-52.974	23.027	0.149	0.004	1.899	0.035
W109	12/07/22 18:00	-52.198	24.893	0.154	0.002	1.970	0.029
W118	12/07/24 09:00	-50.655	34.559	0.195	0.006	1.961	0.032
W119	12/07/24 12:00	-50.817	35.695	0.189	0.008	2.064	0.040
W128	12/07/26 19:30	-46.502	41.844	0.201	0.006	2.035	0.038
W139	12/07/30 04:00	-44.919	36.496	0.270	0.004	2.137	0.035
GHS15	13/11/30 02:55	-37.032	12.379	0.712	0.007	2.068	0.034
GHS21	13/11/30 15:00	-38.955	10.883	0.761	0.012	2.164	0.036
GHS25	13/11/30 23:54	-40.721	9.483	0.316	0.007	2.294	0.033
GHS29	13/12/01 08:08	-42.398	8.113	0.510	0.010	1.834	0.032

GHS37	13/12/01 04:03	-44.192	7.472	0.539	0.008	1.878	0.033
GHS39	13/12/02 08:04	-44.78	6.909	0.690	0.009	1.713	0.029
GHS43	13/12/02 15:55	-45.932	5.774	1.093	0.009	1.543	0.025
GHS45	13/12/02 20:03	-46.519	5.187	1.015	0.015	1.666	0.024
GHS53	13/12/03 12:03	-48.195	3.524	0.484	0.009	1.805	0.033
GHS63	13/12/04 08:04	-50.232	1.313	0.802	0.011	1.645	0.029
GHS67	13/12/04 15:59	-51.204	0.198	0.669	0.010	1.656	0.031
GHS69	13/12/04 19:55	-51.882	0.049	0.449	0.009	1.748	0.036
GHS71	13/12/04 23:56	-52.588	0.191	0.276	0.011	1.835	0.032
GHS73	13/12/05 04:14	-53.38	0.01	0.380	0.012	2.114	0.033
GHS75	13/12/05 08:04	-54.147	-0.002	0.617	0.012	1.759	0.031
GHS77	13/12/05 15:15	-54.776	-0.007	0.407	0.010	1.913	0.028
GHS78	13/12/05 19:57	-55.515	-0.011	0.815	0.018	1.692	0.030
GHS80	13/12/05 23:55	-56.286	0	0.752	0.018	1.667	0.036
GHS84	13/12/06 08:06	-57.846	0.004	0.797	0.017	1.640	0.025
GHS88	13/12/06 15:58	-59.414	-0.011	0.790	0.009	1.637	0.026
GHS90	13/12/06 19:57	-60.117	0.112	0.929	0.008	1.604	0.027
BR14	14/01/05 15:59	-56.381	-32.903	0.405	0.009	2.001	0.038
BR25	14/01/07 16:02	-52.289	-30.057	1.174	0.010	1.415	0.030
BR35	14/01/08 12:09	-55.027	-23.982	0.756	0.011	1.578	0.029
BR49	14/01/09 16:02	-58.932	-15.284	0.487	0.009	1.890	0.034
BR51	14/01/09 19:50	-59.376	-14.308	0.651	0.010	1.848	0.032
BR53	14/01/10 00:01	-59.948	-12.961	0.363	0.009	1.910	0.037
BR55	14/01/10 04:05	-60.515	-11.655	1.186	0.011	1.684	0.029
GHN05	14/02/02 00:02	-65.028	-3.899	0.335	0.009	1.713	0.044
GHN07	14/02/02 04:05	-64.999	-3.432	0.314	0.010	1.826	0.040
GHN09	14/02/02 07:58	-64.184	-2.852	0.352	0.010	1.739	0.038
GHN11	14/02/02 12:00	-63.339	-2.239	0.417	0.010	1.718	0.031
GHN13	14/02/02 16:00	-62.525	-1.009	0.342	0.010	1.937	0.039
GHN21	14/02/03 08:01	-59.311	0	0.294	0.009	1.658	0.037
GHN23	14/02/03 12:00	-58.485	-0.01	0.713	0.007	1.786	0.028
GHN35	14/02/04 12:03	-54.054	-0.014	0.413	0.007	1.823	0.032
GHN37	14/02/04 20:03	-53.377	0	0.326	0.007	2.031	0.036
GHN39	14/02/05 00:04	-52.561	0	0.422	0.010	1.817	0.034
GHN41	14/02/05 04:04	-51.729	0	0.849	0.011	1.422	0.025
GHN58	14/02/07 16:04	-46.45	4.641	0.330	0.010	2.176	0.037
GHN60	14/02/07 20:04	-45.644	5.353	0.266	0.005	2.258	0.040
GHN77	14/02/10 22:01	-38.516	11.248	0.172	0.008	3.213	0.040
GHN79	14/02/11 02:03	-37.498	12.021	0.255	0.007	2.576	0.042

A.2 MFL-derived $\Phi_F(\lambda)$ means

Table A.2: $\Phi_F(\lambda)$ means for all stations. All values are reported in arbitrary units.

Station	Φ_{F375}	SD	Φ_{F400}	SD	Φ_{F420}	SD	Φ_{F435}	SD	Φ_{F470}	SD	Φ_{F505}	SD	Φ_{F525}	SD	Φ_{F570}	SD	Φ_{F590}	SD
W013	0.038	0.001	0.033	0.001	0.032	0.001	0.034	0.001	0.033	0.001	0.032	0.001	0.063	0.002	0.078	0.008	0.071	0.003
W015	0.035	0.002	0.031	0.001	0.030	0.001	0.031	0.002	0.030	0.002	0.030	0.001	0.060	0.002	0.074	0.008	0.070	0.003
W017	0.037	0.001	0.032	0.001	0.031	0.001	0.032	0.001	0.031	0.001	0.032	0.001	0.063	0.002	0.077	0.007	0.073	0.003
W036	0.049	0.003	0.043	0.003	0.043	0.003	0.045	0.003	0.045	0.003	0.043	0.003	0.075	0.003	0.089	0.008	0.081	0.004
W042	0.067	0.002	0.057	0.002	0.056	0.002	0.058	0.002	0.057	0.003	0.058	0.003	0.092	0.003	0.108	0.009	0.094	0.003
W045	0.055	0.002	0.047	0.002	0.048	0.002	0.049	0.002	0.050	0.003	0.049	0.002	0.082	0.002	0.097	0.009	0.086	0.003
W050	0.062	0.003	0.053	0.002	0.054	0.002	0.056	0.002	0.055	0.002	0.053	0.002	0.086	0.002	0.105	0.009	0.091	0.003
W052	0.071	0.002	0.061	0.001	0.061	0.002	0.063	0.002	0.062	0.002	0.059	0.002	0.091	0.002	0.105	0.007	0.095	0.003
W055	0.046	0.002	0.041	0.001	0.041	0.001	0.043	0.001	0.042	0.001	0.040	0.002	0.072	0.002	0.088	0.008	0.079	0.003
W056	0.053	0.002	0.046	0.002	0.047	0.001	0.049	0.001	0.048	0.002	0.047	0.002	0.082	0.002	0.097	0.006	0.084	0.003
W062	0.056	0.003	0.049	0.003	0.047	0.003	0.048	0.003	0.047	0.003	0.048	0.003	0.085	0.003	0.098	0.007	0.086	0.004
W064	0.045	0.003	0.040	0.003	0.039	0.003	0.040	0.003	0.039	0.003	0.040	0.003	0.075	0.004	0.089	0.008	0.079	0.004
W074	0.037	0.002	0.032	0.002	0.030	0.002	0.030	0.002	0.030	0.002	0.032	0.002	0.066	0.003	0.079	0.008	0.071	0.003
W095	0.012	0.002	0.012	0.002	0.011	0.001	0.011	0.001	0.011	0.001	0.012	0.002	0.036	0.003	0.072	0.017	0.048	0.008
W098	0.012	0.002	0.012	0.001	0.011	0.001	0.011	0.001	0.011	0.001	0.012	0.001	0.036	0.002	0.089	0.020	0.106	0.014
W101	0.011	0.002	0.011	0.001	0.010	0.001	0.011	0.001	0.011	0.001	0.011	0.001	0.037	0.002	0.027	0.008	0.039	0.003
W103	0.012	0.001	0.012	0.001	0.011	0.001	0.012	0.001	0.011	0.001	0.012	0.001	0.035	0.001	0.039	0.013	0.042	0.005
W107	0.014	0.001	0.014	0.001	0.013	0.001	0.013	0.001	0.013	0.001	0.014	0.001	0.038	0.002	0.025	0.007	0.037	0.002
W109	0.011	0.001	0.013	0.001	0.011	0.001	0.012	0.001	0.011	0.001	0.013	0.001	0.035	0.002	0.111	0.045	0.088	0.025
W118	0.015	0.002	0.015	0.002	0.015	0.001	0.014	0.002	0.014	0.001	0.014	0.001	0.040	0.002	0.041	0.008	0.050	0.003
W119	0.019	0.001	0.018	0.001	0.017	0.001	0.017	0.001	0.017	0.001	0.017	0.001	0.044	0.002	0.044	0.009	0.059	0.003
W128	0.055	0.002	0.048	0.002	0.048	0.002	0.048	0.002	0.047	0.002	0.046	0.002	0.079	0.003	0.089	0.009	0.083	0.003
W139	0.034	0.007	0.030	0.006	0.030	0.006	0.029	0.006	0.029	0.006	0.029	0.006	0.056	0.007	0.059	0.013	0.091	0.014
GHS15	0.006	0.000	0.007	0.000	0.006	0.000	0.006	0.000	0.005	0.000	0.005	0.000	0.017	0.001	0.021	0.003	0.023	0.001
GHS21	0.031	0.002	0.031	0.002	0.033	0.002	0.033	0.002	0.030	0.002	0.028	0.001	0.040	0.002	0.046	0.003	0.042	0.001
GHS25	0.030	0.001	0.029	0.001	0.031	0.001	0.032	0.002	0.031	0.002	0.025	0.001	0.036	0.001	0.038	0.003	0.041	0.001
GHS29	0.023	0.001	0.026	0.001	0.028	0.001	0.026	0.001	0.024	0.001	0.021	0.001	0.033	0.001	0.116	0.009	0.093	0.003
GHS37	0.034	0.001	0.032	0.001	0.034	0.001	0.036	0.001	0.034	0.002	0.028	0.001	0.040	0.001	0.044	0.003	0.055	0.001
GHS39	0.020	0.001	0.020	0.001	0.020	0.001	0.021	0.001	0.020	0.001	0.019	0.001	0.031	0.001	0.035	0.003	0.036	0.001
GHS43	0.038	0.003	0.037	0.002	0.037	0.003	0.038	0.003	0.037	0.003	0.034	0.002	0.047	0.003	0.049	0.004	0.047	0.002
GHS45	0.114	0.002	0.128	0.002	0.126	0.003	0.149	0.003	0.144	0.003	0.113	0.002	0.124	0.003	0.148	0.003	0.108	0.002

GHS53	0.014	0.001	0.017	0.001	0.013	0.000	0.016	0.001	0.010	0.001	0.013	0.001	0.023	0.001	0.189	0.006	0.173	0.012		
GHS63	0.057	0.004	0.056	0.004	0.067	0.005	0.069	0.005	0.064	0.005	0.058	0.004	0.073	0.005	0.074	0.005	0.059	0.003		
GHS67	0.042	0.003	0.044	0.003	0.047	0.004	0.047	0.004	0.042	0.004	0.040	0.003	0.057	0.004	0.059	0.004	0.049	0.002		
GHS69	0.036	0.002	0.036	0.002	0.041	0.002	0.044	0.002	0.039	0.002	0.031	0.002	0.047	0.002	0.062	0.003	0.047	0.001		
GHS71	0.026	0.002	0.027	0.002	0.029	0.002	0.030	0.002	0.026	0.002	0.021	0.002	0.036	0.002	0.080	0.003	0.054	0.002		
GHS73	0.025	0.002	0.025	0.002	0.027	0.002	0.027	0.002	0.027	0.002	0.018	0.001	0.034	0.002	0.138	0.003	0.078	0.001		
GHS75	0.019	0.002	0.020	0.001	0.021	0.002	0.020	0.002	0.019	0.002	0.017	0.002	0.032	0.002	0.037	0.003	0.035	0.002		
GHS77	0.018	0.001	0.022	0.001	0.020	0.001	0.023	0.001	0.021	0.001	0.016	0.001	0.030	0.001	0.147	0.005	0.061	0.002		
GHS78	0.068	0.004	0.072	0.004	0.060	0.003	0.077	0.004	0.074	0.005	0.051	0.003	0.085	0.005	0.341	0.019	0.122	0.004		
GHS80	0.094	0.005	0.106	0.005	0.110	0.008	0.101	0.009	0.090	0.005	0.071	0.004	0.105	0.006	0.351	0.015	0.183	0.014		
GHS84	0.038	0.003	0.041	0.003	0.041	0.003	0.037	0.003	0.037	0.003	0.036	0.003	0.050	0.003	0.054	0.004	0.047	0.002		
GHS88	0.038	0.002	0.040	0.002	0.041	0.002	0.039	0.002	0.036	0.003	0.034	0.002	0.049	0.002	0.143	0.004	0.067	0.002		
GHS90	0.091	0.002	0.101	0.002	0.094	0.007	0.085	0.005	0.094	0.003	0.077	0.002	0.087	0.002	0.301	0.007	0.152	0.006		
BR14	0.007	0.000	0.009	0.001	0.009	0.003	0.009	0.001	0.007	0.000	0.007	0.000	0.013	0.000	0.055	0.009	0.022	0.008		
BR25	0.021	0.001	0.021	0.002	0.023	0.003	0.024	0.002	0.021	0.002	0.021	0.002	0.029	0.002	0.026	0.002	0.041	0.003		
BR35	0.010	0.002	0.011	0.002	0.010	0.002	0.010	0.001	0.009	0.001	0.009	0.001	0.015	0.001	0.019	0.005	0.028	0.007		
BR49	0.011	0.001	0.012	0.002	0.011	0.001	0.010	0.001	0.009	0.001	0.008	0.001	0.014	0.001	0.039	0.013	0.035	0.010		
BR51	0.016	0.001	0.019	0.002	0.017	0.001	0.019	0.002	0.015	0.001	0.013	0.001	0.019	0.001	0.038	0.011	0.033	0.009		
BR53	0.017	0.001	0.017	0.001	0.020	0.001	0.020	0.001	0.016	0.001	0.014	0.001	0.020	0.001	0.025	0.005	0.026	0.005		
BR55	0.054	0.004	0.053	0.002	0.056	0.003	0.058	0.002	0.051	0.003	0.045	0.003	0.053	0.004	0.075	0.012	0.069	0.014		
GHN05	0.097	0.008	0.096	0.008	0.094	0.008	0.094	0.008	0.089	0.008	0.089	0.008	0.142	0.011	0.126	0.012	0.138	0.008		
GHN07	0.117	0.018	0.116	0.018	0.112	0.018	0.114	0.017	0.104	0.017	0.108	0.016	0.168	0.022	0.158	0.024	0.165	0.021		
GHN09	0.056	0.005	0.058	0.004	0.052	0.005	0.053	0.005	0.051	0.005	0.053	0.005	0.095	0.006	0.096	0.009	0.116	0.005		
GHN11	0.059	0.009	0.062	0.008	0.056	0.008	0.056	0.008	0.056	0.009	0.056	0.008	0.098	0.011	0.108	0.012	0.126	0.008		
GHN13	0.076	0.007	0.082	0.007	0.077	0.008	0.075	0.007	0.074	0.008	0.074	0.007	0.122	0.010	0.131	0.012	0.148	0.008		
GHN21	0.052	0.004	0.059	0.004	0.049	0.004	0.048	0.004	0.045	0.004	0.047	0.004	0.088	0.006	0.097	0.009	0.124	0.006		
GHN23	0.085	0.010	0.085	0.010	0.076	0.009	0.075	0.008	0.072	0.008	0.078	0.007	0.130	0.012	0.133	0.016	0.152	0.014		
GHN35	0.033	0.003	0.039	0.003	0.030	0.002	0.028	0.002	0.025	0.002	0.030	0.002	0.064	0.004	0.057	0.008	0.087	0.007		
GHN37	0.062	0.014	0.073	0.012	0.073	0.008	0.067	0.010	0.059	0.010	0.059	0.011	0.105	0.012	0.133	0.012	0.162	0.008		
GHN39	0.082	0.011	0.097	0.009	0.081	0.011	0.085	0.009	0.079	0.009	0.081	0.009	0.126	0.011	0.140	0.014	0.171	0.014		
GHN41	0.090	0.009	0.112	0.009	0.096	0.008	0.100	0.009	0.101	0.009	0.101	0.008	0.164	0.012	0.155	0.014	0.193	0.006		
GHN58	0.040	0.002	0.060	0.002	0.051	0.002	0.042	0.002	0.037	0.003	0.037	0.002	0.068	0.003	0.142	0.016	0.191	0.022		
GHN60	0.043	0.003	0.054	0.004	0.042	0.003	0.047	0.004	0.045	0.003	0.041	0.003	0.070	0.003	0.123	0.008	0.155	0.007		
GHN77	0.015	0.001	0.024	0.001	0.019	0.001	0.016	0.000	0.012	0.001	0.013	0.001	0.037	0.001	0.087	0.010	0.108	0.011		
GHN79	0.024	0.002	0.031	0.001	0.027	0.001	0.025	0.002	0.023	0.002	0.025	0.002	0.050	0.002	0.114	0.013	0.164	0.008		

Appendix B

Chapter 4

B.1 Drivers of Φ_F variability: Table 1

Table B.1: Values of the potential drivers of $\Phi_F(\lambda)$ variability are listed below (part 1/2). All measurements were collected from the ship's uncontaminated underway seawater supply (∼7 m below the surface). Temp is in °C, NO_3 and $Si(OH)_4$ in μM, chl-a in mg m^{-3}, and PAR in mol m^{-2} s^{-1}.

Station	Temp	NO_3	$Si(OH)_4$	chl-a	Dd + Dt	Dt / Dd + Dt	Σ PAR20	Σ PAR6	Σ PAR12	Σ PAR24
W013	17.05	1.80	3.00	0.21	0.03	0.00	0.000	0.000	0.004	0.504
W015	16.52	1.40	2.70	0.28	0.04	0.00	0.007	0.002	0.002	0.503
W017	15.74	1.40	2.30	0.29	0.05	0.09	0.050	0.216	0.216	0.400
W036	10.68	9.70	2.00	0.27	0.05	0.08	0.000	0.000	0.000	0.540
W042	7.75	16.90	3.00	0.27	0.05	0.07	0.000	0.000	0.217	0.576
W045	8.33	16.20	2.90	0.31	0.05	0.07	0.000	0.000	0.000	0.576
W050	6.33	17.90	3.30	0.30	0.05	0.07	0.000	0.044	0.120	0.120
W052	5.60	19.40	3.70	0.26	0.05	0.00	0.000	0.000	0.047	0.120
W055	4.60	18.40	6.70	0.26	0.05	0.06	0.000	0.000	0.000	0.120
W056	3.96	18.60	6.90	0.25	0.05	0.06	0.000	0.057	0.133	0.133
W062	2.84	18.90	15.60	0.28	0.06	0.07	0.000	0.000	0.061	0.133
W064	2.74	19.20	20.30	0.24	0.05	0.00	0.000	0.000	0.000	0.133
W074	0.99	25.00	43.40	0.17	0.05	0.09	0.000	0.000	0.000	0.112
W095	-1.13	24.9 6	9.60	0.13	0.06	0.00	0.000	0.028	0.032	0.032
W098	-0.69	22.69	62.25	0.17	0.05	0.06	0.000	0.000	0.013	0.032
W101	-0.09	20.09	55.60	0.19	0.06	0.09	0.006	0.019	0.019	0.046
W103	0.23	24.47	64.00	0.18	0.06	0.11	0.000	0.053	0.072	0.072
W107	0.62	28.83	61.50	0.15	0.06	0.08	0.000	0.000	0.000	0.072
W109	0.72	28.87	59.12	0.15	0.07	0.10	0.000	0.035	0.063	0.063
W118	2.91	21.68	22.40	0.20	0.06	0.16	0.007	0.006	0.006	0.158
W119	2.69	20.14	18.60	0.19	0.06	0.13	0.017	0.079	0.079	0.172
W128	5.00	20.31	5.84	0.20	0.07	0.09	0.000	0.025	0.132	0.134
W139	7.15	15.89	4.76	0.27	0.05	0.12	0.000	0.000	0.000	0.362
GHS15	21.55	0.53	0.09	0.71	0.05	0.07	0.000	0.000	0.155	0.978
GHS21	20.45	0.66	0.33	0.76	0.13	0.15	0.034	0.444	0.623	0.771
GHS25	16.06	4.03	0.83	0.32	0.17	0.09	0.000	0.002	0.344	0.723
GHS29	11.73	7.94	0.89	0.51	0.14	0.13	0.023	0.059	0.059	0.671

GHS37	8.49	19.76	1.13	0.54	0.12	0.06	0.001	0.000	0.060	0.723
GHS39	7.80	20.31	1.40	0.69	0.16	0.12	0.019	0.085	0.085	0.574
GHS43	6.78	19.58	1.46	1.09	0.22	0.11	0.061	0.563	0.801	0.855
GHS45	6.71	13.08	1.26	1.01	0.16	0.03	0.000	0.331	0.870	0.953
GHS53	5.64	22.80	1.11	0.48	0.16	0.14	0.047	0.377	0.419	0.940
GHS63	3.55	25.86	0.95	0.80	0.11	0.09	0.011	0.029	0.029	0.617
GHS67	3.53	24.53	1.25	0.67	0.11	0.12	0.032	0.384	0.470	0.554
GHS69	2.66	29.72	2.26	0.45	0.13	0.08	0.001	0.203	0.521	0.547
GHS71	2.23	29.21	1.46	0.28	0.12	0.00	0.000	0.015	0.347	0.547
GHS73	1.30	19.39	1.22	0.38	0.13	0.08	0.002	0.001	0.067	0.548
GHS75	0.81	29.48	1.51	0.62	0.14	0.14	0.016	0.079	0.079	0.597
GHS77	0.91	29.85	1.37	0.41	0.17	0.13	0.017	0.322	0.468	0.586
GHS78	0.60	31.10	1.43	0.81	0.15	0.06	0.001	0.115	0.468	0.542
GHS80	0.53	32.23	1.66	0.75	0.17	0.06	0.000	0.015	0.198	0.542
GHS84	0.07	31.39	1.52	0.80	0.14	0.14	0.028	0.076	0.077	0.538
GHS88	-0.15	24.97	1.44	0.79	0.20	0.13	0.020	0.256	0.419	0.476
GHS90	-0.31	13.48	1.56	0.93	0.16	0.06	0.002	0.122	0.405	0.476
BR14	2.33	34.21	28.05	0.41	0.22	0.16	0.056	0.361	0.411	0.519
BR25	4.24	51.40	33.86	1.17	0.12	0.11	0.020	0.395	0.470	0.764
BR35	2.53	16.13	25.38	0.76	0.12	0.11	0.019	0.198	0.199	1.915
BR49	1.28	34.42	73.57	0.49	0.13	0.11	0.019	0.225	0.326	0.381
BR51	1.04	58.92	92.14	0.65	0.19	0.09	0.005	0.147	0.371	0.395
BR53	1.11	48.54	69.40	0.36	0.30	0.08	0.000	0.027	0.217	0.396
BR55	1.63	28.55	57.40	1.19	0.23	0.07	0.001	0.000	0.069	0.396
GHN05	2.34	19.94	0.89	0.33	0.15	0.06	0.000	0.009	0.066	0.174
GHN07	2.53	20.73	0.95	0.31	0.17	0.05	0.001	0.001	0.028	0.175
GHN09	2.34	20.25	1.07	0.35	0.16	0.09	0.010	0.036	0.038	0.199
GHN11	2.03	21.13	1.17	0.42	0.20	0.13	0.031	0.131	0.138	0.204
GHN13	2.25	14.00	0.98	0.34	0.17	0.09	0.006	0.182	0.258	0.288
GHN21	2.41	20.84	1.16	0.29	0.17	0.10	0.014	0.044	0.045	0.312
GHN23	2.45	21.64	1.16	0.71	0.19	0.11	0.027	0.171	0.184	0.350
GHN35	2.98	18.16	1.53	0.41	0.17	0.22	0.027	0.178	0.187	0.333
GHN37	2.97	29.12	1.56	0.33	0.20	0.08	0.000	0.138	0.482	0.495
GHN39	3.51	31.33	1.26	0.42	0.16	0.07	0.000	0.009	0.307	0.495
GHN41	4.10	25.71	1.35	0.85	0.12	0.05	0.000	0.000	0.042	0.495
GHN58	8.30	14.96	1.62	0.33	0.13	0.11	0.013	0.267	0.361	0.421
GHN60	8.37	16.12	0.92	0.27	0.11	0.00	0.000	0.081	0.375	0.386
GHN77	20.74	1.03	0.31	0.17	0.04	0.00	0.000	0.012	0.361	0.603
GHN79	20.36	1.17	0.31	0.25	0.05	0.00	0.000	0.000	0.059	0.603

B.2 Drivers of Φ_F variability: Table 2

Table B.2: Values of the potential drivers of $\Phi_F(\lambda)$ variability are listed below (part 2/2). Micro, Nano, and Pico (micro-, nano-, and picoplankton) in %; Fuco, Hex, Allo, and Zea (fucoxanthin, 19' hexanoyloxyfucoxanthin, alloxanthin, and zeaxanthin) are all normalised to [chl-*a*]; Prasinos, Chloros, Cryptos, Diatoms, Dinos, Haptos, and Syn (prasinophytes, chlorophytes, cryptophytes, diatoms, dinoflagellates, haptophytes, and *Synechococcus*) in %.

Station	Micro	Nano	Pico	Fuco	Hex	Allo	Zea	Prasinos	Chloros	Cryptos	Diatoms	Dinos	Haptos	Syn
W013	18.19	53.60	28.20	0.07	0.22	0.02	0.08	22.47	2.92	12.21	4.16	1.90	29.40	26.94
W015	15.66	50.30	34.04	0.06	0.24	0.03	0.09	19.29	9.73	13.60	2.54	1.73	28.00	25.12
W017	16.00	51.29	32.71	0.07	0.25	0.02	0.08	20.69	9.79	10.64	3.31	1.62	29.47	24.50
W036	19.89	57.50	22.61	0.07	0.32	0.01	0.03	18.32	13.52	7.38	2.30	4.61	44.39	9.47
W042	18.59	47.81	33.60	0.08	0.29	0.01	0.05	34.57	12.71	6.69	3.43	3.22	29.42	9.95
W045	21.32	52.47	26.20	0.09	0.32	0.01	0.04	27.14	11.70	6.56	4.21	4.32	35.29	10.78
W050	18.61	48.78	32.61	0.08	0.27	0.01	0.05	32.71	9.38	6.44	3.99	3.09	34.43	9.96
W052	16.10	55.53	28.37	0.08	0.36	0.01	0.02	32.45	12.30	4.36	2.60	2.36	45.94	0.00
W055	29.94	50.67	19.39	0.13	0.27	0.02	0.02	34.13	1.83	10.74	12.00	4.01	34.35	2.93
W056	36.51	43.57	19.92	0.15	0.23	0.02	0.02	32.14	1.67	9.53	12.85	5.95	34.57	3.29
W062	52.12	35.85	12.03	0.25	0.19	0.02	0.01	10.55	1.30	18.09	46.15	5.43	18.35	0.13
W064	55.61	35.65	8.74	0.30	0.19	0.02	0.00	8.45	0.61	20.12	51.81	3.71	15.29	0.00
W074	52.21	41.78	6.01	0.28	0.22	0.02	0.00	5.06	0.71	18.14	50.68	3.23	21.80	0.38
W095	51.52	47.02	1.45	0.33	0.29	0.02	0.00	0.00	1.29	19.70	51.42	1.92	25.67	0.00
W098	62.31	34.57	3.11	0.41	0.20	0.01	0.00	2.62	0.36	8.65	68.01	0.00	19.85	0.51
W101	63.99	27.88	8.14	0.36	0.13	0.02	0.00	7.21	0.82	13.24	65.69	1.22	11.83	0.00
W103	64.66	27.79	7.56	0.37	0.13	0.02	0.00	7.71	0.00	13.76	64.96	1.45	12.12	0.00
W107	53.21	43.73	3.05	0.30	0.21	0.02	0.00	0.00	2.54	17.16	57.10	1.54	21.66	0.00
W109	51.82	45.79	2.39	0.28	0.22	0.02	0.00	0.00	1.98	20.61	52.22	2.08	23.11	0.00
W118	22.25	52.75	25.01	0.11	0.29	0.01	0.01	25.50	12.57	5.96	9.26	2.38	43.26	1.08
W119	38.30	43.42	18.27	0.20	0.23	0.02	0.01	29.14	2.31	11.90	16.78	2.08	37.79	0.00
W128	21.21	56.81	21.97	0.11	0.33	0.01	0.01	25.31	11.89	6.36	9.66	2.28	43.97	0.52
W139	19.91	55.68	24.42	0.10	0.35	0.01	0.02	24.42	11.97	5.86	5.75	2.70	46.80	2.49
GHS15	48.24	30.30	21.46	0.27	0.18	0.02	0.12	13.78	1.78	5.17	40.75	2.04	24.68	11.79
GHS21	44.00	28.06	27.94	0.23	0.16	0.02	0.16	11.28	6.63	5.22	35.83	2.22	22.99	15.83
GHS25	26.79	65.81	7.41	0.17	0.46	0.01	0.02	0.00	13.52	1.47	23.62	2.16	57.80	1.41
GHS29	49.13	41.95	8.92	0.30	0.30	0.00	0.02	3.30	9.96	0.27	60.92	4.44	20.42	0.69
GHS37	55.64	34.79	9.57	0.19	0.18	0.02	0.04	12.61	0.00	6.64	32.48	13.96	30.91	3.41
GHS39	52.66	39.85	7.49	0.24	0.14	0.02	0.01	10.64	0.57	12.12	37.23	3.47	35.21	0.76
GHS43	63.33	33.35	3.32	0.36	0.11	0.01	0.00	5.89	0.00	3.64	40.22	2.24	47.95	0.06

GHS45	63.85	32.64	3.51	0.35	0.11	0.00	0.00	4.96	1.28	1.38	44.89	1.68	45.82	0.00	
GHS53	55.64	38.34	6.02	0.33	0.23	0.01	0.01	11.21	0.36	3.85	40.41	3.39	40.66	0.13	
GHS63	75.83	21.64	2.53	0.43	0.15	0.01	0.00	5.00	0.29	5.04	57.55	9.42	22.65	0.04	
GHS67	75.66	21.43	2.91	0.46	0.15	0.01	0.00	5.92	0.18	5.64	56.92	7.54	23.78	0.03	
GHS69	74.65	22.48	2.87	0.42	0.14	0.01	0.00	4.67	0.81	5.58	58.74	6.23	23.92	0.05	
GHS71	69.01	26.88	4.11	0.41	0.16	0.01	0.01	6.00	0.65	3.67	60.14	1.73	27.07	0.73	
GHS73	63.10	35.02	1.88	0.39	0.23	0.01	0.00	3.12	0.29	6.24	55.41	1.35	33.42	0.17	
GHS75	74.56	24.22	1.22	0.46	0.15	0.01	0.00	0.83	0.61	4.35	69.39	0.00	24.61	0.21	
GHS77	66.06	32.11	1.83	0.41	0.21	0.01	0.00	2.82	0.29	5.96	57.63	1.38	31.71	0.23	
GHS78	87.53	11.96	0.50	0.58	0.08	0.00	0.00	0.57	0.33	2.75	78.40	1.56	16.39	0.00	
GHS80	86.79	13.21	0.00	0.61	0.09	0.00	0.00	0.00	0.00	2.10	75.01	1.31	21.58	0.00	
GHS84	76.68	23.32	0.00	0.54	0.17	0.00	0.00	0.00	0.00	1.25	68.35	0.00	30.39	0.00	
GHS88	75.26	24.74	0.00	0.55	0.20	0.00	0.00	0.00	0.00	0.00	68.82	0.00	31.18	0.00	
GHS90	47.61	52.39	0.00	0.35	0.42	0.00	0.00	0.26	0.00	1.73	35.93	0.00	62.08	0.00	
BR14	81.28	17.65	1.07	0.62	0.13	0.01	0.01	0.35	0.00	5.21	73.21	0.00	20.03	1.21	
BR25	83.06	16.39	0.55	0.54	0.12	0.00	0.00	1.10	0.00	0.76	69.72	4.50	23.86	0.07	
BR35	73.34	26.35	0.30	0.44	0.18	0.00	0.00	0.50	0.00	2.23	62.71	2.79	31.50	0.27	
BR49	32.57	67.18	0.25	0.21	0.51	0.00	0.00	0.01	0.00	1.86	19.29	1.27	77.27	0.29	
BR51	50.86	44.55	4.59	0.30	0.29	0.01	0.01	7.78	0.76	5.20	40.90	1.10	44.09	0.17	
BR53	85.24	14.76	0.00	0.59	0.11	0.00	0.00	0.82	0.00	0.00	78.16	2.10	18.92	0.00	
BR55	79.16	20.01	0.82	0.58	0.16	0.01	0.00	2.04	0.00	2.78	63.66	0.00	31.52	0.00	
GHN05	72.95	26.37	0.68	0.52	0.20	0.00	0.01	0.00	0.00	0.09	64.45	0.00	34.69	0.77	
GHN07	71.31	28.10	0.59	0.47	0.21	0.00	0.01	0.00	0.00	0.10	62.01	1.93	35.31	0.64	
GHN09	69.19	30.32	0.49	0.45	0.22	0.00	0.01	0.00	0.00	1.91	59.42	1.97	36.18	0.52	
GHN11	53.95	46.05	0.00	0.36	0.36	0.00	0.00	0.00	0.00	0.00	43.32	1.95	54.73	0.00	
GHN13	62.92	36.68	0.39	0.40	0.27	0.00	0.00	0.00	0.00	1.88	51.94	2.11	43.65	0.42	
GHN21	66.90	32.44	0.66	0.46	0.25	0.00	0.01	0.00	0.00	2.02	54.98	2.07	40.19	0.74	
GHN23	85.89	13.06	1.05	0.67	0.11	0.00	0.00	0.65	0.74	1.06	69.96	3.19	24.25	0.17	
GHN35	71.02	28.42	0.56	0.43	0.16	0.01	0.01	0.01	0.00	4.39	66.15	1.67	27.20	0.57	
GHN37	66.50	32.30	1.19	0.40	0.19	0.01	0.00	0.00	1.82	4.11	59.66	1.44	32.97	0.00	
GHN39	72.26	27.40	0.34	0.45	0.18	0.01	0.00	0.00	0.00	3.37	61.22	4.12	30.94	0.35	
GHN41	77.83	22.17	0.00	0.34	0.18	0.00	0.00	0.00	0.00	0.81	48.69	24.35	26.15	0.00	
GHN58	23.48	63.88	12.64	0.13	0.43	0.00	0.01	22.11	3.25	0.07	17.65	2.24	54.68	0.00	
GHN60	17.05	61.80	21.15	0.08	0.43	0.00	0.01	36.03	3.38	1.33	5.99	2.57	50.71	0.00	
GHN77	10.28	24.71	65.01	0.03	0.16	0.00	0.56	0.00	0.00	0.00	1.27	5.25	29.14	64.35	
GHN79	13.12	45.56	41.32	0.05	0.26	0.00	0.28	4.25	8.22	0.22	4.95	3.18	54.28	24.90	

B.3 K-means clustering

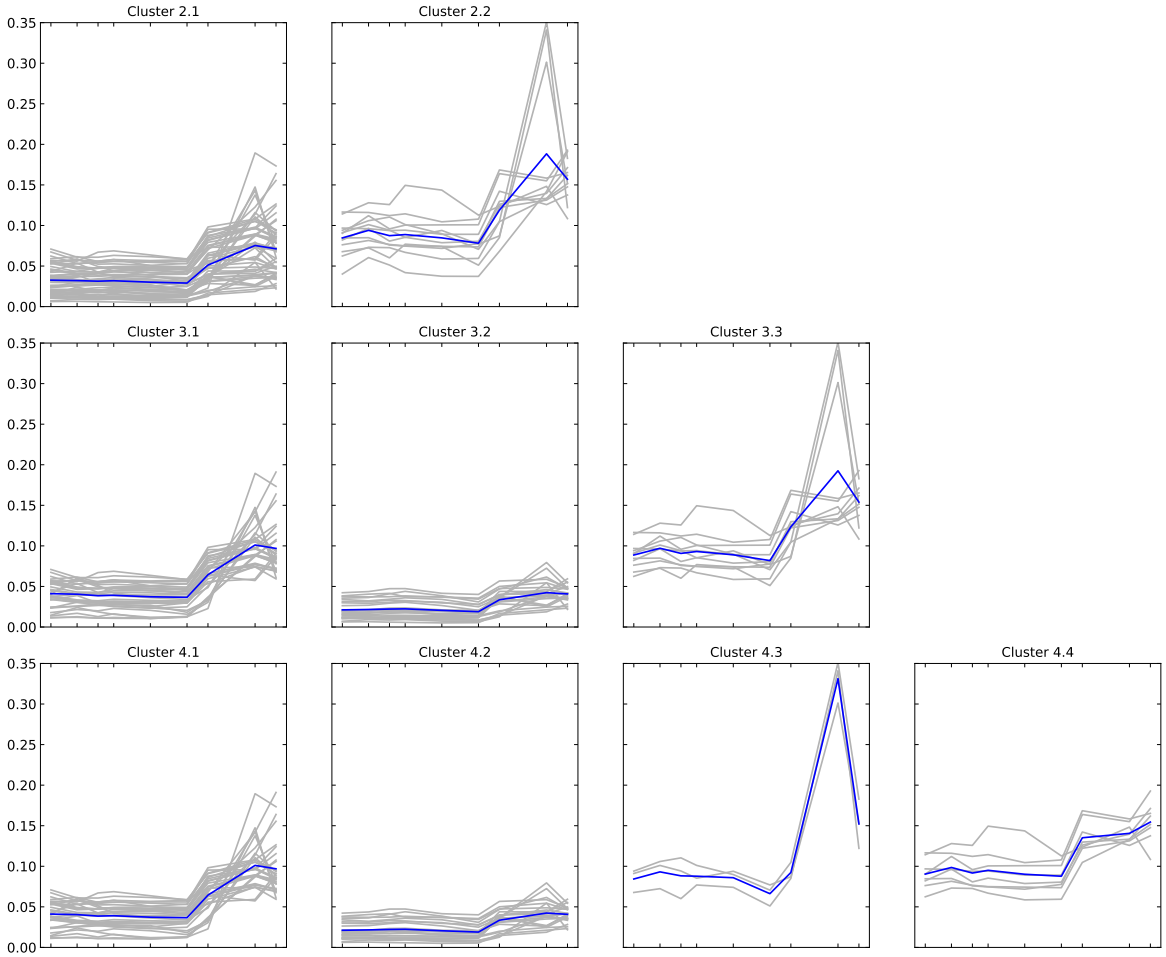

Figure B.1: K-means clustering of $\Phi_F(\lambda)$ spectra. All $\Phi_F(\lambda)$ were subjected to hard clustering into 2, 3, or 4 groups, with the y-scale illustrating the magnitude of $\Phi_F(\lambda)$, and the x-scale depicting the 9 MFL LED excitation wavebands for which the wavelength-specific $\Phi_F(\lambda)$ was derived (λ (nm)).

Appendix C

Chapter 5

C.1 Validation of Φ_{sat} algorithms

Table C.1: MODIS level 2 (daily, 1 km) ocean colour products used to derive Φ_{sat} (extracted from 3×3 megapixel grids), that coincided with *in situ* MFL-derived $\Phi_F(435)$ stations. Time is in GMT; Δtime is the time difference between the station and the satellite overpass (negative times are prior to station times and positive are post); theta is the sensor zenith angle in radians; chl mean in mg m^{-3}; flh mean in W m^{-2} μm^{-1} sr^{-1}; ipar mean in E m^{-2} s^{-1}; K_d mean in m^{-1}.

Station	Date	Time	Lat	Lon	Δtime	theta	chl pix	chl mean	chl std	flh pix	flh mean	flh std	ipar pix	ipar mean	ipar std	K_d pix	K_d mean	K_d std
GHS39	13/12/02	08:04	-44.78	6.909	5.85	0.44	8	0.318	0.002	9	0.0928	0.0114	8	1724.76	1.00	8	0.0576	0.0003
GHS43	13/12/02	15:55	-45.932	5.774	-2	0.27	9	0.9036	0.0159	9	0.1512	0.0117	9	1733.77	0.98	8	0.1003	0.0006
GHS45	13/12/02	20:03	-46.519	5.187	-6.13	0.18	9	0.9102	0.0202	9	0.2082	0.0086	8	1728.38	0.86	9	0.0991	0.0012
GHN09	14/02/02	07:58	-64.184	-2.852	-17.05	0.04	9	0.3676	0.0053	9	0.0801	0.0173	9	1283.68	0.72	9	0.0624	0.0008
GHN35	14/02/04	12:03	-54.054	-0.014	1.78	0.58	9	0.2134	0.0153	8	0.0954	0.0218	8	1619.20	3.11	8	0.0468	0.001
GHN41	14/02/05	04:04	-51.729	0	-14.23	0.56	8	0.2897	0.0078	9	0.1442	0.018	8	1670.10	1.01	9	0.0603	0.0015

C.2 Statistical metrics of Φ_{sat} algorithm performance

Table C.2: Φ_{sat} values derived from Babin et al. (1996b), Huot et al. (2005), and Behrenfeld et al. (2009) are listed below; All Φ_{sat} "original" values are from the original models, with data treated as stated in their respective papers; "*is* chl" refers to addition of *in situ* chl-*a*, "$\overline{a}^*_\phi$(full)" refers to the addition of *in situ* $\overline{a}^*_\phi$ over the full visible spectrum (400-700 nm); "$\overline{a}^*_\phi$(nar.)" refers to the addition of *in situ* $\overline{a}^*_\phi$ over the portion of the spectrum covering the 435 nm region (415-455 nm). Φ_{sat} "Babin" values are the output of the Huot et al. (2005) and Behrenfeld et al. (2009) equations substituted with the Babin et al. (1996b) $\overline{a}^*_\phi$ and Q^*_a terms. The addition of the qN correction employed by Behrenfeld et al. (2009) generates "qN cor." values, and the difference between the inclusion of the correction and original values are listed under "SD".

Babin				
Station	Φ_{sat} original	Φ_{sat} *is* chl	Φ_{sat} $\overline{a}^*_\phi$(full)	Φ_{sat} $\overline{a}^*_\phi$(nar.)
GHN09	0.0382	0.0392	0.0274	0.0134
GHN35	0.0492	0.0337	0.0283	0.0128
GHN41	0.0605	0.0328	0.0313	0.0169
GHS39	0.0358	0.0230	0.0185	0.0090
GHS43	0.0320	0.0287	0.0249	0.0125
GHS45	0.0440	0.0413	0.0329	0.0174

Huot					
Station	Φ_{sat} original	Φ_{sat} Babin	Φ_{sat} *is* chl	Φ_{sat} $\overline{a}^*_\phi$(full)	Φ_{sat} $\overline{a}^*_\phi$(nar.)
GHN09	0.0141	0.0122	0.0126	0.0088	0.0043
GHN35	0.0101	0.0174	0.012	0.01	0.0046
GHN41	0.0075	0.022	0.0119	0.0114	0.0062
GHS39	0.006	0.0123	0.0079	0.0063	0.0031
GHS43	0.0073	0.0116	0.0105	0.0091	0.0046
GHS45	0.0099	0.0157	0.0148	0.0118	0.0062

Beh.							
Station	Φ_{sat} original	Φ_{sat} qN cor.	Φ_{sat} SD	Φ_{sat} Babin	Φ_{sat} *is* chl	Φ_{sat} $\overline{a}^*_\phi$(full)	Φ_{sat} $\overline{a}^*_\phi$(nar.)
GHN09	0.0139	0.0139	0.00001	0.0057	0.0058	0.0041	0.002
GHN35	0.0423	0.0423	0.00001	0.0101	0.0062	0.0052	0.0023
GHN41	0.0397	0.0397	0.00001	0.0121	0.0055	0.0052	0.0028
GHS39	0.0209	0.0209	0.00003	0.0073	0.0041	0.0033	0.0016
GHS43	0.0062	0.0062	0.00003	0.0055	0.0047	0.0041	0.0021
GHS45	0.0085	0.0085	0.00002	0.0075	0.0069	0.0055	0.0029

C.3 Relationship between *in situ* [DFe] and Φ_{sat}

Table C.3: MODIS level 2 (daily, 1 km) ocean colour products used to derive Φ_{HB} (extracted from 5×5 megapixel grids), that coincided with *in situ* measurements of [DFe]. Time is in GMT; Δtime is the time difference between the station and the satellite overpass (negative times are prior to station times and positive are post); theta is the sensor zenith angle in radians; chl mean in mg m^{-3}; flh mean in W m^{-2} μm^{-1} sr^{-1}; ipar mean in E m^{-2} s^{-1}; K_d mean in m^{-1}; [DFe] in nM.

ID	Date	Time	Lat	Lon	Δtime	theta	chl pix	chl mean	chl std	flh pix	flh mean	flh std	ipar pix	ipar mean	ipar std	K_d pix	K_d mean	K_d std	Φ_{HB}	[DFe]
Fe01	08/09/20	18:30	-39.2	-178.75	7.25	0.29	25	0.535	0.025	25	0.17	0.016	25	1374.4	1.29	25	0.074	0.002	0.021	0.17
Fe02	08/09/22	19:30	-39.38	-178.72	7.08	0.63	25	0.631	0.034	25	0.188	0.017	25	1434.76	1.14	25	0.081	0.002	0.023	0.59
Fe03	08/09/23	18:30	-39.33	-178.79	7.83	0.61	25	0.88	0.093	25	0.202	0.016	25	1272	0.48	25	0.097	0.006	0.024	0.12
Fe04	08/10/02	19:30	-39.28	-179.42	6.67	0.39	25	0.431	0.039	25	0.12	0.022	25	1398.81	2.81	25	0.068	0.002	0.017	0.38
Fe05	10/02/14	23:17	-43.61	148.02	5.8	1.03	25	0.287	0.048	25	0.053	0.018	25	1519.92	1.05	25	0.053	0.005	0.014	0.46
Fe06	11/12/28	02:20	-34.61	17.05	10.83	0.74	23	0.188	0.023	23	0.019	0.062	23	1893.87	8.81	23	0.046	0.005	0.004	0.22
Fe07	11/12/28	16:36	-35.47	15	-3.43	0.51	15	0.142	0.017	15	0.132	0.119	15	1930.49	7.79	15	0.042	0.005	0.024	0.11
Fe08	11/12/28	23:34	-35.84	14.19	-10.4	0.41	25	0.142	0.007	25	0.122	0.043	25	1950.98	5.78	25	0.05	0.001	0.022	0.14
Fe09	12/01/02	08:54	-40	1.74	4.6	0.67	21	0.291	0.037	21	0.26	0.109	21	2008.09	7.75	21	0.062	0.005	0.035	0.08
Fe10	12/01/02	12:50	-40.07	1.29	0.67	0.71	25	0.366	0.011	25	0.299	0.025	25	2025.77	2.67	25	0.07	0.001	0.037	0.36
Fe11	12/01/06	02:45	-40.01	-8.53	12	0.29	25	0.245	0.006	25	0.172	0.041	25	1879.76	2.68	25	0.052	0.001	0.023	0.15
Fe12	12/01/09	19:04	-40	-16.38	-3.82	0.28	15	0.318	0.043	15	0.231	0.07	15	1886.35	4.54	15	0.064	0.005	0.027	0.06
Fe13	12/01/09	06:59	-40	-13.7	8.27	0.57	22	0.291	0.018	22	0.122	0.024	22	1872.15	5.21	22	0.061	0.002	0.017	0.09
Fe14	12/01/14	05:21	-40	-27.19	10.23	0.48	25	0.259	0.052	22	0.184	0.058	25	1945.57	4.63	25	0.045	0.007	0.024	0.25
Fe15	12/01/14	11:42	-40	-28	3.88	0.56	25	0.229	0.007	25	0.125	0.017	25	1976.96	1.56	25	0.042	0.001	0.018	0.15
Fe16	12/01/14	12:19	-40	-28	3.27	0.56	25	0.229	0.007	25	0.125	0.017	25	1976.96	1.56	25	0.042	0.001	0.018	0.4
Fe17	12/01/14	08:40	-40	-27.93	6.92	0.55	25	0.234	0.008	25	0.139	0.017	25	1975.47	1.53	25	0.043	0.001	0.019	0.18
Fe18	12/01/16	21:39	-40	-37.37	-4.65	0.78	25	0.19	0.013	25	0.045	0.015	25	1843.43	0.77	25	0.046	0.002	0.009	0.2
Fe19	12/01/18	15:00	-40	-42.3	1.75	0.07	25	0.229	0.023	25	0.101	0.044	25	1928.94	3.95	25	0.047	0.004	0.013	0.23
Fe20	12/01/18	08:59	-40	-40.63	8.27	0.14	25	0.204	0.009	25	0.005	0.017	25	1924.61	1.28	25	0.044	0.001	0.001	0.31
Fe21	12/01/18	12:34	-40	-41.68	4.18	0.01	21	0.197	0.035	20	0.08	0.056	21	1910.26	11.6	21	0.042	0.007	0.011	0.3
Fe22	12/01/21	18:14	-39.42	-48.46	-0.9	0.16	25	0.278	0.023	25	0.015	0.019	25	1905.9	9.42	25	0.051	0.002	0.002	0.62
Fe23	12/01/22	02:01	-38.59	-49.95	-8.68	0.01	25	0.15	0.003	25	0.046	0.009	25	1965.44	3.1	25	0.037	0.001	0.007	0.21
Fe24	12/01/23	21:00	-37.05	-52.43	-3.92	0.62	24	0.153	0.029	24	0.038	0.067	24	2039.04	14.3	24	0.039	0.008	0.007	0.31
Fe25	12/01/23	19:12	-37.27	-52.1	-2.12	0.59	24	0.215	0.023	24	0.083	0.057	24	2025.74	9.73	24	0.044	0.005	0.012	0.37
Fe26	12/01/26	02:24	-36	-54	10.27	0.18	25	2.065	0.181	25	0.149	0.013	25	1959.34	1.23	25	0.166	0.01	0.007	0.74

References

Abbott, M. R. and Letelier, R. M. (1999). Algorithm theoretical basis document: Chlorophyll fluorescence, MODIS Product Number 20. Technical report, NASA.

Abbott, M. R., Richman, J. G., Letelier, R. M., and Bartlett, J. S. (2000). The spring bloom in the Antarctic Polar Frontal Zone as observed from a mesoscale array of bio-optical sensors. *Deep-Sea Research Part II: Topical Studies in Oceanography*, 47(15-16):3285–3314.

Abbott, M. R., Richman, J. G., Nahorniak, J. S., and Barksdale, B. S. (2001). Meanders in the Antarctic Polar Frontal Zone and their impact on phytoplankton. *Deep-Sea Research Part II: Topical Studies in Oceanography*, 48(19-20):3891–3912.

Alder, V., Cuzin-Roudy, J., Fransz, G., Graneli, E., Larsen, J., Rabbani, M., and Thomsen, H. (1989). Macro- and micrograzing effects on phytoplankton communities. The expedition Antarktis VII/3 (EPOS LEG 2) of RV "Polarstern" in 1988/89. *Berichte zur Polarforschung*, 65:123–130.

Alderkamp, A.-C., de Baar, H. J., Visser, R. J. W., and Arrigo, K. R. (2010). Can photoinhibition control phytoplankton abundance in deeply mixed water columns of the Southern Ocean? *Limnology and Oceanography*, 55(3):1248–1264.

Alderkamp, A.-C., Mills, M. C., van Dijken, G. I., and Arrigo, K. R. (2013). Photoacclimation and non-photochemical quenching under in situ irradiance in natural phytoplankton assemblages from the Amundsen Sea, Antarctica. *Marine Ecology Progress Series*, 475:15–34.

Allali, K., Bricaud, A., and Claustre, H. (1997). Spatial variations in the chlorophyll-specific absorption coefficients of phytoplankton and photosynthetically active pigments in the equatorial Pacific. *Journal of Geophysical Research: Oceans*, 102(C6):12413–12423.

Alvain, S., Moulin, C., Dandonneau, Y., Loisel, H., and Bréon, F.-M. (2006). A species-dependent bio-optical model of case I waters for global ocean color processing. *Deep Sea Research Part I: Oceanographic Research Papers*, 53:917–925.

Arrigo, K. R. (1999). Phytoplankton community structure and the drawdown of nutrients and CO2 in the Southern Ocean. *Science*, 283:365–367.

Arrigo, K. R., Ditullio, G. R., Dunbar, R. B., Robinson, D. H., Vanwoert, M., Worthen, D. L., and Lizotte, M. P. (2000). Phytoplankton taxonomic variability in nutrient utilization and primary production in the Ross Sea. *Journal of Geophysical Research*, 105(C4):8827–8846.

Arrigo, K. R. and McClain, C. R. (1994). Spring phytoplankton production in the western Ross Sea. *Science*, 266(5183):261–263.

Arrigo, K. R., Mills, M. M., Kropuenske, L. R., van Dijken, G. L., Alderkamp, A.-C., and Robinson, D. H. (2010). Photophysiology in two major southern ocean phytoplankton taxa: photosynthesis and growth of Phaeocystis antarctica and Fragilariopsis cylindrus under different irradiance levels. *Integrative and Comparative Biology*, 50(6):950–66.

Arrigo, K. R. and van Dijken, G. L. (2004). Annual changes in sea-ice, chlorophyll a, and primary production in the Ross Sea, Antarctica. *Deep Sea Research II*, 51:117–138.

Arrigo, K. R., van Dijken, G. L., and Bushinsky, S. (2008). Primary production in the Southern Ocean, 1997-2006. *Journal of Geophysical Research*, 113(C8004):1–27.

Arrigo, K. R., Weiss, A. M., and Smith Jr, W. O. (1998). Physical forcing of phytoplankton dynamics in the southwestern Ross Sea. *Journal of Geophysical Research*, 103(C1):1007–1021.

Asada, K. (1999). The water-water cycle in chloroplasts: Scavenging of active oxygens and dissipation of excess photons. *Annual Review of Plant Physiology and Plant Molecular Biology*, 50:601–639.

Asada, K. (2000). The water-water cycle as alternative photon and electron sinks. *Philosophical Transactions of the Royal Society of London. Series B, Biological Sciences*, 355:1419–1431.

Asada, K. (2006). Production and scavenging of reactive oxygen species in chloroplasts and their functions. *Plant Physiology*, 141:391–396.

Babin, M., Morel, A., Claustre, H., Bricaud, A., Kolber, Z., and Falkowski, P. G. (1996a). Nitrogen- and irradiance-dependent variations of the maximum quantum yield of carbon fixation in eutrophic, mesotrophic and oligotrophic marine systems. *Deep-Sea Research Part I: Oceanographic Research Papers*, 43(8):1241–1272.

Babin, M., Morel, A., and Gentili, B. (1996b). Remote sensing of sea surface Sun-induced chlorophyll fluorescence: consequences of natural variations in the optical characteristics of phytoplankton and the quantum yield of chlorophyll a fluorescence. *International Journal of Remote Sensing*, 17(12):2417–2448.

Babin, M., Stramski, D., Ferrari, G., Claustre, H., Bricaud, A., Obolensky, G., and Hoepffner, N. (2003). Variations in the light absorption coefficients of phytoplankton, nonalgal particles, and dissolved organic matter in coastal waters around Europe. *Journal of Geophysical Research*, 108(C7):3211.

Babin, M., Therriault, J.-C., Legendre, L., and Condal, A. (1993). Variations in the specific absorption coefficient for natural phytoplankton assemblages: Impact on estimates of primary production. *Limnology and Oceanography*, 38(l):154–177.

Babin, M., Therriault, J.-C., Legendre, L., Nieke, B., Reuter, R., and Condal, A. (1995). Relationship between the maximum quantum yield of carbon fixation and the minimum quantum yield of chlorophyll a in vivo fluorescence in the Gulf of St. Lawrence. *Limnology and Oceanography*, 40(5):956–968.

Balch, W. M. (2004). Re-evaluation of the physiological ecology of coccolithophores. Technical report, Bigelow Laboratory for Ocean Sciences, Boothbay, Maine.

Balch, W. M., Bates, N. R., Lam, P. J., Twining, B. S., Rosengard, S. Z., Bowler, B. C., Drapeau, D. T., Garley, R., Lubelczyk, L. C., Mitchell, C., and Rauschenberg, S. (2016). Factors regulating the Great Calcite Belt in the Southern Ocean and its biogeochemical significance. *Global Biogeochemical Cycles*, 30:1124–1144.

Balch, W. M., Drapeau, D. T., Bowler, B. C., Lyczskowski, E., Booth, E. S., and Alley, D. (2011). The contribution of coccolithophores to the optical and inorganic carbon budgets during the Southern Ocean Gas Exchange Experiment: New evidence in support of the Great Calcite Belt hypothesis. *Journal of Geophysical Research*, 116:1–14.

Balch, W. M., Gordon, H. R., Bowler, B., Drapeau, D., and Booth, E. (2005). Calcium carbonate measurements in the surface global ocean based on Moderate-Resolution

Imaging Spectroradiometer data. *Journal of Geophysical Research C: Oceans*, 110(7):1–21.

Balch, W. M. and Utgoff, P. (2009). Potential interactions among ocean acidification, coccolithophores, and the optical properties of seawater. *Oceanography*, 22(4):146–159.

Banse, K. (1994). Grazing and zooplankton production as key controls of phytoplankton production in the open ocean. *Oceanography*, 7(1):13–20.

Banse, K. (1996). Low seasonality of low concentrations of surface chlorophyll in the Subantarctic water ring: underwater irradiance, iron, or grazing? *Progress in Oceanography*, 37:241–291.

Bathmann, U. V., Scharek, R., Klaas, C., Dubischarr, C. D., and Smetacek, V. (1997). Spring development of phytoplankton biomass and composition in major water masses of the Atlantic sector of the Southern Ocean. *Deep Sea Research II*, 44(1-2):51–67.

Becquevort, S., Mathot, S., and Lancelot, C. (1992). Interactions in the microbial community of the marginal ice zone of the northwestern Weddell Sea through size distribution analysis. *Polar Biology*, 12(2):211–218.

Behrenfeld, M. J. (2010). Abandoning Sverdrup's Critical Depth Hypothesis on phytoplankton blooms. *Ecology*, 91(4):977–989.

Behrenfeld, M. J., Bale, A. J., Kolber, Z. S., Aiken, J., and Falkowski, P. G. (1996). Confirmation of iron limitation of phytoplankton photosynthesis in the equatorial Pacific Ocean.

Behrenfeld, M. J., Chavez, F. P., Shea, D. M., Worthington, K., Sherrell, R. M., Strutton, P., and McPhaden, M. (2006). Controls on tropical Pacific Ocean productivity revealed through nutrient stress diagnostics. *Nature*, 442(7106):1025–1028.

Behrenfeld, M. J. and Falkowski, P. G. (1997). Photosynthetic rates derived from satellite-based chlorophyll concentration. *Limnology and Oceanography*, 42(1):1–20.

Behrenfeld, M. J. and Milligan, A. J. (2013). Photophysiological expressions of iron stress in phytoplankton. *Annual Review of Marine Science*, 5(4):1–30.

Behrenfeld, M. J., Westberry, T. K., Boss, E. S., O'Malley, R. T., Siegel, D. A., Wiggert, J. D., Franz, B. A., McClain, C. R., Feldman, G. C., Doney, S. C., Moore, J., Dall'Olmo, G., Milligan, A. J., Lima, I., and Mahowald, N. (2009). Satellite-detected fluorescence reveals global physiology of ocean phytoplankton. *Biogeosciences*, 6(5):779–794.

Belkin, I. M. and Gordon, A. L. (1996). Southern Ocean fronts from the Greenwich meridian to Tasmania. *Journal of Geophysical Research*, 101(C2):3675.

Bellafiore, S., Barneche, F., Peltier, G., and Rochaix, J.-D. (2005). State transitions and light adaptation require chloroplast thylakoid protein kinase STN7. *Nature*, 433:892–895.

Beutler, M., Wiltshire, K. H., Arp, M., Kruse, J., Reineke, C., Moldaenke, C., and Hansen, U. P. (2003). A reduced model of the fluorescence from the cyanobacterial photosynthetic apparatus designed for the in situ detection of cyanobacteria. *Biochimica et Biophysica Acta (BBA) - Bioenergetics*, 1604(1):33–46.

Beutler, M., Wiltshire, K. H., Meyer, B., Moldaenke, C., and Dau, H. (1998). Rapid depth-profiling of the distribution of spectral groups of microalgae in lakes, rivers and in the sea. In Garab, G., editor, *Photosynthesis: Mechanisms and Effects*, pages 4301–4304. Springer Netherlands.

Beutler, M., Wiltshire, K. H., Meyer, B., Moldaenke, C., Lüring, C., Meyerhöfer, M., Hansen, U. P., and Dau, H. (2002). A fluorometric method for the differentiation of algal populations in vivo and in situ. *Photosynthesis Research*, 72(1):39–53.

Bibby, T. S., Gorbunov, M. Y., Wyman, K. W., and Falkowski, P. G. (2008). Photosynthetic community responses to upwelling in mesoscale eddies in the subtropical North Atlantic and Pacific Oceans. *Deep-Sea Research Part II: Topical Studies in Oceanography*, 55:1310–1320.

Bidigare, R. R., Schofield, O., and Prezelin, B. B. (1989). Influence of zeaxanthin on quantum yield of photosynthesis of Synechococcus clone WH7803 (DC2). *Marine Ecology Progress Series*, 56(1):177–188.

Blackman, F. (1905). Optima and limiting factors. *Annals of Botany*, 19(74):281–295.

Blain, S., Quéguiner, B., Armand, L., Belviso, S., Bombled, B., Bopp, L., Bowie, A., Brunet, C., Brussaard, C., Carlotti, F., Christaki, U., Corbière, A., Durand, I., Ebersbach, F., Fuda, J. L., Garcia, N., Gerringa, L., Griffiths, B., Guigue, C., Guillerm, C., Jacquet, S., Jeandel, C., Laan, P., Lefèvre, D., Lo Monaco, C., Malits, A., Mosseri, J., Obernosterer, I., Park, Y. H., Picheral, M., Pondaven, P., Remenyi, T., Sandroni, V., Sarthou, G., Savoye, N., Scouarnec, L., Souhaut, M., Thuiller, D., Timmermans, K., Trull, T., Uitz, J., Van Beek, P., Veldhuis, M., Vincent, D., Viollier, E., Vong, L., and

Wagener, T. (2007). Effect of natural iron fertilization on carbon sequestration in the Southern Ocean. *Nature*, 446(7139):1070–1074.

Boatman, T. G., Geider, R. J., and Oxborough, K. (2019). Improving the accuracy of single turnover active fluorometry (STAF) for the estimation of phytoplankton primary productivity (PhytoPP). *Frontiers in Marine Science*, 6(JUN):1–16.

Bolhàr-Nordenkampf, H. R. and Öquist, G. (1993). *Chlorophyll fluorescence as a tool in photosynthesis research*. Chapman and Hall, London.

Boyd, P. W. (2002). Environmental factors controlling phytoplankton processes in the Southern Ocean. *Journal of Phycology*, 38(5):844–861.

Boyd, P. W. and Abraham, E. R. (2001). Iron-mediated changes in phytoplankton photosynthetic competence during SOIREE. *Deep Sea Research Part II: Topical Studies in Oceanography*, 48(11-12):2529–2550.

Boyd, P. W., Arrigo, K. R., Strzepek, R., and van Dijken, G. L. (2012). Mapping phytoplankton iron utilization: Insights into Southern Ocean supply mechanisms. *Journal of Geophysical Research: Oceans*, 117(6):1–18.

Boyd, P. W., Crossley, A. C., DiTullio, G. R., Griffiths, F. B., Hutchins, D. A., Queguiner, B., Sedwick, P. N., and Trull, T. W. (2001). Control of phytoplankton growth by iron supply and irradiance in the subantarctic Southern Ocean: Experimental results from the SAZ Project. *Journal of Geophysical Research*, 106(C12):31573.

Boyd, P. W. and Ellwood, M. J. (2010). The biogeochemical cycle of iron in the ocean. *Nature Geoscience*, 3(10):675–682.

Boyd, P. W., LaRoche, J., Gall, M., Frew, R., and Mckay, R. M. L. (1999). Role of iron, light, and silicate in controlling algal biomass in subantarctic waters SE of New Zealand. *Journal of Geophysical Research*, 104(C6):13395–13408.

Boyd, P. W., Watson, A. J., Law, C. S., Abraham, E. R., Trull, T., Murdoch, R., Bakker, D. C., Bowie, A. R., Buesseler, K. O., Chang, H., Charette, M., Croot, P., Downing, K., Frew, R., Gall, M., Hadfield, M., Hall, J., Harvey, M., Jameson, G., LaRoche, J., Liddicoat, M., Ling, R., Maldonado, M. T., McKay, R. M., Nodder, S., Pickmere, S., Pridmore, R., Rintoul, S., Safi, K., Sutton, P., Strzepek, R. F., Tanneberger, K., Turner, S., Waite, A., and Zeldis, J. (2000). A mesoscale phytoplankton bloom in the polar Southern Ocean stimulated by iron fertilization. *Nature*, 407:695–702.

Brand, L. E. (1991). Minimum iron requirements of marine phytoplankton and the implications for the biogeochemical control of new production. *Limnology and Oceanography*, 36(8):1756–1771.

Brand, L. E., Sunda, W. G., and Guillard, R. R. L. (1983). Limitation of marine phytoplankton reproductive rates by zinc, manganese, and iron. *Limnology and Oceanography Oceanography*, 28(6):1182–1198.

Brewin, R. J., Hardman-Mountford, N. J., Lavender, S. J., Raitsos, D. E., Hirata, T., Uitz, J., Devred, E., Bricaud, A., Ciotti, A., and Gentili, B. (2011). An intercomparison of bio-optical techniques for detecting dominant phytoplankton size class from satellite remote sensing. *Remote Sensing of Environment*, 115(2):325–339.

Bricaud, A., Babin, M., Morel, A., and Claustre, H. (1995). Variability in the chlorophyll-specific absorption coefficients of natural phytoplankton: Analysis and parameterization phytoplankton. *Journal of Geophysical Research*, 100(C7):13321–13332.

Bricaud, A., Claustre, H., Ras, J., and Oubelkheir, K. (2004). Natural variability of phytoplanktonic absorption in oceanic waters: Influence of the size structure of algal populations. *Journal of Geophysical Research*, 109(C11010):1–12.

Bricaud, A., Morel, A., Babin, M., Allali, K., and Claustre, H. (1998). Variations of light absorption by suspended particles with chlorophyll a concentration in oceanic (case 1) waters: Analysis and implications for bio-optical models. *Journal of Geophysical Research*, 103(C13):31033–31044.

Bricaud, A., Prieur, L., and Morel, A. (1983). Optical efficiency factors of some phytoplankters. *Limnology and Oceanography*, 28(5):816–832.

Bricaud, A. and Stramski, D. (1990). Spectral absorption coefficients of living phytoplankton and nonalgal biogenous matter: A comparison between the Peru upwelling area and the Sargasso Sea. *Limnology and Oceanography*, 35(3):562–582.

Brown, C. A., Huot, Y., Werdell, P. J., Gentili, B., and Claustre, H. (2008). The origin and global distribution of second order variability in satellite ocean color and its potential applications to algorithm development. *Remote Sensing of Environment*, 112:4186–4203.

Brown, C. W. and Yoder, J. A. (1994). Coccolithophorid blooms in the global ocean. *Journal of Geophysical Research*, 99:7467–7482.

Browning, T. J., Bouman, H. A., and Moore, C. M. (2014a). Satellite-detected fluorescence: Decoupling nonphotochemical quenching from iron stress signals in the South Atlantic and Southern Ocean. *Global Biogeochemical Cycles*, 28:510–524.

Browning, T. J., Bouman, H. A., Moore, C. M., Schlosser, C., Tarran, G. A., Woodward, E. M. S., and Henderson, G. M. (2014b). Nutrient regimes control phytoplankton ecophysiology in the South Atlantic. *Biogeosciences*, 11(2):463–479.

Brunet, C., Brylinski, J. M., and Lemoine, Y. (1993). In situ variations of the xanthophylls diatoxanthin and diadinoxanthin- Photoadaptation and relationships with a hydrodynamical system in the eastern English Channel. *Marine Ecology Progress Series*, 102(1-2):69–78.

Buesseler, K. O., Ball, L., Andrews, J., Cochran, J. K., Hirschberg, D. J., Bacon, M. P., Fleer, A., and Brzezinski, M. (2001). Upper ocean export of particulate organic carbon and biogenic silica in the Southern Ocean along 170W. *Deep Sea Research Part II: Topical Studies in Oceanography*, 48(19-20):4275–4297.

Buma, A. G., Gieskes, W. W., and Thomsen, H. A. (1992). Abundance of cryptophyceae and chlorophyll b-containing organisms in the Weddell-Scotia Confluence area in the spring of 1988. *Polar Biology*, 12(1):43–52.

Caldeira, K. and Duffy, P. B. (2000). The role of the Southern Ocean in uptake and storage of anthropogenic carbon dioxide. *Science*, 287(5453):620–622.

Campbell, J. W. (1995). The lognormal distribution as a model for bio-optical variability in the sea. *Journal of Geophysical Research*, 100(C7):13237–13254.

Carder, K. L., Chen, F. R., and Hawes, S. K. (2003). Algorithm theoretical basis document ATBD 20 instantaneous photosynthetically available radiation and absorbed radiation by phytoplankton. Technical report, NASA.

Carranza, M. M. and Gille, S. T. (2015). Southern Ocean wind-driven entrainment enhances satellite chlorophyll-a through the summer. *Journal of Geophysical Research C: Oceans*, 120(1):304–323.

Casper-Lindley, C. and Björkman, O. (1998). Fluorescence quenching in four unicellular algae with different light-harvesting and xanthophyll-cycle pigments. *Photosynthesis research*, 56:277–289.

Cassar, N., DiFiore, P. J., Barnett, B. A., Bender, M. L., Bowie, A. R., Tilbrook, B., Petrou, K., Westwood, K. J., Wright, S. W., and Lefevre, D. (2011). The influence of iron and light on net community production in the Subantarctic and Polar Frontal Zones. *Biogeosciences*, 8(2):227–237.

Cheah, W., McMinn, A., Griffiths, F. B., Westwood, K. J., Wright, S. W., and Clementson, L. A. (2013). Response of phytoplankton photophysiology to varying environmental conditions in the Sub-Antarctic and Polar Frontal Zone. *PLoS ONE*, 8(8):1–13.

Cheregi, O., Kotabová, E., Prášil, O., Schröder, W. P., Kana, R., and Funk, C. (2015). Presence of state transitions in the cryptophyte alga Guillardia theta. *Journal of Experimental Botany*, 66(20):6461–6470.

Chereskin, B. M. and Castelfranco, P. A. (1982). Effects of iron and oxygen on chlorophyll biosynthesis: Observations of the biosynthetic pathway in isolatated etiochloroplasts. *Plant physiology*, 69:112–116.

Chever, F., Bucciarelli, E., Sarthou, G., Speich, S., Arhan, M., Penven, P., and Tagliabue, A. (2010). Physical speciation of iron in the Atlantic sector of the Southern Ocean along a transect from the subtropical domain to the Weddell Sea Gyre. *Journal of Geophysical Research: Oceans*, 115(10):1–15.

Chisholm, S. W. (2000). Stirring times in the Southern Ocean. *Nature*, 407(6805):685–687.

Ciotti, Á. M., Lewis, M. R., and Cullen, J. J. (2002). Assessment of the relationships between dominant cell size in natural phytoplankton communities and the spectral shape of the absorption coefficient. *Limnology and Oceanography*, 47(2):404–417.

Clarke, G. L., Ewing, G. C., and Lorenzen, C. J. (1970). Spectra of backscattered light from the sea obtained from aircraft as a measure of chlorophyll concentration. *Science*, 167(3921):1119–21.

Claustre, H. (1994). The trophic status of various oceanic provinces as revealed by phytoplankton pigment signatures. *Limnology and Oceanography*, 39(5):1206–1210.

Cleveland, J. S. and Perry, M. J. (1987). Quantum yield, relative spective absorption and fluorescence in nitrogen-limited Chaetoceros gracilis. *Marine Biology*, 94:489–497.

Closset, I., Lasbleiz, M., Leblanc, K., Quéguiner, B., Cavagna, A. J., Elskens, M., Navez, J., and Cardinal, D. (2014). Seasonal evolution of net and regenerated silica production

around a natural Fe-fertilized area in the Southern Ocean estimated from Si isotopic approaches. *Biogeosciences Discussions*, 11(5):6329–6381.

Coale, K. H., Johnson, K. S., Chavez, F. P., Buesseler, K. O., Barber, R. T., Brzezinski, M. A., Cochlan, W. P., Millero, F. J., Falkowski, P. G., Bauer, J. E., Wanninkhof, R. H., Kudela, R. M., Altabet, M. A., Hales, B. E., Takahashi, T., Landry, M. R., Bidigare, R. R., Wang, X., Chase, Z., Strutton, P. G., Friederich, G. E., Gorbunov, M. Y., Lance, V. P., Hilting, A. K., Hiscock, M. R., Demarest, M., Hiscock, W. T., Sullivan, K. F., Tanner, S. J., Gordon, R. M., Hunter, C. N., Elrod, V. A., Fitzwater, S. E., Jones, J. L., Tozzi, S., Koblizek, M., Roberts, A. E., Herndon, J., Brewster, J., Ladizinsky, N., Smith, G., Cooper, D., Timothy, D., Brown, S. L., Selph, K. E., Sheridan, C. C., Twining, B. S., and Johnson, Z. I. (2004). Southern Ocean Iron Enrichment Experiment: Carbon cycling in high- and low-Si waters. *Science*, 304(5669):408–414.

Collins, D. J., Kiefer, D. A., Soohoo, J. B., and Stuart McDermid, I. (1985). The role of reabsorption in the spectral distribution of phytoplankton fluorescence emission. *Deep Sea Research Part A. Oceanographic Research Papers*, 32(8):983–1003.

Comiso, J. C., McClain, C. R., Sullivan, C. W., Ryan, J., and Leonard, C. (1993). Coastal Zone Color Scanner pigment concentration in the Southern Ocean and relationships to geophysical surface features. *Journal of Geophysical Research*, 98(C2):2419–2451.

Cournac, L., Redding, K., Ravenel, J., Rumeau, D., Josse, E. M., Kuntz, M., and Peltier, G. (2000). Electron flow between photosystem II and oxygen in chloroplasts of photosystem I-deficient algae is mediated by a quinol oxidase involved in chlororespiration. *The Journal of Biological Chemistry*, 275(23):17256–62.

Cowles, T. J. (1993). In situ characterization of phytoplankton from vertical profiles of fluorescence emission spectra. *Marine Biology*, 222:217–222.

Cox, P. M., Betts, R. A., Jones, C. D., Spall, S. A., and Totterdell, I. J. (2000). Acceleration of global warming due to carbon-cycle feedbacks in a coupled climate model. *Nature*, 408:184–187.

Craig, S. E., Jones, C. T., Li, W. K., Lazin, G., Horne, E., Caverhill, C., and Cullen, J. J. (2012). Deriving optical metrics of coastal phytoplankton biomass from ocean colour. *Remote Sensing of Environment*, 119:72–83.

Cubillos, J. C., Wright, S. W., Nash, G., De Salas, M. F., Griffiths, B., Tilbrook, B., Poisson, A., and Hallegraeff, G. M. (2007). Calcification morphotypes of the coccol-

ithophorid Emiliania huxleyi in the Southern Ocean: Changes in 2001 to 2006 compared to historical data. *Marine Ecology Progress Series*, 348(October 2007):47–54.

Cullen, J. J., Ciotti, A. M., Davis, R. F., and Neale, P. J. (1997). Relationship between near-surface chlorophyll and solar-stimulated fluorescence: biological effects. In *Proc. SPIE Ocean Optics XIII*, number 2963, pages 272–277, Halifax, Nova Scotia, Canada.

Cullen, J. J. and Lewis, M. R. (1995). Biological processes and optical measurements near the sea surface: Some issues relevant to remote sensing. *Journal of Geophysical Research*, 100(C7):13255–13266.

Dafner, E. V. and Mordasova, N. V. (1994). Influence of biotic factors on the hydrochemical structure of surface water in the Polar Frontal Zone of the Atlantic Antarctic. *Marine Chemistry*, 45(1-2):137–148.

Dandonneau, Y. and Neveux, J. (1997). Diel variations of in vivo fluorescence in the eastern equatorial Pacific: An unvarying pattern. *Deep-Sea Research Part II: Topical Studies in Oceanography*, 44(9-10):1869–1880.

Davis, K. M. and Pushkar, Y. N. (2015). Structure of the Oxygen Evolving Complex of photosystem II at room temperature. *The Journal of Physical Chemistry B*, 119:3492–3498.

de Baar, H. J. W., Boyd, P. W., Coale, K. H., Landry, M. R., Tsuda, A., Assmy, P., Bakker, D. C. E., Bozec, Y., Barber, R. T., Brzezinski, M. A., Buesseler, K. O., Boye, M., Croot, P. L., Gervais, F., Gorbunov, M. Y., Harrison, P. J., Hiscock, W. T., Laan, P., Lancelot, C., Law, C. S., Levasseur, M., Marchetti, A., Millero, F. J., Nishioka, J., Nojiri, Y., van Oijen, T., Riebesell, U., Rijkenberg, M. J. A., Saito, H., Takeda, S., Timmermans, K. R., Veldhuis, M. J. W., Waite, A. M., and Wong, C. S. (2005). Synthesis of iron fertilization experiments: From the Iron Age in the Age of Enlightenment. *Journal of Geophysical Research*, 110(2005):1–24.

de Baar, H. J. W., Buma, A. G. J., Nolting, R. F., Cadee, G. C., Jacques, G., and Treguer, P. J. (1990). On iron limitation of the Southern Ocean: experimental observations in the Weddell and Scotia Seas. *Marine Ecology Progress Series*, 65:105–122.

de Baar, H. J. W., de Jong, J. T. M., Bakker, D. C. E., Löscher, B. M., Veth, C., Bathmann, U., and Smetacek, V. (1995). Importance of iron for plankton blooms and carbon dioxide drawdown in the Southern Ocean. *Nature*, 373(6513):412–415.

de Boyer Montégut, C., Madec, G., Fischer, A. S., Lazar, A., and Iudicone, D. (2004). Mixed layer depth over the global ocean: An examination of profile data and a profile-based climatology. *Journal of Geophysical Research*, 109(C12003):1–20.

de Salas, M. F., Eriksen, R., Davidson, A. T., and Wright, S. W. (2011). Protistan communities in the Australian sector of the Sub-Antarctic Zone during SAZ-Sense. *Deep-Sea Research Part II: Topical Studies in Oceanography*, 58(21-22):2135–2149.

Delosme, R., Olive, J., and Wollman, F.-A. (1996). Changes in light energy distribution upon state transitions: An in vivo photoacoustic study of the wild type and photosynthesis mutants from Chlamydomonas reinhardtii. *Biochimica et Biophysica Acta - Bioenergetics*, 1273:150–158.

Demas, J. N. and Crosby, G. A. (1971). The measuremet of photolumininescence quatum yields. A review. *The Journal of Physical Chemistry*, 75(8):991–1024.

DeMaster, D. J. (1981). The supply and accumulation of silica in the marine environment. *Geochimica et Cosmochimica Acta*, 45(10):1715–1732.

Demers, S., Roy, S., Gagnon, R., and Vignault, C. (1991). Rapid light-induced changes in cell fluorescence and in xanthophyll-cycle pigments of Alexandrium excavatum (Dinophyceae) and Thalassiosira pseudonana (Bacillario-phyceae): a photo-protection mechanism . *Marine Ecology Progress Series*, 76(February):185–193.

Demmig-Adams, B. (1990). Carotenoids and photoprotection in plants: a role for the xanthophyll zeaxanthin. *Biochimica et Biophysica Acta (BBA) - Bioenergetics*, 1020(1):1–24.

Depège, N., Bellafiore, S., and Rochaix, J.-D. (2003). Role of chloroplast protein kinase Stt7 in LHCII phosphorylation and state transition in Chlamydomonas. *Science (New York, N.Y.)*, 299(5612):1572–1575.

Desiderio, R. A., Moore, C. M., Lantz, C., and Cowles, T. J. (1997). Multiple excitation fluorometer for in situ oceanographic applications. *Applied Optics*, 36(6):1289–1296.

Detmer, A. and Bathmann, U. (1997). Distribution patterns of autotrophic pico- and nanoplankton and their relative contribution to algal biomass during spring in the Atlantic sector of the Southern Ocean. *Deep Sea Research Part II: Topical Studies in Oceanography*, 44(1-2):299–320.

DeVries, T., Holzer, M., and Primeau, F. (2017). Recent increase in oceanic carbon uptake driven by weaker upper-ocean overturning. *Nature*, 542(7640):215–218.

Dickey, T., Granata, T., Marra, J., Langdon, C., Wiggert, J., Chai-Jochner, Z., Hamilton, M., Vazquez, J., Stramska, M., Bidigare, R., and Siegel, D. (1993). Seasonal variability of bio-optical and physical properties in the Sargasso Sea. *Journal of Geophysical Research*, 98(C1):865–898.

Dickey, T., Marra, J., Sigurdson, D., Waller, R., Kinskade, C., Zedler, S., Wiggert, J., and Langdon, J. (1998). Seasonal variability of bio-optical and physical properties in the Arabian Sea: October 1994 - October 1995. *Deep Sea Research II*, 45:2001–2025.

Dierssen, H. M. and Smith, R. C. (2000). Bio-optical properties and remote sensing ocean color algorithms for Antarctic Peninsula waters. *Journal of Geophysical Research*, 105(C11):26301–26312.

DiTullio, G., Garcia, N., Riseman, S., and Sedwick, P. (2007). Effects of iron concentration on pigment composition in Phaeocystis antarctica grown at low irradiance. *Biochemistry*, 83(1-3):71–81.

DiTullio, G. R., Geesey, M. E., Jones, D. R., Daly, K., Smith, W. O., and Campbell, L. (2003). Phytoplankton assemblage structure and primary productivity along 170 degrees W in the South Pacific Ocean. *Marine Ecology-Progress Series*, 255:55–80.

DiTullio, G. R., Grebmeier, J. M., Arrigo, K. R., Lizotte, M. P., Robinson, D. H., Leventer, A., Barry, J. P., Van Woert, M. L., and Dunbar, R. B. (2000). Rapid and early export of Phaeocystis antarctica blooms in the Ross Sea, Antarctica. *Nature*, 404:595–598.

Doerffer, R. (1981). Factor Analysis in Ocean Colour Interpretation. In Gower, J. F. R., editor, *Oceanography from Space*, pages 339–345. Springer US, Boston, MA.

Domingues, N., Matos, A. R., Marques da Silva, J., and Cartaxana, P. (2012). Response of the diatom Phaeodactylum tricornutum to photooxidative stress resulting from high light exposure. *PLoS ONE*, 7(6):e38162.

Doolittle, D. F., Li, W. K. W., and Wood, A. M. (2008). Wintertime abundance of picoplankton in the Atlantic sector of the Southern Ocean. *Nova Hedwigia*, Suppl. 133(February):147–160.

Doust, A. B., Marai, C. N., Harrop, S. J., Wilk, K. E., Curmi, P. M., and Scholes, G. D. (2004). Developing a structure-function model for the cryptophyte phycoerythrin 545

using ultrahigh resolution crystallography and ultrafast laser spectroscopy. *Journal of Molecular Biology*, 344(1):135–153.

Doust, A. B., Wilk, K. E., Curmi, P. M., and Scholes, G. D. (2006). The photophysics of cryptophyte light-harvesting. *Journal of Photochemistry and Photobiology A: Chemistry*, 184(1-2):1–17.

du Plessis, M., Swart, S., Ansorge, I. J., and Mahadevan, A. (2017). Submesoscale processes promote seasonal restratification in the Subantarctic Ocean. *Journal of Geophysical Research: Oceans*, 122:2960–2975.

Dugdale, R. C., Wilkerson, F. P., and Minas, H. J. (1995). The role of a silicate pump in driving new production. *Deep Sea Research Part I: Oceanographic Research Papers*, 42(5):697–719.

Duysens, L. N. M. (1956). The flattening of the absorption spectrum of suspensions, as compared to that of solutions. *Biochimica et biophysica acta*, 19:1–12.

Egan, L. (2008). Nitrate and/ or nitrite in brackish or seawater. Technical report, Colorado, USA.

Esaias, W. E., Abbott, M., Barton, I., Brown, O. B., Campbell, J. W., Carder, K. L., Clark, D. K., Evans, R. H., Hoge, F. E., Gordon, H. R., Balch, W. M., Letelier, R., and Minnett, P. J. (1998). An overview of MODIS capabilities for ocean science observations. *IEEE Transactions on Geoscience and Remote Sensing*, 36(4):1250–1265.

Everitt, D. A., Wright, S. W., Volkman, J. K., Thomas, D. P., and Lindstrom, E. J. (1990). Phytoplankton community compositions in the western equatorial Pacific determined from chlorophyll and carotenoid pigment distributions. *Deep Sea Research Part A. Oceanographic Research Papers*, 37(6):975–997.

Falkowski, P. G., Katz, M. E., Knoll, A. H., Quigg, A., Raven, J. A., Schofield, O., and Taylor, F. J. R. (2004). The evolution of modern eukaryotic phytoplankton. *Science*, 305:354–60.

Falkowski, P. G. and Kiefer, D. A. (1985). Chlorophyll-a fluorescence in phytoplankton: relationship to photosynthesis and biomass. *Journal of Plankton Research*, 7(5):715–731.

Falkowski, P. G. and Kolber, Z. (1993). Estimation of phytoplankton photosynthesis by active fluorescence. *ICES Marine Science Symposium*, 197:92–103.

Falkowski, P. G. and LaRoche, J. (1991). Acclimation to spectral irradiance in algae. *Journal of Phycology*, 27(1):8–14.

Falkowski, P. G., Lin, H., and Gorbunov, M. Y. (2017). What limits photosynthetic energy conversion efficiency in nature? Lessons from the oceans. *Philosophical Transactions of the Royal Society B: Biological Sciences*, 372(1730):2–8.

Falkowski, P. G. and Owens, T. G. (1980). Light- shade adaptation: Two strategies in marine phytoplankton. *Plant Physiology*, 66:592–595.

Falkowski, P. G. and Raven, J. A. (2007). *Aquatic Photosynthesis*. Princeton University Press, second edition.

Fauchereau, N., Tagliabue, A., Bopp, L., and Monteiro, P. M. S. (2011). The response of phytoplankton biomass to transient mixing events in the Southern Ocean. *Geophysical Research Letters*, 38(17):1–6.

Feely, R. A., Sabine, C. L., Takahashi, T., and Wanninkhof, R. (2001). Uptake and Storage of Carbon Dioxide in the Ocean: The Global CO2 Survey. *Oceanography*, 14(4):18–32.

Feikema, W. O., Marosvölgyi, M. A., Lavaud, J., and van Gorkom, H. J. (2006). Cyclic electron transfer in photosystem II in the marine diatom Phaeodactylum tricornutum. *Biochimica et Biophysica Acta*, 1757(7):829–834.

Ferreira, A., Ciotti, Á. M., Mendes, C. R. B., Uitz, J., and Bricaud, A. (2017). Phytoplankton light absorption and the package effect in relation to photosynthetic and photoprotective pigments in the northern tip of Antarctic Peninsula. *Journal of Geophysical Research: Oceans*, 122(9):7344–7363.

Field, C. B., Behrenfeld, M. J., Randerson, J. T., and Falkowski, P. G. (1998). Primary production of the biosphere: Integrating terrestrial and oceanic components. *Science*, 281:237–240.

Finazzi, G., Furia, A., Barbagallo, R. P., and Forti, G. (1999). State transitions, cyclic and linear electron transport and photophosphorylation in Chlamydomonas reinhardtii. *Biochimica et Biophysica Acta (BBA) - Bioenergetics*, 1413(3):117–129.

Finazzi, G., Rappaport, F., Furia, A., Fleischmann, M., Rochaix, J. D., Zito, F., and Forti, G. (2002). Involvement of state transitions in the switch between linear and cyclic electron flow in Chlamydomonas reinhardtii. *EMBO Reports*, 3(3):280–285.

Finkel, Z. V., Beardall, J., Flynn, K. J., Quigg, A., Rees, T. A. V., and Raven, J. A. (2010). Phytoplankton in a changing world: cell size and elemental stoichiometry. *Journal of Plankton Research*, 32(1):119–137.

Fitch, D. T. and Moore, J. K. (2007). Wind speed influence on phytoplankton bloom dynamics in the Southern Ocean Marginal Ice Zone. *Journal of Geophysical Research*, 112(C08006):1–13.

Fouilland, E., Descolas-Gros, C., Courties, C., and Pons, V. (1999). Autotrophic carbon assimilation and biomass from size-fractionated phytoplankton in the surface waters across the subtropical frontal zone (Indian Ocean). *Polar Biology*, 21(2):90–96.

Foyer, C. H. and Harbinson, J. (1999). Relationships between anti-oxidant metabolism and carotenoids in the regulation of photosynthesis. In Frank, H., Young, A., Britton, G., and Cogdell, R., editors, *The Photochemistry of Carotenoids*, pages 305–325. Kluwer Academic Publishers, Dordrecht, The Netherlands.

Franck, V. M., Brzezinski, M. A., Coale, K. H., and Nelson, D. M. (2000). Iron and silicic acid concentrations regulate Si uptake north and south of the Polar Frontal Zone in the Pacific Sector of the Southern Ocean. *Deep-Sea Research Part II: Topical Studies in Oceanography*, 47(15-16):3315–3338.

Frölicher, T. L., Sarmiento, J. L., Paynter, D. J., Dunne, J. P., Krasting, J. P., and Winton, M. (2015). Dominance of the Southern Ocean in anthropogenic carbon and heat uptake in CMIP5 models. *Journal of Climate*, 28(2):862–886.

Fujita, Y. and Ohki, K. (2004). On the 710 nm Fluorescence Emitted by the Diatom Phaeodactylum tricornutum at Room Temperature. *Plant and Cell Physiology*, 45(4):392–397.

Fung, I. Y., Meyn, S. K., Tegen, I. T., Doney, S. C., John, J. G., and Bishop, J. K. B. (2000). Iron supply and demand in the upper ocean. *Global Biogeochemical Cycles*, 14(1):281–295.

Funk, C., Alami, M., Tibiletti, T., and Green, B. R. (2011). High light stress and the one-helix LHC-like proteins of the cryptophyte Guillardia theta. *Biochimica et Biophysica Acta - Bioenergetics*, 1807(7):841–846.

Gall, M. P., Boyd, P. W., Hall, J., Safi, K. A., and Chang, H. (2001). Phytoplankton processes. Part 1: Community structure during the Southern Ocean Iron RElease

Experiment (SOIREE). *Deep-Sea Research Part II: Topical Studies in Oceanography*, 48(11-12):2551–2570.

Garibotti, I. A., Vernet, M., and Ferrario, M. E. (2005). Annually recurrent phytoplanktonic assemblages during summer in the seasonal ice zone west of the Antarctic Peninsula (Southern Ocean). *Deep-Sea Research Part I: Oceanographic Research Papers*, 52(10):1823–1841.

Gerbi, G. P., Boss, E., Werdell, P. J., Proctor, C. W., Haëntjens, N., Lewis, M. R., Brown, K., Sorrentino, D., Zaneveld, J. R. V., Barnard, A. H., Koegler, J., Fargher, H., DeDonato, M., and Wallace, W. (2016). Validation of ocean color remote sensing reflectance using autonomous floats. *Journal of Atmospheric and Oceanic Technology*, 33(11):2331–2352.

Gervais, F., Riebesell, U., and Gorbunov, M. Y. (2016). Changes in primary productivity and chlorophyll a in Response to iron fertilization in the Southern Polar Frontal Zone. *Limnology and Oceanography*, 47(5):1324–1335.

Gibberd, M. J., Kean, E., Barlow, R., Thomalla, S., and Lucas, M. (2013). Phytoplankton chemotaxonomy in the Atlantic sector of the Southern Ocean during late summer 2009. *Deep-Sea Research Part I: Oceanographic Research Papers*, 78:70–78.

Gieskes, W. W. C. and Kraay, G. W. (1983). Dominance of Cryptophyceae during the phytoplankton spring bloom in the central North Sea detected by HPLC analysis of pigments. *Marine Biology*, 75(2-3):179–185.

Gieskes, W. W. C. and Kraay, G. W. (1986). Floristic and physiological differences between the shallow and the deep nanophytoplankton community in the euphotic zone of the open tropical Atlantic revealed by HPLC analysis of pigments. *Marine Biology*, 91(4):567–576.

Gieskes, W. W. C., Kraay, G. W., Nontji, A., Setiapermana, D., and Sutomo (1988). Monsoonal alternation of a mixed and a layered structure in the phytoplankton of the euphotic zone of the banda sea (Indonesia): a mathematical analysis of algal pigment fingerprints. *Netherlands Journal of Sea Research*, 22(2):123–137.

Goericke, R. and Montoya, J. P. (1998). Estimating the contribution of microalgal taxa to chlorophyll a in the field- variations of pigment ratios under nutrient- and light-limited growth. *Marine Ecology Progress Series*, 169:97–112.

Goffart, A., Catalano, G., and Hecq, J. H. (2000). Factors controlling the distribution of diatoms and Phaeocystis in the Ross Sea. *Journal of Marine Systems*, 27:161–175.

Goldman, J. C. (1993). Potential role of large oceanic diatoms in new primary production. *Deep Sea Research Part I: Oceanographic Research Papers*, 40(1):159–168.

Gondwe, M., Krol, M., Gieskes, W., Klaassen, W., and de Baar, H. (2003). The contribution of ocean-leaving DMS to the global atmospheric burdens of DMS, MSA, SO2, and NSS SO4. *Global Biogeochemical Cycles*, 17(4):n/a–n/a.

Gordon, H. R. (1979). Diffuse reflectance of the ocean: the theory of its augmentation by chlorophyll a fluorescence at 685 nm. *Applied Optics*, 18(8):1161–1166.

Gordon, H. R., Brown, J. W., Brown, O. B., Evans, R. H., and Smith, R. C. (1988). A semianalytic radiance model of ocean color. *Journal of Geophysical Research*, 93:10909–10924.

Gordon, H. R., Brown, O. B., and Jacobs, M. M. (1975). Computed relationships between the inherent and apparent optical properties of a flat homogeneous ocean. *Applied Optics*, 14(2):417–27.

Gordon, H. R., Clark, D. K., Brown, J. W., Brown, O. B., Evans, R. H., and Broenkow, W. W. (1983). Phytoplankton pigment concentrations in the Middle Atlantic Bight: comparison of ship determinations and CZCS estimates. *Applied Optics*, 22(1):20–36.

Goss, R., Latowski, D., Grzyb, J., Vieler, A., Lohr, M., Wilhelm, C., and Strzalka, K. (2007). Lipid dependence of diadinoxanthin solubilization and de-epoxidation in artificial membrane systems resembling the lipid composition of the natural thylakoid membrane. *Biochimica et Biophysica Acta*, 1768(1):67–75.

Goss, R. and Lepetit, B. (2015). Biodiversity of NPQ. *Journal of Plant Physiology*, 172:13–32.

Gower, J. F. R. (1980). Observations of in situ fluorescence of chlorophyll-a in Saanich Inlet. *Boundary-Layer Meteorology*, 18(3):235–245.

Gower, J. F. R., Brown, L., and Borstad, G. A. (2004). Observation of chlorophyll fluorescence in the west coast waters of Canada using the MODIS satellite sensor. *Can. J. Remote Sensing*, 30(1):17–25.

Graff, J. R. and Behrenfeld, M. J. (2018). Photoacclimation responses in subarctic Atlantic phytoplankton following a natural mixing-restratification event. *Frontiers in Marine Science*, 5(June):1–11.

Gran, H. H. (1933). Studies on the biology and chemistry of the Gulf of Maine. II. Distribution of phytoplankton in August, 1932. *Biological Bulletin*, 64(2):159–182.

Gravalosa, J. M., Flores, J. A., Sierro, F. J., and Gersonde, R. (2008). Sea surface distribution of coccolithophores in the eastern Pacific sector of the Southern Ocean (Bellingshausen and Amundsen Seas) during the late austral summer of 2001. *Marine Micropaleontology*, 69(1):16–25.

Greene, R. M., Kolber, Z. S., Swift, D. G., Tindale, N. W., and Falkowski, P. G. (1994). Physiological limitation of phytoplankton photosynthesis in the eastern equatorial Pacific determined from variability in the quantum yield of fluorescence. *Limnology and Oceanography*, 39(5):1061–1074.

Gregor, L., Kok, S., and Monteiro, P. M. S. (2018). Interannual drivers of the seasonal cycle of CO2 in the Southern Ocean. *Biogeosciences*, 15(8):2361–2378.

Griffith, D. J., Bone, E. L., Thomalla, S. J., and Bernard, S. (2018). Calibration of an in-water multi-excitation fluorometer for the measurement of phytoplankton chlorophyll-a fluorescence quantum yield. *Optics Express*, 26(15):18863–18877.

Grouneva, I., Jakob, T., Wilhelm, C., and Goss, R. (2009). The regulation of xanthophyll cycle activity and of non-photochemical fluorescence quenching by two alternative electron flows in the diatoms Phaeodactylum tricornutum and Cyclotella meneghiniana. *Biochimica et Biophysica Acta - Bioenergetics*, 1787(7):929–938.

Gruber, N., Gloor, M., Mikaloff Fletcher, S. E., Doney, S. C., Dutkiewicz, S., Follows, M. J., Gerber, M., Jacobson, A. R., Joos, F., Lindsay, K., Menemenlis, D., Mouchet, A., Müller, S. A., Sarmiento, J. L., and Takahashi, T. (2009). Oceanic sources, sinks, and transport of atmospheric CO2. *Global Biogeochemical Cycles*, 23(1):1–21.

Guinet, C., Xing, X., Walker, E., Monestiez, P., Marchand, S., Picard, B., Jaud, T., Authier, M., Cotté, C., Dragon, A. C., Diamond, E., Antoine, D., Lovell, P., Blain, S., D'Ortenzio, F., and Claustre, H. (2013). Calibration procedures and first dataset of Southern Ocean chlorophyll a profiles collected by elephant seals equipped with a newly developed CTD-fluorescence tags. *Earth System Science Data*, 5(1):15–29.

Gwizdala, M., Wilson, A., and Kirilovsky, D. (2011). In vitro reconstitution of the cyanobacterial photoprotective mechanism mediated by the Orange Carotenoid Protein in Synechocystis PCC 6803. *The Plant Cell*, 23(7):2631–43.

Haëntjens, N., Boss, E., and Talley, L. D. (2017). Revisiting Ocean Color algorithms for chlorophyll a and particulate organic carbon in the Southern Ocean using biogeochemical floats. *Journal of Geophysical Research: Oceans*, 122(8):6583–6593.

Hager, A. and Stransky, H. (1970). Das Carotinoidmuster und die Verbreitung des lichtinduzierten Xanthophyllcyclus in verschiedenen Algenklassen. *Archiv Mikrobiologie*, 71(2):132–163.

Halsey, K. H. and Jones, B. M. (2015). Phytoplankton strategies for photosynthetic energy allocation. *Annual Review of Marine Science*, 7(1):265–297.

Harris, G. (1986). *Phytoplankton Ecology: Structure, Function and Fluctuation*. Chapman & Hall, London.

Harvey, H. W. (1937). The Supply of Iron to Diatoms. *Journal of the Marine Biological Association of the United Kingdom*, 22(01):205–219.

Hauck, J., Völker, C., Wolf-Gladrow, D. A., Laufkotter, C., Vogt, M., Aumont, O., Bopp, L., Buitenhuis, E. T., Doney, S. C., Dunne, J. P., Gruber, N., Hashioka, T., Le Quéré, C., Lima, I. D., Nakano, H., Seferian, R., and Totterdell, I. (2015). A multi-model study on the Southern Ocean CO2 uptake and the role of the biological carbon pump in the 21st century. *Global Biogeochemical Cycles*, 29:1451–1470.

Havskum, H., Schlüter, L., Scharek, R., Berdalet, E., and Jacquet, S. (2004). Routine quantification of phytoplankton groups- Microscopy or pigment analyses? *Marine Ecology Progress Series*, 273:31–42.

Haynes, J. M., Jakob, C., Rossow, W. B., Tselioudis, G., and Brown, J. (2011). Major characteristics of Southern Ocean cloud regimes and their effects on the energy budget. *Journal of Climate*, 24:5061–5080.

Hazzard, C., Lesser, M. P., and Kinzie, R. A. (1997). Effects of ultraviolet radiation on photosynthesis in the subtropical marine diatom, Chaetoceros gracilis (Bacillariophycese). *Journal of Phycology*, 33(6):960–968.

Helbling, E. W., Chalker, B. E., Dunlap, W. C., Holm-Hansen, O., and Villafañe, V. E. (1996). Photoacclimation of antarctic marine diatoms to solar ultraviolet radiation. *Journal of Experimental Marine Biology and Ecology*, 204(1-2):85–101.

Hess, W. R., Partensky, F., van der Staay, G. W., Garcia-Fernandez, J. M., Borner, T., and Vaulot, D. (1996). Coexistence of phycoerythrin and a chl a/b antenna in a marine prokayote. *Proceedings of the National Academy of Sciences of the United States of America*, 93:11126–111230.

Hickman, A. E., Dutkiewicz, S., Williams, R. G., and Follows, M. J. (2010). Modelling the effects of chromatic adaptation on phytoplankton community structure in the oligotrophic ocean. *Marine Ecology Progress Series*, 406:1–17.

Higgins, H. W., Wright, S. W., and Schlüter, L. (2011). Quantitative interpretation of chemotaxotaxonic pigment data. In Roy, S., Llewellyn, C., Egeland, E., and Johnsen, G., editors, *Phytoplankton pigments: Characterization, chemotaxonomy and applications in oceanography*, pages 257–313. Cambridge University Press.

Hill, R. and Bendall, F. (1960). Function of the two cytochrome components in chloroplasts: A working hypothesis. *Nature*, 186:136–137.

Hoepffner, N. and Sathyendranath, S. (1991). Effect of pigment composition on absorption properties of phytoplankton. *Marine Ecology Progress Series*, 73:11–23.

Hoepffner, N. and Sathyendranath, S. (1992). Bio-optical characteristics of coastal waters: Absorption spectra of phytoplankton and pigment distribution in the western North Atlantic. *Limnology and Oceanography*, 37(8):1660–1679.

Hoffmann, L. J., Peeken, I., and Lochte, K. (2008). Iron, silicate, and light co-limitation of three Southern Ocean diatom species. *Polar Biology*, 31(9):1067–1080.

Hoge, F. E. and Lyon, P. E. (1996). Satellite retrieval of inherent optical properties by linear matrix inversion of oceanic radiance models: An analysis of model and radiance measurement errors. *Journal of Geophysical Research*, 101(C7):16631–16648.

Hoge, F. E., Lyon, P. E., Swift, R. N., Yungel, J. K., Abbott, M. R., Letelier, R. M., and Esaias, W. E. (2003). Validation of Terra-MODIS phytoplankton chlorophyll fluorescence line height. I. Initial airborne lidar results. *Applied Optics*, 42(15):2767–2771.

Holm-Hansen, O. and Hewes, C. D. (2004). Deep chlorophyll-a maxima (DCMs) in Antarctic waters: I. Relationships between DCMs and the physical, chemical, and optical conditions in the upper water column. *Polar Biology*, 27(11):699–710.

Holm-Hansen, O., Kahru, M., and Hewes, C. D. (2005). Deep chlorophyll a maxima (DCMs) in pelagic Antarctic waters. II. Relation to bathymetric features and dissolved iron concentrations. *Marine Ecology Progress Series*, 297:71–81.

Honjo, S. (2004). Particle export and the biological pump in the Southern Ocean. *Antarctic Science*, 16(4):501–516.

Hope, A. B. (2000). Electron transfers amongst cytochrome f, plastocyanin and photosystem I: Kinetics and mechanisms. *Biochimica et Biophysica Acta - Bioenergetics*, 1456:5–26.

Horton, P. and Ruban, A. (2005). Molecular design of the photosystem II light-harvesting antenna: Photosynthesis and photoprotection. *Journal of Experimental Botany*, 56(411):365–373.

Hu, C., Lee, Z., and Franz, B. (2012). Chlorophyll a algorithms for oligotrophic oceans: A novel approach based on three-band reflectance difference. *Journal of Geophysical Research: Oceans*, 117(1):1–25.

Hu, C., Muller-Karger, F. E., Taylor, C., Carder, K. L., Kelble, C., Johns, E., and Heil, C. A. (2005). Red tide detection and tracing using MODIS fluorescence data: A regional example in SW Florida coastal waters. *Remote Sensing of Environment*, 97:311–321.

Hughes, D. J., Campbell, D. A., Doblin, M. A., Kromkamp, J. C., Lawrenz, E., Moore, C. M., Oxborough, K., Prášil, O., Ralph, P. J., Alvarez, M. F., and Suggett, D. J. (2018). Roadmaps and detours: Active chlorophyll-a assessments of primary productivity across marine and freshwater systems. *Environmental Science and Technology*, 52(21):12039–12054.

Huot, Y. and Babin, M. (2010). Overview of fluorescence protocols: Theory, basic concepts and practice. In Suggett, D., Prasil, O., and Borowitzka, M., editors, *Chlorophyll a fluorescence in aquatic sciences: Methods and applications*, chapter 3, pages 31–74. Springer.

Huot, Y., Brown, C. A., and Cullen, J. J. (2005). New algorithms for MODIS sun-induced chlorophyll fluorescence and a comparison with present data products. *Limnology and Oceanography: Methods*, 3:108–130.

Huot, Y., Franz, B. A., and Fradette, M. (2013). Estimating variability in the quantum yield of sun-induced chlorophyll fluorescence: A global analysis of oceanic waters. *Remote Sensing of Environment*, 132:238–253.

Hutchins, D. A., Sedwick, P. N., DiTullio, G. R., Boyd, P. W., Queguiner, B., Griffiths, F. B., and Crossley, C. (2001). Control of phytoplankton growth by iron supply and

irradiance in the subantarctic Southern Ocean: Experimental results from the SAZ Project. *Journal of Geophysical Research: Oceans*, 106(C12):31573–31583.

IOCCG (2000). Remote sensing of ocean colour in coastal, and other optically-complex, waters. Technical report, Sathyendranath, S. (ed.), Reports of the International Ocean-Colour Coordinating Group, No. 3, IOCCG, Dartmouth, Canada.

IOCCG (2015). Ocean colour remote sensing in polar seas. Technical report, Babin, M., Arrigo, K., Belanger, S. and Forget, M-H (eds.), Reports of the International Ocean-Colour Coordinating Group, No. 16, IOCCG, Dartmouth, Canada.

Irigoien, X., Meyer, B., Harris, R., and Harbour, D. (2004). Using HPLC pigment analysis to investigate phytoplankton taxonomy: The importance of knowing your species. *Helgoland Marine Research*, 58(2):77–82.

Itoh, S. and Iwaki, M. (1989). Vitamin K1 (phylloquinone) restores the turnover of FeS centers in the ether-extracted spinach PS I particles. *FEBS Letters*, 243(1):47–52.

Iturriaga, R. and Siegel, D. A. (1989). Microphotometric characterization of phytoplankton and detrital absorption properties in the Sargasso Sea. *Limnology and Oceanography*, 34(8):1706–1726.

Jacques, G. and Panouse, M. (1991). Biomass and composition of size fractionated phytoplankton in the Weddell-Scotia Confluence area. *Polar Biology*, 11(5):315–328.

Jain, A. K., Murty, M. N., and Flynn, P. J. (1999). Data clustering: a review. *ACM Computing Surveys*, 31(3):264–323.

Jakob, T., Goss, R., and Wilhelm, C. (1999). Activation of diadinoxanthin de-epoxidase due to a chlororespiratory proton gradient in the dark in the diatom Phaeodactylum tricornutum. *Plant Biology*, 1:76–82.

Jakob, T., Goss, R., and Wilhelm, C. (2001). Unusual pH-dependence of diadinoxanthin de-epoxidase activation causes chlororespiratory induced accumulation of diatoxanthin in the diatom Phaeodactylum tricornutum. *Journal of Plant Physiology*, 158:383–390.

Jeffrey, S. W. and Vesk, M. (1997). Introduction to marine phytoplankton and their pigment signatures. In Jeffrey, S., Mantoura, R., and Wright, S., editors, *Phytoplankton pigments in oceanography: guidelines to modern methods*, pages 37–84. UNESCO, Paris.

Johnsen, G., Nelson, N. B., Jovine, R. V. M., and Prezelin, B. B. (1994). Chromoprotein- and pigment dependent modeling of spectral light absorption in two dinoflagellates, Prorocentrum minimum and Heterocapsa pygmaea. *Marine Ecology Progress Series*, 114(3):245–258.

Johnsen, G., Prezelin, B. B., and Jovine, R. V. M. (1997). Fluorescence excitation spectra and light utilization in two red tide dinoflagellates. *Limnology and Oceanography*, 42(5):1166–1177.

Johnson, R., Strutton, P. G., Wright, S. W., McMinn, A., and Meiners, K. M. (2013). Three improved satellite chlorophyll algorithms for the Southern Ocean. *Journal of Geophysical Research: Oceans*, 118(7):3694–3703.

Johnson, Z. I., Zinser, E. R., Coe, A., McNulty, N. P., Woodward, E. M. S., and Chrisholm, S. W. (2006). Niche partitioning among Prochloroccocus ecotypes along ocean-scale environmental gradients. *Science*, 311(5768):1737–1740.

Joliot, P. and Joliot, A. (2002). Cyclic electron transfer in plant leaf. *Proceedings of the National Academy of Sciences*, 99(15):10209–10214.

Joubert, W. R., Swart, S., Tagliabue, A., Thomalla, S. J., and Monteiro, P. M. S. (2014). The sensitivity of primary productivity to intra-seasonal mixed layer variability in the sub-Antarctic Zone of the Atlantic Ocean. *Biogeosciences Discussions*, 11:4335–4358.

Junge, W. (1999). ATP synthase and other motor proteins. *Proceedings of the National Academy of Sciences*, 96:4735–4737.

Kana, R., Kotabová, E., Sobotka, R., and Prášil, O. (2012). Non-photochemical quenching in cryptophyte alga Rhodomonas salina is located in chlorophyll a/c antennae. *PLoS ONE*, 7(1).

Kana, R., Prášil, O., and Mullineaux, C. W. (2009). Immobility of phycobilins in the thylakoid lumen of a cryptophyte suggests that protein diffusion in the lumen is very restricted. *FEBS Letters*, 583(4):670–674.

Kautsky, H. and Hirsch, A. (1931). Neue Versuche zur Kohlensäureassimilation. *Naturwissenschaften*, 19(48):964.

Kerfeld, C. A., Sawaya, M. R., Brahmandam, V., Cascio, D., Ho, K. K., Trevithick-Sutton, C. C., Krogmann, D. W., and Yeates, T. O. (2003). The crystal structure of a cyanobacterial water-soluble carotenoid binding protein. *Structure*, 11:55–65.

Kiefer, D. A., Chamberlin, W. S., and Booth, C. R. (1989). Natural fluorescence of chlorophyll a: Relationship to photosynthesis and chlorophyll concentration in the Western South Pacific Gyre. *Limnology and Oceanography*, 34(5):868–881.

Kiefer, D. A. and Reynolds, R. A. (1992). Advances in understanding phytoplankton fluorescence and photosynthesis. In Falkowski, P. and Woodhead, A., editors, *Primary Productivity and Biogeochemical Cycles in the Sea*, pages 155–174. Plenum, New York.

Kirk, J. T. O. (1975a). A theoretical analysis of the contribution of algal cells to the attenuation of light within natural waters I. General treatment of suspensions of pigmented cells. *New Phytologist*, 75:21–36.

Kirk, J. T. O. (1975b). A theoretical analysis of the contribution of algal cells to the attenuation of light within natural waters II. Spherical cells. *New Phytologist*, 75:21–36.

Kirk, J. T. O. (1976). A theoretical analysis of the contribution of algal cells to the attenuation of light within natural waters III. Cylindrical and spheroidal cells. *New Phytologist*, 77:341–358.

Kirk, J. T. O. (2011). Light capture by aquatic plants. In *Light and Photosynthesis in Aquatic Ecosystems*, chapter 9, pages 308–329. Cambridge University Press, 3rd edition.

Kishino, M., Takahashi, M., Okami, N., and Ichimura, S. (1985). Estimation of the Spectral Absorption Coefficients of Phytoplankton in the Sea. *Bulletin of Marine Science*, 37(2):634–642.

Klunder, M. B., Laan, P., Middag, R., de Baar, H. J. W., and van Ooijen, J. C. (2011). Dissolved iron in the Southern Ocean (Atlantic sector). *Deep-Sea Research Part II: Topical Studies in Oceanography*, 58(25-26):2678–2694.

Koga, S., Nomura, D., and Wada, M. (2014). Variation of dimethylsulfide mixing ratio over the Southern Ocean from 36 S to 70 S. *Polar Science*, pages 1–8.

Kolbowski, J. and Schreiber, U. (1995). Computer-controlled phytoplankton analyzer based on 4-wavelengths PAM chlorophyll fluorometer. *Photosynthesis: From Light to Biosphere*, 5:825–828.

Korb, R. E., Whitehouse, M. J., and Ward, P. (2004). SeaWiFS in the southern ocean: Spatial and temporal variability in phytoplankton biomass around South Georgia. *Deep-Sea Research Part II: Topical Studies in Oceanography*, 51(1-3):99–116.

Kozlowski, W. A., Deutschman, D., Garibotti, I., Trees, C., and Vernet, M. (2011). An evaluation of the application of CHEMTAX to Antarctic coastal pigment data. *Deep-Sea Research Part I: Oceanographic Research Papers*, 58(4):350–364.

Krause, G. H. and Weis, E. (1991). Chlorophyll fluorescence and photosynthesis: The basics. *Annual Review of Plant Physiology and Plant Molecular Biology*, 42:313–349.

Kropuenske, L. R., Mills, M. M., van Dijken, G. L., Alderkamp, A.-C., Mine Berg, G., Robinson, D. H., Welschmeyer, N. A., and Arrigo, K. R. (2010). Strategies and rates of photoacclimation in two major Southern Ocean phytoplankton taxa: Phaeocystis Antarctica (Haptophyta) and Fragilariopsis cylindrus (Bacillariophyceae). *Journal of Phycology*, 46(6):1138–1151.

Kropuenske, L. R., Mills, M. M., van Dijken, G. L., Bailey, S., Robinson, D. H., Welschmeyer, N. A., and Arrigo, K. R. (2009). Photophysiology in two major Southern Ocean phytoplankton taxa: Photoprotection in Phaeocystis antarctica and Fragilariopsis cylindrus. *Limnology and Oceanography*, 54(4):1176–1196.

Kuzminov, F. I. and Gorbunov, M. Y. (2016). Energy dissipation pathways in photosystem 2 of the diatom, Phaeodactylum tricornutum, under high-light conditions. *Photosynthesis Research*, 127(2):219–235.

Kwon, E. Y., Primeau, F., and Sarmiento, J. L. (2009). The impact of remineralization depth on the air-sea carbon balance. *Nature Geoscience*, 2(9):630–635.

Lakowicz, J. R. and Masters, B. R. (2008). Principles of Fluorescence Spectroscopy, Third Edition. *Journal of Biomedical Optics*, 13(2):029901.

Lancelot, C., de Montety, A., Goosse, H., Becquevort, S., Schoemann, V., Pasquer, B., and Vancoppenolle, M. (2009). Spatial distribution of the iron supply to phytoplankton in the Southern Ocean: a model study. *Biogeosciences Discussions*, 6(3):4919–4962.

Landschützer, P., Gruber, N., Haumann, F. A., Rödenbeck, C., Bakker, D. C. E., Heuven, S. V., Hoppema, M., Metzl, N., Sweeney, C., Takahashi, T., Tilbrook, B., and Wanninkhof, R. (2015). The reinvigoration of the Southern Ocean carbon sink. *Science*, 349(6253):1221–1224.

Laney, S. R., Letelier, R. M., and Abbott, M. R. (2005). Parameterizing the natural fluorescence kinetics of Thalassiosira weissflogii. *Limnology and Oceanography*, 50(5):1499–1510.

Lapucci, C., Rella, M. A., Brandini, C., Ganzin, N., Gozzini, B., Maselli, F., Massi, L., Nuccio, C., Ortolani, A., and Trees, C. (2012). Evaluation of empirical and semi-analytical chlorophyll algorithms in the Ligurian and North Tyrrhenian Seas. *Journal of Applied Remote Sensing*, 6:063565–1:21.

Lavaud, J. and Kroth, P. G. (2006). In diatoms, the transthylakoid proton gradient regulates the photoprotective non-photochemical fluorescence quenching beyond its control on the xanthophyll cycle. *Plant and Cell Physiology*, 47(7):1010–1016.

Lavaud, J., Rousseau, B., and Etienne, A. L. (2002a). In diatoms, a transthylakoid proton gradient alone is not sufficient to induce a non-photochemical fluorescence quenching. *FEBS letters*, 523(1-3):163–6.

Lavaud, J., Rousseau, B., and Etienne, A. L. (2004). General features of photoprotection by energy dissipation in planktonic diatoms (Bacillariophyceae). *Journal of Phycology*, 40:130–137.

Lavaud, J., Rousseau, B., van Gorkom, H. J., and Etienne, A. L. (2002b). Influence of the diadinoxanthin pool size on photoprotection in the marine planktonic diatom Phaeodactylum tricornutm. *Plant physiology*, 129(July):1398–1406.

Lavaud, J., Strzepek, R. F., and Kroth, P. G. (2007). Photoprotection capacity differs among diatoms: Possible consequences on the spatial distribution of diatoms related to fluctuations in the underwater light climate. *Limnology and Oceanography*, 52(3):1188–1194.

Lavaud, J., van Gorkom, H. J., and Etienne, A. L. (2002c). Photosystem II electron transfer cycle and chlororespiration in planktonic diatoms. *Photosynthesis research*, 74:51–59.

Law, C. S., Abraham, E. R., Watson, A. J., and Liddicoat, M. I. (2003). Vertical eddy diffusion and nutrient supply to the surface mixed layer of the Antarctic Circumpolar Current. *Journal of Geophysical Research*, 108(C8, 3272):1–14.

Laws, E. A. and Bannister, T. T. (1980). Nutrient- and light-limited growth of Thalassiosira fluviatilis in continuous culture , with implications for phytoplankton growth in the ocean. *Limnology and Oceanography*, 25(3):457–473.

Le Moigne, F. A., Boye, M., Masson, A., Corvaisier, R., Grossteffan, E., Guéneugues, A., and Pondaven, P. (2013). Description of the biogeochemical features of the subtropical

southeastern Atlantic and the Southern Ocean south of South Africa during the austral summer of the International Polar Year. *Biogeosciences*, 10(1):281–295.

Le Quéré, C., Buitenhuis, E. T., Moriarty, R., Alvain, S., Aumont, O., Bopp, L., Chollet, S., Enright, C., Franklin, D. J., Geider, R. J., Harrison, S. P., Hirst, A., Larsen, S., Legendre, L., Platt, T., Prentice, I. C., Rivkin, R. B., Sathyendranath, S., Stephens, N., Vogt, M., Sailley, S., and Vallina, S. M. (2015). Role of zooplankton dynamics for Southern Ocean phytoplankton biomass and global biogeochemical cycles. *Biogeosciences Discussions*, 12(14):11935–11985.

Le Quéré, C., Rodenbeck, C., Buitenhuis, E. T., Conway, T. J., Langenfelds, R., Gomez, A., Labuschagne, C., Ramonet, M., Nakazawa, T., Metzl, N., Gillett, N. P., and Heimann, M. (2007). Saturation of the Southern Ocean CO2 sink due to recent climate change. *Science*, 316:1735–1738.

Lee, Z., Carder, K. L., and Arnone, R. A. (2002). Deriving inherent optical properties from water color: a multiband quasi-analytical algorithm for optically deep waters. *Applied Optics*, 41(27):5755–5772.

Legendre, L. and Rassoulzadegan, F. (1995). Plankton and nutrient dynamics in marine waters. *Ophelia*, 41(1):153–172.

Lepetit, B., Sturm, S., Rogato, A., Gruber, A., Sachse, M., Falciatore, A., Kroth, P. G., and Lavaud, J. (2013). High light acclimation in the secondary plastids containing diatom Phaeodactylum tricornutum is triggered by the redox state of the plastoquinone pool. *Plant Physiology*, 161(2):853–65.

Lesser, M. P. (2006). Oxidative stress in marine environments: biochemistry and physiological ecology. *Annual Review of Physiology*, 68:253–78.

Letelier, R. M. and Abbott, M. R. (1996). An analysis of chlorophyll fluorescence algorithms for the moderate resolution imaging spectrometer (MODIS). *Remote Sensing of Environment*, 58:215–223.

Letelier, R. M., Abbott, M. R., and Karl, D. M. (1997). Chlorophyll natural fluorescence response to upwelling events in the Southern Ocean. *Geophysical Research Letters*, 24(4):409–412.

Letelier, R. M., Bidigare, R. R., Hebel, D. V., Ondrusek, M., Winn, C. D., and Karl, D. M. (1993). Temporal variability of phytoplankton community structure based on pigment analysis. *Limnology and Oceanography*, 38(7):1420–1437.

Letelier, R. M. and Karl, D. M. (1989). Phycoerythrin-containing cyanobacteria in surface waters of the Drake Passage. *Antarctic Journal*, 24:185–188.

Letelier, R. M., White, A. E., Bidigare, R. R., Barone, B., Church, M. J., and Karl, D. M. (2017). Light absorption by phytoplankton in the North Pacific Subtropical Gyre. *Limnology and Oceanography*, 62(4):1526–1540.

Levitus, S., Conkright, M. E., Reid, J. L., Najjar, R. G., and Mantyla, A. (1993). Distribution of nitrate, phosphate and silicate in the world oceans. *Progress in Oceanography*, 31(3):245–273.

Lewis, M. R., Horne, E. P. W., Cullen, J., Oakey, N. S., and Platt, T. (1984). Turbulent motions may control phytoplankton photosynthesis in the uper ocean. *Nature*, 311(5981):49–50.

Liaaen-Jensen, S. (1978). Marine carotenoids. In Scheuer, P., editor, *Marine natural products*, chapter 1, pages 1–73. Academic Press, New York.

Lin, H., Lin, H., Kuzminov, F. I., Park, J., Lee, S., Falkowski, P. G., and Gorbunov, M. Y. (2016). The fate of photons absorbed by phytoplankton in the global ocean. *Science*, 351(6270):1–7.

Liu, J., Curry, J. A., and Martinson, D. G. (2004). Interpretation of recent Antarctic sea ice variability. *Geophysical Research Letters*, 31(L02205):2004.

Llort, J., Levy, M., Sallee, J.-B., and Tagliabue, A. (2015). Onset, intensification, and decline of phytoplankton blooms in the Southern Ocean. *ICES Journal of Marine Science*.

Lodish, H. (2004). Photosynthetic stages and light-absorbing pigments. In Lodish, H., Berk, A., Kaiser, C., Krieger, M., Scott, M., Zipursky, S., and Darnell, J., editors, *Molecular Cell Biology*, chapter Cellular E, page 973. W. H. Freeman and Company, New York, fifth edit edition.

Lohrenz, S. E., Weidemann, A. D., and Tuel, M. (2003). Phytoplankton spectral absorption as influenced by community size structure and pigment composition. *Journal of Plankton Research*, 25(1):35–61.

Lorenzen, C. J. (1966). A method for the continuous measurement of in vivo chlorophyll concentration. *Deep-Sea Research*, 13:223–227.

Lorenzen, C. J. (1972). Extinction of light in the ocean by phytoplankton. *ICES Journal of Marine Science*, 34(2):262–267.

Lovenduski, N., Gruber, N., Doney, S., and Lima, I. (2007). Enhanced CO2 outgassing in the Southern Ocean from a positive phase of the Southern Annular Mode. *Global Biogeochemical Cycles*, 21(GB2026):1–14.

Lovenduski, N. S., Gruber, N., and Doney, S. C. (2008). Toward a mechanistic understanding of the decadal trends in the Southern Ocean carbon sink. *Global Biogeochemical Cycles*, 22(3):1–9.

Lutz, V. A. and Sathyendaranath, S. (2001). Changes in the in vivo absorption and fluorescence excitation spectra with growth irradiance in three species of phytoplankton. *Journal of Plankton Research*, 23(6):555–569.

MacIntyre, H. L., Kana, T. M., Anning, T., and Geider, R. (2002). Photoacclimation of photosynthesis irradiance response curves and photosynthetic pigments in microalgae and cyanobacteria. *Journal of Phycology*, 38(1):17–38.

Mackey, M. D., Mackey, D. J., Higgins, H. W., and Wright, S. W. (1996). CHEMTAX - A program for estimating class abundances from chemical markers: Application to HPLC measurements of phytoplankton. *Marine Ecology Progress Series*, 144(1-3):265–283.

Mahowald, N. M., Baker, A. R., Bergametti, G., Brooks, N., Duce, R. A., Jickells, T. D., Kubilay, N., Prospero, J. M., and Tegen, I. (2005). Atmospheric global dust cycle and iron inputs to the ocean. *Global Biogeochemical Cycles*, 19(4).

Marchant, H. J., Davidson, A. T., and Wright, S. W. (1987). The distribution and abundance of the chroococcoid cyanobacteria in the Southern Ocean (Ninth Symposium on Polar Biology). *Proceedings of the NIPR Symposium on Polar Biology*, 1:1–9.

Maritorena, S., Morel, A., and Gentili, B. (2000). Determination of the fluorescence quantum yield by oceanic phytoplankton in their natural habitat. *Applied Optics*, 39(36):6725–37.

Maritorena, S., Siegel, D. A., and Peterson, A. R. (2002). Optimization of a semianalytical ocean color model for global-scale applications. *Applied Optics*, 41(15):2705–2714.

Martin, J. H., Fitzwater, S. E., and Gordon, R. M. (1990a). Iron deficiency limits phytoplankton growth in Antarctic waters. *Global Biogeochemical Cycles*, 4(1):5–12.

Martin, J. H., Gordon, R. M., and Fitzwater, S. E. (1990b). Iron in Antarctic waters. *Nature*, 345:156–158.

Martin, J. H., Gordon, R. M., and Fitzwater, S. E. (1991). Iron limitation? 36(8):1793–1802.

Martin, P., van der Loeff, M. R., Cassar, N., Vandromme, P., D'Ovidio, F., Stemmann, L., Rengarajan, R., Soares, M., González, H. E., Ebersbach, F., Lampitt, R. S., Sanders, R., Barnett, B. A., Smetacek, V., and Naqvi, S. W. A. (2013). Iron fertilization enhanced net community production but not downward particle flux during the Southern Ocean iron fertilization experiment LOHAFEX. *Global Biogeochemical Cycles*, 27:871–881.

Martin-Jézéquel, V., Hildebrand, M., and Brzezinski, M. A. (2000). Silicon metabolism in diatoms: Implications for growth. *Journal of Phycology*, 36:821–840.

Mathis, P. and Pailloton, G. (1981). Primary processes of photosynthesis. In Hatch, M. and Boardman, N., editors, *The biochemistry of plants: A comprehensive treatise, Volume 8, Photosynthesis*, chapter 3, pages 97–161. Academic Press.

Mehler, A. H. (1951). Studies on reactions of illuminated chloroplasts. *Archives of Biochemistry and Biophysics*, 33(1):65–77.

Meler, J., Ostrowska, M., Ficek, D., and Zdun, A. (2017). Light absorption by phytoplankton in the southern Baltic and Pomeranian lakes: mathematical expressions for remote sensing applications. *Oceanologia*, 59(3):195–212.

Mendes, C. R. B., de Souza, M. S., Garcia, V. M. T., Leal, M. C., Brotas, V., and Garcia, C. A. E. (2012). Dynamics of phytoplankton communities during late summer around the tip of the Antarctic Peninsula. *Deep-Sea Research Part I: Oceanographic Research Papers*, 65:1–14.

Mendes, C. R. B., Tavano, V. M., Leal, M. C., de Souza, M. S., Brotas, V., and Garcia, C. A. E. (2013). Shifts in the dominance between diatoms and cryptophytes during three late summers in the Bransfield Strait (Antarctic Peninsula). *Polar Biology*, 36(4):537–547.

Menzel, D. and Ryther, J. (1961). Nutrients limiting the production of phytoplankton in the Sargasso sea, with special reference to iron. *Deep Sea Research (1953)*, 7(4):276–281.

Metzl, N., Tilbrook, B., and Poisson, A. (1999). The annual fCO2 cycle and the air-sea CO2 flux in the sub-Antarctic Ocean. *Tellus B*, 51(4):849–861.

Meyer, A. A., Tackx, M., and Daro, N. (2000). Xanthophyll cycling in Phaeocystis globosa and Thalassiosira sp.: A possible mechanism for species succession. *Journal of Sea Research*, 43(3-4):373–384.

Michaels, A. F. and Silver, M. W. (1988). Primary production, sinking fluxes and the microbial food web. *Deep Sea Research Part A. Oceanographic Research Papers*, 35(4):473–490.

Mikaloff Fletcher, S. E., Gruber, N., Jacobson, A. R., Doney, S. C., Dutkiewicz, S., Gerber, M., Follows, M., Joos, F., Lindsay, K., Menemenlis, D., Mouchet, A., Müller, S. A., and Sarmiento, J. L. (2006). Inverse estimates of anthropogenic CO2 uptake, transport, and storage by the ocean. *Global Biogeochemical Cycles*, 20(2):1–16.

Miller, W. L., Moran, M. A., Sheldon, W. M., Zepp, R. G., and Opsahl, S. (2002). Determination of apparent quantum yield spectra for the formation of biologically labile photoproducts. *Limnology and Oceanography*, 47(2):343–352.

Milligan, A. J., Aparicio, U. A., and Behrenfeld, M. J. (2012). Fluorescence and non-photochemical quenching responses to simulated vertical mixing in the marine diatom Thalassiosira weissflogii. *Marine Ecology Progress Series*, 448:67–78.

Minas, H. J. and Minas, M. (1992). Net community production in "High Nutrient-Low Chlorophyll" waters of the tropical and antarctic oceans: grazing vs iron hypothesis. *Oceanologica Acta*, 15(2):145–162.

Mitchell, B. G., Brody, E. A., Holm-Hansen, O., McClain, C., and Bisho, J. (1991). Light limitation of phytoplankton biomass and macronutrient utilization in the Southern Ocean. *Limnology and Oceanography*, 36(8):1662–1677.

Mitchell, B. G. and Holm-Hansen, O. (1991). Bio-optical properties of Antarctic Peninsula waters: Differentiation from temperate ocean model. *Deep Sea Research Part A. Oceanographic Research Papers*, 38(8-9):1009–1028.

Mitchell, B. G. and Kiefer, D. A. (1988a). Chlorophyll a specific absorption and fluorescence excitation spectra for light-limited phytoplankton. *Deep-Sea Research*, 35(5):639–663.

Mitchell, B. G. and Kiefer, D. A. (1988b). Variability in pigment specific particulate fluorescence and absorption spectra in the northeastern Pacific Ocean. *Deep-Sea Research*, 35(5):665–689.

Mobley, C. M. (1994). *Light and water: Radiative transfer in natural waters*. Academic Press, first edition.

Modigh, M. and Castaldo, S. (2005). Effects of fixatives on ciliates as related to cell size. *Journal of Plankton Research*, 27(8):845–849.

Mohan, R., Mergulhao, L., Guptha, M., Rajakumar, A., Thamban, M., AnilKumar, N., Sudhakar, M., and Ravindra, R. (2008). Ecology of coccolithophores in the Indian sector of the Southern Ocean. *Marine Micropaleontology*, 67(1-2):30–45.

Moisan, T. A., Ellisman, M. H., Buitenhuys, C. W., and Sosinsky, G. E. (2006). Differences in chloroplast ultrastructure of Phaeocystis antarctica in low and high light. *Marine Biology*, 149:1281–1290.

Moisan, T. A. and Mitchell, B. G. (1999). Photophysiological acclimation of Phaeocystis antarctica Karsten under light limitation. *Limnology and Oceanography*, 44(2):247–258.

Moisan, T. A. and Mitchell, B. G. (2001). UV absorption by mycosporine-like amino acids in Phaeocystis antarctica Karsten induced by photosynthetically available radiation. *Marine Biology*, 138(1):217–227.

Moisan, T. A., Moisan, J. R., Linkswiler, M. A., and Steinhardt, R. A. (2013). Algorithm development for predicting biodiversity based on phytoplanktonabsorption. *Continental Shelf Research*, 55:17–28.

Moisan, T. A., Olaizola, M., and Mitchell, B. G. (1998). Xanthophyll cycling in Phaeocystis antarctica:changes in cellular fluorescence. *Marine Ecology Progress Series*, 169:113–121.

Monteiro, P. M. S., Boyd, P. W., and Bellerby, R. (2011). Role of the seasonal cycle in coupling climate and carbon cycling in the Subantarctic Zone. *Eos*, 92(28):235–236.

Moon-van der Staay, S. Y., van der Staay, G. W. M., Guillou, L., Vaulot, D., Claustre, H., and Medlin, L. K. (2000). Abundance and diversity of prymnesiophytes in the picoplankton community from the equatorial Pacific Ocean inferred from 18S rDNA sequences. *Limnology and Oceanography*, 45(1):98–109.

Moore, C. M., Mills, M. M., Langlois, R., Milne, A., Achterberg, E. P., LaRoche, J., and Geider, R. J. (2008). Relative influence of nitrogen and phosphorus availability on phytoplankton physiology and productivity in the oligotrophic sub-tropical North Atlantic Ocean. *Limnology and Oceanography*, 53(1):291–305.

Moore, C. M., Suggett, D. J., Hickman, A. E., Kim, Y. N., Tweddle, J. F., Sharples, J., Geider, R. J., and Holligan, P. M. (2006). Phytoplankton photoacclimation and photoadaptation in response to environmental gradients in a shelf sea. *Limnology and Oceanography*, 51(2):936–949.

Moore, J. K. and Abbott, M. R. (2000). Phytoplankton chlorophyll distributions and primary production in the Southern Ocean. *Journal of Geophysical Research*, 105(C12):28709.

Moore, J. K., Geider, R. J., Lenton, T. M., Tsuda, A., Boyd, P. W., LaRoche, J., Galbraith, E. D., Arrigo, K. R., Bopp, L., Moore, C. M., Mahowald, N. M., Marinov, I., Berman-Frank, I., Oschlies, A., Mills, M. M., Marañón, E., Nakatsuka, T., Guieu, C., Jaccard, S. L., Saito, M. A., Thingstad, T. F., and Ulloa, O. (2013). Processes and patterns of oceanic nutrient limitation. *Nature Geoscience*, 6(9):701–710.

Moore, T. S., Dowell, M. D., and Franz, B. A. (2012). Detection of coccolithophore blooms in ocean color satellite imagery: A generalized approach for use with multiple sensors. *Remote Sensing of Environment*, 117:249–263.

Morel, A. (1988). Optical modeling of the upper ocean in relation to its biogenous matter content (case I waters). *Journal of Geophysical Research*, 93(8):10749.

Morel, A. (2009). Are the empirical relationships describing the bio-optical properties of case 1 waters consistent and internally compatible? *Journal of Geophysical Research*, 114(1):1–15.

Morel, A. and Bricaud, A. (1981). Theoretical results concerning light absorption in a discrete medium, and application to specific absorption of phytoplankton. *Deep Sea Research Part A. Oceanographic Research Papers*, 28A(11):1375–1393.

Morel, A. and Prieur, L. (1977). Analysis of variations in ocean color. *Limnology and Oceanography*, 22(4):709–722.

Morrison, J. R. (2003). In situ determination of the quantum yield of phytoplankton chlorophyll a fluorescence: A simple algorithm, observations, and a model. *Limnology and Oceanography*, 48(2):618–631.

Morrison, J. R. and Goodwin, D. S. (2010). Phytoplankton photocompensation from space-based fluorescence measurements. *Geophysical Research Letters*, 37:L06603.

Morrow, J. H., Chamberlin, W. S., and Kiefer, D. A. (1989). A two-component description of spectral absorption by marine particles. *Limnology and Oceanography*, 34(8):1500–1509.

Moutier, W., Thomalla, S., Bernard, S., Wind, G., Ryan-Keogh, T. J., and Smith, M. (2019). Evaluation of Chlorophyll-a and POC MODIS Aqua 2 products in the Southern Ocean.

Mtshali, T. N., Horsten, N., Thomalla, S. J., RyanKeogh, T. J., Nicholson, S. A., Roychoudhury, A. N., Bucciarelli, E., Sarthou, G., Tagliabue, A., and Monteiro, P. M. S. (2019). Seasonal depletion of the dissolved iron reservoirs in the sub-Antarctic zone of the Southern Atlantic Ocean. *Geophysical Research Letters*, 46(8):4386–4395.

Muller, P., Li, X. P., and Niyogi, K. K. (2001). Non-photochemical quenching. A response to excess light energy. *Plant Physiology*, 125:1558–1566.

Munekage, Y., Hashimoto, M., Miyake, C., Tomizawa, K. I., Endo, T., Tasaka, M., and Shikanai, T. (2004). Cyclic electron flow around photosystem I is essential for photosynthesis. *Nature*, 429(6991):579–582.

Munro, D. R., Lovenduski, N. S., Takahashi, T., Stephens, B. B., Newberger, T., and Sweeney, C. (2015). Recent evidence for a strengthening CO2 sink in the Southern Ocean from carbonate system measurements in the Drake Passage (2002-2015). *Geophysical Research Letters*, pages 1–8.

Nelson, J. R. and Robertson, C. Y. (1993). Detrital spectral absorption: Laboratory studies of visible light effects on phytodetritus absorption, bacterial spectral signal, and comparison to field measurements. *Journal of Marine Research*, 51:181–207.

Neukermans, G., Reynolds, R. A., and Stramski, D. (2016). Optical classification and characterization of marine particle assemblages within the western Arctic Ocean. *Limnology and Oceanography*, 61:1472–1494.

Neville, R. A. and Gower, J. F. R. (1977). Passive remote sensing of phytoplankton via chlorophyll α fluorescence. *Journal of Geophysical Research*, 82(24):3487.

Nicholson, S.-A., Lévy, M., Llort, J., Swart, S., and Monteiro, P. M. S. (2016). Investigation into the impact of storms on sustaining summer primary productivity in the Sub-Antarctic Ocean. *Geophysical Research Letters*, 43:9192–9199.

Odate, T. and Fukuchi, M. (1995). Distribution and community structure of picophytoplankton in the southern ocean during the late austral summer of 1992. *Proceedings of the NIPR Symposium on Polar Biology*, 8:86–100.

Okami, N., Kishino, M., Sugihara, S., Takematsu, N., and Unoki, S. (1982). Analysis of ocean color spectra (III) Measurements of optical properties of sea water. *Journal of the Oceanographical Society of Japan*, 38(6):362–372.

Olaizola, M., Bienfang, P. K., and Ziemann, D. A. (1992). Pigment analysis of phytoplankton during a Subarctic spring bloom: xanthophyll cycling. *Journal of Experimental Marine Biology and Ecology*, 158(1):59–74.

Olaizola, M., LaRoche, J., Kolber, Z., and Falkowski, P. G. (1994). Non-photochemical fluorescence quenching and the diadinoxanthin cycle in a marine diatom. *Photosynthesis Research*, 41:357–370.

Olson, R. J., Chrisholm, S., Zettler, E., and Armbrust, A. (1988). Analysis of Synechoccocus pigment types in the sea using single and dual beam fluorometry. *Deep Sea Research Part A. Oceanographic Research Papers*, 35(3):425–440.

O'Reilly, J. E., Maritorena, S., Mitchell, B. G., Siegel, D. A., Carder, K. L., Garver, S. A., Kahru, M., and McClain, C. (1998). Ocean color chlorophyll algorithms for SeaWiFS. *Journal of Geophysical Research*, 103(C11):24937–24953.

O'Reilly, J. E., Maritorena, S., Siegel, D. A., O'Brien, M. C., Toole, D., Mitchell, B. G., Kahru, M., Chavez, F. P., Strutton, P., Cota, G. F., Hooker, S. B., McClain, C. R., Carder, K. L., Muller-Karger, F., Harding, L., Magnuson, A., Phinney, D., Moore, G. F., Aiken, J., Arrigo, K. R., Letelier, R., and Culver, M. (2000). Ocean color chlorophyll a algorithms for SeaWiFS, OC2 and OC4: Version 4. Technical report, NASA Tech. Memo. 2000-206892, Vol. 11.

Organelli, E., Bricaud, A., Gentili, B., Antoine, D., and Vellucci, V. (2016). Retrieval of Colored Detrital Matter (CDM) light absorption coefficients in the Mediterranean Sea using field and satellite ocean color radiometry: Evaluation of bio-optical inversion models. *Remote Sensing of Environment*, 186:297–310.

Organelli, E., Nuccio, C., Lazzara, L., Uitz, J., Bricaud, A., and Massi, L. (2017). On the discrimination of multiple phytoplankton groups from light absorption spectra of assemblages with mixed taxonomic composition and variable light conditions. *Applied Optics*, 56(14):3952–3968.

Orr, J. C., Fabry, V. J., Aumont, O., Bopp, L., Doney, S. C., Feely, R. A., Gnanadesikan, A., Gruber, N., Ishida, A., Joos, F., Key, R. M., Lindsay, K., Maier-Reimer, E., Matear, R., Monfray, P., Mouchet, A., Najjar, R. G., Plattner, G.-K., Rodgers, K. B., Sabine, C. L., Sarmiento, J. L., Schlitzer, R., Slater, R. D., Totterdell, I. J., Weirig, M.-F., Yamanaka, Y., and Yool, A. (2005). Anthropogenic ocean acidification over the twenty-first century and its impact on calcifying organisms. *Nature*, 437:681–686.

Orsi, A. H., Whitworth III, T., and Nowlin Jr, W. D. (1995). On the meridional extent and fronts of the Antarctic Circumpolar Current. *Deep Sea Research Part I: Oceanographic Research Papers*, 42(5):641–673.

Ort, D. R. and Baker, N. R. (2002). A photoprotective role for O2 as an alternative electron sink in photosynthesis? *Current Opinion in Plant Biology*, 5:193–8.

Ostrowska, M. (2011). Dependence between the quantum yield of chlorophyll a fluorescencein marine phytoplankton and trophicity in low irradiance level. *Optica Applicata*, 41(3):567–577.

Ostrowska, M. (2012). Model of the dependence of the sun-induced chlorophyll a fluorescence quantum yield on the environmental factors in the sea. *Optics Express*, 20(21):23300–23317.

Ostrowska, M., Darecki, M., and Wozniak, B. (1997). An attempt to use measurements of sun-induced chlorophyll fluorescence to estimate chlorophyll a concentration in the Baltic Sea. *Proc. SPIE*, 3222:528–537.

Ostrowska, M., Woźniak, B., and Dera, J. (2012). Modelled quantum yields and energy efficiency of fluorescence, photosynthesis and heat production by phytoplankton in the World Ocean. *Oceanologia*, 54(4):565–610.

Owens, T. G. (1986). Light-harvesting function in the diatom Phaeodactylum tricornutum. *Plant physiology*, 80:739–746.

Pakhomov, E. A. and Froneman, P. W. (1999). The Prince Edward Islands pelagic ecosystem, south Indian Ocean: A review of achievements, 1976 -1990. *Journal of Marine Systems*, 18:355–367.

Park, J., Kuzminov, F. I., Bailleul, B., Yang, E. J., Lee, S. H., Falkowski, P. G., and Gorbunov, M. Y. (2017). Light availability rather than Fe controls the magnitude of massive phytoplankton bloom in the Amundsen Sea polynyas, Antarctica. *Limnology and Oceanography*, 62(5):2260–2276.

Parkhill, J.-P., Maillet, G., and Cullen, J. J. (2001). Fluorescence-based maximal quantum yield for PSII as a diagnostic of nutrient stress. *Journal of Phycology*, 37:517–529.

Partensky, F., Blanchot, J., and Vaulot, D. (1999a). Differential distribution and ecology of Prochlorococcus and Synechococcus in oceanic waters : a review. *Bulletin de l'Institut océanographique*, 19(19):457–475.

Partensky, F., Hess, W. R., and Vaulot, D. (1999b). Prochlorococcus, a marine photosynthetic prokaryote of global significance. *Microbiology and Molecular Biology Reviews*, 63(1):106–127.

Patil, S., Mohan, R., Shetye, S., and Gazi, S. (2013). Phytoplankton abundance and community structure in the Antarctic polar frontal region during austral summer of 2009. *Chinese Journal of Oceanography and Limnology*, 31(1):21–30.

Peltier, G. and Cournac, L. (2002). Chlororespiration. *Annual Review of Plant Biology*, 53:523–550.

Peltier, G., Tolleter, D., Billon, E., and Cournac, L. (2010). Auxiliary electron transport pathways in chloroplasts of microalgae. *Photosynthesis Research*, 106:19–31.

Pereira, E. S. and Garcia, C. A. (2018). Evaluation of satellite-derived MODIS chlorophyll algorithms in the northern Antarctic Peninsula. *Deep-Sea Research Part II: Topical Studies in Oceanography*, 149(December):124–137.

Perissinotto, R., Lutjeharms, J. R. E., and van Ballegooyen, R. C. (2000). Biological-physical interactions and pelagic productivity at the Prince Edward Islands, Southern Ocean. *Journal of Marine Systems*, 24(3-4):327–341.

Pollard, R. T., Lucas, M. I., and Read, J. F. (2002). Physical controls on biogeochemical zonation in the Southern Ocean. *Deep Sea Research Part II: Topical Studies in Oceanography*, 49:3289–3305.

Pollard, R. T. and Read, J. F. (2001). Circulation pathways and transports of the Southern Ocean in the vicinity of the Southwest Indian Ridge. *Journal of Geophysical Research: Oceans*, 106(C2):2881–2898.

Pondaven, P., Ragueneau, O., Treguer, P., Hauvespre, A., Dezileau, L., and Reyss, J. (2000). Resolving the opal paradox in the Southern Ocean. *Nature*, 405:168–72.

Pope, R. M. and Fry, E. S. (1997). Absorption spectrum (380-700 nm) of pure water. II. Integrating cavity measurements. *Applied Optics*, 36(33):8710–8723.

Poulton, A. J., Moore, C. M., Seeyave, S., Lucas, M. I., Fielding, S., and Ward, P. (2007). Phytoplankton community composition around the Crozet Plateau, with emphasis on diatoms and Phaeocystis. *Deep Sea Research Part II: Topical Studies in Oceanography*, 54(18-20):2085–2105.

Preisendorfer, R. W. (1976). Hydrologic Optics. Volume 5. Properties. page 305. Honolulu: U.S. Dept. of Commerce, National Oceanic and Atmospheric Administration, Environmental Research Laboratories, Pacific Marine Environmental Laboratory.

Prieur, L. and Sathyendranath, S. (1981). An optical classification of coastal and oceanic waters based on the specific spectral absorption curves of phytoplankton pigments, dissolved organic matter, and other particulate materials. *Limnology and Oceanography Oceanography*, 26(4):671–689.

Quéguiner, B. and Brzezinski, M. A. (2002). Biogenic silica production rates and particulate organic matter distribution in the Atlantic sector of the Southern Ocean during austral spring 1992. *Deep Sea Research Part II: Topical Studies in Oceanography*, 49(9-10):1765–1786.

Ragni, M., Airs, R. L., Leonardos, N., and Geider, R. J. (2008). Photoinhibition of PSII in Emiliania huxleyi (Haptophyta) under high light stress: The roles of photoacclimation, photoprotection, and photorepair. *Journal of Phycology*, 44(3):670–683.

Ramsey, P. H. (1989). Critical values for Spearman's rank order correlation. *Journal of Educational Statistic*, 14(3):245–253.

Ras, J., Uitz, J., and Claustre, H. (2008). Spatial variability of phytoplankton pigment distributions in the Subtropical South Pacific Ocean: comparison between in situ and modelled data. *Biogeosciences*, 5:353–369.

Rau, W. (1988). Functions of carotenoids other than in photosynthesis. In Goodwin, T. W., editor, *Plant Pigments*, pages 231–255. Academic Press, London.

Raven, J. A. (1990). Predictions of Mn and Fe use efficiencies of phototrophic growth as a function of light availability for growth and of C assimilation pathway. *New Phytologist*, 116:1–18.

Redfield, A. C. (1934). *On the proportions of organic derivatives in sea water and their relation to the composition of plankton.* University Press of Liverpool, Liverpool, UK.

Redfield, A. C. (1958). The biological control of chemical factors in the environment. *American Scientist*, 46(3):205–221.

Rintoul, S. R., Hughes, C., and Olbers, D. (2001). The Antarctic Circumpolar Current System. In *Ocean Circulation and Climate*, pages 271–301. Academic Press.

Rio, M. H., Guinehut, S., and Larnicol, G. (2011). New CNES-CLS09 global mean dynamic topography computed from the combination of GRACE data, altimetry, and in situ measurements. *Journal of Geophysical Research: Oceans*, 116(7):1–25.

Roesler, C. S. (1998). Theoretical and experimental approaches to improve the accuracy of particulate absorption coefficients derived from the quantitative filter technique. *Limnology and Oceanography*, 43(7):1649–1660.

Roesler, C. S. and Perry, M. J. (1995). In situ phytoplankton absorption, fluorescence emission, and particulate backscattering spectra determined from reflectance. *Journal of Geophysical Research*, 100(C7):13279–13294.

Roesler, C. S., Perry, M. J., and Carder, K. L. (1989). Modeling in situ phytoplankton absorption from total absorption spectra in productive inland marine waters. *Limnology and Oceanography*, 34(8):1510–1523.

Rousseau, V., Vaulot, D., Casotti, R., Cariou, V., Lenz, J., Gunkel, J., and Baumann, M. (1994). The life cycle of Phaeocystis (Prymnesiophycaea): evidence and hypotheses. *Journal of Marine Systems*, 5:23–39.

Roy, T., Rayner, P., Matear, R., and Francey, R. (2003). Southern hemisphere ocean CO2 uptake: reconciling atmospheric and oceanic estimates. *Tellus*, 55B:701–710.

Rozema, P. D., Venables, H. J., van de Poll, W. H., Clarke, A., Meredith, M. P., and Buma, A. G. J. (2017). Interannual variability in phytoplankton biomass and species composition in northern Marguerite Bay (West Antarctic Peninsula) is governed by both winter sea ice cover and summer stratification. *Limnology and Oceanography*, 62(1):235–252.

Russo, A. D. P. G., de Souza, M. S., Mendes, C. R. B., Jesus, B., Tavano, V. M., and Garcia, C. A. E. (2015). Photophysiological effects of Fe concentration gradients on diatom-dominated phytoplankton assemblages in the Antarctic Peninsula region. *Journal of Experimental Marine Biology and Ecology*, 466:49–58.

Ryan-Keogh, T. J., DeLizo, L. M., Smith, W. O., Sedwick, P. N., McGillicuddy, D. J., Moore, C. M., and Bibby, T. S. (2017a). Temporal progression of photosynthetic-strategy in phytoplankton in the Ross Sea, Antarctica. *Journal of Marine Systems*, 166:87–96.

Ryan-Keogh, T. J., Thomalla, S. J., Mtshali, T. N., Horsten, N. R. V., and Little, H. J. (2018). Seasonal development of iron limitation in the sub-Antarctic zone. *Biogeosciences*, 15:4647–4660.

Ryan-Keogh, T. J., Thomalla, S. J., Mtshali, T. N., and Little, H. (2017b). Modelled estimates of spatial variability of iron stress in the Atlantic sector of the Southern Ocean. *Biogeosciences*, 14(17):3883–3897.

Ryther, J. H. and Kramer, D. D. (1961). Relative iron requirement of some coastal and offshore plankton algae. *Ecology*, 42(2):444–446.

Sabine, C. L., Feely, R. A., Gruber, N., Key, R. M., Lee, K., Bullister, J. L., Wanninkhof, R., Wong, C. S., Wallace, D. W. R., Tilbrook, B., Millero, F. J., Peng, T.-H., Kozyr, A., Ono, T., and Rios, A. F. (2004). The oceanic sink for anthropogenic CO2. *Science (New York, N.Y.)*, 305(5682):367–71.

Sakshaug, E., Johnsen, G., Andresen, K., and Vernet, M. (1991). Modeling of light-dependent algal photosynthesis and growth: experiments with the Barents sea diatoms Thalassiosira nordenskioldii and Chaetoceros furcellatus. *Deep Sea Research Part A. Oceanographic Research Papers*, 38(4):415–430.

Salter, I., Lampitt, R. S., Sanders, R., Poulton, A., Kemp, A. E. S., Boorman, B., Saw, K., and Pearce, R. (2007). Estimating carbon, silica and diatom export from a naturally fertilised phytoplankton bloom in the Southern Ocean using PELAGRA: A novel drifting sediment trap. *Deep-Sea Research Part II: Topical Studies in Oceanography*, 54(18-20):2233–2259.

Sarmiento, J. L., Gruber, N., Brzezinski, M. A., and Dunne, J. P. (2004). High-latitude controls of thermocline nutrients and low latitude biological productivity. *Nature*, 427(6969):56–60.

Sarmiento, J. L., Hughes, T. M. C., Stouffer, R. J., and Manabe, S. (1998). Simulated response of the ocean carbon cycle to anthropogenic climate warming. *Nature*, 393:245–249.

Sathyendranath, S., Lazzara, L., and Prieur, L. (1987). Variations in the spectral values of specific absorption of phytoplankton. *Limnology and Oceanography*, 32(2):403–415.

Sauer, M. J., Roesler, C. S., Werdell, P. J., and Barnard, A. (2012). Under the hood of satellite empirical chlorophyll a algorithms: revealing the dependencies of maximum band ratio algorithms on inherent optical properties. *Optics Express*, 20(19):20920–20933.

Savtchenko, A., Ouzounov, D., Ahmad, S., Acker, J., Leptoukh, G., Koziana, J., and Nickless, D. (2004). Terra and Aqua MODIS products available from NASA GES DAAC. *Advances in Space Research*, 34:710–714.

Schallenberg, C., Lewis, M. R., Kelley, D. E., and Cullen, J. J. (2008). Inferred influence of nutrient availability on the relationship between Sun-induced chlorophyll fluorescence and incident irradiance in the Bering Sea. *Journal of Geophysical Research*, 113:1–21.

Schaller-Laudel, S., Volke, D., Redlich, M., Kansy, M., Hoffmann, R., Wilhelm, C., and Goss, R. (2015). The diadinoxanthin diatoxanthin cycle induces structural rearrangements of the isolated FCP antenna complexes of the pennate diatom Phaeodactylum tricornutum. *Plant Physiology and Biochemistry*, 96:364–76.

Schlitzer, R. (2002). Carbon export fluxes in the Southern Ocean: results from inverse modeling and comparison with satellite-based estimates. *Deep Sea Research Part II: Topical Studies in Oceanography*, 49:1623–1644.

Schlitzer, R., Anderson, R. F., Dodas, E. M., Lohan, M., Geibert, W., Tagliabue, A., Bowie, A., Jeandel, C., Maldonado, M. T., Landing, W. M., Cockwell, D., Abadie, C., Abouchami, W., Achterberg, E. P., Agather, A., Aguliar-Islas, A., van Aken, H. M., Andersen, M., Archer, C., Auro, M., de Baar, H. J., Baars, O., Baker, A. R., Bakker, K., Basak, C., Baskaran, M., Bates, N. R., Bauch, D., van Beek, P., Behrens, M. K., Black, E., Bluhm, K., Bopp, L., Bouman, H., Bowman, K., Bown, J., Boyd, P., Boye, M., Boyle, E. A., Branellec, P., Bridgestock, L., Brissebrat, G., Browning, T., Bruland, K. W., Brumsack, H. J., Brzezinski, M., Buck, C. S., Buck, K. N., Buesseler, K., Bull, A., Butler, E., Cai, P., Mor, P. C., Cardinal, D., Carlson, C., Carrasco, G., Casacuberta, N., Casciotti, K. L., Castrillejo, M., Chamizo, E., Chance, R., Charette, M. A., Chaves, J. E., Cheng, H., Chever, F., Christl, M., Church, T. M., Closset, I., Colman, A., Conway, T. M., Cossa, D., Croot, P., Cullen, J. T., Cutter, G. A., Daniels, C., Dehairs, F., Deng, F., Dieu, H. T., Duggan, B., Dulaquais, G., Dumousseaud, C., Echegoyen-Sanz, Y., Edwards, R. L., Ellwood, M., Fahrbach, E., Fitzsimmons,

J. N., Russell Flegal, A., Fleisher, M. Q., van de Flierdt, T., Frank, M., Friedrich, J., Fripiat, F., Fröllje, H., Galer, S. J., Gamo, T., Ganeshram, R. S., Garcia-Orellana, J., Garcia-Solsona, E., Gault-Ringold, M., George, E., Gerringa, L. J., Gilbert, M., Godoy, J. M., Goldstein, S. L., Gonzalez, S. R., Grissom, K., Hammerschmidt, C., Hartman, A., Hassler, C. S., Hathorne, E. C., Hatta, M., Hawco, N., Hayes, C. T., Heimbürger, L. E., Helgoe, J., Heller, M., Henderson, G. M., Henderson, P. B., van Heuven, S., Ho, P., Horner, T. J., Hsieh, Y. T., Huang, K. F., Humphreys, M. P., Isshiki, K., Jacquot, J. E., Janssen, D. J., Jenkins, W. J., John, S., Jones, E. M., Jones, J. L., Kadko, D. C., Kayser, R., Kenna, T. C., Khondoker, R., Kim, T., Kipp, L., Klar, J. K., Klunder, M., Kretschmer, S., Kumamoto, Y., Laan, P., Labatut, M., Lacan, F., Lam, P. J., Lambelet, M., Lamborg, C. H., Le Moigne, F. A., Le Roy, E., Lechtenfeld, O. J., Lee, J. M., Lherminier, P., Little, S., López-Lora, M., Lu, Y., Masque, P., Mawji, E., Mcclain, C. R., Measures, C., Mehic, S., Barraqueta, J. L. M., van der Merwe, P., Middag, R., Mieruch, S., Milne, A., Minami, T., Moffett, J. W., Moncoiffe, G., Moore, W. S., Morris, P. J., Morton, P. L., Nakaguchi, Y., Nakayama, N., Niedermiller, J., Nishioka, J., Nishiuchi, A., Noble, A., Obata, H., Ober, S., Ohnemus, D. C., van Ooijen, J., O'Sullivan, J., Owens, S., Pahnke, K., Paul, M., Pavia, F., Pena, L. D., Peters, B., Planchon, F., Planquette, H., Pradoux, C., Puigcorbé, V., Quay, P., Queroue, F., Radic, A., Rauschenberg, S., Rehkämper, M., Rember, R., Remenyi, T., Resing, J. A., Rickli, J., Rigaud, S., Rijkenberg, M. J., Rintoul, S., Robinson, L. F., Roca-Martí, M., Rodellas, V., Roeske, T., Rolison, J. M., Rosenberg, M., Roshan, S., Rutgers van der Loeff, M. M., Ryabenko, E., Saito, M. A., Salt, L. A., Sanial, V., Sarthou, G., Schallenberg, C., Schauer, U., Scher, H., Schlosser, C., Schnetger, B., Scott, P., Sedwick, P. N., Semiletov, I., Shelley, R., Sherrell, R. M., Shiller, A. M., Sigman, D. M., Singh, S. K., Slagter, H. A., Slater, E., Smethie, W. M., Snaith, H., Sohrin, Y., Sohst, B., Sonke, J. E., Speich, S., Steinfeldt, R., Stewart, G., Stichel, T., Stirling, C. H., Stutsman, J., Swarr, G. J., Swift, J. H., Thomas, A., Thorne, K., Till, C. P., Till, R., Townsend, A. T., Townsend, E., Tuerena, R., Twining, B. S., Vance, D., Velazquez, S., Venchiarutti, C., Villa-Alfageme, M., Vivancos, S. M., Voelker, A. H., Wake, B., Warner, M. J., Watson, R., van Weerlee, E., Alexandra Weigand, M., Weinstein, Y., Weiss, D., Wisotzki, A., Woodward, E. M. S., Wu, J., Wu, Y., Wuttig, K., Wyatt, N., Xiang, Y., Xie, R. C., Xue, Z., Yoshikawa, H., Zhang, J., Zhang, P., Zhao, Y., Zheng, L., Zheng, X. Y., Zieringer, M., Zimmer, L. A., Ziveri, P., Zunino, P., and Zurbrick, C. (2018). The GEOTRACES Intermediate Data Product 2017. *Chemical Geology*, 493(June):210–223.

Schrader, P. S., Milligan, A. J., and Behrenfeld, M. J. (2011). Surplus photosynthetic antennae complexes underlie diagnostics of iron limitation in a cyanobacterium. *PLoS ONE*, 6(4).

Sedwick, P. N. and Ditullio, G. R. (1997). Regulation of algal blooms in Antarctic shelf waters by the release of iron from melting sea ice waters. *Geophysical Research Letters*, 24(20):2515–2518.

Seegers, B. N., Stumpf, R. P., Schaeffer, B. A., Loftin, K. A., and Werdell, P. J. (2018). Performance metrics for the assessment of satellite data products: an ocean color case study. *Optics Express*, 26(6):7404.

Shaw, T. J., Raiswell, R., Hexel, C. R., Vu, H. P., Moore, W. S., Dudgeon, R., and Smith, K. L. (2011). Input, composition, and potential impact of terrigenous material from free-drifting icebergs in the Weddell Sea. *Deep Sea Research Part II: Topical Studies in Oceanography*, 58(11-12):1376–1383.

Sieburth, J. M. N., Smetacek, V., and Lenz, J. (1978). Pelagic ecosystem structure: Heterotrophic compartments of the plankton and their relationship to plankton size fractions. *Limnology and Oceanography*, 23(6):1256–1263.

Siegel, D. A., Buesseler, K. O., Doney, S. C., Sailley, S. F., Behrenfeld, M. J., and Boyd, P. W. (2014). Global assessment of ocean carbon export by combining satellite observations and food-web models. *Global Biogeochemical Cycles*, 28:181–196.

Sloyan, B. M. and Rintoul, S. R. (2001a). Circulation, renewal, and modification of Antarctic Mode and Intermediate Water. *Journal of Physical Oceanography*, 31(4):1005–1030.

Sloyan, B. M. and Rintoul, S. R. (2001b). The Southern Ocean limb of the global deep overturning circulation. *Journal of Physical Oceanography*, 31(1):143–173.

Smetacek, V., Assmy, P., and Henjes, J. (2004). The role of grazing in structuring Southern Ocean pelagic ecosystems and biogeochemical cycles. *Antarctic Science*, 16(4):541–558.

Smith, M. E. and Pitcher, G. C. (2015). Saldanha Bay, South Africa I: the use of ocean colour remote sensing to assess phytoplankton biomass. *African Journal of Marine Science*, 37(4):503–512.

Sokolov, S. and Rintoul, S. R. (2002). Structure of Southern Ocean fronts at 140E. *Journal of Marine Systems*, 37(1):151–184.

Sokolov, S. and Rintoul, S. R. (2009). Circumpolar structure and distribution of the antarctic circumpolar current fronts: 1. Mean circumpolar paths. *Journal of Geophysical Research: Oceans*, 114(11):1–19.

Sosik, H. M. and Mitchell, B. G. (1991). Absorption, fluorescence, and quantum yield for growth in nitrogen-limited Dunaliella tertiolecta.

Sosik, H. M. and Mitchell, B. G. (1995). Light absorption by phytoplankton, photosynthetic pigments and detritus in the California Current System. *Deep Sea Research Part I: Oceanographic Research Papers*, 42(10):1717–1748.

Sosik, H. M. and Olson, R. J. (2002). Phytoplankton and iron limitation of photosynthetic efficiency in the Southern Ocean during late summer. *Deep Sea Research Part I: Oceanographic Research Papers*, 49(7):1195–1216.

Stammerjohn, S. E., Yuan, X., Smith, R. C., Rind, D., and Martinson, D. G. (2008). Trends in Antarctic annual sea ice retreat and advance and their relation to El Nino-Southern Oscillation and Southern Annular Mode variability. *Journal of Geophysical Research*, 113(C3):1–20.

Stefels, J. and Van Boekel, W. H. M. (1993). Production of DMS from dissolved DMSP in axenic cultures of the marine phytoplankton species Phaeocystis sp. *Marine Ecology Progress Series*, 97(1):11–18.

Stoecker, D. K., Gifford, D. J., and Putt, M. (1994). Preservation of marine planktonic ciliates - Losses and cell shrinkage during fixation. *Marine Ecology Progress Series*, 110(2-3):293.

Stokes, G. G. (1852). On the change of refrangibility of light. *Philosophical transactions of the Royal Society of London*, 142:463–562.

Stramski, D., Bricaud, A., and Morel, A. (2001). Modeling the inherent optical properties of the ocean based on the detailed composition of the planktonic community. *Applied Optics*, 40(18):2929–2945.

Stransky, H. and Hager, A. (1970). Das Carotinoidmuster und die Verbreitung des lichtinduzierten Xanthophyllcyclus in verschiedenen Algenklassen. *Archiv Mikrobiologie*, 71(2):164–190.

Strzepek, R. F., Hunter, K. A., Frew, R. D., Harrison, P. J., and Boyd, P. W. (2012). Iron-light interactions differ in Southern Ocean phytoplankton. *Limnology and Oceanography*, 57(4):1182–1200.

Strzepek, R. F., Maldonado, M. T., Hunter, K. A., Frew, R. D., and Boyd, P. W. (2011). Adaptive strategies by Southern Ocean phytoplankton to lessen iron limitation: Uptake of organically complexed iron and reduced cellular iron requirements. *Limnology and Oceanography*, 56(6):1983–2002.

Strzepek, R. F. and Price, N. M. (2000). Influence of irradiance and temperature on the iron content of the marine diatom Thalassiosira weissflogii (Bacillariophyceae). *Marine Ecology Progress Series*, 206:107–117.

Stuart, V., Sathyendranath, S., Platt, T., Maass, H., and Irwin, B. D. (1998). Pigments and species composition of natural phytoplankton populations: effect on the absorption spectra. *Journal of Plankton Research*, 20(2):187–217.

Styring, S., Sjöholm, J., and Mamedov, F. (2012). Two tyrosines that changed the world: Interfacing the oxidizing power of photochemistry to water splitting in photosystem II. *Biochimica et biophysica acta*, 1817:76–87.

Suggett, D., Kraay, G., Holligan, P., Davey, M., Aiken, J., and Geider, R. (2001). Assessment of photosynthesis in a spring cyanobacterial bloom by use of a fast repetition rate fluorometer. *Limnology and Oceanography*, 46(4):802–810.

Suggett, D., Moore, C., Hickman, A., and Geider, R. (2009). Interpretation of fast repetition rate (FRR) fluorescence: signatures of phytoplankton community structure versus physiological state. *Marine Ecology Progress Series*, 376:1–19.

Suggett, D. J., Macintyre, H. L., and Geider, R. J. (2004). Evaluation of biophysical and optical determinations of light absorption by photosystem II in phytoplankton. *Limnology and Oceanography: Methods*, 2(10):316–332.

Sullivan, C. W., Arrigo, K. R., McClain, C. R., Comiso, J. C., and Firestone, J. (1993). Distributions of phytoplankton blooms in the southern ocean. *Science (New York, N.Y.)*, 262(5141):1832–7.

Sunda, W. G. and Huntsman, S. A. (1995). Iron uptake and growth limitation in oceanic and coastal phytoplankton. *Marine Chemistry*, 50(1-4):189–206.

Sunda, W. G. and Huntsman, S. A. (1997). Interrelated influence of iron, light and cell size on marine phytoplankton growth. *Nature*, 390:389–392.

Sverdrup, H. U. (1953). On Conditions for the vernal blooming of phytoplankton. *ICES Journal of Marine Science*, 18(3):287–295.

Swart, S., Speich, S., Ansorge, I. J., and Lutjeharms, J. R. E. (2010). An altimetry-based gravest empirical mode south of Africa: 1. Development and validation. *Journal of Geophysical Research*, 115(C3):C03002.

Swart, S., Thomalla, S. J., and Monteiro, P. M. S. (2015). The seasonal cycle of mixed layer dynamics and phytoplankton biomass in the Sub-Antarctic Zone: A high-resolution glider experiment. *Journal of Marine Systems*, 147:103–115.

Swart, S., Thomalla, S. J., Monteiro, P. M. S., and Ansorge, I. J. (2012). Mesoscale features and phytoplankton biomass at the GoodHope line in the Southern Ocean during austral summer. *African Journal of Marine Science*, 34(4):511–524.

Takahashi, T., Sutherland, S. C., Wanninkhof, R., Sweeney, C., Feely, R. A., Chipman, D. W., Hales, B., Friederich, G., Chavez, F., Sabine, C., Watson, A., Bakker, D. C., Schuster, U., Metzl, N., Yoshikawa-Inoue, H., Ishii, M., Midorikawa, T., Nojiri, Y., Körtzinger, A., Steinhoff, T., Hoppema, M., Olafsson, J., Arnarson, T. S., Tilbrook, B., Johannessen, T., Olsen, A., Bellerby, R., Wong, C., Delille, B., Bates, N., and de Baar, H. J. (2009). Climatological mean and decadal change in surface ocean pCO2, and net sea-air CO2 flux over the global oceans. *Deep Sea Research Part II: Topical Studies in Oceanography*, 56:554–577.

Talmy, D., Blackford, J., Hardman-Mountford, N. J., Dumbrell, A. J., and Geider, R. J. (2013). An optimality model of photoadaptation in contrasting aquatic light regimes. *Limnology and Oceanography*, 58(5):1802–1818.

Taylor, M. H., Losch, M., and Bracher, A. (2013). On the drivers of phytoplankton blooms in the Antarctic marginal ice zone: A modeling approach. *Journal of Geophysical Research: Oceans*, 118:63–75.

Thomalla, S. J., Fauchereau, N., Swart, S., and Monteiro, P. M. S. (2011). Regional scale characteristics of the seasonal cycle of chlorophyll in the Southern Ocean. *Biogeosciences*, 8(10):2849–2866.

Timmermans, K. R., Davey, M. S., van der Wagt, B., Snoek, J., Geider, R. J., Veldhuis, M. J. W., Gerringa, L. J. A., and de Baar, H. J. W. (2001). Co-limitation by iron and

light of Chaetoceros brevis, C. dichaeta and C. calcitrans (Bacillariophyceae). *Marine Ecology Progress Series*, 217:287–297.

Timmermans, K. R., van der Wagt, B., and de Baar, H. J. (2004). Growth rates, half-saturation constants, and silicate, nitrate, and phosphate depletion in relation to iron availability of four large, open-ocean diatoms from the Southern Ocean. *Limnology and Oceanography*, 49(6):2141–2151.

Timmermans, K. R., van der Woerd, H. J., Wernand, M. R., Sligting, M., Uitz, J., and de Baar, H. J. W. (2008). In situ and remote-sensed chlorophyll fluorescence as indicator of the physiological state of phytoplankton near the Isles Kerguelen (Southern Ocean). *Polar Biology*, 31(5):617–628.

Ting, C. S. and Owens, T. G. (1993). Photochemical and nonphotochemical fluorescence quenching processes in the diatom Phaeodactylum tricornutum. *Plant Physiology*, 101(4):1323–1330.

Ting, C. S., Rocap, G., King, J., Chisholm, S. W., and Rocap, G. (2002). Cyanobacterial photosynthesis in the oceans: the origins and significance of divergent light-harvesting strategies. *Trends in Microbiology*, pages 1–9.

Tréguer, P. and Jacques, G. (1992). Dynamics of nutrients and phytoplankton, and fluxes of carbon, nitrogen, and silicon in the Antarctic Ocean. *Polar Biology*, 12:149–162.

Tremblay, J. E., Lucas, M. I., Kattner, G., Pollard, R., Strass, V. H., Bathmann, U., and Bracher, a. (2002). Significance of the Polar Frontal Zone for large-sized diatoms and new production during summer in the Atlantic sector of the Southern Ocean. *Deep-Sea Research Part II: Topical Studies in Oceanography*, 49(18):3793–3811.

Trull, T., Bray, S. G., Manganini, S., Honjo, S., and Francois, R. (2001a). Moored sediment trap measurements of carbon export in the Subantarctic and Polar Frontal Zones of the Southern Ocean, south of Australia. *Journal of Geophysical Research*, 106(C12):31489–31509.

Trull, T., Rintoul, S. R., Hadfield, M., and Abraham, E. R. (2001b). Circulation and seasonal evolution of polar waters south of Australia: implications for iron fertilization of the Southern Ocean. *Deep Sea Research Part II: Topical Studies in Oceanography*, 48:2439–2466.

Uitz, J., Claustre, H., Morel, A., and Hooker, S. B. (2006). Vertical distribution of phytoplankton communities in open ocean: An assessment based on surface chlorophyll. *Journal of Geophysical Research*, 111(C08005):1–23.

van de Poll, W. H., Alderkamp, A.-C., Janknegt, P. J., Roggeveld, J., and Buma, A. G. J. (2006). Photoacclimation modulates excessive photosynthetically active and ultraviolet radiation effects in a temperate and an Antarctic marine diatom. *Limnology and Oceanography*, 51(3):1239–1248.

van de Poll, W. H., Janknegt, P., van Leeuwe, M. A., Visser, R. J. W., and Buma, A. G. J. (2009). Excessive irradiance and antioxidant responses of an Antarctic marine diatom exposed to iron limitation and to dynamic irradiance. *Journal of Photochemistry and Photobiology B: Biology*, 94:32–37.

van de Poll, W. H., Lagunas, M., De Vries, T., Visser, R. J. W., and Buma, A. G. J. (2011). Non-photochemical quenching of chlorophyll fluorescence and xanthophyll cycle responses after excess PAR and UVR in Chaetoceros brevis, Phaeocystis antarctica and coastal Antarctic phytoplankton. *Marine Ecology Progress Series*, 426:119–131.

van de Poll, W. H., van Leeuwe, M. A., Roggeveld, J., and Buma, A. G. J. (2005). Nutrient limitation and high irradiance acclimation reduce par and UV-induced viability loss in the Antarctic diatom Chaetoceros Brevis (Bacillariophyceae). *Journal of Phycology*, 41:840–850.

van de Poll, W. H., Visser, R. J. W., and Buma, A. G. J. (2007). Acclimation to a dynamic irradiance regime changes excessive irradiance sensitivity of Emiliania huxleyi and Thalassiosira weissflogii. *Limnology and Oceanography*, 52(4):1430–1438.

Vassiliev, I. R., Antonkine, M. L., and Golbeck, J. H. (2001). Iron-sulfur clusters in type I reaction centers. *Biochimica et Biophysica Acta - Bioenergetics*, 1507:139–160.

Veldhuis, M. J. and Kraay, G. W. (2000). Application of flow cytometry in marine phytoplankton research: current applications and future perspectives. *Scientia Marina*, 64(2):121–134.

Vidussi, F., Claustre, H., Manca, B. B., Luchetta, A., and Marty, J. C. (2001). Phytoplankton pigment distribution in relation to upper thermocline circulation in the eastern Mediterranean Sea during winter. *Journal of Geophysical Research*, 106:939–956.

von Liebig, J. F. (1841). *Organic chemistry in its applications to agriculture and physiology*. J. Owen.

Vredenberg, W. J. and Slooten, L. (1967). Chlorophyll a fluorescence and photochemical activities of chloroplast fragments. *Biochimica et Biophysica Acta (BBA) - Bioenergetics*, 143(3):583–594.

Wang, S., Maltrud, M., Elliott, S., Cameron-Smith, P., and Jonko, A. (2018). Influence of dimethyl sulfide on the carbon cycle and biological production. *Biogeochemistry*, 138(1):49–68.

Welschmeyer, N. A. and Hoepffner, N. (1986). Rapid xanthophyll cycling: an in situ tracer mixing in the upper ocean. *Eos Transactions American Geophysical Union*, 67:969.

Werdell, P. J. and Bailey, S. W. (2005). An improved in-situ bio-optical data set for ocean color algorithm development and satellite data product validation. *Remote Sensing of Environment*, 98(1):122–140.

Westberry, T. K., Behrenfeld, M. J., Milligan, A. J., and Doney, S. C. (2013). Retrospective satellite ocean color analysis of purposeful and natural ocean iron fertilization. *Deep-Sea Research Part I: Oceanographic Research Papers*, 73:1–16.

Westberry, T. K. and Siegel, D. A. (2003). Phytoplankton natural fluorescence variability in the Sargasso Sea. *Deep-Sea Research Part I: Oceanographic Research Papers*, 50(3):417–434.

Wilhelm, C. (1990). The biochemistry and physiology of light-harvesting processes in chlorophyll b- and chlorophyll c-containing algae. *Plant physiology and biochemistry*, 28(2):293–306.

Wilkins, D., Lauro, F. M., Williams, T. J., Demaere, M. Z., Brown, M. V., Hoffman, J. M., Andrews-Pfannkoch, C., Mcquaid, J. B., Riddle, M. J., Rintoul, S. R., and Cavicchioli, R. (2013). Biogeographic partitioning of Southern Ocean microorganisms revealed by metagenomics. *Environmental Microbiology*, 15(5):1318–1333.

Wilson, A., Ajlani, G., Verbavatz, J.-M., Vass, I., Kerfeld, C. A., and Kirilovsky, D. (2006). A soluble carotenoid protein involved in phycobilisome-related energy dissipation in cyanobacteria. *The Plant cell*, 18:992–1007.

Wilson, A., Punginelli, C., Gall, A., Bonetti, C., Alexandre, M., Routaboul, J.-M., Kerfeld, C. A., van Grondelle, R., Robert, B., Kennis, J. T. M., and Kirilovsky, D. (2008). A photoactive carotenoid protein acting as light intensity sensor. *Proceedings of the National Academy of Sciences of the United States of America*, 105(33):12075–80.

Wollman, F. A. (1984). Correlation between changes in light energy distribution and changes in thylakoid membrane polypeptide phosphorylation in Chlamydomonas reinhardtii. *The Journal of Cell Biology*, 98(1):1–7.

Wolters, M. (2002). Silicate in brackish or seawater. In *QuickChem Method 31-114-27-1-D*. Lachat Instruments, Colorado, USA.

Wright, S. W., Ishikawa, A., Marchant, H. J., Davidson, A. T., van den Enden, R. L., and Nash, G. V. (2009). Composition and significance of picophytoplankton in Antarctic waters. *Polar Biology*, 32(5):797–808.

Wright, S. W., Thomas, D. P., Marchant, H. J., Higgins, H. W., Mackey, M. D., and Mackey, D. J. (1996). Analysis of phytoplankton of the Australian sector of the Southern Ocean: comparisons of microscopy and size frequency data with interpretations of pigment HPLC data using the CHEMTAX matrix factorisation program. *Marine Ecology Progress Series*, 144:285–298.

Wright, S. W., van den Enden, R. L., Pearce, I., Davidson, A. T., Scott, F. J., and Westwood, K. J. (2010). Phytoplankton community structure and stocks in the Southern Ocean (30-80E) determined by CHEMTAX analysis of HPLC pigment signatures. *Deep-Sea Research Part II: Topical Studies in Oceanography*, 57(9-10):758–778.

Wu, H., Roy, S., Alami, M., Green, B. R., and Campbell, D. A. (2012). Photosystem II photoinactivation, repair, and protection in marine centric diatoms. *Plant physiology*, 160(1):464–76.

Wulff, A. and Wängberg, S. Å. (2004). Spatial and vertical distribution of phytoplankton pigments in the eastern Atlantic sector of the Southern Ocean. *Deep-Sea Research Part II: Topical Studies in Oceanography*, 51(22-24):2701–2713.

Yentsch, C. S. (1960). The influence of phytoplankton pigments on the colour of sea water. *Deep Sea Research*, 7(1):1–9.

Yentsch, C. S. (1962). Measurement of visible light absorption by particulate matter in the ocean. *Limnology and Oceanography*, 7(2):207–217.

Yentsch, C. S. and Menzel, D. W. (1963). A method for the determination of phytoplankton chlorophyll and phaeophytin by fluorescence. *Deep Sea Research and Oceanographic Abstracts*, 10(3):221–231.

Yentsch, C. S. and Yentsch, C. M. (1979). Fluorescence spectral signatures: the characterization of phytoplankton populations by the use of excitation and emission spectra. *Journal of Marine Research*, 37:471–483.

Yoshida, M., Horiuchi, T., and Nagasawa, Y. (2011). In situ multi-excitation chlorophyll fluorometer for phytoplankton measurements: Technologies and applications beyond conventional fluorometers. In *Proceedings of the OCEANS*, pages 1–4, Waikoloa, HI, USA. IEEE Conference Publications.

Zapata, M., Jeffrey, S. W., Wright, S. W., Rodríguez, F., Garrido, J. L., and Clementson, L. (2004). Photosynthetic pigments in 37 species (65 strains) of Haptophyta: Implications for oceanography and chemotaxonomy. *Marine Ecology Progress Series*, 270:83–102.

Zavafer, A., Chow, W. S., and Cheah, M. H. (2015). The action spectrum of Photosystem II photoinactivation in visible light. *Journal of Photochemistry and Photobiology B: Biology*.

Zentara, S.-J. and Kamykowski, D. (1981). Geographic variations in the relationship between silicic acid and nitrate in the South Pacific Ocean. *Deep Sea Research Part A. Oceanographic Research Papers*, 28(5):455–465.

Zhai, P.-W., Boss, E., Franz, B., Werdell, P., and Hu, Y. (2018). Radiative transfer modeling of phytoplankton fluorescence quenching processes. *Remote Sensing*, 10(8):1309.

Zhu, S. H. and Green, B. R. (2010). Photoprotection in the diatom Thalassiosira pseudonana: Role of LI818-like proteins in response to high light stress. *Biochimica et Biophysica Acta*, 1797:1449–1457.

Zibordi, G., Donlon, C. J., and Parr, A. C. (2014). *Optical radiometry for ocean climate measurements*. Academic Press.